Dissertation zur Erlangung des Doktorgrades

der Fakultät Chemie und Pharmazie

der Ludwig-Maximilians-Universität München

From Amides over Imides to Nitrides – A Journey Through the Synthesis Potential of Ammonothermal Synthesis

Florian Maximilian Engelsberger

aus

Dresden, Deutschland

2024

Erklärung

Diese Dissertation wurde im Sinne von §7 der Promotionsordnung vom 28. November 2011 von Herrn Prof. Dr. Wolfgang Schnick betreut.

Eidesstattliche Versicherung

Diese Dissertation wurde eigenständig und ohne unerlaubte Hilfe erarbeitet.

München, den 10.12.2024 ……..……

Florian Maximilian Engelsberger

Dissertation eingereicht am:	10.12.2024
1. Gutachter:	Prof. Dr. Wolfgang Schnick
2. Gutachter:	Prof. Dr. Dirk Johrendt
Mündliche Prüfung am:	22.01.2025

Das schönste Glück des denkenden Menschen ist,

das Erforschliche erforscht zu haben und das

Unerforschliche zu verehren.

Johann Wolfgang von Goethe

Danksagung

An erster Stelle möchte ich mich bei meinem Doktorvater, Prof. Wolfgang Schnick, dafür bedanken, dass er es mir ermöglicht hat, meine Promotion in seinem Arbeitskreis durchzuführen. Unter seiner Betreuung seit der Bachelorarbeit habe ich stets perfekte Bedingungen vorgefunden, um an verschiedensten mehr oder weniger lumineszierenden Verbindungen zu forschen. Dabei war mir stets ein selbstständiges Vorgehen möglich, wofür ich ihm sehr dankbar bin. Weiterhin möchte ich mich bei ihm für die Gelegenheiten bedanken, bei denen ich meine Ergebnisse auf diversen Tagungen in inspirierenden Umfeldern präsentieren konnte.

Prof. Dirk Johrendt danke ich dafür, dass er die Bewertung dieser Arbeit als Zweitgutachter übernimmt. Weiterhin möchte ich mich bei Prof. Oliver Oeckler, Prof. Silvija Markic, Prof. Thomas Klapötke und Prof. Konstantin Karaghiosoff dafür bedanken, dass sie als weitere Mitglieder für meine Prüfungskommission zur Verfügung stehen.

Für die Einarbeitung in die Themengebiete der Nitridosilicate und der Ammonothermalsynthese, die beide eine zentrale Rolle in meiner Promotion gespielt haben, möchte ich mich bei Dr. Philipp Bielec und Dr. Mathias Mallmann bedanken, die mir während meiner Bachelor- und Masterarbeit stets mit Rat und Tat zur Seite standen.

Meinen Laborkolleginnen und -kollegen Dr. Mathias Mallmann, Dr. Lisa Gamperl, Dr. Stefan Rudel, Lina Beisswenger, Robert Calaminus, Thanh Chau, und Mirjam Zipkat, die mich alle für unterschiedliche Zeiträume meiner Masterarbeit und Promotion begleitet haben, möchte ich für eine stets positive und konstruktive Arbeitsatmosphäre in Labor D2.107 danken. Diese war auch außerhalb des Labors stets durch ein harmonisches Miteinander geprägt, wofür ich mich bei allen Mitgliedern der Arbeitskreise Schnick, Johrendt, Lotsch, Hoch und Kloß bedanken möchte.

Für ihre jeweiligen Beiträge zu den präsentierten Ergebnissen und Publikationen möchte ich mich bei meinen Praktikanten Matthias Klimpel, Amelie Heilmaier und Kilian Möchel, sowie den Co-Autoren Thanh Chau, Dr. Thomas Bräuniger, Kristian Witthaut, Reinhard Pritzl, Jennifer Steinadler und Dr. Peter Schmidt bedanken.

Da für eine Auswertung und Einordung von Messdaten, ihre Erstellung unabdingbar ist, möchte ich mich bei Christian Minke, Dr. Peter Mayer, Dr. Sophia Wandelt, Reinhard Pritzl, Lukas Nusser, Dr. Marwin Dialer und Dr. Peter Schmidt für diverse Messungen am REM, am NMR, am Einkristall-Diffraktometer und an verschiedenen Lumineszenzmessgeräten bedanken.

Olga Lorenz, Wolfgang Wünschheim und Dr. Dieter Rau möchte ich dafür danken, dass sie während meiner Promotion für einen reibungslosen Ablauf gesorgt haben und stets geholfen haben, wenn es Probleme mit Verwaltung, EDV oder diversen Geräten gab.

Bei meinen Freunden und Kollegen Amalina Buda, Thanh Chau, Dr. Marwin Dialer, Dr. Lisa Gamperl, Dr. Tobias Giftthaler, Dr. Simon Kloß, Thaddäus Koller, Reinhard Pritzl, Dr. Sophia Wandelt und Mirjam Zipkat möchte ich mich bedanken, dass sie nicht nur für fachliche Diskussionen, Korrekturlesen oder Messungen immer Ansprechpartner waren, sondern besonders auch dafür, dass die nötige gedankliche Zerstreuung während der Promotionsphase in der Freizeit und den Pausen nie zu kurz kam.

Meinen langjährigen Studienfreunden Alex, Silena, Yannick, Singer und Thaddl möchte ich dafür danken, dass wir uns während der Reise, die wir vor über 10 Jahren gemeinsam im Vorpraktikum begonnen haben, nie aus den Augen verloren haben und während dieser Zeit immer schöne gemeinsame Momente erleben.

Meiner gesamten Familie möchte ich danken, dass sie mich während meines ganzen Studiums stets unterstützt haben, wenn es mal nicht so glatt lief und sich mit mir über alle kleinen und großen Erfolge in der Zeit gefreut haben. Vielen Dank für alles!

Zum Schluss möchte ich mich noch bei meiner Ehefrau Madlen bedanken. Danke, dass du seit so langer Zeit immer an meiner Seite stehst und dadurch einfach alles leichter, schöner und besser machst!

Table of Contents

1 Introduction

The synthesis of nitride materials always requires considerable effort. This originates from the characteristics that molecular nitrogen contains a triple bond resulting in a bond energy of 941 kJ(mol)$^{-1}$ that has to be overcome for bond cleavage and that nitrogen has a positive electron affinity of 0.07 eV which further impedes the formation of nitride ions.[1-2] Additionally, the formation of nitrides always competes with the formation of oxides when atmospheric conditions are provided. Here, the lower energy of the oxygen double bond (498 kJ(mol)$^{-1}$) and the strongly negative electron affinity (−1.46 eV) leads to a preferred formation of oxide compounds over nitride compounds.[1,3] Consequently, nitride minerals are very rare in nature and mostly observed in meteorites.[4] While the exclusion of the competing oxygen from the reaction atmosphere can be realized using closed reaction systems, the activation of molecular nitrogen as a nitrogen source is usually energy-consuming. Therefore, high-temperature methods have been developed which offer a broad access to several nitrides at temperatures of up to 2270 K in resistance heating or high frequency furnaces which allow the activation of molecular nitrogen.[5-7] On the other hand, some nitrides, such as P_3N_5, decompose at higher temperatures. Following the principle of Le Chatelier, this degradation can be counteracted by applying external pressure.[8] Here, the application of the high-pressure/high-temperature synthesis allows the access to compound classes like the nitridophosphates at pressures of up to 25 GPa and temperatures of up to 2070 K.[9-10] The downside of such high-pressure methods lies in the sample quantities which are limited to small amounts to enable the application of large pressures during the reaction and therefore impede an industrial application.

The ammonothermal synthesis allows to overcome some of these problems that arise during nitride synthesis. It is part of the larger group of solvothermal syntheses which are broadly defined as processes in closed reaction vessels inducing chemical reactions in the presence of a solvent at a temperature higher than the boiling temperature of this solvent and at elevated pressures.[11] These processes are often applied to achieve well-defined and large single crystals of various compounds.[12] The ammonothermal synthesis was developed by Prof. Herbert Jacobs and coworkers in analogy to the hydrothermal synthesis.[13-14] While the hydrothermal synthesis employs water as a solvent and is widely used to obtain oxides, the ammonothermal synthesis uses anhydrous ammonia as a solvent. Like water, ammonia is a protic solvent that shows to a small amount autoprotolysis according to equation (1):

$$2\,NH_3 \rightarrow NH_4^+ + NH_2^- \qquad (1)$$

Ammonia as an amphoteric solvent can act as both an acid and as a base as it comprises not only a free electron pair to act as proton acceptor but also contains three protons that can be released. While protonation of ammonia leads to the formation of ammonium ions (NH_4^+), formal step-wise

deprotonation of ammonia results in the formation of amides (NH_2^-), imides (NH^{2-}), and nitrides (N^{3-}).[15]

Ammonothermal reactions are usually performed at temperatures and pressures above the critical point of ammonia (405.2 K, 113 MPa).[16-17] The supercritical state of ammonia, generated at these conditions, provides some advantages such as an increased relative permittivity which comes with higher solubility for inorganic materials. This allows synthetic access towards amides, imides and nitrides in a dissolution-recrystallization-based process.[18] For a further improvement of the solubility of inorganic materials in supercritical ammonia, so-called mineralizers are utilized. They allow to adjust the reaction environment into ammonobasic (NH_2^- predominant), ammononeutral or ammonoacidic (NH_4^+ predominant) conditions by increasing the concentration of the respective ions. While alkali metal amides or azides are frequently used as ammonobasic mineralizers, the ammonium halides are commonly employed to create ammonoacidic reaction conditions.[18] The desired reaction environment is as well decisive for the selection of autoclave and liner materials as ammonoacidic conditions are more corrosive than the ammonobasic ones.[19-20] Additionally, mineralizers are crucial to control dissolution recrystallization processes as they might lead to severe changes in the solubility. So, for the ammonoacidic growth of GaN, a higher solubility at higher temperatures is observed while ammonobasic conditions show a retrograde solubility with a precipitation of the product in the hot section of the autoclave at higher temperatures.[21] For a deeper understanding of the dissolution and recrystallization mechanisms involved during the ammonothermal crystal growth, the characterization of intermediate species is crucial to enable an increased synthetic control using this method.[22]

To withstand the reaction conditions involving not only high temperatures and pressures but as well the highly corrosive solvent ammonia in a supercritical state, specially designed reaction vessels, so-called autoclaves, are required. The custom-built autoclaves used in the context of this dissertation were designed and built within the project "*Ammono-FOR: Chemistry and technology of ammonothermal synthesis of nitrides*", funded by the German Science Foundation (DFG). The interdisciplinary cooperation within this group resulted in the construction of two different types of autoclaves made from the two nickel-based superalloys Inconel® 718 and Haynes® 282® exhibiting high yield and tensile strength (Figure 1.1). These autoclaves allow to apply temperatures of up to 1070 K and pressures of up to 300 MPa during the reactions.[22-23] To separate the starting materials from the inner wall of the autoclave in order to prevent contaminations, open reaction containers, which are referred to as liners, are employed. As liner materials, metals that are stable in supercritical ammonia, like niobium and tantalum, are often used, but ceramic materials such as Si_3N_4 can be employed as well.[18,20,24]

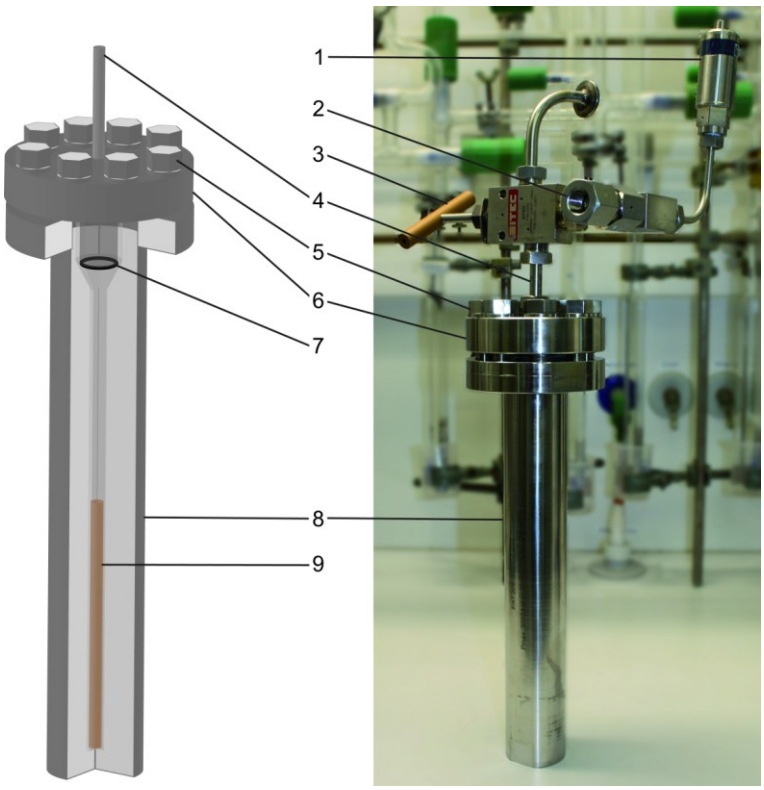

Figure 1.1: Schematic representation of the autoclave body (left) and picture of an assembled autoclave made from Inconel® 718 (right) with pressure transmitter (1), safety head with rupture disc (2), hand valve (3), Inconel® 718 connection pipe (4), screws (5), lid (6), silver-coated sealing C-ring (7), autoclave body (8) and liner (9).

During ammonothermal reactions, the utilization of a closed autoclave enables exclusion of atmospheric oxygen from the reaction atmosphere. Furthermore, the application of supercritical ammonia as a significantly more reactive nitrogen source than molecular nitrogen as well as the utilization of mineralizers to increase solubility of inorganic compounds allow to apply relatively mild synthesis temperatures during ammonothermal nitride synthesis. Thereby, oxidation states that are difficult to attain can be stabilized and metastable chemical compounds can be synthesized.[25] Furthermore, the ammonothermal synthesis does not only prevent decomposition of the synthesized nitride materials by application of an elevated pressure, but also allows to obtain higher sample quantities compared to the high-pressure/high-temperature methods mentioned before. Regarding these characteristic features, the ammonothermal synthesis presents itself as a versatile synthesis method for amide, imide and nitride materials.[22]

Among the ammonothermally synthesized nitride materials, the crystal growth of the binary nitride GaN is by far the best-investigated system.[18,26] The relevance of this system arises from the application of GaN as the most important optoelectronic semiconductor. While the chemical vapor phase synthesis is by now a well-established industrial process, whose development was awarded with the Nobel Price in 2014, the synthesis of large single crystals is still challenging.[27-30] Such single crystals of sufficient size with low defect concentrations could be used for homo-epitaxial growth of GaN which has the potential to reduce the defect concentration, a critical parameter in

the production of semiconductor components.[29] A congruent melting of GaN to obtain single crystals from melts necessitates a nitrogen pressure of 6 GPa to prevent decomposition of the product resulting in a melting point of 2470 K.[31] Here, the ammonothermal growth of GaN single crystals at pressures up to 600 MPa and temperatures up to 1070 K presents an industrially more applicable approach. Intensive research in the past decades shows promising results as high-purity single crystals of GaN and growth rates of up to 170 µm per day could be achieved while waver diameters of up to 100 mm can be employed in this method.[32-34]

As the ammonothermal growth of GaN was prospect of several investigations in the past decades, research results on the ammonothermal synthesis of other nitride materials are quite limited.[22] As early investigations focused on the synthesis of single crystals of amides with sufficient size for X-ray diffraction analysis at that time, the application of higher temperatures resulted in the observation of different imides as well as some examples of nitride materials. These ammonothermally prepared compounds are well reviewed by Richter *et al.* and a review from Häusler *et al*. that focuses on the ammonothermal progress of nitride synthesis up to 2017.[18,35] As this dissertation focuses mainly on nitride compounds comprising three or more elements, a general overview on ternary and higher nitride compounds from ammonothermal preparations is given as an excerpt of the ammonothermal synthesis progress in the following. Additionally, the respective introductions within the respective chapters will give detailed information on the compounds from ammonothermal preparations relevant for the respective chapters.

From the discovery of the first nitride from ammonothermal reactions, Be_3N_2, in 1966, it took some time until the first ternary nitrides $ATaN_2$ (A = Na, K, Rb, Cs) were prepared using this method in 1989.[36-37] In the following years, a few more ternary nitrides were prepared by Jacobs and coworkers, namely $Li_2Ta_3N_5$, $NaSi_2N_3$ and $K_3P_6N_{11}$.[38-40] After establishing the Ammono-FOR research group, the ammonothermally accessible nitrides were complemented by the synthesis of the ternary Grimm–Sommerfeld analogous nitrides *II-IV*-N_2 and Li-IV_2-N_3 (II = Mg, Mn, Zn; IV = Si, Ge) crystallizing in wurtzite-related crystal structures.[41-42] Additionally, ternary nitridophosphates $LiPN_2$, α- and β-$Li_{10}P_4N_{10}$, $Li_{18}P_6N_{16}$, M_2PN_3 (M = Mg, Ca, Zn), SrP_8N_{14}, and $Sr_3P_3N_7$ could be accessed using the ammonothermal method.[18,35,43-45] The preparation of these nitridophosphates shows that the ammonothermal approach is suitable to obtain different structural features in tetrahedra-based networks from isolated units over chains and layers up to complex three-dimensional networks in different condensation degrees.

When it comes to multinary nitrides, oxide nitrides or imide nitrides comprising four or more elements from ammonothermal conditions, the number of reported examples is very limited. Multinary compounds containing only nitride ions could be prepared ammonothermally for the first time in wurtzite-related crystal structures for the compounds $MAlSiN_3$ (M = Ca, Sr),

$CaGaSiN_3$, $Ca_{1-x}Li_xAl_{1-x}Ge_{1+x}N_3$, as well as for the two solid solution series $(II^a,II^b)SiN_2$ and $(II^a,II^b)GeN_2$ (II = Mg, Mn, Zn).[23,46-52]

The reported oxide nitrides from ammonothermal reactions comprise mainly the compounds $RETaON_2$ (RE = La, Ce, Pr, Nd, Sm, Gd), $LaNbON_2$, $BaTaON_2$, and $AEMO_2N$ (AE = Sr, Ba; M = Nb, Ta) crystallizing in perovskite structures next to the Ruddlesden-Popper phase $Eu_3Ta_2N_4O_3$.[53-58] Additionally, it was possible to synthesize multinary compounds comprising tetrahedra-based structures with isolated tetrahedra for the oxonitridophosphate Ba_2PO_3N and exhibiting one-dimensional tetrahedral chains for oxonitridosilicate $Ca_{1+x}Y_{1-x}SiN_{3-x}O_x$ ($x > 0$).[59-60]

The group of imide nitrides might play a crucial role during nitride formation in the ammonothermal process, as the imide anion NH^{2-} could serve as intermediate species during the reaction from the uncharged NH_3 to the final N^{3-} anion. However, only few imide nitrides from ammonothermal reactions were prepared until now. They were mainly observed containing the elements phosphorus or silicon and forming tetrahedra-based structures. As a parent compound for the imidonitridophosphates, the ternary phosphorus imide nitride HPN_2 could be obtained ammonothermally enabling the determination of the hydrogen positions in the crystal structure.[61] Isolated $P(NH)_4$ tetrahedra were observed in the imidophosphate amide $Cs_5[P(NH)_4](NH_2)_2$, while adamantane-like anions could be observed for the imidonitridophosphate amides with the lighter alkali metals in $Na_{10}[P_4(NH)_6N_4](NH_2)_6(NH_3)_{0.5}$ and $Rb_8[P_4N_6(NH)_4](NH_2)_2$.[62-64] However, the phosphimates $A_3(PO_2NH)_3$ (A = K, Rb) form isolated tetrahedra-based *dreier*-ring* anions.[65-66] Among the silicon-containing possible intermediates during ammonothermal conditions, only few examples were reported until now. The ternary imide nitride Si_2N_2NH forms a three-dimensional structure, while the amido silicates $M_2SiO_2(NH_2)_2$ (M = K, Rb, Cs) comprise isolated $[SiO_2(NH_2)_2]$ tetrahedra.[67-68] Additionally, the potassium imidonitridosilicate $K_3Si_6N_5(NH)_6$, containing a three-dimensional tetrahedra network, was observed during ammonothermal reactions.[69]

The incorporation of oxide or imide groups into nitride materials comes with some difficulties in the analysis of such mixed anionic compounds. As the inner surface of the autoclaves may contain oxide species, oxide contaminations arising from the autoclave wall are occasionally observed during ammonothermal reactions.[60] Therefore, both of the anions O^{2-} and NH^{2-} can be formed in solution during ammonothermal reactions and may be incorporated into the structure of the product. Due to their identical charge, they cannot be distinguished from charge-neutrality considerations. For X-ray diffraction (XRD) experiments, the atomic form factor f describes how effective X-rays are diffracted by a respective atom type. The difference in the f values of oxygen and nitrogen atoms is pretty small. Additionally, the atomic form factor of hydrogen atoms is close to zero, making a determination of its atomic position from XRD data difficult.[70] This means that

* The terms *dreier*, *vierer*, *sechser*, *siebener* and *achter* rings were coined by Liebau and are derived from the German words „dreier, vierer, sechser, siebener and achter“; a *dreier* ring comprises three tetrahedra centers, a *vierer* ring four tetrahedra centers, and so on.

XRD as the standard analytical method in solid-state chemistry is often not sufficient to distinguish between an oxide and an imide functionalization within the crystal structure.

Therefore, the analysis of the synthesized products during this thesis was complemented by spectroscopic methods. Here, Fourier-Transform infrared (FTIR) spectroscopy of the samples can be conducted to detect the characteristic IR active N−H stretching vibrations of the NH^{2-} group in the region of 3000−3500 cm^{-1}.[71] Additionally, a theoretical IR spectrum may be calculated using density functional theory (DFT) quantum chemical calculations. A comparison of the theoretical to the experimental spectrum can serve as further evidence for the assumption of the correct structure model as well as for the presence of N−H functionality. Furthermore, solid-state nuclear magnetic resonance (NMR) experiments provide a possibility to detect certain nuclei in the sample. Here, the measurement of the nucleus ^{1}H with a spin of ½ and a natural abundance of over 99% is a standard method. To verify that the detected ^{1}H signal originates from the respective main phase and not from a hydrogen-containing side phase, cross polarization (CP) experiments with a different nucleus present in the main product can be performed. During the CP experiment, the polarization is transferred from one nucleus of high natural abundancy (e.g. ^{1}H) to a different nucleus of another element in local proximity to the hydrogen atoms in the structure. This can be exploited if the nucleus which is cross-polarized has a low natural abundancy (e.g. 0.03% for ^{15}N).[72] An assignment of the respective NMR signals to different crystallographic positions may then be attempted using the spectra of the direct polarization and the CP experiments as well as the chemical environment of the different crystallographic positions from the structure model. A combination of these different analytical methods as well as a verification of the resulting structure model to charge density (CHARDI) and bond valence sum (BVS) calculations can subsequently be used as a further indication that the developed structure model is correct and in agreement to all employed analysis methods.[73-74]

The ammonothermal method could already be used to access several structural possibilities in a wide range of compound classes and is not limited to the preparation of thermodynamically stable binary or ternary nitrides in crystal structures such as the perovskite or wurtzite-related structures that were initially prepared. The observation of a rising number of representatives from the multinary nitrides shows that the ammonothermal method generally provides a suitable synthetic access towards these compounds. The few already discovered examples may present only the beginning of the access towards ammonothermal synthesis' untapped potential in multinary nitride synthesis.

This dissertation aims to expand the presented list of multinary nitride compounds as well as to add further information on possible intermediate species during the formation of nitrides and possibilities of synthetic control on this sparsely investigated synthesis method. Additionally, different combination of analytical methods allowed to elucidate the respective compositions and

crystal structures of the presented compounds. Furthermore, a differentiation of the oxide and imide functionality is possible by this comprehensive characterization.

The dissertation will start with the ammonothermal preparation of the pseudo-ternary amide $Na_2Ba(NH_2)_4$ in Chapter 2. This amide comprises a crystal structure showing ordering in the occupation of the octahedral voids for the first time in ternary amides. The discovery of this amide allows a division of this compound class into different groups according to their crystal structures. Additionally, a correlation between a structure-directing influence of the ion radius ratio $r_{A/AE}$ is discussed in detail.

Chapter 3 reports on the successful ammonothermal preparation of the imidonitridophosphate $Ba_4P_4N_8(NH)_2$. The imide nitride forms a crystal structure comprising isolated adamantane-like anions. A multi-step analytical process allowed to determine a crystal structure model showing preferred amide positions among the possible crystallographic nitrogen positions. Additionally, the luminescent behavior of doped samples of $Ba_4P_4N_8(NH)_2:Eu^{2+}$ was analyzed providing data on the internal quantum efficiency of an imidonitridophosphate phosphor for the first time. The ammonothermal access to this compound class allows also to obtain larger sample quantities than before which is a crucial step on the way of these materials towards industrial application.

The imidonitridosilicate $Rb_3Si_6N_5(NH)_6$ presented in Chapter 4, crystallizes isotypically to the potassium compound known from literature. Nevertheless, it is one of only few examples of rubidium ions stabilized in nitride environment. Additionally, NMR spectroscopic investigations not only allowed to proof the presence of the imide functionality in the compound, but the unique conditions of the crystal structure allowed to obtain a first benchmark value for a ^{15}N signal in nitridosilicate environment.

Subsequently, in Chapter 5, the ammonothermal synthesis of the literature-known nitridosilicate compounds $AESiN_2$ (*AE* = Sr, Ba), $Li_2CaSi_2N_4$ and $Ba_2AlSi_5N_9$ is reported. These examples allow to establish, together with the preliminary work from the literature, a universal ammonothermal route towards nitridosilicate compounds allowing access not only towards a variety of structural characteristics but also to a controlled synthesis of ternary and quaternary nitridosilicate compounds.

This approach is then used and refined in Chapter 6, where the access towards nitridosilicate zeolites is established. Here, the choice of the mineralizer from Li_3N, NaN_3, and KN_3, allows to obtain the compounds $Li_2RE_4[Si_4N_8]O_3$ (*RE* = La, Ce), $Ce_3[Si_6N_{11}]$, and $K_{1.25}Ce_{7.75}[Si_{11}N_{21}O_2]O_{0.75}$. Additionally, the complex tetrahedra networks of these compounds are investigated and compared to known nitridosilicate representatives. The results of this chapter might enable a more general access towards nitride zeolites from ammonothermal synthesis as it is already well-established for oxide zeolites from hydrothermal reactions.

1.1 References

[1] E. Riedel, C. Janiak, "Anorganische Chemie", 8th ed., De Gruyter, Berlin, New York, **2011**.

[2] J. Mazeau, F. Gresteau, R. I. Hall, A. Huetz, "Energy and width of $N^-(^3P)$ from observation of its formation by dissociative attachment to N_2 and NO", *J. Phys. B: At. Mol. Phys.* **1978**, *11*, L557–L560.

[3] C. Blondel, "Recent experimental achievements with negative ions", *Phys. Scr.* **1995**, *T58*, 31–42.

[4] W. H. Baur, "Occurrence of Nitride Nitrogen in Silicate Minerals", *Nature* **1972**, *240*, 461–462.

[5] R. Niewa, H. Jacobs, "Group V and VI Alkali Nitridometalates: A Growing Class of Compounds with Structures Related to Silicate Chemistry", *Chem. Rev. (Washington, DC, U. S.)* **1996**, *96*, 2053–2062.

[6] R. Niewa, F. J. DiSalvo, "Recent Developments in Nitride Chemistry", *Chem. Mater.* **1998**, *10*, 2733-2752.

[7] M. Zeuner, S. Pagano, W. Schnick, "Nitridosilicates and Oxonitridosilicates: From Ceramic Materials to Structural and Functional Diversity", *Angew. Chem.* **2011**, *123*, 7898–7920; *Angew. Chem. Int. Ed.* **2011**, *50*, 7754–7775.

[8] H. L. Le Chatelier, "A general statement of the laws of chemical equilibrium", *C. R. Hebd. Seances Acad. Sci.* **1884**, *99*, 786–789.

[9] H. Huppertz, "Multianvil high-pressure / high-temperature synthesis in solid state chemistry", *Z. Kristallogr.* **2004**, *219*, 330–338.

[10] S. D. Kloß, W. Schnick, "Nitridophosphates: A Success Story of Nitride Synthesis", *Angew. Chem.* **2019**, *131*, 8015–8027; *Angew. Chem. Int. Ed.* **2019**, *58*, 7933–7944.

[11] G. Demazeau, "Review. Solvothermal Processes: Definition, Key Factors Governing the Involved Chemical Reactions and New Trends", *Z. Naturforsch., B: J. Chem. Sci.* **2010**, *65*, 999–1006.

[12] K. Byrappa, M. Yoshimura, "Handbook of Hydrothermal Technology", William Andrew Publishing, Oxford, UK, **2012**.

[13] R. Juza, H. Jacobs, H. Gerke, "Ammonothermalsynthese von Metallamiden und Metallnitriden", *Ber. Bunsenges. Phys. Chem.* **1966**, *70*, 1103–1105.

[14] H. Jacobs, D. Schmidt, "High-pressure Ammonolysis in Solid State Chemistry", *Curr. Top. Mater. Sci.* **1982**, *8*, 381–427.

[15] J. Jander, "Anorganische und allgemeine Chemie in flüssigem Ammoniak", Vieweg, Braunschweig, **1966**.

[16] L. Glasser, "Equations of State and Phase Diagrams of Ammonia", *J. Chem. Educ.* **2009**, *86*, 1457−1458.

[17] S. Pimputkar, S. Nakamura, "Decomposition of supercritical ammonia and modeling of supercritical ammonia–nitrogen–hydrogen solutions with applicability toward ammonothermal conditions", *J. Supercrit. Fluids* **2016**, *107*, 17-30.

[18] T. M. M. Richter, R. Niewa, "Chemistry of Ammonothermal Synthesis", *Inorganics* **2014**, *2*, 29−78.

[19] A. C. L. Kimmel, T. F. Malkowski, S. Griffiths, B. Hertweck, T. G. Steigerwald, L. P. Freund, S. Neumeier, M. Göken, J. S. Speck, E. Schluecker, "High-temperature corrosion of Inconel®Alloy 718, Haynes®282®Alloy and CoWAlloy1&2 in supercritical ammonia/ammonium chloride solution", *J. Cryst. Growth* **2018**, *498*, 289−300.

[20] S. Pimputkar, T. F. Malkowski, S. Griffiths, A. Espenlaub, S. Suihkonen, J. S. Speck, S. Nakamura, "Stability of materials in supercritical ammonia solutions", *J. Supercrit. Fluids* **2016**, *110*, 193-229.

[21] S. Schimmel, M. Koch, P. Macher, A.-C. L. Kimmel, T. G. Steigerwald, N. S. A. Alt, E. Schlücker, P. Wellmann, "Solubility and dissolution kinetics of GaN in supercritical ammonia in presence of ammonoacidic and ammonobasic mineralizers", *J. Cryst. Growth* **2017**, *479*, 59−66.

[22] E. Meissner, R. Niewa, (Eds.), "Ammonothermal Synthesis and Crystal Growth of Nitrides – Chemistry and Technology", Springer, Cham, **2021**.

[23] J. Häusler, L. Neudert, M. Mallmann, R. Niklaus, A.-C. L. Kimmel, N. S. A. Alt, E. Schlücker, O. Oeckler, W. Schnick, "Ammonothermal Synthesis of Novel Nitrides: Case Study on $CaGaSiN_3$", *Chem. Eur. J.* **2017**, *23*, 2583−2590.

[24] P. Becker, R. Niewa, "Progress in ammonothermal crystal growth of indium nitride", *J. Cryst. Growth* **2022**, *581*, 126480.

[25] A. Rabenau, "The Role of Hydrothermal Synthesis in Preparative Chemistry", *Angew. Chem.* **1985**, *97*, 1017–1031; *Angew. Chem. Int. Ed.* **1985**, *24*, 1026–1040.

[26] R. Dwilinski, A. Wysmolek, J. Baranowski, M. Kaminska, R. Doradzinski, J. Garczynski, L. Sierzputowski, H. Jacobs, "GaN Synthesis by Ammonothermal Method", *Acta Phys. Pol. A* **1995**, *88*, 833−836.

[27] Nobel Prize Outreach AB 2024, "*The Nobel Prize in Physics 2014*", https://www.nobelprize.org/prizes/physics/2014/summary/ (last visit: 15.10.2024).

[28] S. Nakamura, "Background Story of the Invention of Efficient InGaN Blue-Light-Emitting Diodes (Nobel Lecture)", *Angew. Chem.* **2015**, *127*, 7880−7899; *Angew. Chem. Int. Ed.* **2015**, *54*, 7770−7788.

[29] J.-J. Wu, K. Wang, T.-J. Yu, G.-Y. Zhang, "GaN substrate and GaN homo-epitaxy for LEDs: Progress and challenges", *Chin. Phys. B* **2015**, *24*, 068106.

[30] M. Boćkowski, I. Grzegory, "Recent Progress in Crystal Growth of Bulk GaN", *Acta Phys. Pol., A* **2022**, *141*, 167–174.

[31] W. Utsumi, H. Saitoh, H. Kaneko, T. Watanuki, K. Aoki, O. Shimomura, "Congruent melting of gallium nitride at 6 GPa and its application to single-crystal growth", *Nat. Mater.* **2003**, *2*, 735–738.

[32] N. Stoddard, S. Pimputkar, "Progress in Ammonothermal Crystal Growth of Gallium Nitride from 2017–2023: Process, Defects and Devices", *Crystals* **2023**, *13*, 1004.

[33] D. Tomida, Q. Bao, M. Saito, R. Osanai, K. Shima, K. Kojima, T. Ishiguro, S. F. Chichibu, "Ammonothermal growth of 2 inch long GaN single crystals using an acidic NH_4F mineralizer in a Ag-lined autoclave", *Appl. Phys. Express* **2020**, *13*, 055505.

[34] T. Hashimoto, E. R. Letts, D. Key, "Progress in Near-Equilibrium Ammonothermal (NEAT) Growth of GaN Substrates for GaN-on-GaN Semiconductor Devices", *Crystals* **2022**, *12*, 1085.

[35] J. Häusler, W. Schnick, "Ammonothermal Synthesis of Nitrides: Recent Developments and Future Perspectives", *Chem. Eur. J.* **2018**, *24*, 11864–11879.

[36] R. Juza, H. Jacobs, "Ammonothermal Synthesis of Magnesium and Beryllium Amides", *Angew. Chem.* **1966**, *78*, 208–208; *Angew. Chem. Int. Ed.* **1966**, *5*, 247–247.

[37] H. Jacobs, E. von Pinkowski, "Synthese ternärer Nitride von Alkalimetallen: Verbindungen mit Tantal, MTaN$_2$ mit $M \equiv$ Na, K, Rb und Cs", *J. Less-Common Met.* **1989**, *146*, 147–160.

[38] T. Brokamp, H. Jacobs, "Synthese und Kristallstruktur eines gemischtvalenten Lithium-Tantalnitrids $Li_2Ta_3N_5$", *J. Alloys Compd.* **1991**, *176*, 47–60.

[39] H. Jacobs, H. Mengis, "Preparation and Crystal Structure of a Sodium Silicon Nitride, $NaSi_2N_3$", *Eur. J. Solid State Inorg. Chem.* **1993**, *30*, 45–53.

[40] H. Jacobs, R. Nymwegen, "Darstellung und Kristallstruktur eines Kaliumnitridophosphats, $K_3P_6N_{11}$", *Z. Anorg. Allg. Chem.* **1997**, *623*, 429–433.

[41] J. Häusler, S. Schimmel, P. Wellmann, W. Schnick, "Ammonothermal Synthesis of Earth-Abundant Nitride Semiconductors $ZnSiN_2$ and $ZnGeN_2$ and Dissolution Monitoring by In Situ X-ray Imaging", *Chem. Eur. J.* **2017**, *23*, 12275–12282.

[42] J. Häusler, R. Niklaus, J. Minár, W. Schnick, "Ammonothermal Synthesis and Optical Properties of Ternary Nitride Semiconductors Mg-*IV*-N_2, Mn-*IV*-N_2 and Li-IV_2-N_3 (*IV*=Si, Ge)", *Chem. Eur. J.* **2018**, *24*, 1686–1693.

[43] M. Mallmann, C. Maak, R. Niklaus, W. Schnick, "Ammonothermal Synthesis, Optical Properties, and DFT Calculations of Mg_2PN_3 and Zn_2PN_3", *Chem. Eur. J.* **2018**, *24*, 13963–13970.

[44] M. Mallmann, S. Wendl, W. Schnick, "Crystalline Nitridophosphates by Ammonothermal Synthesis", *Chem. Eur. J.* **2020**, *26*, 2067–2072.

[45] M. Mallmann, S. Wendl, P. Strobel, P. J. Schmidt, W. Schnick, "$Sr_3P_3N_7$: Complementary Approach by Ammonothermal and High-Pressure Syntheses", *Chem. Eur. J.* **2020**, *26*, 6257–6263.

[46] J. Li, T. Watanabe, H. Wada, T. Setoyama, M. Yoshimura, "Low-Temperature Crystallization of Eu-Doped Red-Emitting $CaAlSiN_3$ from Alloy-Derived Ammonometallates", *Chem. Mater.* **2007**, *19*, 3592−3594.

[47] H. Watanabe, N. Kijima, "Synthesis of $Sr_{0.99}Eu_{0.01}AlSiN_3$ from intermetallic precursor", *J. Ceram. Soc. Jpn.* **2009**, *117*, 115−119.

[48] T. Watanabe, K. Nonaka, J. Li, K. Kishida, M. Yoshimura, "Low temperature ammonothermal synthesis of europium-doped $SrAlSiN_3$ for a nitride red phosphor", *J. Ceram. Soc. Jpn.* **2012**, *120*, 500−502.

[49] K. Nonaka, K. Kishida, C. Izawa, T. Watanabe, "Low temperature ammonothermal synthesis of europium-doped $SrAlSiN_3$: effect of mineralizers", *J. Ceram. Soc. Jpn.* **2014**, *122*, 17−20.

[50] Y. Maruyama, Y. Yanase, T. Watanabe, "Ammonothermal synthesis of charge-compensated $SrAlSiN_3:Ce^{3+}$ phosphor", *J. Ceram. Soc. Jpn.* **2017**, *125*, 399−401.

[51] J. Häusler, L. Eisenburger, O. Oeckler, W. Schnick, "Ammonothermal Synthesis and Crystal Structure of the Nitridoalumogermanate $Ca_{1-x}Li_xAl_{1-x}Ge_{1+x}N_3$ ($x \approx 0.2$)", *Eur. J. Inorg. Chem.* **2018**, *2018*, 759−764.

[52] M. Mallmann, R. Niklaus, T. Rackl, M. Benz, T. G. Chau, D. Johrendt, J. Minár, W. Schnick, "Solid Solutions of Grimm-Sommerfeld Analogous Nitride Semiconductors *II*-*IV*-N_2 with *II* = Mg, Mn, Zn; *IV* = Si, Ge – Ammonothermal Synthesis and DFT Calculations", *Chem. Eur. J.* **2019**, *25*, 15887–15895.

[53] T. Watanabe, K. Tajima, J. Li, N. Matsushita, M. Yoshimura, "Low-temperature Ammonothermal Synthesis of $LaTaON_2$", *Chem. Lett.* **2011**, *40*, 1101−1102.

[54] C. Izawa, T. Kobayashi, K. Kishida, T. Watanabe, "Ammonothermal Synthesis and Photocatalytic Activity of Lower Valence Cation-Doped $LaNbON_2$", *Adv. Mater. Sci. Eng.* **2014**, *2014*, 1−5.

[55] T. Toshima, K. Kishida, Y. Maruyama, T. Watanabe, "Low-temperature synthesis of $BaTaO_2N$ by an ammonothermal method", *J. Ceram. Soc. Jpn.* **2017**, *125*, 643−647.

[56] N. Cordes, W. Schnick, "Ammonothermal Synthesis of Crystalline Oxonitride Perovskites *Ln*$TaON_2$ (*Ln*=La, Ce, Pr, Nd, Sm, Gd)", *Chem. Eur. J.* **2017**, *23*, 11410−11415.

[57] N. Cordes, T. Bräuniger, W. Schnick, "Ammonothermal Synthesis of *EAM*O_2N (*EA* = Sr, Ba; *M* = Nb, Ta) Perovskites and ^{14}N Solid-State NMR Spectroscopic Investigations of *AM*$(O,N)_3$ (*A* = Ca, Sr, Ba, La)", *Eur. J. Inorg. Chem.* **2018**, *2018*, 5019−5026.

[58] N. Cordes, M. Nentwig, L. Eisenburger, O. Oeckler, W. Schnick, "Ammonothermal Synthesis of the Mixed-Valence Nitrogen-Rich Europium Tantalum Ruddlesden-Popper Phase $Eu^{II}Eu^{III}_2Ta_2N_4O_3$", *Eur. J. Inorg. Chem.* **2019**, *2019*, 2304–2311.

[59] S. Wendl, M. Mallmann, P. Strobel, P. J. Schmidt, W. Schnick, "Ammonothermal Synthesis of Ba_2PO_3N – An Oxonitridophosphate with Non-Condensed PO_3N Tetrahedra", *Eur. J. Inorg. Chem.* **2020**, *2020*, 841–846.

[60] M. Mallmann, C. Maak, W. Schnick, "Ammonothermal Synthesis and Crystal Growth of the Chain-type Oxonitridosilicate $Ca_{1+x}Y_{1-x}SiN_{3-x}O_x$ ($x > 0$)", *Z. Anorg. Allg. Chem.* **2020**, *646*, 1539–1544.

[61] H. Jacobs, R. Nymwegen, S. Doyle, T. Wroblewski, W. Kockelmann, "Kristallines Phoshor(V)-nitrid-imid, HPN_2 bzw. DPN_2 – Strukturbestimmung mit Röntgen-, Synchrotron- und Neutronenstrahlung", *Z. Anorg. Allg. Chem.* **1997**, *623*, 1467–1474.

[62] H. Jacobs, F. Golinski, "Synthese und Struktur eines Caesium-tetraimidophosphat-diamids, $Cs_5[P(NH)_4](NH_2)_2 = Cs_3[P(NH)_4] \cdot 2\ CsNH_2$", *Z. Anorg. Allg. Chem.* **1994**, *620*, 531–534.

[63] H. Jacobs, S. Pollok, F. Golinski, "Synthese und Kristallstruktur von $Na_{10}[P_4(NH)_6N_4](NH_2)_6(NH_3)_{0,5}$ mit dem adamantanartig aufgebauten Anion $[P_4(NH)_6N_4]^{4-}$", *Z. Anorg. Allg. Chem.* **1994**, *620*, 1213–1218.

[64] F. Golinski, H. Jacobs, "Synthese und Kristallstruktur von $Rb_8[P_4N_6(NH)_4](NH_2)_2$ mit dem adamantanartigen Anion $[P_4N_6(NH)_4]^{6-}$", *Z. Anorg. Allg. Chem.* **1995**, *621*, 29–33.

[65] H. Jacobs, R. Nymwegen, "Darstellung und Strukturbestimmung zweier Salze der Trimetaphosphimsäure, $K_3(PO_2NH)_3$ und $Rb_3(PO_2NH)_3$", *Z. Anorg. Allg. Chem.* **1998**, *624*, 199–204.

[66] F. Liebau, "Structural Chemistry of Silicates", Springer, Berlin, **1985**.

[67] D. Peters, H. Jacobs, "Ammonothermalsynthese von kristallinem Siliciumnitridimid, Si_2N_2NH", *J. Less-Common Met.* **1989**, *146*, 241–249.

[68] H. Jacobs, H. Mengis, "Synthese und Kristallstruktur von Alkalimetalldiamidodioxosilicaten $M_2SiO_2(NH_2)_2$ mit M ≙ K, Rb und Cs", *Z. Anorg. Allg. Chem.* **1993**, *619*, 303–310.

[69] D. Peters, E. F. Paulus, H. Jacobs, "Darstellung und Kristallstruktur eines Kaliumimidonitridosilicats, $K_3Si_6N_5(NH)_6$", *Z. Anorg. Allg. Chem.* **1990**, *584*, 129–137.

[70] E. Prince, "International Tables for Crystallography, Volume C", Wiley-VCH, New Jersey, **2006**.

[71] J. Workman Jr., L. Weyer, "Practical Guide to Interpretive Near-Infrared Spectroscopy", 1st ed., CRC Press, Boc Raton, **2007**.

[72] W. Kolodziejski, J. Klinowski, "Kinetics of Cross-Polarization in Solid-State NMR: A Guide for Chemists", *Chem. Rev. (Washington, DC, U. S.)* **2002**, *102*, 613–628.

[73] M. Nespolo, "Charge distribution as a tool to investigate structural details. IV. A new route to heteroligand polyhedra", *Acta Crystallogr., Sect. B: Struct. Sci., Cryst. Eng. Mater.* **2016**, *72*, 51–66.

[74] N. E. Brese, M. O'Keeffe, "Bond-valence parameters for solids", *Acta Crystallogr., Sect. B: Struct. Sci.* **1991**, *47*, 192–197.

2 Ammonothermal Synthesis and Crystal Structure of the Ternary Amide $Na_2Ba(NH_2)_4$

Published in: *Z. Anorg. Allg. Chem.* **2024**, *650*, e202400053

Authors: Florian M. Engelsberger, Kristian Witthaut, and Wolfgang Schnick

DOI: 10.1002/zaac.202400053

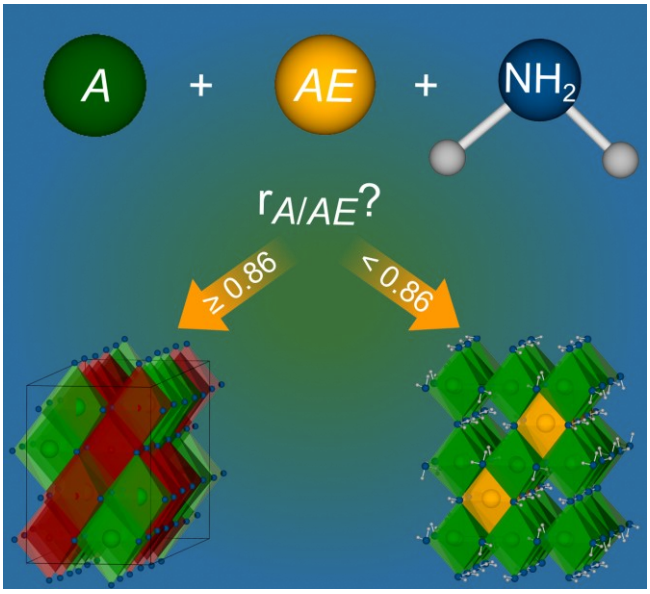

Dedicated to Professor Martin Jansen on the Occasion of his 80th Birthday

Abstract: The ternary amide $Na_2Ba(NH_2)_4$ was synthesized at ammonothermal conditions (870 K, 135 MPa) in custom-built high-pressure autoclaves. The compound was structurally characterized using X-ray diffraction and crystallizes in space group *Pccn* (no. 56) with lattice parameters a = 10.6492(2), b = 7.8064(2) and c = 8.1046(2) Å. To the best of our knowledge, the structure type has not yet been observed in any ternary amide before and can be described as a defective variant of the NaCl structure type. The presence of amide ions in the compound is verified by Fourier-transform infrared (FTIR) spectroscopy and the experimental spectrum is compared to the theoretical spectrum obtained through density functional theory (DFT) calculations. $Na_2Ba(NH_2)_4$ complements the range of reported ternary alkali metal alkaline earth metal amides with the smallest Shannon radius ratio of $r_{A/AE}$ = 0.76. The influence of this ratio on the formation of the new structure type is discussed as well. The characterization of intermediate species such as this ternary amide extends the understanding of the ammonothermal synthesis and can be useful for synthetic control in the formation of nitrides at ammonothermal conditions.

2.1 Introduction

The ammonothermal synthesis is a versatile solution-based high-pressure method suitable for the synthesis of functional nitrides at relatively low temperatures.[1-2] Especially the preparation of large single-crystal wafers of up to 100 mm of the binary nitride GaN for the application in optoelectronic devices under ammonothermal conditions has attracted considerable industrial interest in recent years.[3-5] During synthesis, supercritical ammonia is generated at the applied temperatures and pressures which favors the dissolution of inorganic compounds due to the increased relative permittivity of the solvent.[6] The solubility can be further enhanced by employing mineralizing agents. These additives react with the starting materials to form soluble species. Since a variation of the mineralizer can cause a considerable change of the reaction result, the investigation and understanding of intermediary formed ternary and multinary species is of crucial importance to enable a synthesis optimization by the selection of the employed mineralizers.[6-7] Alkali metal amides are frequently utilized mineralizing agents for syntheses under ammonobasic conditions.[6] Next to these binary amides, a wide range of ternary amides containing an alkali metal *A* and an alkaline earth metal *AE* are described in the literature. This compound class can be divided into six groups regarding the main building blocks of their crystal structure. The first group contains cations in trigonal planar coordination and is represented by $KBe(NH_2)_3$ and $RbBe(NH_2)_3$.[8] In the second group, isolated magnesium-centered tetrahedra are the main structural characteristic in the amides $K_2[Mg(NH_2)_4]$, $Rb_2[Mg(NH_2)_4]$ and $Cs_2[Mg(NH_2)_4]$.[9-10] The third group shows octahedral building blocks connected by faces to form one-dimensional chains, as in the $CsCuCl_3$ structure type (for $KCa(NH_2)_3$ and $RbCa(NH_2)_3$).[11-12] In the fourth group, a three-dimensional octahedra network is formed in a hexagonal perovskite structure for $CsAE(NH_2)_3$ with *AE* = Ca, Sr.[13] For the crystal structure of $CsBa(NH_2)_3$, the octahedra are connected at the edges to form double chains representing the NH_4CdCl_3 structure type.[14]

The group with the highest number of known representatives shows a distorted cubic closest packing of nitrogen atoms. The metal ions statistically occupy the octahedral voids of this packing in two possible structure types with different compositions, namely $KEu(NH_2)_3$ and $Na_2Sr_3(NH_2)_8$.[15-17]

An important criterion that seems to determine which of the respective structure types is formed, is the ratio of the ionic radii of the respective alkali and alkaline earth metals $r_{A/AE} = r_A/r_{AE}$.[16] Table 2.1 summarizes the reported compounds according to their $r_{A/AE}$, calculated from their ionic Shannon radii, as well as an assignment to their respective structural group.[18] There is a recognizable correlation between $r_{A/AE}$ and the structure type. Only in the range of $r_{A/AE}$ = 1.38–1.67 more than one structure is stable and other criteria than the ionic radius ratio influence the formation of the preferred crystal structure. In this work, we present the ammonothermal synthesis

Table 2.1: Summary of the Shannon radii ratios of the ternary A-AE-amides and their respective crystal structure features.

Formula	Ratio $r_{A/AE}$ of ionic radii A^+/AE^{2+}[18]	Structural group and structure type description
$RbBe(NH_2)_3$[8]	3.38	1 – Isolated trigonal planar units
$KBe(NH_2)_3$[8]	3.07	1 – Isolated trigonal planar units, related to $RbBe(NH_2)_3$
$Cs_2[Mg(NH_2)_4]$[10]	2.93	2 – Isolated tetrahedra
$Rb_2[Mg(NH_2)_4]$[9]	2.67	2 – Isolated tetrahedra, similar to $Cs_2[Mg(NH_2)_4]$
$K_2[Mg(NH_2)_4]$[9]	2.42	2 – Isolated tetrahedra, related to β-K_2SO_4
$CsCa(NH_2)_3$[13]	1.67	4 – Octahedra, hexagonal perovskite
$RbCa(NH_2)_3$[12]	1.52	3 – Octahedra chains, similar to $CsCuCl_3$
$CsSr(NH_2)_3$[13]	1.42	4 – Octahedra, hexagonal perovskite
$KCa(NH_2)_3$[11]	1.38	3 – Octahedra chains, similar to $CsCuCl_3$
$CsBa(NH_2)_3$[14]	1.23	5 – Double octahedra chains, related to NH_4CdCl_3
$KSr(NH_2)_3$[16]	1.17	6 – Octahedra, similar to $KEu(NH_2)_3$
$RbBa(NH_2)_3$[17]	1.13	6 – Octahedra, similar to $KEu(NH_2)_3$
$KBa(NH_2)_3$[17]	1.02	6 – Octahedra, similar to $KEu(NH_2)_3$
$NaCa(NH_2)_3$[15,17]	1.02	6 – Octahedra, similar to $KEu(NH_2)_3$
$Na_2Sr_3(NH_2)_8$[16]	0.86	6 – Octahedra, similar to $Na_2Sr_3(NH_2)_8$
$Na_2Ba(NH_2)_4$	0.76	Octahedra, related to Mn_2SnS_4

of the new ternary amide $Na_2Ba(NH_2)_4$ which extends the reported range of the ionic radius ratios with $r_{A/AE}$ = 0.76 and introduces a new structure type. The ammonothermally synthesized amide is characterized using single-crystal and powder X-ray diffraction as well as Fourier-transform infrared (FTIR) spectroscopy. The structural relationship of the new compound to the literature-known ternary *A-AE*-amides is discussed.

2.2 Results and Discussion

2.2.1 Synthesis

The amide $Na_2Ba(NH_2)_4$ was synthesized at ammonobasic conditions from supercritical ammonia in custom-built high-pressure autoclaves made of Inconel® 718. As starting materials, sodium azide and barium metal were employed. NaN_3 was used as sodium source due to its high purity and its higher insensitivity against air and moisture compared to elemental Na or $NaNH_2$. $Na_2Ba(NH_2)_4$ crystallizes as rod-like transparent crystals (Figure 2.1) which grow from the liner wall in the cold zone of the autoclave. The product is sensitive towards air and moisture and was therefore handled under inert gas conditions.

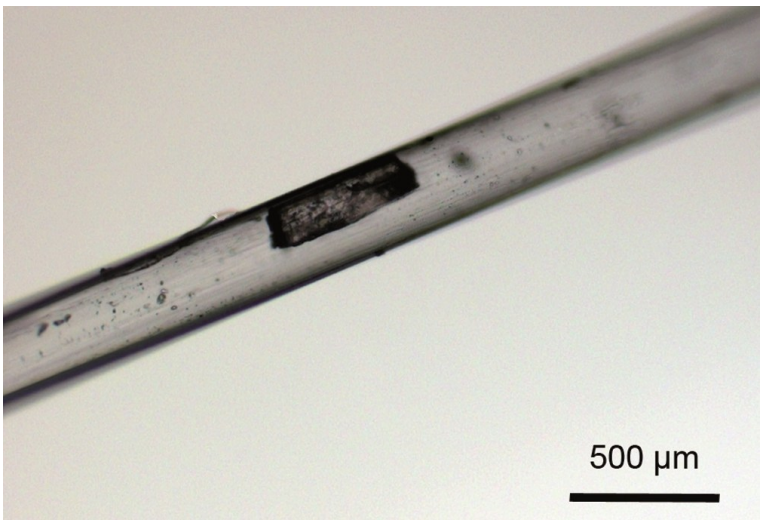

Figure 2.1: Micrograph of a transparent crystallite of $Na_2Ba(NH_2)_4$ in a sealed glass capillary.

The new ternary amide was first observed during synthesis attempts containing NaN_3 and Ba in the molar ratio 3:1. These reaction attempts led to sodium amide as a side phase, which is formed by the excess of sodium azide among the starting materials. Further experiments showed that the reduction of the sodium content in the starting materials to a molar ratio of 2:1 is not feasible, since $Na_2Ba(NH_2)_4$ could not be detected as the main phase at these conditions. It seems that the excess of NaN_3 is necessary to create an oversaturation of the amide in supercritical ammonia.

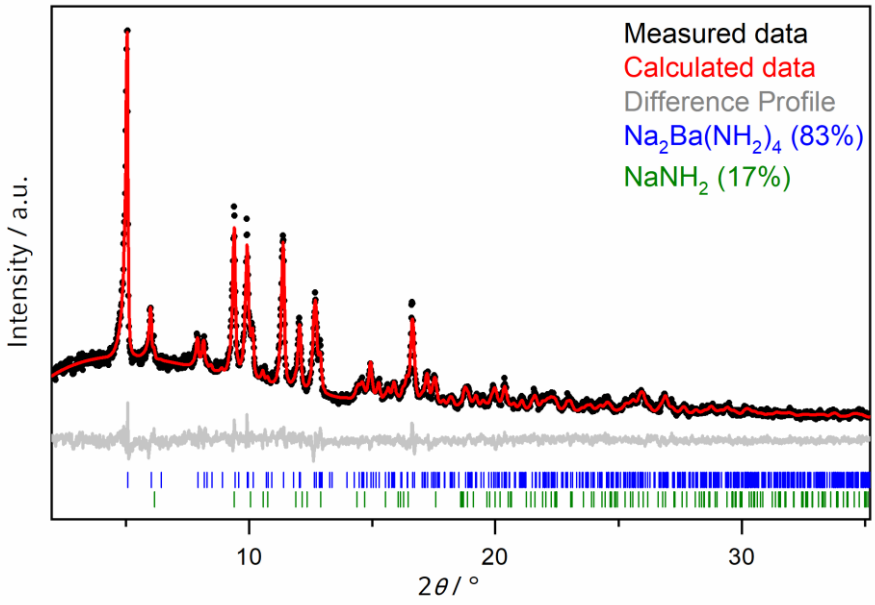

Figure 2.2: Rietveld refinement based on powder X-ray diffraction (PXRD) data of $Na_2Ba(NH_2)_4$ with experimental data (black dots, Ag-$K_{\alpha 1}$ radiation), calculated diffraction pattern (red line), difference profile (gray line) and reflection positions of $Na_2Ba(NH_2)_4$ (blue bars) and $NaNH_2$ (green bars).

The phase fraction of the side phase $NaNH_2$ in the samples was estimated to be 17 wt% according to the Rietveld refinement (Figure 2.2). Additionally, the reaction temperature of 870 K, which is

relatively high compared to the synthesis of other ternary amides, seems to be necessary for the crystal growth of $Na_2Ba(NH_2)_4$. Experiments at lower temperatures resulted in products with low crystallinity.

2.2.2 Crystal Structure

$Na_2Ba(NH_2)_4$ crystallizes in the orthorhombic space group *Pccn* (no. 56). Crystallographic data obtained from single-crystal X-ray diffraction data are summarized in Table 2.2. Atomic coordinates, respective Wyckoff positions and displacement parameters are listed in Table 9.1–Table 9.3 (Supporting Information).

Table 2.2: Crystallographic data for $Na_2Ba(NH_2)_4$ obtained from single-crystal X-ray diffraction, standard deviations are given in parentheses.

Formula	**$Na_2Ba(NH_2)_4$**
Crystal system	Orthorhombic
Space group	*Pccn* (no. 56)
Lattice parameters / Å	a = 10.6492(2) b = 7.8064(2) c = 8.1046(2)
Cell volume / Å^3	673.75(3)
Formula units Z / cell	4
Density / g·cm^{-3}	2.439
μ / mm^{-1}	5.916
T / K	294(2)
Diffractometer	Bruker D8 Venture
Radiation (λ / Å)	Mo-K_α (0.71073)
F(000)	456
θ range / °	3.236–33.133
Total no. of reflections	16846
Independent reflections	1289
Refined parameters / restraints	49/4
Goodness of fit (χ^2)	1.130
R indices (all data)	$R1$ = 0.0215, $wR2$ = 0.0253
R indices [$F^2 > 2\sigma(F^2)$]	$R1$ = 0.0137, $wR2$ = 0.0234
$\Delta\rho_{max}$ / $\Delta\rho_{min}$ [e Å^{-3}]	0.63/−0.27
R_{int}, R_σ	0.0270, 0.0147

The crystal structure of $Na_2Ba(NH_2)_4$ can be derived from the Mn_2SnS_4 structure type which represents a deficient NaCl superstructure.[19-20] The crystal structure of $Na_2Ba(NH_2)_4$ is built up from a distorted cubic closest packing of nitrogen atoms of the amide groups with Na and Ba

located in the octahedral voids (Figure 2.2a). Half of the octahedral voids in this closest packing are filled with Na atoms forming $Na(NH_2)_6$ octahedra which are interconnected via edges along [010] and [001] and via vertices along [100]. Half of the remaining octahedral voids (resulting in a total occupation of $\frac{1}{4}$ of the octahedral voids) are occupied by Ba forming infinite chains of edge-sharing $Ba(NH_2)_6$ octahedra along [001]. The remaining $\frac{1}{4}$ of the octahedral voids are empty, resulting in the stoichiometry Na:Ba:N of 2:1:4. The positions of the hydrogen atoms of the amide groups could be isotropically refined from the residual electron density in the Fourier map. The N–H bond lengths were restricted to a length of 0.90(2) Å using DFIX commands and are orientated towards the empty octahedral voids in the structure.

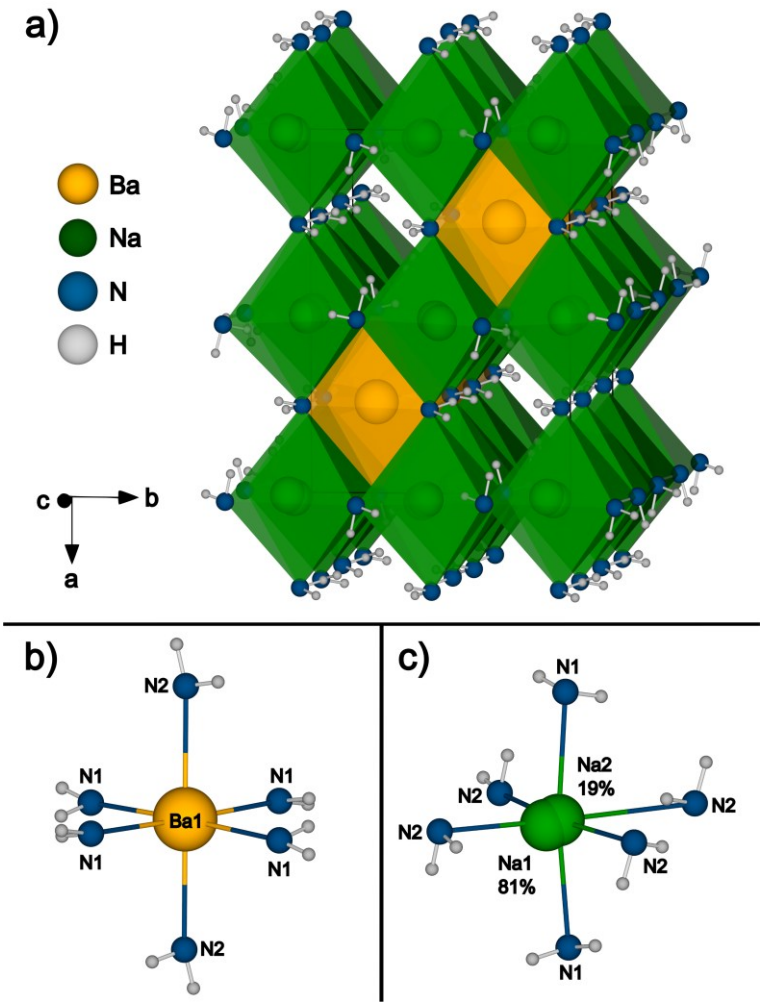

Figure 2.2: Representation of the crystal structure of $Na_2Ba(NH_2)_4$ (a) with coordination environment of Ba (b) and Na (c) atoms. Ellipsoids are displayed at 70% probability level.

A superstructure could be identified resulting in a doubling of the *c*-axis compared to the initial unit cell from ≈4.05 Å to a final length of c = 8.1046(2) Å. The respective reflections that confirm this larger unit cell are highlighted in the precession image of the *h*1*l* plane in the Supporting Information (Figure 9.1).

The positions of the Na atoms are split into two distinct crystallographic positions with an occupation of 95% for Na1 and 5% for Na2, respectively (Figure 2.2c). This disorder is probably caused by the smaller ionic radius of sodium (1.02 Å) compared to barium (1.35 Å) which both occupy octahedral voids of nearly the same volume (28.1 $Å^3$ for Na and 28.3 $Å^3$ for Ba).[18] The Na–N distances vary between 2.46(2) and 2.88(3) Å, which is in agreement to the reported distances in the literature for comparable amides (Table 9.3).[16-17,21-22] The Ba–N distances in the $Ba(NH_2)_6$ octahedra (Figure 2.2b) range from 2.7328(12) to 2.8113(10) Å. These values correspond to the reported values for barium ions in octahedral coordination in barium-containing amides.[14,17,23]

The Rietveld refinement of the PXRD data confirms the crystal structure model obtained from the single-crystal data (Figure 2.2). The crystallographic data and Wyckoff positions of the refinement are presented in Table 9.4 and Table 9.5 in the Supporting Information. Next to $Na_2Ba(NH_2)_4$, the sample contains residual $NaNH_2$ as a minor side phase which is formed by the employed excess of NaN_3 for the synthesis and could not be removed from the sample.

When compared to the reported *A*-*AE*-amides, the stoichiometry of $Na_2Ba(NH_2)_4$ is similar to the compounds $A_2[Mg(NH_2)_4]$ with *A* = K, Rb, Cs. In these compounds, the $Mg(NH_2)_4$ tetrahedra are the main structural feature. Due to the larger ionic radius of Ba^{2+} (1.42 Å) compared to Mg^{2+} (0.57 Å), a tetrahedral coordination and therefore the formation of a structure type similar with the Mg^{2+} containing amides is unlikely.[18]

Other representatives of the ternary *A*-*AE*-amides form the structural motif of a cubic closest packing of amide ions as it is observed in $Na_2Ba(NH_2)_4$. These other ternary amides all show a statistical occupation of the octahedral voids with the respective *A* and *AE* ions, resulting in a composition ratio of *A*:*AE* from 1:1 or 2:3.[16-17] Therefore, the described structure with the ordering in the occupation of the octahedral voids of $Na_2Ba(NH_2)_4$ presents a new structure type for this group of ternary amides. The ratio of the ionic radii was discussed before as a criterion for the formation of the different structure types containing a cubic closest packing of amide ions.[16] A reduction of the Shannon radii ratio $r_{A/AE}$ seems to induce a change in the crystal structure and the stoichiometry from $RbBa(NH_2)_3$ ($r_{A/AE}$ = 1.13) over $Na_2Sr_3(NH_2)_8$ ($r_{A/AE}$ = 0.86) to $Na_2Ba(NH_2)_4$ ($r_{A/AE}$ = 0.76) (Table 2.1). Here, the crystal structures of the compounds only vary in the occupation of the octahedral voids of a cubic closest packing of amide ions.[18]

2.2.3 Fourier-Transform Infrared Spectroscopy

To verify the presence of the amide groups in the compound, a FTIR-spectrum of the sample containing $Na_2Ba(NH_2)_4$ was recorded at ambient temperature. In advance to the measurement, transparent crystals of $Na_2Ba(NH_2)_4$ were manually separated from the powdery secondary phase and ground in an agate mortar. A comparison with the positions of the vibrational maxima of $NaNH_2$ from the literature shows that the sample prepared this way contained only small amounts

of the side phase.[24] The comparison of the experimental spectrum to the theoretical spectrum obtained through quantum chemical calculations using the DFT-PBE method is shown in Figure 2.3.

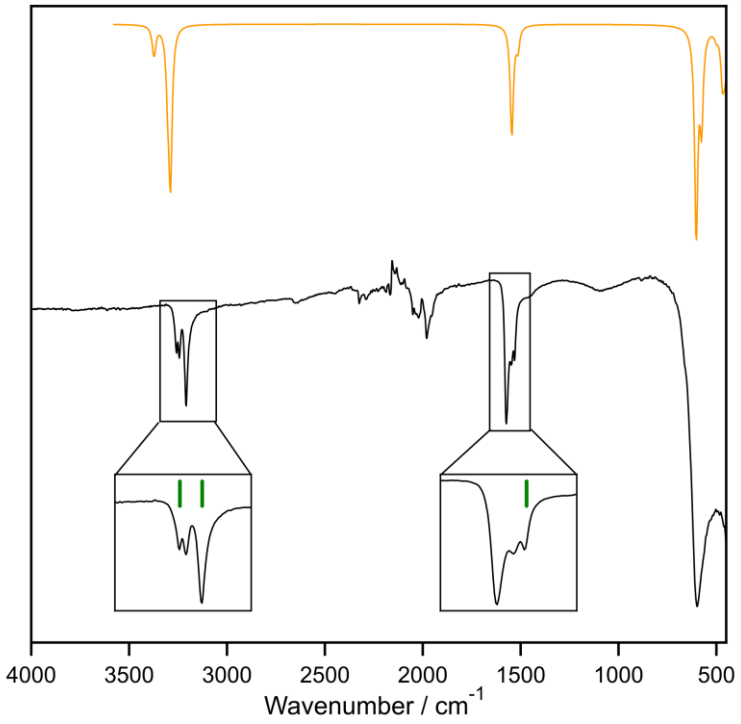

Figure 2.3: Comparison of the experimental FTIR spectrum of a sample containing $Na_2Ba(NH_2)_4$ (black line) with the theoretical spectrum from DFT-PBE calculations (orange line) and the positions of the maximal absorbance of $NaNH_2$ (green bars).[24] The areas showing the N−H stretching vibrations (3100−3300 cm^{-1}) and the H−N−H shear vibrations (1400−1600 cm^{-1}) are shown as enlargements.

The experimental spectrum shows absorbance resulting from the typical vibrations for amide ions. The stretching vibrations $\nu(NH_2^-)$ are observed in the range of 3000−3500 cm^{-1}, shear vibrations δ(HNH) in the range of 1500−1600 cm^{-1} and deformation vibrations $\delta(NH_2^-)$ in the range of 500−700 cm^{-1}. An assignment of the observed signals to their vibrational modes according to the DFT calculations is given in Table 9.6.[25] The vibrations observed in the range of 2000−2500 cm^{-1} originate from the ATR unit of the employed FTIR spectrometer.

The absorption maxima at 1531 and 3257 cm^{-1} can be assigned to the side phase sodium amide which are reported at 1528 and 3257 cm^{-1} in the literature.[24] The maximum at 3208 cm^{-1} could not be resolved into two distinct maxima, so it is most likely caused by a mixture of stretching vibrations of $Na_2Ba(NH_2)_4$ and the side phase $NaNH_2$.

2.3 Conclusions

The ternary *A-AE*-amide $Na_2Ba(NH_2)_4$ was synthesized under ammonothermal conditions forming a well-crystallized product with sodium amide as minor side phase. The new structure type of the amide is based on a cubic closest packing of the nitrogen atoms and an ordering in the occupation

of the octahedral voids with the cations which has not been observed in this compound class before. The formation of this ordered structure type might be a consequence of the ratio of the ionic radii $r_{A/AE}$ which is smaller for $Na_2Ba(NH_2)_4$ than for any other reported ternary *A*-*AE*-amide. The FTIR spectrum of the compound shows stretching, shear and deformation vibrations of the amide ions in their typical ranges and is in accordance with the theoretical spectrum obtained from quantum chemical calculations. This confirms the presence of hydrogen atoms in the sample and substantiates the structure model refined from single-crystal X-ray diffraction data. Since the ratio of the ionic radii seems to be crucial for the structure formation in this compound class, the investigation of a broader range of $r_{A/AE}$ will be promising for the observation of new structure types and may also allow structure predictions for new amides. A further understanding of these intermediary formed species can help to control the reaction outcome of ammonothermal synthesis experiments for nitrides, where they are already frequently employed as mineralizers.

2.4 Experimental Section

Due to the instability of the product and some starting materials towards air and moisture, all manipulations were carried out under inert gas conditions either in argon-filled gloveboxes (Unilab, MBraun, Garching, O_2 < 1 ppm, H_2O < 1 ppm) or in dried Schlenk-type glassware using a vacuum line ($\rho \leq 0.1$ Pa) with argon and ammonia supply. The gases argon and ammonia (both Air liquide, 99.999%) passed through gas cartridges (Micro Torr FT400-902 for Ar and MC400-702FV for NH3, SAES Pure Gas Inc., San Luis Obispo, CA, USA) for further purification, resulting in a purity level of < 1ppbV H_2O, O_2 and CO_2. The determination of the amount of ammonia added to the autoclave was performed using a mass flow meter (D-6320-DR, Bronkhorst, Ruurlo, Netherlands).

2.4.1 Ammonothermal synthesis

$Na_2Ba(NH_2)_4$ was synthesized from elemental barium (137.3 mg, 1.000 mmol, smart-elements, 99.9%) and sodium azide (195.0 mg, 3.000 mmol, Sigma-Aldrich, 99.5%) in custom-built autoclaves (Inconel® 718, max. 900 K, 300 MPa, 10 mL volume). In a glovebox, the sodium azide was ground and placed together with barium metal pieces in a niobium liner. The liner was then transferred into the autoclave which was sealed using a silver-coated Inconel® 718 ring (GFD seals) and flange joints. The autoclave was connected to the peripheral devices consisting of a hand valve (SITEC), a pressure transmitter (HBM P2VA1/5000 bar) and a bursting disk holder (SITEC) equipped with a bursting disk (Dieckers GmbH & Co. KG, pressure limit: 3300 bar). The autoclave was filled with ammonia (purification described above, ca. 6 mL) which was directly condensed in the autoclave, that was cooled with an ethanol / liquid nitrogen mixture, via a pressure regulating valve. The autoclave was heated in a tube furnace to 670 K within 2 h, held at this temperature for 14 h and subsequently heated to 870 K within 2 h. After 48 h at this temperature, reaching a maximum pressure of 135 MPa, the furnace was switched off. When the autoclave was cooled to

room temperature, residual ammonia was removed and the colorless product was isolated from the liner.

2.4.2 Single-crystal X-ray diffraction

For the single-crystal X-ray diffraction measurements, a rod-like shaped transparent crystal of $Na_2Ba(NH_2)_4$ with a size of 0.02 × 0.03 × 0.04 mm^3 was separated from the side phase manually under a microscope in a glove box. The crystal was subsequently transferred to a glass capillary (d = 0.3 mm, wall thickness 0.01 mm, Hilgenberg GmbH). Diffraction data were collected employing a Bruker D8 Venture single-crystal X-ray diffractometer with Mo-K_α radiation (λ = 0.71073 Å) and Göbel mirror optics. In a combined Φ-ω-scan, reflections of a hemisphere were collected. For integration and absorption correction, the program package APEX3 was used.[26-27] Data were absorption-corrected using the Multi-Scan Method (SADABS).[28] The initial crystal structure solution was carried out by Direct Methods (SHELXT).[29-30] The structure was refined by full-matrix least-squares methods (SHELXL).[31-32]

Crystallographic data (excluding structure factors) for the structure reported in this paper have been deposited with the Cambridge Crystallographic Data Centre as supplementary publication no. CSD-2348264. Copies of the data can be obtained free of charge on application to CCDC, 12 Union Road, Cambridge CB2 1EZ, UK [fax: (internat.) + 44 1223/336-033; e-mail: deposit@ccdc.cam.ac.uk, http://www.ccdc.cam.ac.uk].

2.4.3 Powder X-ray diffraction

The powder sample was ground in an agate mortar and sealed in a glass capillary (d = 0.3 mm, wall thickness 0.01 mm, Hilgenberg GmbH) at argon atmosphere. The powder X-ray diffraction measurements were conducted using a STOE STADI P diffractometer with Ag-$K_{\alpha1}$ radiation (λ = 0.71073 Å), a Ge(111) monochromator and a Mythen 1K detector in modified Debye-Scherrer geometry. The Rietveld-refinement of the collected data was performed with the TOPAS program package.[33]

2.4.4 Fourier transform infrared (FTIR) spectroscopy

An infrared spectrum of the sample was collected with a Bruker Alpha II FTIR spectrometer equipped with a diamond attenuated total reflectance (ATR) unit. The spectrum was recorded at ambient temperature in a glovebox under argon atmosphere in the range of 400-4000 cm^{-1} with a resolution of 2 cm^{-1}. For data collection, the OPUS 8.7 program was used.[34]

2.4.5 Density functional theory (DFT) calculations

To simulate a theoretical IR spectrum, the vibrational frequencies were determined by first principle electronic structure calculations. For this purpose, periodic DFT calculations were performed using the Vienna *ab intio* Simulation package (VASP).[35-38] VASP separates core and valence electrons using projector-augmented waves (PAW).[39-40] The exchange- and correlation-

energy was calculated using the generalized gradient approximation (GGA), as described by Perdew, Burke and Ernzerhof (PBE).[41] A dense k-point sampling with a 6x6x8 Γ-centered grid and a plane wave energy cutoff of 520 eV ensured a well-converged structure. Structure parameters were optimized using the conjugate gradient algorithm.[42] The vibrational frequencies were extracted from a density-functional perturbation theory (DFPT) linear response calculation with the plotIR script provided by Dr. Karhánek. The energy convergence criterion was set to 10^{-5} eV and the residual atomic forces were relaxed until the convergence criterion of 10^{-3} eV/Å was reached. Same convergence criteria were used for the DFPT calculation.

2.4.6 Microscopy

Micrographs of the sample were taken from crystallites isolated in a glass capillary (d = 0.3 mm, wall thickness 0.01 mm, Hilgenberg GmbH) using a Zeiss Axio Imager.M1m microscope equipped with an AxioCam camera module.

2.5 Acknowledgements

The authors thank Dr. Stefan Rudel, Dr. Peter Mayer and Prof. Dirk Johrendt (all at Department of Chemistry, LMU Munich) for collection of micrographs, single-crystal X-ray diffraction data and for providing the resources for the DFT calculations, respectively. Open Access funding enabled and organized by Projekt DEAL.

2.6 References

[1] R. Niewa in: "*Ammonothermal Synthesis and Crystal Growth of Nitrides – Chemistry and Technology*" (Eds.: E. Meissner, R. Niewa), Springer, Cham, **2021**, pp. 3–12.

[2] J. Häusler, W. Schnick, "Ammonothermal Synthesis of Nitrides: Recent Developments and Future Perspectives", *Chem. Eur. J.* **2018**, *24*, 11864–11879.

[3] R. Dwilinski, A. Wysmolek, J. Baranowski, M. Kaminska, R. Doradzinski, J. Garczynski, L. Sierzputowski, H. Jacobs, "GaN Synthesis by Ammonothermal Method", *Acta Phys. Pol. A* **1995**, *88*, 833–836.

[4] K. Grabianska, R. Kucharski, A. Puchalski, T. Sochacki, M. Bockowski, "Recent progress in basic ammonothermal GaN crystal growth", *J. Cryst. Growth* **2020**, *547*, 125804.

[5] N. Stoddard, S. Pimputkar, "Progress in Ammonothermal Crystal Growth of Gallium Nitride from 2017–2023: Process, Defects and Devices", *Crystals* **2023**, *13*, 1004.

[6] T. M. M. Richter, R. Niewa, "Chemistry of Ammonothermal Synthesis", *Inorganics* **2014**, *2*, 29–78.

[7] R. Niewa in: "*Ammonothermal Synthesis and Crystal Growth of Nitrides – Chemistry and Technology*" (Eds.: E. Meissner, R. Niewa), Springer, Cham, **2021**, pp. 227–251.

[8] M. G. B. Drew, J. E. Goulter, L. Guémas-Brisseau, P. Palvadeau, J. Rouxel, P. Herpin, "Etude structurale d'amido-béryllates de rubidium et de potassium", *Acta Crystallogr., Sect. B: Struct. Crystallogr. Cryst. Chem.* **1974**, *30*, 2579–2582.

[9] H. Jacobs, J. Birkenbeul, J. Kockelkorn, "Darstellung und Eigenschaften der Amidomagnesate des Kaliums und Rubidiums $K_2[Mg(NH_2)_4]$- und $Rb_2[Mg(NH_2)_4]$-Verbindungen mit isolierten $[Mg(NH_2)_4]^{2-}$-Tetraedern", *J. Less-Common Met.* **1984**, *97*, 205–214.

[10] H. Jacobs, J. Birkenbeul, D. Schmitz, "Strukturverwandtschaft des Dicaesiumamidomagnesats, $Cs_2[Mg(NH_2)_4]$, zum β-K_2SO_4-Typ", *J. Less-Common Met.* **1982**, *85*, 79–86.

[11] H. Jacobs, U. Fink, "Darstellung und Kristallstruktur von $KCa(NH_2)_3$", *Z. Anorg. Allg. Chem.* **1977**, *435*, 137–145.

[12] H. Jacobs, J. Kockelkorn, "Darstellung und Kristallstruktur des Rubidiumcalciumamids, $RbCa(NH_2)_3$", *Z. Anorg. Allg. Chem.* **1979**, *456*, 147–154.

[13] H. Jacobs, J. Kockelkorn, "Über Cäsiumamidometallate ($CsM(NH_2)_3$) des Calciums, Strontiums und Europiums; Verbindungen mit der Struktur "hexagonaler Perowskite"", *J. Less-Common Met.* **1981**, *81*, 143–154.

[14] H. Jacobs, J. Birkenbeul, J. Kockelkorn, "Darstellung und Eigenschaften des Caesiumbarium-Amids, $CsBa(NH_2)_3$: Strukturverwandtschaft zum NH_4CdCl_3-Typ", *J. Less-Common Met.* **1982**, *85*, 71–78.

[15] H. Jacobs, U. Fink, "Untersuchung des Systems Kalium/Europium/Ammoniak", *Z. Anorg. Allg. Chem.* **1978**, *438*, 151–159.

[16] H. Jacobs, U. Fink, "Über Natrium- und Kaliumamidometallate des Calciums, Strontiums und Europiums", *J. Less-Common Met.* **1979**, *63*, 273–286.

[17] H. Jacobs, J. Kockelkorn, J. Birkenbeul, "Struktur und Eigenschaften der ternären Metallamide $NaCa(NH_2)_3$, $KBa(NH_2)_3$, $RbBa(NH_2)_3$, $RbEu(NH_2)_3$ und $RbSr(NH_2)_3$", *J. Less-Common Met.* **1982**, *87*, 215–224.

[18] R. Shannon, "Revised effective ionic radii and systematic studies of interatomic distances in halides and chalcogenides", *Acta Crystallogr., Sect. A: Found. Adv.* **1976**, *32*, 751–767.

[19] M. Wintenberger, J. C. Jumas, "Etude par diffraction neutronique de Mn_2SnS_4. Affinement de la structure cristallographique et determination de la structure magnetique", *Acta Crystallogr., Sect. B: Struct. Crystallogr. Cryst. Chem.* **1980**, *36*, 1993–1996.

[20] M. Partik, T. Stingl, H. D. Lutz, H. Sabrowsky, P. Vogt, "Strukturverfeinerung und magnetische Messungen an Mn_2SnS_4", *Z. Anorg. Allg. Chem.* **1995**, *621*, 1600–1604.

[21] S. Kunkel, R. Niewa, "$Na_2La_4(NH_2)_{14}{\cdot}NH_3$, a lanthanum-rich intermediate in the ammonothermal synthesis of LaN and the effect of ammonia loss on the crystal structure", *Z. Naturforsch., B: J. Chem. Sci.* **2021**, *76*, 567–575.

[22] S. Kunkel, J. Grill, R. Niewa, "Sodium rare earth metal amides $Na_3RE(NH_2)_6$ (*RE* = La–Nd, Er, Yb) from ammonothermal synthesis", *Z. Naturforsch., B: J. Chem. Sci.* **2021**, *77*, 335–346.

[23] H. Jacobs, C. Hadenfeldt, "Die Kristallstruktur von Bariumamid, $Ba(NH2)_2$", *Z. Anorg. Allg. Chem.* **1975**, *418*, 132–140.

[24] L. Bonometti, F. Kraus, T. Graubner, A. J. Karttunen, B. Civalleri, L. Donà, L. Maschio, "A Fresh Look at a Well-Known Solid: Structure, Vibrational Spectra, and Formation Energy of $NaNH_2$", *J. Phys. Chem. C* **2023**, *127*, 12287–12294.

[25] G. Linde, R. Juza, "IR-Spektren von Amiden und Imiden zwei- und dreiwertiger Metalle", *Z. Anorg. Allg. Chem.* **1974**, *409*, 199–214.

[26] Bruker-AXS, *APEX3*, Vers.2016.5-0, Karlsruhe, Germany, **2016**.

[27] Bruker-AXS, *XPREP*: Reciprocal Space Exploration, Vers.6.12, Karlsruhe, Germany, **2001**.

[28] G. M. Sheldrick, *SADABS*: Multi-Scan Absorption Correction, 2016-2, Bruker-AXS, Madison, WI, USA, **2012**.

[29] G. M. Sheldrick, *SHELXT 2018/2*: A programm for crystal structure solution, University of Göttingen, Germany, **2018**.

[30] G. M. Sheldrick, "SHELXT - Integrated space-group and crystal-structure determination", *Acta Crystallogr., Sect. A: Found. Adv.* **2015**, *71*, 3–8.

[31] G. M. Sheldrick, *SHELXL-2018/3*: A programm for crystal structure refinement, University of Göttingen, Germany, **2018**.

[32] G. M. Sheldrick, "Crystal structure refinement with SHELXL", *Acta Crystallogr., Sect. C: Cryst. Struct. Commun.* **2015**, *71*, 3–8.

[33] A. Coelho, *TOPAS Academic*, Version 6, Coelho Software, Brisbane, Australia, **2016**.

[34] Bruker Optik GmbH, *OPUS V8.7*, Ettlingen, Germany, **2012**.

[35] G. Kresse, J. Hafner, "Ab initio molecular dynamics for liquid metals", *Phys. Rev. B: Condens. Matter Mater. Phys.* **1993**, *47*, 558–561.

[36] G. Kresse, J. Hafner, "Ab initio molecular-dynamics simulation of the liquid-metal--amorphous-semiconductor transition in germanium", *Phys. Rev. B: Condens. Matter Mater. Phys.* **1994**, *49*, 14251–14269.

[37] G. Kresse, J. Furthmüller, "Efficiency of ab-initio total energy calculations for metals and semiconductors using a plane-wave basis set", *Comput. Mater. Sci.* **1996**, *6*, 15–50.

[38] G. Kresse, J. Furthmüller, "Efficient iterative schemes for ab initio total-energy calculations using a plane-wave basis set", *Phys. Rev. B: Condens. Matter Mater. Phys.* **1996**, *54*, 11169–11186.

[39] G. Kresse, D. Joubert, "From ultrasoft pseudopotentials to the projector augmented-wave method", *Phys. Rev. B: Condens. Matter Mater. Phys.* **1999**, *59*, 1758–1775.

[40] P. E. Blöchl, "Projector augmented-wave method", *Phys. Rev. B: Condens. Matter Mater. Phys.* **1994**, *50*, 17953–17979.

[41] J. P. Perdew, K. Burke, M. Ernzerhof, "Generalized Gradient Approximation Made Simple", *Phys. Rev. Lett.* **1996**, *77*, 3865–3868.

[42] W. H. Press, B. P. Flannery, S. A. Teukolsky, T. Vetterling, "Numerical Recipes: The Art of Scientific Computing", 1st ed., Cambridge University Press, New York, **1986**.

3 Ammonothermal Synthesis of Luminescent Imidonitridophosphate $Ba_4P_4N_8(NH)_2:Eu^{2+}$

Published in: *Chem. Eur. J.* **2024**, *30*, e202402743

Authors: Florian M. Engelsberger, Reinhard M. Pritzl, Jennifer Steinadler, Kristian Witthaut, Thomas Bräuniger, Peter J. Schmidt, and Wolfgang Schnick

DOI: 10.1002/chem.202402743

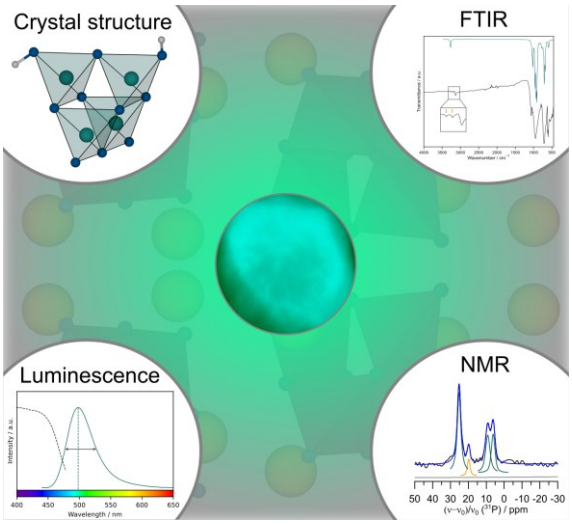

Abstract: The structural variability of a compound class is an important criterion for the research into phosphor host lattices for phosphor-converted light-emitting diodes (pc-LEDs). Especially, nitridophosphates and the related class of imidonitridophosphates are promising candidates. Recently, the ammonothermal approach has opened a systematic access to this substance class with larger sample quantities. We present the successful ammonothermal synthesis of the imidonitridophosphate $Ba_4P_4N_8(NH)_2:Eu^{2+}$. Its crystal structure is solved by X-ray diffraction and it crystallizes in space group *Cc* (no. 9) with lattice parameters $a = 12.5250(3)$, $b = 12.5566(4)$, $c = 7.3882(2)$ Å and $\beta = 102.9793(10)°$. For the first time, adamantane-type (imido)nitridophosphate anions $[P_4N_8(NH)_2]^{8-}$ are observed next to metal ions other than alkali metals in a compound. The presence of imide groups in the structure and the identification of preferred positions for the hydrogen atoms are performed using a combination of quantum chemical calculations, Fourier-transform infrared, and solid-state NMR spectroscopy. Eu^{2+} doped samples exhibit cyan emission ($\lambda_{max} = 498$ nm, *fwhm* = 50 nm/1981 cm^{-1}) when excited with ultraviolet light with an impressive internal quantum efficiency (IQE) of 41 %, which represents the first benchmark for imidonitridophosphates and is promising for potential industrial application of this compound class.

3.1 Introduction

In the search for suitable compound classes to be used as phosphor host lattices for application in phosphor-converted light-emitting diodes (pcLEDs), the importance of multifarious structural possibilities is often emphasized. With respect to this key feature, nitridophosphates have gained increasing interest in recent years.[1-5] Here, the high structural variability is expected corresponding to the variety observed in oxosilicates due to the isoelectronic relation of P/N to Si/O. The challenge to gain synthetic access to this compound class arises from the combination of low thermal stability of P_3N_5 together with the necessity of high reaction temperatures for the crystallization of nitridophosphates. Therefore, only a limited number of nitridophosphates could be prepared at ambient pressures. As appropriate solution pathways to this challenges, based on Le Chateliers' principle, various high-pressure synthesis routes in large volume presses have been developed in the past to synthesize a large number of nitridophosphates.[6]

Furthermore, additional medium pressure methods have been reported as suitable tools for the synthesis of nitridophosphates. These overcome the problem of small sample quantities obtained from the large volume press and allow a systematic access to larger amounts of the compounds, making an industrial application attractive.[3,7]

In addition to hot isostatic press approaches, where nitrogen gas pressures are applied during the synthesis, the ammonothermal approach is one of these medium pressure methods. Here, supercritical ammonia is generated during the reaction in specially designed autoclaves and used as a solvent, mainly for the synthesis of amides, imides or nitrides.[8-9] To increase the solubility of the starting materials in this solution-based process, mineralizers are usually used generating ammonobasic, ammononeutral, or ammonoacidic environments during synthesis.[10] After some first reports on ammonothermal syntheses of nitridophosphates, a more universal approach was presented by Mallmann et al.[7,11-12] Subsequently, also first luminescent samples were obtained successfully from ammonothermal approaches.[4,13]

Next to nitridophosphates, N−H functionalized phosphorus nitride imides and imidonitridophosphates have attracted considerable interest in recent years as well. Two stoichiometric compositions of phosphorus nitride imides are known: HPN_2 and HP_4N_7, the former of which was also prepared ammonothermally. They consist of three-dimensional networks built up from PN_4 tetrahedra.[14-17] For both compounds, high-pressure polymorphs are reported, namely β-HPN_2, β-HP_4N_7 and γ-HP_4N_7.[18-20] Furthermore, the incorporation of ammonia gas molecules into pores of a tetrahedra network is reported for the nitridic clathrate $P_4N_4(NH)_4(NH_3)$.[21]

For the imidonitridophosphates, syntheses in the large volume press allowed to incorporate negatively charged three-dimensional imidonitridophosphate networks next to alkaline earth cations as observed in SrP_3N_5NH, $Ba_4P_6N_{10}NH:Eu^{2+}$ and $AE_2AlP_8N_{15}(NH):Eu^{2+}$ (*AE* = Ca, Sr, Ba)

as well as in imide-doped samples of $Sr_3SiP_3O_2N_7:(NH)^{2-}$ and $Sr_5Si_2P_4ON_{12}:(NH)^{2-}$.[22-25] Additionally, imidonitridophosphate layers could be realized in $AEP_6N_8(NH)_4$ (*AE* = Mg, Ca, Sr) using this method.[26-27]

From the ammonothermal approach with alkali metal amides and P_3N_5 as starting materials, on the other hand, several imido(nitride)phosphate amides with isolated imidonitridophosphate anions could be prepared. In $Cs_5[P(NH)_4](NH_2)_2$, isolated $P(NH)_4$ tetrahedra are formed while in $Na_{10}[P_4(NH)_6N_4](NH_2)_6(NH_3)_{0.5}$ and $Rb_8[P_4N_6(NH)_4](NH_2)_2$ adamantane-type T2 supertetrahedra anions are incorporated next to free amide ions.[28-30] These structural units have also been observed in lithium-containing nitridophosphates.[31-33]

Therefore, with only few reported representatives of the imidonitridophosphate compound class, already a wide range of structural features could be realized.

While imidonitridophosphates were initially only discussed as possible intermediate products during the formation of nitridophosphates, they already showed interesting luminescent properties themselves.[27] Despite the expectation that oscillators such as N–H would quench the emission, luminescent samples of $Ba_4P_6N_{10}NH:Eu^{2+}$ and $AE_2AlP_8N_{15}(NH):Eu^{2+}$ (*AE* = Ca, Sr, Ba) could be prepared and show bright emission in the blue to green spectral region. Here, a low ratio of the NH groups among the anions (NH:N = 1:10 and 1:15, respectively) was discussed as a possible reason for the observed luminescence.[23-24]

In the following, we present the successful ammonothermal synthesis of the alkaline earth imidonitridophosphate $Ba_4P_4N_8(NH)_2$. X-ray diffraction analysis revealed for the first time a structure type containing $[P_4N_8(NH)_2]^{8-}$ anions next to alkaline earth metal ions. The presence of N–H functionality is confirmed by Fourier-transform infrared (FTIR) and magic angle spinning (MAS) NMR spectroscopy, which allow the determination of the nitrogen atoms that are preferentially bound to hydrogen atoms. Finally, the optical properties and the luminescent behavior of Eu^{2+}-doped samples of $Ba_4P_4N_8(NH)_2$ are investigated showing promising results for future research on luminescent imidonitridophosphates.

3.2 Results and Discussion

3.2.1 Synthesis

The ammonothermal synthesis of the barium imidonitridophosphate $Ba_4P_4N_8(NH)_2$ was performed at ammonobasic conditions in custom-built high-pressure autoclaves made from a nickel-based superalloy. The colorless product crystallizes in block-like crystals (Figure 3.1). The product decomposes at ambient conditions after a few days and is therefore sensitive towards moisture. To prevent decomposition, the product was handled under inert gas conditions.

First synthesis attempts contained BaH_2 and P_3N_5 in the molar ratio 9:5 as well as an excess of the mineralizer NaN_3 to increase the solubility of the starting materials in supercritical ammonia. After the correct stoichiometry of the compound was determined from X-ray diffraction data, samples were obtained from stoichiometric ratios of the starting materials BaH_2 and red phosphorus with an excess of NaN_3 as mineralizer.

From the so-prepared samples, an unidentified side phase could be removed by washing the sample with dry ethanol. Luminescent samples were obtained using the dopant $Eu(NH_2)_2$ (1 mol% with respect to the barium content). Doped samples show a yellow body color and cyan luminescence upon irradiation with ultraviolet (UV) light which is further discussed in the luminescence part.

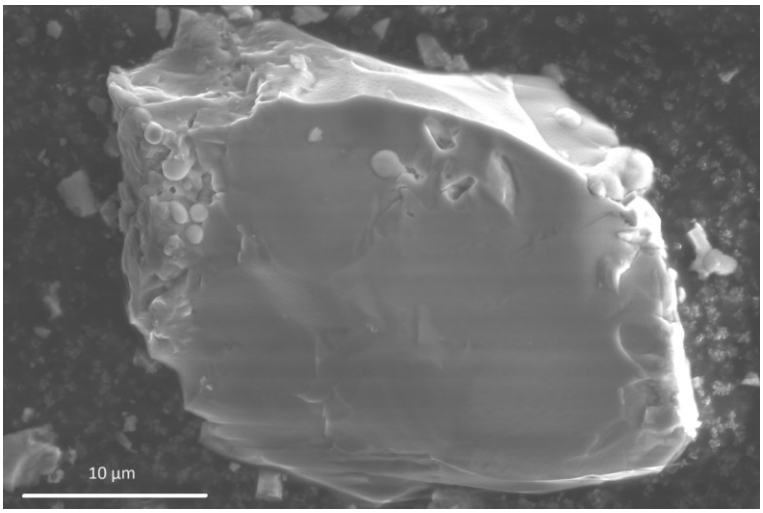

Figure 3.1: SEM image of a $Ba_4P_4N_8(NH)_2$ crystallite.

3.2.2 Crystal Structure Description

As the structure elucidation of $Ba_4P_4N_8(NH)_2$ comprised a multi-step process involving several analytical methods which can be followed more easily with the knowledge of the final structure model, a description of this model is given here in advance to the structure determination.

The structure of $Ba_4P_4N_8(NH)_2$ is composed of adamantane-type $[P_4N_8(NH)_2]^{8-}$ anions which can be described as T2 supertetrahedra consisting of four $P(N/NH)_4$ tetrahedra. These anions occur in two orientations (green and pink in Figure 3.2a). Along [001], columns of adjacent supertetrahedra ions are formed, all oriented in the same direction. Along [100] and [010], the orientation of the adjacent supertetrahedra alternates (Figure 3.2b). The $P(N/NH)_4$ tetrahedra exhibit minimal distortion as evidenced by the P–N distances and bonding angles, which fall within the typical range reported in the literature (Figure 3.2c, Table 9.9).[29-32] As the following structure determination will show, it is most probable that the hydrogen atoms are connected to terminal nitrogen positions of the supertetrahedra with a higher probability of a connection to nitrogen atoms N1 and N3.

The space between the $[P_4N_8(NH)_2]^{8-}$ anions is occupied by barium atoms. They are coordinated by six to eight nitrogen atoms (Figure 3.2d), respectively. The coordination polyhedra of the barium atoms can be described as distorted polyhedra, namely as monocapped trigonal frustum (Ba1), monocapped trigonal prism (Ba2), biaugmented isosceles wedge (Ba3) and isosceles wedge (Ba4).[34] The Ba–N distances range from 2.767(6) to 3.162(7) Å. This is consistent with other reported barium nitridophosphate compounds.[13,23,35-37]

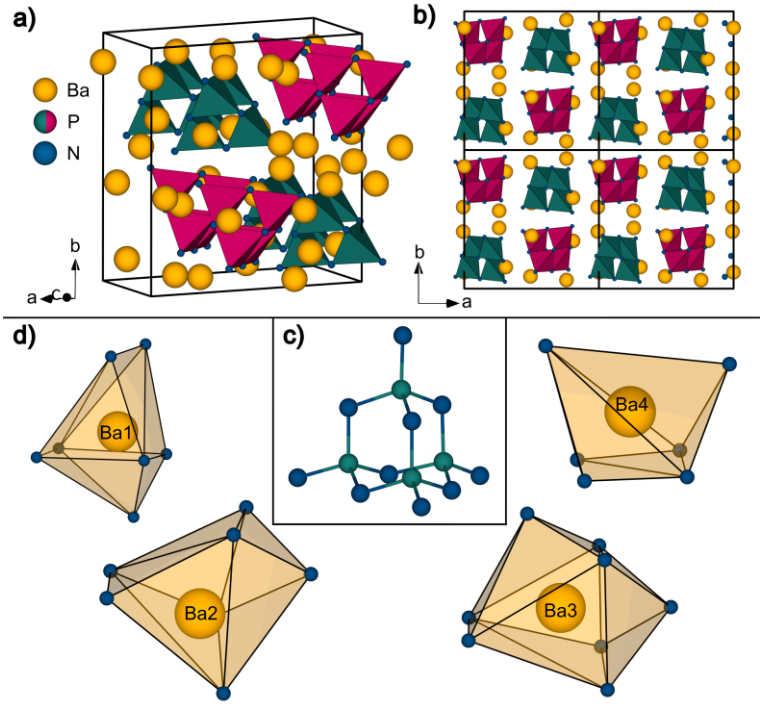

Figure 3.2: Representation of the crystal structure of $Ba_4P_4N_8(NH)_2$ showing columns of $[P_4N_8(NH)_2]^{8-}$ anions (a) with view along [001] (b). The barium atoms are shown in orange, the phosphorus atoms in green and the nitrogen atoms in blue. The two orientations of the adamantane-type $[P_4N_8(NH)_2]^{8-}$ anions (c) are represented in green and pink, respectively. The coordination spheres of the barium atoms are shown below (d).

Regarding the compositions of (imido)nitridophosphate compounds comprising T2 supertetrahedra anions, they all show the same condensation degree $\kappa = 0.4$ which is defined as the ratio of tetrahedron centers to tetrahedron corners.[29-32] $Ba_4P_4N_8(NH_2)_2$ exhibits an unprecedented arrangement of the supertetrahedra anions resulting in a new structure type. While two orientations of the anions are observed frequently in this structural family, only $Rb_8[P_4N_6(NH)_4](NH_2)_2$ exhibits columns of supertetrahedra with the same orientation along [001] in the structure. The orientation of the anion columns alternates along [100] and [010] as well.[29] In contrast to $Rb_8[P_4N_6(NH)_4](NH_2)_2$, where one corner of the supertetrahedra points in the direction of the columns, the supertetrahedra in $Ba_4P_4N_8(NH_2)_2$ point with edges in the direction of the columns.

However, next to the structural similarity of the supertetrahedra anions, the compositions of the imidonitridophosphate (amides) $Na_{10}[P_4(NH)_6N_4](NH_2)_6(NH_3)_{0.5}$, $Rb_8[P_4N_6(NH)_4](NH_2)_2$ and $Ba_4P_4N_8(NH)_2$ vary significantly. This phenomenon can be attributed to a multitude of factors, including the relative quantity of metal cations, the ratio of additional amide anions, and the

proportion of imide groups present in the T2 supertetrahedra. Among these compounds, $Ba_4P_4N_8(NH)_2$ shows the lowest hydrogen content. This may be achieved by the incorporation of the large divalent alkaline earth metal ion Ba^{2+} next to the T2 supertetrahedra structural motif for the first time which could render the incorporation of additional amide anions unnecessary to form a stable structure.

3.2.3 Crystal Structure Determination

From single-crystal X-ray diffraction data, a first structure model was obtained without hydrogen atoms. $Ba_4P_4N_8(NH)_2$ crystallizes in the monoclinic space group *Cc* (no. 9) with the lattice parameters a = 12.5250(3), b = 12.5566(4), c = 7.3882(2) Å and β = 102.9793(10)°. Information on the structure refinement is summarized in Table 1. The atomic coordinates together with the respective Wyckoff positions and displacement parameters are reported in the Supporting Information in Table 9.7–Table 9.9.[38]

The refined structure model is supported by CHARDI and BVS calculations (Table 9.15 and Table 9.16). Additionally, Rietveld refinement of powder X-ray diffraction (PXRD) data confirmed that $Ba_4P_4N_8(NH)_2$ is formed without crystalline side phases as bulk material after the ethanol washing (Figure 3.3, Table 9.13 and Table 9.14).

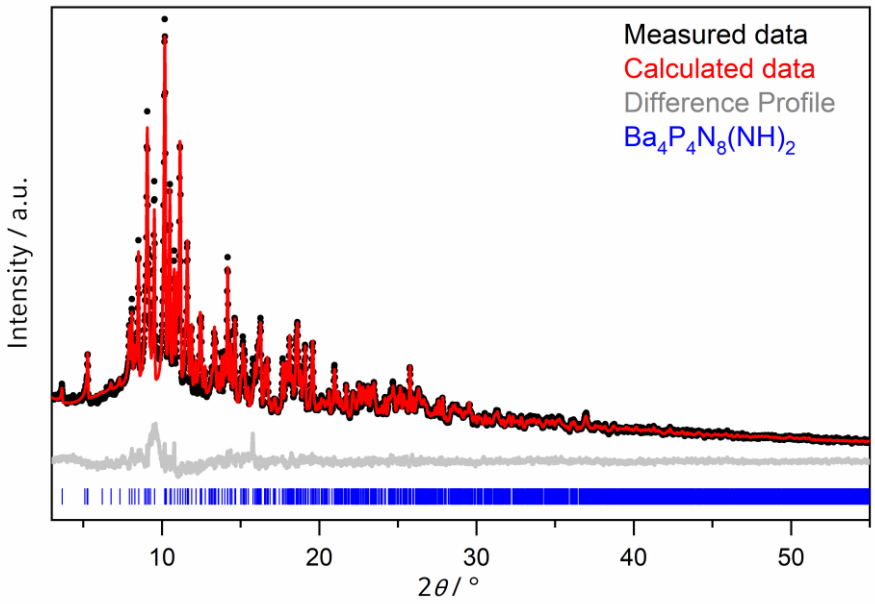

Figure 3.3: Rietveld refinement based on PXRD data of $Ba_4P_4N_8(NH_2)$ with experimental data (black dots, Ag-Kα_1 radiation), calculated diffraction pattern (red line), difference profile (gray line) and reflection positions of $Ba_4P_4N_8(NH_2)$ (blue bars).

Table 3.1: Crystallographic data for $Ba_4P_4N_8(NH)_2$ obtained from single-crystal X-ray diffraction, standard deviations are given in parentheses.

Formula	**$Ba_4P_4N_8(NH)_2$**
Crystal system	monoclinic
Space group	*Cc* (no. 9)
a / Å	12.5250(3)
b / Å	12.5566(4)
c / Å	7.3882(2)
β / °	102.9793(10)
Cell volume / Å^3	1132.27(5)
Formula units *Z* / cell	4
Density / g·cm^{-3}	4.783
μ / mm^{-1}	14.285
T / K	298(2)
Diffractometer	Bruker D8 Venture
Radiation (λ / Å)	Mo-K_α (0.71073)
F(000)	1424
θ range / °	3.245−36.965
Total no. of reflections	8923
No. of independent reflections	4321
Observed reflections [$F^2 > 2\sigma(F^2)$]	4077
R_{int}, R_σ	0.0328, 0.0514
Refined parameters / restraints	163 / 2
Flack parameter	0.044(17)
Goodness of fit (χ^2)	1.051
*R*1 (all data) / *R*1 [$F^2 > 2\sigma(F^2)$]	0.0336 / 0.0297
*wR*2 (all data) / *wR*2 indices [$F^2 > 2\sigma(F^2)$]	0.0555 / 0.0540
$\Delta\rho_{max}$ / $\Delta\rho_{min}$ [eÅ^{-3}]	1.62 / –1.95

From the refined atomic positions, two charge-neutral sum formulas $Ba_4P_4N_8X_2$ where *X* is either O^{2-} or $(NH)^{2-}$ were reasonable, since oxygen incorporation cannot be excluded due to contamination from the autoclave wall.[13] From the residual electron density obtained from the difference Fourier map, maxima in reasonable distances to the nitrogen atoms for an imide functionality were found. Therefore, further spectroscopic investigations were performed to clarify the structural composition.

The results of the EDX measurements support the Ba:P ratio obtained from the XRD structure model (Table 9.17). However, the differentiation of the lighter elements oxygen and nitrogen by this method is not reliable for the investigated compound due to its moisture-sensitivity. It is possible that the measured oxygen content results from surface hydrolysis of the sample, as the sample is in contact with air during preparation for the EDX measurement, as well as from the washing step with dry ethanol.

In the FTIR spectrum (Figure 3.4), typical N–H stretching vibrations in the region of 3100–3300 cm^{-1} were observed. The absorption bands at 612, 3208 and 3258 cm^{-1} (literature: 591, 3208 and 3257 cm^{-1}) can be assigned to $NaNH_2$ which is formed during the reaction from the excess of mineralizer employed.[39] In general, the measured spectrum agrees well with a theoretical spectrum obtained from quantum chemical density functional theory calculations based on a structure model containing hydrogen atoms, as described later. The signal at 3132 cm^{-1} can be assigned to the stretching vibration $\nu(NH^{2-})$ of $Ba_4P_4N_8(NH)_2$ with the help of the theoretical spectrum (Table 9.18). This indicates the presence of NH groups in the sample in general. In contrast to $Na_{10}[P_4(NH)_6N_4](NH_2)_6(NH_3)_{0.5}$, $Ba_4P_4N_8(NH)_2$ shows a sharp band at 3132 cm^{-1} and therefore a structure without disorder of the amide ions is expected. The signals in the region of 500–1200 cm^{-1} can be assigned to various lattice vibrations of the anionic $[P_4N_8(NH)_2]^{8-}$ units.

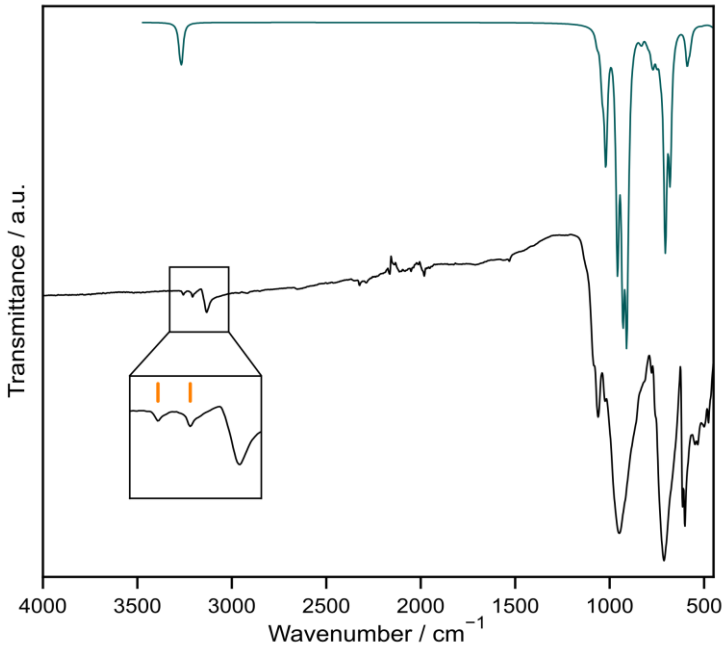

Figure 3.4: Comparison of the experimental FTIR spectrum of a sample containing $Ba_4P_4N_8(NH_2)_2$ (black line) with the theoretical spectrum from DFT-PBE calculations (green line) and the positions of the maximum absorption of $NaNH_2$ (orange bars). The area showing the N–H stretching vibrations (3100–3300 cm^{-1}) is shown as enlargement.

For a further assignment of the imide groups among the nitrogen positions, ^{1}H, ^{31}P and cross polarization $^{31}P\{^{1}H\}$ solid-state MAS NMR experiments were performed.

The ^{1}H spectrum shows a strong signal with a maximum at 2.1 ppm and a smaller broad shoulder around 2.4 ppm (Figure 3.5a). The observation of a ^{1}H NMR signal confirms the presence of hydrogen-containing groups in the sample. In combination with the FTIR spectrum that shows no O–H vibrations, this allows the presumption that the compound contains imide ions. While the strong signal can be assigned to the main phase, the shoulder may originate from a disorder of the hydrogen atoms which could be statistically bound to different nitrogen atoms of the $[P_4N_8(NH)_2]^{8-}$ units next to preferred positions which are responsible for the main signal. Another possible explanation for the shoulder of the signal could be unidentified minor side phases or hydrolysis products from the decomposition of $Ba_4P_4N_8(NH)_2$. In comparison to other alkaline earth metal imidonitridophosphates, for which ranges of the ^{1}H chemical shift from 9–5 ppm are reported, an upfield shift for the signal of $Ba_4P_4N_8(NH)_2$ is observed.[22-24,26-27] This shift might be caused by a higher electron density in close proximity to the hydrogen atoms due to the higher relative content of the alkaline earth metal in $Ba_4P_4N_8(NH)_2$ compared to the compounds in the literature, such as $BaP_6N_{10}(NH)$.[23]

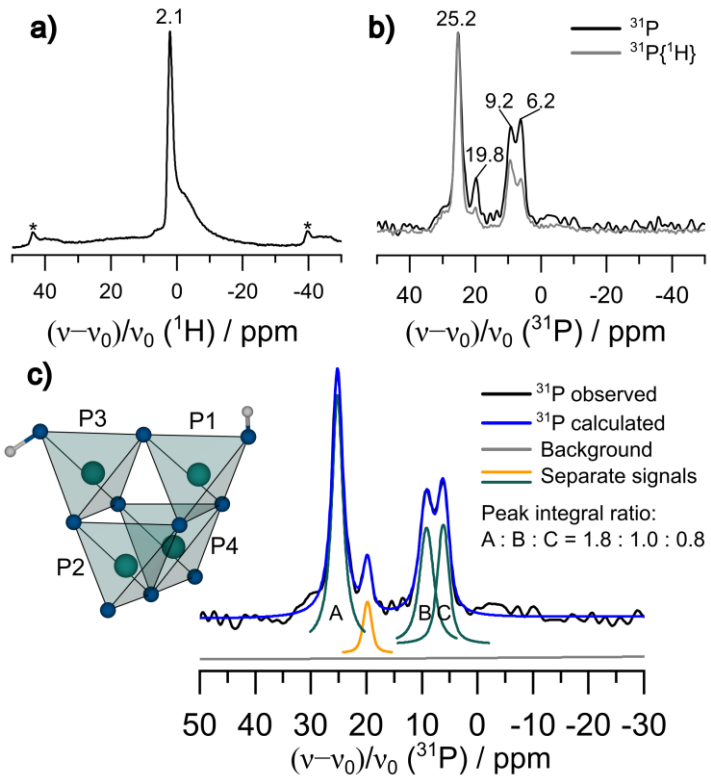

Figure 3.5: Solid-state NMR spectra of the ^{1}H measurement (a) and normalized spectra of ^{31}P and ^{31}P{^{1}H} measurements (b), all at 19 kHz MAS rate. Rotational side bands are marked with an asterisk. The deconvolution of the ^{31}P spectrum is shown next to a representation of a $[P_4N_8(NH)_2]^{8-}$ unit from the structural model with the preferred positions of the hydrogen atoms (c).

The ^{31}P NMR spectrum shows four separate signals at 25.2, 19.8, 9.2 and 6.2 ppm with small full widths at half maximum (*fwhm*) of 1.8–3 ppm (Figure 3.5b). These chemical shifts are in the range reported for nitridophosphates containing T2 supertetrahedra as structural feature.[32-33] In the cross-

polarized $^{31}P\{^1H\}$ spectrum, it is visible that all four signals occur as well under indirect polarization. Normalized to the signal at 25.2 ppm, however, the other three signals lose intensity under indirect polarization compared to the ones under direct polarization. The observation of the signals in the cross-polarized spectrum proofs the presence of hydrogen in a phosphor-containing compound and, therefore, confirms the presence of the imide groups in $Ba_4P_4N_8(NH)_2$. For an assignment of the signals to the crystallographic positions, a deconvolution of the ^{31}P spectrum was conducted (Figure 3.5c). From this, it can be derived that the signals at 25.2 ppm (signal A), 9.2 ppm (signal B) and 6.2 ppm (signal C) show an integral ratio of 1.8:1.0:0.8. This fits well to the four independent crystallographic phosphorus positions from the structure model (with an equal site multiplicity of Wyckoff positions 4*a*). It seems that the chemical environments of two of the phosphorus nuclei are very similar so that no separation into two signals is observed for signal A. Furthermore, the signal at 19.8 ppm is smaller than the others and its relative intensity loss in the $^{31}P\{^1H\}$ spectrum is significantly higher. Therefore, it can be assigned to an unidentified minor side phase which also contains hydrogen in the spatial proximity of phosphorus and which might be the same phase that contributes to the shoulder in the ^1H spectrum.

A possible assignment of the signals A to C to crystallographic phosphorus sites can be attempted regarding their respective chemical shift and the distances of the phosphorus atoms to their neighboring atoms (Table 9.9). In their first coordination sphere, all phosphorus atoms are surrounded by four nitrogen atoms. The respective P–N distances deviate only slightly among the different phosphorus positions ($d_{P–N}$ = 1.572(7)–1.702(6) Å). Therefore, no significant variations in the chemical shifts are expected due to this coordination. In the second coordination sphere, the distance to the barium atoms is regarded. Here, differences in the distances to the closest barium atom are obtained from the crystal structure refinement. The atoms P2 and P4 show significantly shorter P–Ba distances of 3.147(2) and 3.129(2) Å compared to the positions P1 (3.421(2) Å) and P3 (3.446(2) Å). Therefore, for the nuclei P2 and P4, an upfield shift could be expected compared to the nuclei P1 and P3 due to the electron density of the barium atoms in closer proximity to their nuclei. Subsequently, an assignment of the signals B and C to atom positions P2 and P4 is reasonable, although a further distinction of the two sites is not feasible. Accordingly, signal A may be assigned to positions P1 and P3 which show less electron density close to their nuclei.

Comparing the ^{31}P and $^{31}P\{^1H\}$ spectra, the proximity of the hydrogen atoms to the phosphorus atoms may be derived according to the relative changes in signal intensity. The magnetization transfer under cross polarization is mediated by dipolar couplings through space, which scale with the inverse cube of the distance. Therefore, the further away a phosphorus atom is from the next hydrogen atoms, the larger is the loss of signal intensity in the cross polarization experiment.[40] From the spectra in Figure 3.5b, it is consistent to say that the probability of hydrogen atoms is highest close to the positions belonging to signal A, most likely P1 and P3. As the signals B and C are still visible in the cross polarization spectrum, a local proximity to hydrogen atoms for these

positions may still be assumed, which could cause the observed shoulder in the ^{1}H spectrum as well.

To determine the imide positions among the ten possible crystallographic nitrogen positions, the results of the NMR spectra were used. From the small *fwhm* of signal A, a regular environment for these ^{31}P nuclei is expected which makes mixed occupations of several positions and the simultaneous presence of a terminal and a bridging imide group close to P1 and P3 improbable as both of these possibilities would cause a broadening of the signal. Additionally, the simultaneous occupation of two bridging nitrogen atoms can be ruled out, as the intensity loss for the $^{31}P\{^{1}H\}$ signals then should be in the same dimension for at least three signals. Therefore, it is expected that the hydrogen positions are bound to the terminal nitrogen positions N1, N2, N3 and N4 of the supertetrahedra which is in accordance to Pauling's second rule.[41]

From the NMR data, it is reasonable to say that the hydrogen atoms are partly statistically bound to all four terminal nitrogen atoms since all ^{31}P signals of $Ba_4P_4N_8(NH)_2$ are present in the cross polarization spectrum as well. Additionally, a preferred occupation of positions close to P1 and P3 can be derived from the data and therefore, the hydrogen is preferably bound to the imide positions N1 and N3. This assignment is supported by the results from CHARDI and BVS calculations (Table 9.15 and Table 9.16).

Based on these considerations, a second structure model for the quantum chemical calculations of the theoretical IR spectrum was generated by adding two hydrogen positions to residual electron density peaks from the Fourier map close to N1 and N3 and restricting the N–H distance to 0.90(2) Å. Information on this structure model is summarized in Table 9.10–Table 9.12.

3.2.4 UV/Vis Reflectance Spectroscopy

To allow an estimation of the optical band gap of $Ba_4P_4N_8(NH)_2$, a diffuse reflectance spectrum of an undoped sample was collected (Figure 9.2). To determine the optical band gap from this spectrum, a pseudo-absorption spectrum was generated using the Kubelka-Munk function $F(R) = (1-R)^2/2R$, with the measured reflectance R.[42] From a Tauc plot (Figure 3.6), a linear region is evident assuming a direct band gap.[43] By applying a tangent to the inflection point, an optical band gap of ≈3.5(2) eV was estimated.

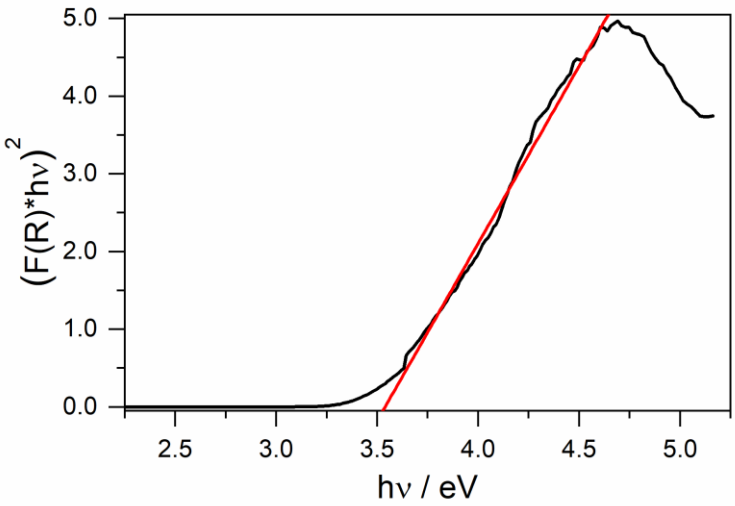

Figure 3.6: Tauc Plot of an undoped sample of $Ba_4P_4N_8(NH)_2$ (black) with a tangent to the inflection point (red line).

3.2.5 Luminescence

Due to the observation of promising luminescence properties in other compound classes with tetrahedra-based, isolated anions, such as orthosilicates and orthophosphates, doping experiments were performed.[44-45]

When doped with approximately 1 mol% Eu^{2+} with respect to the barium content, $Ba_4P_4N_8(NH)_2:Eu^{2+}$ shows cyan luminescence upon irradiation with near UV to blue light. The room temperature photoluminescence (PL) and photoluminescence excitation (PLE) spectra and a microscope image of the probed microcrystal under 400 nm light excitation are shown in Figure 3.7. $Ba_4P_4N_8(NH)_2:Eu^{2+}$ shows a narrow-band emission (*fwhm*: 50 nm/1981 cm^{-1}) with a maximum at 498 nm.

Due to the different coordination numbers and bond lengths (Figure 3.2d, Table 9.9) for the different barium sites, differences in absorption band positions and the Stokes shifts are expected for the four Ba sites which could explain the broadening of the PL emission band. Additionally, it is possible that not all of the four possible cations are occupied with Eu^{2+} which could explain the narrow-band emission. Future investigations could include overdoping experiments to test this hypothesis. The observed luminescence of $Ba_4P_4N_8(NH)_2:Eu^{2+}$ is comparable to other narrow-band nitride-based phosphors such as $Sr_2AlP_8N_{15}(NH):Eu^{2+}$ (λ_{max} = 496 nm, *fwhm* ≈ 46 nm), β-$MgSrP_3N_5O_2$ (λ_{max} = 502 nm, *fwhm* ≈ 42 nm) or $Ba_{3-x}Sr_x[Mg_2P_{10}N_{20}]:Eu^{2+}$ (x = 0–3, λ_{max} = 492–515 nm, *fwhm* ≈ 36–46 nm).[24,37,46-48] Due to the maximum position and the *fwhm* of the emission, $Ba_4P_4N_8(NH)_2:Eu^{2+}$ is a promising candidate phosphor to close the cyan-gap occurring in state-of-the-art pc-LEDs.[49] Next to the PL emission, the internal quantum efficiency (IQE) and the thermal quenching behavior are important factors to assess the potential of a phosphor for a potential industrial application.

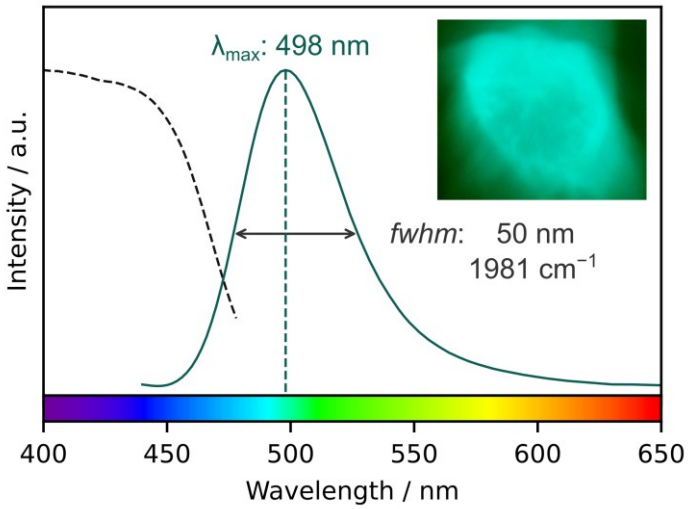

Figure 3.7: Spectra of the photoluminescence excitation (PLE, dashed black line) and photoluminescence (PL, green line) of $Ba_4P_4N_8(NH)_2$ upon excitation at 400 nm at room temperature.

From the IQE measurements in an integrating sphere, an IQE of up to 41 % for as-synthesized samples of for $Ba_4P_4N_8(NH)_2:Eu^{2+}$ upon 443 nm laser excitation at room temperature was determined. This is a promising value for a possible application and can likely be further increased by synthesis and crystallite growth optimization in the future. To estimate the thermal behavior of $Ba_4P_4N_8(NH)_2:Eu^{2+}$ at typical working temperatures of a LED, luminescence spectra at different temperatures were collected. Figure 3.8 shows the thermal quenching (TQ) of $Ba_4P_4N_8(NH)_2:Eu^{2+}$ from room temperature to 200°C derived from these spectra. The compound shows pronounced thermal quenching resulting in 40 % of the photoemission power at 150°C compared to the emission power at room temperature.

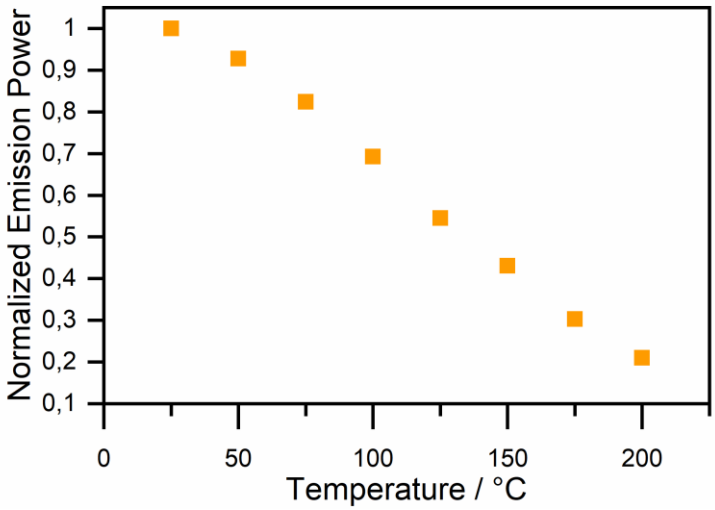

Figure 3.8: Thermal behavior of the normalized integrated emission power of $Ba_4P_4N_8(NH)_2Eu^{2+}$ under 415 nm LED excitation.

Compounds containing imide groups were considered as unsuitable for an industrial application due to possible absorption effects of the oscillator N–H. Additionally, luminescent imidonitridophosphates were until now only prepared using large volume press experiments which produce only small sample quantities that impede an industrial scale up. Therefore, no data on the efficiency and temperature behavior of luminescent imidonitridophosphates is available in the literature.[23] Hence, the data for $Ba_4P_4N_8(NH)_2:Eu^{2+}$ present a first benchmark for the compound class of imidonitridophosphates.

The observation of a high IQE at room temperature in the imidonitridophosphate is surprising as $Ba_4P_4N_8(NH)_2$ shows the highest NH:N ratio of 1:4 compared to reported luminescent imidonitridophosphates which showed NH:N ratios of 1:10 and lower. For them, the low concentration of imide groups among the anions was discussed as possible reason for the observed luminescence despite the presence of imide groups in the structure.[23-24]

The thermal quenching observed for $Ba_4P_4N_8(NH)_2:Eu^{2+}$ might be caused by the discussed absorption of the imide group oscillators. As there are other possible explanations, such as concentration quenching, which could cause the observed decrease in PL intensity at higher temperatures, further measurements, for example for different doping concentrations, should be conducted in the future.

Despite the unfavorable thermal behavior of $Ba_4P_4N_8(NH)_2:Eu^{2+}$, the high IQE at room temperature in a structure with isolated anionic units shows that imidonitridophosphates are a promising compound class for host lattices of LED phosphors even for structures containing higher NH:N ratios.

3.3 Conclusions

We succeeded in the ammonothermal synthesis of the barium imidonitridophosphate $Ba_4P_4N_8(NH)_2$. The multi-step structural characterization revealed the incorporation of the adamantane-type $[P_4N_{10}]$ structural unit next to metal cations other than alkali metal cations for the first time. Furthermore, the spectroscopic investigation enabled the determination of the presence of imide groups in the $[P_4N_8(NH)_2]^{8-}$ anions as evidenced by FTIR, as well as the identification of the nitrogen atoms that are most likely to be bound to the hydrogen atoms, as indicated by solid-state NMR. Doped samples of $Ba_4P_4N_8(NH)_2:Eu^{2+}$ show a narrow-band emission (*fwhm*: 50 nm/1981 cm^{-1}) with a maximum at 498 nm and a promising IQE of 41 %. The luminescence shows pronounced thermal quenching above room temperature.

Overall, this luminescent behavior is highly promising, as $Ba_4P_4N_8(NH)_2$ is built up from isolated anionic supertetrahedra. Additionally, it exhibits the highest NH:N ratio reported for luminescent nitridophosphates, as the latter was previously regarded as a potential impediment for luminescence in imide containing compounds. In light of the promising luminescence behavior

observed for $Ba_4P_4N_8(NH)_2$, imidonitridophosphates should be considered in future research on suitable substance classes to be used as host structures in phosphor materials. Phosphors showing emission in the spectral region observed for $Ba_4P_4N_8(NH)_2:Eu^{2+}$ have the potential to address the so-called cyan gap in white-light emitting pcLEDs.[49] For this possible application, the ammonothermal synthesis enables a medium pressure access to the imidonitridophosphate compound class which has – in contrast to the large volume press synthesis – the potential for industrial scale up.

3.4 Experimental Section

Since some of the starting materials as well as the product show sensitivity towards air and moisture, all handling of these compounds was conducted under inert gas conditions. Therefore, argon-filled glove boxes (MBraun, $O_2 < 1$ ppm, $H_2O < 1$ ppm) or flame-dried Schlenk-type glassware was used in combination with a vacuum line ($\rho \leq 0.1$ Pa) with supply of Ar and NH_3. To purify the two gases (Air liquide, 99.999 %), they passed through purification cartridges Micro Torr FT400-902 for Ar and Micro Torr MC400-702FV for NH_3 (both SAES Pure Gas Inc.) to reach a purity level of < 1ppbV H_2O, O_2 and CO_2 prior to their utilization. The respective amount of NH_3 that was condensed in the autoclave was estimated with the help of a mass flow meter D-6320-DR (Bronkhorst).

3.4.1 Synthesis of P_3N_5

Semi-crystalline P_3N_5 was prepared according to the literature by ammonolysis of P_4S_{10} (approx. 7 g, Sigma-Aldrich, 99.99 %) with ammonia (purification described above) at 850°C in a fused silica boat.[50] First, the insertion of the silica boat was performed in an Ar counter flow and the apparatus was floated with NH_3 for 4 h. Subsequent heating to 850°C with a holding time of 4 h followed by cooling to room temperature yielded P_3N_5 as orange powder. The product was identified by PXRD, FTIR and CHNS analysis.

3.4.2 Synthesis of $Eu(NH_2)_2$

$Eu(NH_2)_2$ was synthesized from supercritical ammonia from elemental Eu (smart-elements, 99.99 %) according to the literature.[51]

3.4.3 Ammonothermal Synthesis

For the synthesis of $Ba_4P_4N_8(NH_2)_2$, custom-built Inconel® 718 autoclaves (max. 900 K, 300 MPa, volume: 10 mL) were used. The autoclave was further equipped with a hand valve (SITEC), a bursting disk (Dieckers GmbH & Co. KG, pressure limit: 330 MPa) in a bursting disk holder (SITEC) and a pressure transmitter (HBM P2VA1/5000 bar). The starting materials BaH_2 (Materion, 99.7 %, 209.0 mg, 1.500 mmol) and P_3N_5 (135.7 mg, 0.8333 mmol) or red phosphorus (Sigma-Aldrich, >97 %, 46.5 mg, 1.50 mmol) were ground together with the employed mineralizer NaN_3 (Sigma-Aldrich, 99.5 %, 162.5 mg, 2.500 mmol). To synthesize doped samples, ≈ 1 mol% of

the BaH_2 were replaced by $Eu(NH_2)_2$. The mixture was placed in a niobium or tantalum liner and subsequently transferred to the autoclave. To seal the autoclave, a silver-coated Inconel® 718 ring (GFD seals) was used by tightening the autoclave screws. Cooling of the autoclave with a liquid nitrogen/ethanol bath allowed to condense ammonia (ca. 8 mL, purification described above) in the autoclave. When the autoclave reached room temperature, it was placed in a tube furnace and heated to 670 K in 2 h, held at that temperature for 12 h and then heated to 870 K in 2 h. The temperature was held for 96–120 h, reaching a maximum pressure of 150 MPa, before the furnace was switched off and the autoclave was cooled to room temperature. After removing residual ammonia from the autoclave, the reaction product was separated from the liner wall in a glove box. The samples were subsequently washed with dry ethanol to remove the side phase.

3.4.4 Single-Crystal X-ray Diffraction

A single crystal (0.04 x 0.04 x 0.03 mm^3) was isolated under oil using a microscope. The crystal was immediately transferred to a Bruker D8 Venture diffractometer to avoid hydrolysis and the data was collected using Mo-K_α radiation (λ = 0.71073 Å) and a combined Φ-ω-scan. To index and integrate the data, the APEX3 program was used as well as for the space group determination and semi-empirical absorption correction (SADABS).[52-53] The structure solution was performed using XPREP and SHELXT and for the refinement full-matrix least-squares methods (SHELXL) were employed in the program WINGX.[54-58]

3.4.5 Powder X-ray Diffraction

Powder X-ray diffraction data were collected on a STOE STADI P diffractometer employing Ag-$K_{\alpha1}$ radiation (λ = 0.5594217 Å), a Ge(111) monochromator as well as a Mythen 1K detector in modified Debye-Scherrer geometry. Prior to the measurement, the sample was prepared at argon atmosphere by grounding in an agate mortar and was transferred into a glass capillary (d = 0.3 mm, wall thickness 0.01 mm, Hilgenberg GmbH). The TOPAS software package was used to perform a Rietveld refinement of the collected diffraction data.[59]

3.4.6 Fourier-Transform (FTIR) Spectroscopy

The FTIR spectroscopy data were collected in an argon-filled glove box on an Alpha II FTIR spectrometer (Bruker) equipped with a diamond attenuated total reflectance (ATR) unit. Using the program OPUS 8.7, a spectrum in the range of 400–4000 cm^{-1} with a resolution of 2 cm^{-1} was collected at ambient temperature.[60]

3.4.7 DFT Calculations

To simulate the theoretical IR spectrum, *ab initio* electronic structure calculations were performed to determine the vibrational frequencies. Periodic DFT calculations were conducted using the Vienna *ab intio* Simulation Package (VASP).[61-64] VASP separates core and valence electrons using projector-augmented waves (PAW).[65-66] The generalized gradient approximation (GGA) was used

to calculate exchange- and correlation-energy, as described by Perdew, Burke and Ernzerhof (PBE).[67] A dense k-point sampling with a 4x4x4 Γ-centered grid (~0.2/Å) and a plane wave energy cutoff of 520 eV ensured a well-converged structure. An optimization with full ionic degrees of freedom, i.e. atomic positions, cell shape and cell volume was performed using the conjugate gradient algorithm.[68] The extraction of vibrational frequencies from a density-functional perturbation theory (DFPT) linear response calculation was performed using the plotIR script provided by Dr. Karhánek. The energy convergence criterion was set to 10^{-5} eV and the Hellmann-Feynmann forces and stresses were relaxed until the convergence criterion of 10^{-3} eV/Å was reached. The same convergence criteria were used for the DFPT calculation.

3.4.8 Solid-State MAS NMR Spectroscopy

The ^{1}H, ^{31}P and $^{31}P\{^{1}H\}$ spectra were recorded employing an Avance III 500 spectrometer (Bruker) operating at a ^{1}H frequency of 500.25 MHz (magnetic field strength: 11.7 T). The sample was ground in a glove box and transferred in a ZrO_2 rotor with an outer diameter of 2.5 mm which was rotated with a frequency of 19−20 kHz. Device-specific software was used for the evaluation of the spectra. As a secondary reference, the ^{1}H resonance of 1 % $Si(CH_3)_4$ in $CDCl_3$ was used, adapting the Ξ values for ^{31}P relative to H_3PO_4 as reported by the IUPAC.[69]

3.4.9 Scanning Electron Microscopy

For the generation of the electron microscope images of the crystallites and the energy dispersive X-ray (EDX) spectroscopy data, a Dualbeam Helios Nanolab G3UC (FEI) equipped with an X-Max80 SDD detector (Oxford instruments) was used. The sample was placed on an aluminium holder using carbon foil. Additionally, to prevent electrostatic charging of the sample, a high-vacuum sputter coater (CCU-010, Safematic GmbH) was used to carbon-coat the sample.

3.4.10 UV/Vis Spectroscopy

Diffuse reflectance spectra were collected using a Jasco V-650 UV/vis spectrophotometer (JASCO) equipped with a deuterium and a halogen lamp, a CzernyTurner monochromator with 1200 lines/mm, concave grating and a photomultiplier tube detector.

3.4.11 Luminescence Spectroscopy

Particles of Eu^{2+}-doped samples of $Ba_4P_4N_8(NH)_2$ were analyzed by luminescence spectroscopy employing a HORIBA Fluoromax4 spectrofluorimeter system connected to an Olympus BX51 microscope. Recording of the respective PL and PLE spectra was performed at room temperature with emission and excitation wavelengths of λ_{emi} = 498 nm and λ_{exc} = 420 nm in a range from 400−650 nm with a step size of 2 nm. For the determination of the internal quantum efficiency, a powder sample of $Ba_4P_4N_8(NH)_2$ was placed in a PTFE sample holder with polymeric lid in a glove box before it was transferred to the spectrometer. The measurements were performed on an in-house built system which is based on an integrating sphere with attached spectrofluorimeter (Instrument Systems CAS 140D). The internal quantum efficiency measurement was performed

using the two measurement method and an excitation wavelength of 443 nm (laser diode).[70] For the temperature-dependent measurements of emission spectra, a very thin powder layer was produced by curing a silicone suspension containing the sample between an alumina substrate and a cover glass at 150°C in a glove box. The so-prepared sample was heated on a Linkam THMS600 stage and the emission spectra at 415 nm excitation were measured after thermal equilibration using a calibrated Ocean Insight HR2000Plus ES spectrometer controlled by the measurement software SweepMe! (Axel Fischer and Felix Kaschura, SweepMe! - A multi-tool measurement software (sweep-me.net)).

3.5 Acknowledgements

The authors thank Christian Minke and Prof. Dirk Johrendt (both at Department of Chemistry, LMU Munich) for the conduction of SEM and NMR measurements and for providing the resources for the DFT calculations, respectively. Open Access funding enabled and organized by Projekt DEAL.

3.6 References

[1] F. J. Pucher, A. Marchuk, P. J. Schmidt, D. Wiechert, W. Schnick, "Luminescent Nitridophosphates $CaP_2N_4:Eu^{2+}$, $SrP_2N_4:Eu^{2+}$, $BaP_2N_4:Eu^{2+}$, and $BaSr_2P_6N_{12}:Eu^{2+}$", *Chem. Eur. J.* **2015**, *21*, 6443–6448.

[2] S. Wendl, L. Eisenburger, P. Strobel, D. Günther, J. P. Wright, P. J. Schmidt, O. Oeckler, W. Schnick, "Nitridophosphate-Based Ultra-Narrow-Band Blue-Emitters: Luminescence Properties of $AEP_8N_{14}:Eu^{2+}$ (*AE*=Ca, Sr, Ba)", *Chem. Eur. J.* **2020**, *26*, 7292–7298.

[3] S. Wendl, S. Mardazad, P. Strobel, P. J. Schmidt, W. Schnick, "HIP to be Square: Simplifying Nitridophosphate Synthesis in a Hot Isostatic Press", *Angew. Chem.* **2020**, *132*, 18397–18400; *Angew. Chem. Int. Ed.* **2020**, *59*, 18240–18243.

[4] M. Mallmann, S. Wendl, P. Strobel, P. J. Schmidt, W. Schnick, "$Sr_3P_3N_7$: Complementary Approach by Ammonothermal and High-Pressure Syntheses", *Chem. Eur. J.* **2020**, *26*, 6257–6263.

[5] M.-H. Fang, H.-P. Hsueh, T. Vasudevan, W.-T. Huang, Z. Bao, N. Majewska, S. Mahlik, H.-S. Sheu, R.-S. Liu, "Dual-emission Eu-doped $Ca_{2-x}Sr_xPN_3$ nitridophosphate phosphors prepared by hot isostatic press", *J. Mater. Chem. C* **2021**, *9*, 8158–8162.

[6] S. D. Kloß, W. Schnick, "Nitridophosphates: A Success Story of Nitride Synthesis", *Angew. Chem.* **2019**, *131*, 8015–8027; *Angew. Chem. Int. Ed.* **2019**, *58*, 7933–7944.

[7] M. Mallmann, S. Wendl, W. Schnick, "Crystalline Nitridophosphates by Ammonothermal Synthesis", *Chem. Eur. J.* **2020**, *26*, 2067–2072.

[8] T. M. M. Richter, R. Niewa, "Chemistry of Ammonothermal Synthesis", *Inorganics* **2014**, *2*, 29–78.

[9] J. Häusler, W. Schnick, "Ammonothermal Synthesis of Nitrides: Recent Developments and Future Perspectives", *Chem. Eur. J.* **2018**, *24*, 11864–11879.

[10] R. Niewa in: "*Ammonothermal Synthesis and Crystal Growth of Nitrides – Chemistry and Technology*" (Eds.: E. Meissner, R. Niewa), Springer, Cham, **2021**, pp. 227–251.

[11] H. Jacobs, R. Nymwegen, "Darstellung und Kristallstruktur eines Kaliumnitridophosphats, $K_3P_6N_{11}$", *Z. Anorg. Allg. Chem.* **1997**, *623*, 429–433.

[12] M. Mallmann, C. Maak, R. Niklaus, W. Schnick, "Ammonothermal Synthesis, Optical Properties, and DFT Calculations of Mg_2PN_3 and Zn_2PN_3", *Chem. Eur. J.* **2018**, *24*, 13963–13970.

[13] S. Wendl, M. Mallmann, P. Strobel, P. J. Schmidt, W. Schnick, "Ammonothermal Synthesis of Ba_2PO_3N – An Oxonitridophosphate with Non-Condensed PO_3N Tetrahedra", *Eur. J. Inorg. Chem.* **2020**, *2020*, 841–846.

[14] W. Schnick, J. Lücke, "Darstellung, Kristallstruktur und IR-spektroskopische Untersuchung von Phosphor(V)-nitrid-imid, HPN_2", *Z. Anorg. Allg. Chem.* **1992**, *610*, 121–126.

[15] H. Jacobs, R. Nymwegen, S. Doyle, T. Wroblewski, W. Kockelmann, "Kristallines Phoshor(V)-nitrid-imid, HPN_2 bzw. DPN_2 – Strukturbestimmung mit Röntgen-, Synchrotron- und Neutronenstrahlung", *Z. Anorg. Allg. Chem.* **1997**, *623*, 1467–1474.

[16] S. Horstmann, E. Irran, W. Schnick, "Phosphorus(V) Nitride Imide HP_4N_7: Synthesis from a Molecular Precursor and Structure Determination with Synchrotron Powder diffraction", *Angew. Chem. Int. Ed.* **1997**, *36*, 1992–1994; *Angew. Chem.* **1997**, *109*, 2085–2087.

[17] S. Horstmann, E. Irran, W. Schnick, "Synthese, Kristallstruktur und Eigenschaften von Phosphor(V)-nitridimid HP_4N_7", *Z. Anorg. Allg. Chem.* **1998**, *624*, 221–227.

[18] A. Marchuk, F. J. Pucher, F. W. Karau, W. Schnick, "A High-Pressure Polymorph of Phosphorus Nitride Imide", *Angew. Chem.* **2014**, *126*, 2501–2504; *Angew. Chem. Int. Ed.* **2014**, *53*, 2469–2472.

[19] D. Baumann, W. Schnick, "High-Pressure Polymorph of Phosphorus Nitride Imide HP_4N_7 Representing a New Framework Topology", *Inorg. Chem.* **2014**, *53*, 7977–7982.

[20] D. Baumann, W. Schnick, "Pentacoordinate Phosphorus in a High-Pressure Polymorph of Phosphorus Nitride Imide $P_4N_6(NH)$", *Angew. Chem.* **2014**, *126*, 14718–14721; *Angew. Chem. Int. Ed.* **2014**, *53*, 14490–14493.

[21] F. Karau, W. Schnick, "A Nitridic Clathrate: $P_4N_4(NH)_4(NH_3)$", *Angew. Chem.* **2006**, *118*, 4617–4620; *Angew. Chem. Int. Ed.* **2006**, *45*, 4505–4508.

[22] S. Vogel, W. Schnick, "SrP_3N_5NH: A Framework-Type Imidonitridophosphate Featuring Structure-Directing Hydrogen Bonds", *Chem. Eur. J.* **2018**, *24*, 14275–14281.

[23] S. Wendl, L. Eisenburger, M. Zipkat, D. Günther, J. P. Wright, P. J. Schmidt, O. Oeckler, W. Schnick, "$BaP_6N_{10}NH:Eu^{2+}$ as a Case Study – An Imidonitridophosphate Showing Luminescence", *Chem. Eur. J.* **2020**, *26*, 5010–5016.

[24] M. M. Pointner, R. M. Pritzl, J. M. Albrecht, L. Blahusch, J. P. Wright, E. Lawrence Bright, C. Giacobbe, O. Oeckler, W. Schnick, "Multicationic Tetrahedra Networks: Alkaline-Earth-Centered Polyhedra and Non-Condensed AlN_6-Octahedra in the Imido-nitridophosphates $AE_2AlP_8N_{15}(NH)$ (AE = Ca, Sr, Ba)", *Chem. Eur. J.* **2024**, *30*, e202400766.

[25] M. Dialer, K. Witthaut, T. Bräuniger, P. J. Schmidt, W. Schnick, "The Fundamental Disorder Unit in (Si, P)–(O, N) Networks", *Angew. Chem.* **2024**, *136*, e202401419; *Angew. Chem. Int. Ed.* **2024**, *63*, e202401419.

[26] A. Marchuk, V. R. Celinski, J. Schmedt auf der Günne, W. Schnick, "$MH_4P_6N_{12}$ (M=Mg, Ca): New Imidonitridophosphates with an Unprecedented Layered Network Structure Type", *Chem. Eur. J.* **2015**, *21*, 5836–5842.

[27] S. Wendl, W. Schnick, "$SrH_4P_6N_{12}$ and SrP_8N_{14}: Insights into the Condensation Mechanism of Nitridophosphates under High Pressure", *Chem. Eur. J.* **2018**, *24*, 15889–15896.

[28] H. Jacobs, F. Golinski, "Synthese und Struktur eines Caesium-tetraimidophosphat-diamids, $Cs_5[P(NH)_4](NH_2)_2 = Cs_3[P(NH)_4] \cdot 2\ CsNH_2$", *Z. Anorg. Allg. Chem.* **1994**, *620*, 531–534.

[29] F. Golinski, H. Jacobs, "Synthese und Kristallstruktur von $Rb_8[P_4N_6(NH)_4](NH_2)_2$ mit dem adamantanartigen Anion $[P_4N_6(NH)_4]^{6-}$", *Z. Anorg. Allg. Chem.* **1995**, *621*, 29–33.

[30] H. Jacobs, S. Pollok, F. Golinski, "Synthese und Kristallstruktur von $Na_{10}[P_4(NH)_6N_4](NH_2)_6(NH_3)_{0,5}$ mit dem adamantanartig aufgebauten Anion $[P_4(NH)_6N_4]^{4-}$", *Z. Anorg. Allg. Chem.* **1994**, *620*, 1213–1218.

[31] W. Schnick, U. Berger, "$Li_{10}P_4N_{10}$ – A Lithium Phosphorus(V) Nitride Containing the New Complex Anion $P_4N_{10}^{10-}$", *Angew. Chem. Int. Ed.* **1991**, *30*, 830–831; *Angew. Chem.* **1991**, *103*, 857–858.

[32] E.-M. Bertschler, C. Dietrich, T. Leichtweiß, J. Janek, W. Schnick, "Li^+ Ion Conductors with Adamantane-Type Nitridophosphate Anions β-$Li_{10}P_4N_{10}$ and $Li_{13}P_4N_{10}X_3$ with X=Cl, Br", *Chem. Eur. J.* **2018**, *24*, 196–205.

[33] E.-M. Bertschler, T. Bräuniger, C. Dietrich, J. Janek, W. Schnick, "$Li_{47}B_3P_{14}N_{42}$ – A Lithium Nitridoborophosphate with $[P_3N_9]^{12-}$, $[P_4N_{10}]^{10-}$, and the Unprecedented $[B_3P_3N_{13}]^{15-}$ Ion", *Angew. Chem. Int. Ed.* **2017**, *56*, 4806–4809; *Angew. Chem.* **2017**, *129*, 4884–4887.

[34] L. Link, R. Niewa, "Polynator: a tool to identify and quantitatively evaluate polyhedra and other shapes in crystal structures", *J. Appl. Crystallogr.* **2023**, *56*, 1855–1864.

[35] F. Karau, W. Schnick, "Hochdrucksynthese von $BaSr_2P_6N_{12}$ und $BaCa_2P_6N_{12}$ und Strukturvergleich der Reihe BaP_2N_4, $BaCa_2P_6N_{12}$ und $BaSr_2P_6N_{12}$", *Z. Anorg. Allg. Chem.* **2006**, *632*, 231–237.

[36] S. J. Sedlmaier, D. Weber, W. Schnick, "Crystal structure of barium oxonitridophosphate, $Ba_3P_6O_6N_8$", *Z. Kristallogr. – New Cryst. Struct.* **2012**, *227*, 1–2.

[37] R. M. Pritzl, M. M. Pointner, K. Witthaut, P. Strobel, P. J. Schmidt, W. Schnick, "Tunable Narrow-Band Cyan-Emission of Eu^{2+}-doped Nitridomagnesophosphates $Ba_{3-x}Sr_x[Mg_2P_{10}N_{20}]:Eu^{2+}$ (x = 0–3)", *Angew. Chem.* **2024**, *136*, e202403648; *Angew. Chem. Int. Ed.* **2024**, *63*, e202403648.

[38] Deposition Numbers 2372017 for the refinement without H atoms and 2372022 for the refinement with H atoms contain the supplementary crystallographic data for this paper. These data are provided free of charge by the joint Cambridge Crystallographic Data Centre and Fachinformationszentrum Karlsruhe Access Structures service.

[39] L. Bonometti, F. Kraus, T. Graubner, A. J. Karttunen, B. Civalleri, L. Donà, L. Maschio, "A Fresh Look at a Well-Known Solid: Structure, Vibrational Spectra, and Formation Energy of $NaNH_2$", *J. Phys. Chem. C* **2023**, *127*, 12287−12294.

[40] W. Kolodziejski, J. Klinowski, "Kinetics of Cross-Polarization in Solid-State NMR: A Guide for Chemists", *Chem. Rev. (Washington, DC, U. S.)* **2002**, *102*, 613−628.

[41] L. Pauling, "The principles determining the structure of complex ionic crystals", *J. Am. Chem. Soc.* **1929**, *51*, 1010−1026.

[42] R. López, R. Gómez, "Band-gap energy estimation from diffuse reflectance measurements on sol–gel and commercial TiO_2: a comparative study", *J. Sol-Gel Sci. Technol.* **2012**, *61*, 1−7.

[43] J. Tauc, R. Grigorovici, A. Vancu, "Optical Properties and Electronic Structure of Amorphous Germanium", *Phys. Status Solidi B* **1966**, *15*, 627−637.

[44] M. Chen, Z. Xia, M. S. Molokeev, Q. Liu, "Structural Phase Transformation and Luminescent Properties of $Ca_{2-x}Sr_xSiO_4:Ce^{3+}$ Orthosilicate Phosphors", *Inorg. Chem.* **2015**, *54*, 11369–11376.

[45] L. He, Z. Song, X. Jia, Z. Xia, Q. Liu, "Control of Luminescence in Eu^{2+}-Doped Orthosilicate-Orthophosphate Phosphors by Chainlike Polyhedra and Electronic Structures", *Inorg. Chem.* **2018**, *57*, 609–616.

[46] J. A. Kechele, O. Oeckler, F. Stadler, W. Schnick, "Structure elucidation of $BaSi_2O_2N_2$ – A host lattice for rare-earth doped luminescent materials in phosphor-converted (pc)-LEDs", *Solid State Sci.* **2009**, *11*, 537−543.

[47] P. Strobel, T. de Boer, V. Weiler, P. J. Schmidt, A. Moewes, W. Schnick, "Luminescence of an Oxonitridoberyllate: A Study of Narrow-Band Cyan-Emitting $Sr[Be_6ON_4]:Eu^{2+}$", *Chem. Mater.* **2018**, *30*, 3122−3130.

[48] R. M. Pritzl, N. Prinz, P. Strobel, P. J. Schmidt, D. Johrendt, W. Schnick, "From Framework to Layers Driven by Pressure – The Monophyllo-Oxonitridophosphate β-$MgSrP_3N_5O_2$ and Comparison to its α-Polymorph", *Chem. Eur. J.* **2023**, *29*, e202301218.

[49] N. Z. Khan, S. A. Khan, W. Chen, M. A. Padhiar, M. T. Abbas, Z. Ullah, M. Runowski, X. Xu, R. K. Zheng, "The developments of cyan emitting phosphors to fulfill the cyan emission gap of white-LEDs", *Front. Chem.* **2023**, *11*, 1274410.

[50] A. Stock, H. Grüneberg, *Ber. Dtsch. Chem. Ges.* **1907**, *40*, 2573−2578.

[51] H. Jacobs, U. Fink, "Untersuchung des Systems Kalium/Europium/Ammoniak", *Z. Anorg. Allg. Chem.* **1978**, *438*, 151−159.

[52] Bruker-AXS, *APEX3*, Vers.2016.5-0, Karlsruhe, Germany, **2016**.

[53] G. M. Sheldrick, *SADABS*: Multi-Scan Absorption Correction, 2016-2, Bruker-AXS, Madison, WI, USA, **2012**.

[54] Bruker-AXS, *XPREP*: Reciprocal Space Exploration, Vers.6.12, Karlsruhe, Germany, **2001**.

[55] G. M. Sheldrick, *SHELXT 2018/2*: A programm for crystal structure solution, University of Göttingen, Germany, **2018**.

[56] G. M. Sheldrick, "SHELXT - Integrated space-group and crystal-structure determination", *Acta Crystallogr., Sect. A: Found. Adv.* **2015**, *71*, 3–8.

[57] G. M. Sheldrick, *SHELXL-2018/3*: A programm for crystal structure refinement, University of Göttingen, Germany, **2018**.

[58] G. M. Sheldrick, "Crystal structure refinement with SHELXL", *Acta Crystallogr., Sect. C: Cryst. Struct. Commun.* **2015**, *71*, 3–8.

[59] A. Coelho, *TOPAS Academic*, Version 6, Coelho Software, Brisbane, Australia, **2016**.

[60] Bruker Optik GmbH, *OPUS V8.7*, Ettlingen, Germany, **2012**.

[61] G. Kresse, J. Hafner, "Ab initio molecular dynamics for liquid metals", *Phys. Rev. B: Condens. Matter Mater. Phys.* **1993**, *47*, 558–561.

[62] G. Kresse, J. Hafner, "Ab initio molecular-dynamics simulation of the liquid-metal--amorphous-semiconductor transition in germanium", *Phys. Rev. B: Condens. Matter Mater. Phys.* **1994**, *49*, 14251–14269.

[63] G. Kresse, J. Furthmüller, "Efficiency of ab-initio total energy calculations for metals and semiconductors using a plane-wave basis set", *Comput. Mater. Sci.* **1996**, *6*, 15–50.

[64] G. Kresse, J. Furthmüller, "Efficient iterative schemes for ab initio total-energy calculations using a plane-wave basis set", *Phys. Rev. B: Condens. Matter Mater. Phys.* **1996**, *54*, 11169–11186.

[65] G. Kresse, D. Joubert, "From ultrasoft pseudopotentials to the projector augmented-wave method", *Phys. Rev. B: Condens. Matter Mater. Phys.* **1999**, *59*, 1758–1775.

[66] P. E. Blöchl, "Projector augmented-wave method", *Phys. Rev. B: Condens. Matter Mater. Phys.* **1994**, *50*, 17953–17979.

[67] J. P. Perdew, K. Burke, M. Ernzerhof, "Generalized Gradient Approximation Made Simple", *Phys. Rev. Lett.* **1996**, *77*, 3865–3868.

[68] W. H. Press, B. P. Flannery, S. A. Teukolsky, T. Vetterling, "Numerical Recipes: The Art of Scientific Computing", 1st ed., Cambridge University Press, New York, **1986**.

[69] R. K. Harris, E. D. Becker, S. M. C. d. Menezes, P. Granger, R. E. Hoffman, K. W. Zilm, "Further conventions for NMR shielding and chemical shifts (IUPAC Recommendations 2008)", *Pure Appl. Chem.* **2008**, *80*, 59–84.

[70] S. Leyre, E. Coutino-Gonzalez, J. J. Joos, J. Ryckaert, Y. Meuret, D. Poelman, P. F. Smet, G. Durinck, J. Hofkens, G. Deconinck, P. Hanselaer, "Absolute determination of photoluminescence quantum efficiency using an integrating sphere setup", *Rev. Sci. Instrum.* **2014**, *85*, 123115.

4 Ammonothermal Synthesis and Solid-State NMR Study of the Imidonitridosilicate $Rb_3Si_6N_5(NH)_6$

Published in: *Chem. Eur. J.* **2024**, *30*, e202401238

Authors: Florian M. Engelsberger, Thanh G. Chau, Thomas Bräuniger, and Wolfgang Schnick

DOI: 10.1002/chem.202401238

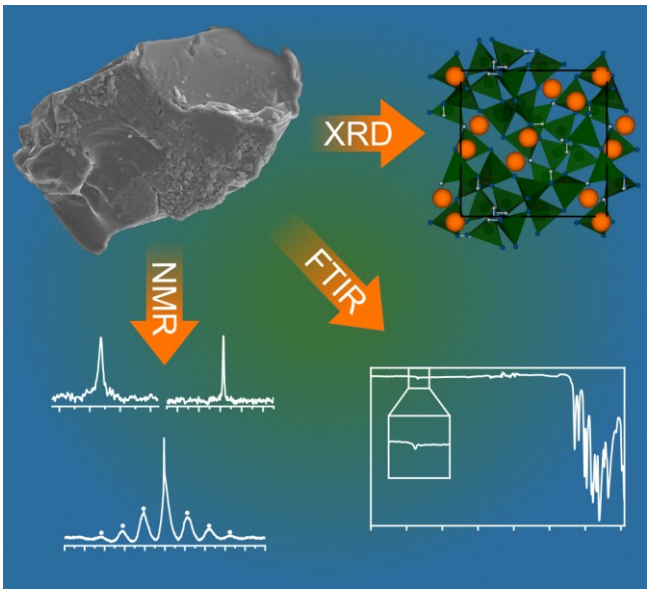

Abstract: The imidonitridosilicate $Rb_3Si_6N_5(NH)_6$, being only the second representative of this compound class, was synthesized ammonothermally at 870 K and 230 MPa. Its crystal structure was solved from single-crystal X-ray diffraction data. The imidonitridosilicate crystallizes isotypically with the respective potassium compound in space group $P4_132$ with the lattice parameter a = 10.9422(4) Å forming a three-dimensional imidonitridosilicate tetrahedra network with voids for the rubidium ions. The structure model and the presence of the imide groups were verified by Fourier-Transform infrared (FTIR) and magic-angle spinning (MAS) NMR spectroscopy, using cross polarization $^{15}N\{^1H\}$ and $^{29}Si\{^1H\}$ MAS NMR experiments. $Rb_3Si_6N_5(NH)_6$ represents a possible intermediate during the ammonothermal synthesis of nitridosilicates. The characterization of such intermediates improves the understanding of the reaction pathway from ammonothermal solutions to nitrides. Thus, the ammonothermal synthesis is an alternative approach to the well-established high-temperature synthesis leading to the compound class of nitridosilicates.

4.1 Introduction

The ammonothermal synthesis is a solvothermal method which employs supercritical ammonia as solvent and is used for the synthesis of nitrides, imides and amides at relatively low reaction temperatures.[1] The employment of mineralizers allows the dissolution of the starting materials via the formation of soluble and reactive intermediate species which often form well-crystallized products.[2]

For the high-temperature synthesis of nitridosilicates, the utilization of an activated silicon-containing starting material, silicon diimide $Si(NH)_2$ (SDI), is a well-established approach.[3] This starting material allows access to the structurally versatile compound class of nitridosilicates which showed relevance as efficient phosphor materials for phosphor-converted light-emitting diodes (pcLEDs), such as $M_2Si_5N_8$ (M = Ca, Sr, Ba).[4]

The ammonothermal synthesis proved to be suitable for obtaining the nitridosilicates MSi_2N_3 (M = Li, Na), $MSiN_2$ (M = Zn, Mg, Mn) and their solid solutions, $CaGaSiN_3$ as well as the oxonitridosilicate $Ca_{1+x}Y_{1-x}SiN_{1-x}O_x$ ($x > 0$).[5-10] For $NaSi_2N_3$, $CaGaSiN_3$ and $Ca_{1+x}Y_{1-x}SiN_{1-x}O_x$, the synthesis was only possible using the ammonothermal route. In these syntheses, the elemental silicon was activated *in situ* by the use of alkali-metal-containing mineralizers. Next to these nitrides, only possible intermediates during the dissolution of elemental silicon in supercritical ammonia, could be observed and isolated: Starting from SiO_2, the amido silicates $M_2SiO_2(NH_2)_2$ with M = K, Rb, Cs were synthesized, while Si_3N_4 as starting material yielded crystalline silicon nitride imide Si_2N_2NH for the first time.[11-12]

Additionally, the first imidonitridosilicate $K_3Si_6N_5(NH)_6$ was synthesized at ammonothermal conditions starting from the elements silicon and potassium.[13] Here, a tendency among the alkali metals can be observed: The lighter alkali metal ions form the wurtzite-derived nitrides $LiSi_2N_3$ and $NaSi_2N_3$ while the larger ionic radius of potassium leads to the formation of an imidonitridosilicate with a complex anionic tetrahedra network.[5,14] $K_3Si_6N_5(NH)_6$ crystallizes in a homeotypic structure to the alkali metal nitridophosphates $M_3P_6N_{11}$ (M = Na, K, Rb, Cs).[15-17] The existence of these nitridophosphates shows that the structure type tolerates alkali metal ions with larger ionic radii than potassium and represents one of only few examples of the heavier alkali metals in nitride environment.

In this contribution, we present the first rubidium imidonitridosilicate $Rb_3Si_6N_5(NH)_6$, which is homologous to the potassium compound. Furthermore, it is only the second representative of this compound class. The compound is characterized using X-ray diffraction, Fourier-Transform infrared (FTIR) and magic-angle spinning (MAS) NMR spectroscopy.

4.2 Results and Discussion

4.2.1 Synthesis

The rubidium imidonitridosilicate $Rb_3Si_6N_5(NH)_6$ was synthesized at ammonothermal conditions in custom-built high-pressure autoclaves made from a nickel-based superalloy using niobium liners. Starting from $RbNH_2$ and elemental silicon, the title compound was obtained at a temperature of 870 K and a pressure of 230 MPa. $RbNH_2$ was employed in excess and acted additionally as a mineralizer to ensure the complete dissolution of silicon in supercritical ammonia. $Rb_3Si_6N_5(NH)_6$ crystallizes as colorless plates at the bottom of the closed niobium liner (Figure 4.1). The size and shape of the crystallites suggest a solution-based growth mechanism. The moisture-sensitive product was handled and stored under inert gas conditions. In comparison to the potassium compound, $Rb_3Si_6N_5(NH)_6$ was obtained at higher temperatures since an increase of the temperature showed to be beneficial for the dissolution of silicon in previous ammonothermal reactions.[18]

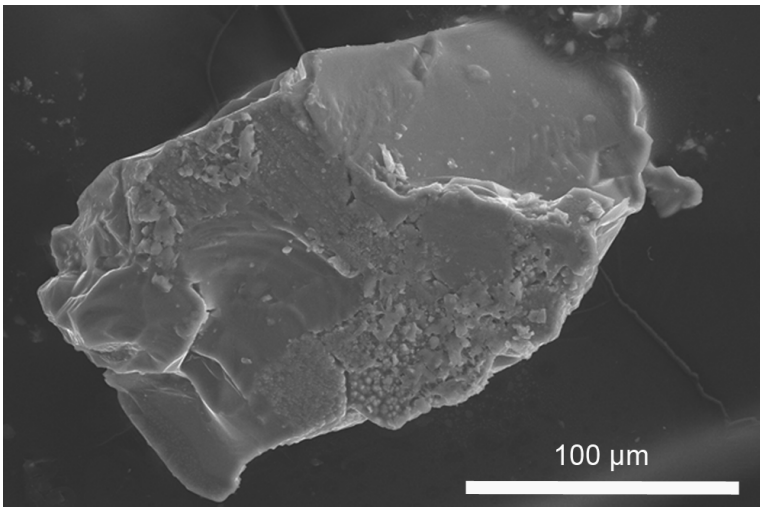

Figure 4.1: SEM image of a $Rb_3Si_6N_5(NH)_6$ crystallite.

4.2.2 Crystal Structure

The crystal structure of $Rb_3Si_6N_5(NH)_6$ was refined in space group $P4_132$ (no. 213) with lattice parameter a = 10.9422(4) Å.[19] Crystallographic information on the structure solution and refinement are given in Table 4.1. Atomic coordinates, respective Wyckoff positions and displacement parameters are summarized in Table 9.19–Table 9.21 in the Supporting Information. $Rb_3Si_6N_5(NH)_6$ is isotypic to the potassium compound $K_3Si_6N_5(NH)_6$ for which the crystal structure determination revealed the corresponding enantiomeric space group $P4_332$ (no. 212).[13] The structure consists of a network of SiN_4 tetrahedra which are interconnected via vertices. The Rb^+ ions are located in voids of this anionic network (Figure 4.2a). Rb1 is coordinated by two N3 and six N2 atoms in a way that can be described as a distorted bicapped trigonal antiprism (Figure 4.2b). In this nitride ion coordination, the two bonds towards N3 are remarkably shorter (3.078(4) Å)

than the other six bonds towards N2 (3.4145(6) Å). Rb2 exhibits a distorted trigonal prismatic coordination by three nitridic N2 atoms and three imide groups (N1−H). Here, the Rb–N distances are both very similar to the shorter Rb1–N3 distance (see Table 9.21).

Table 4.1: Crystallographic data for $Rb_3Si_6N_5(NH)_6$ obtained from single-crystal X-ray diffraction, standard deviations are given in parentheses.

Formula	**$Rb_3Si_6N_5(NH)_6$**
Crystal system	cubic
Space group	$P4_132$ (no. 213)
Lattice parameters / Å	a = 10.9422(4)
Cell volume / Å^3	1310.1(2)
Formula units Z / cell	4
Density / g·cm^{-3}	2.966
μ / mm^{-1}	11.718
T / K	293(2)
Crystal size / mm^3	0.03 × 0.04 × 0.09
Crystal shape	plates
Diffractometer	Bruker D8 Quest
Radiation (λ / Å)	Mo- K_α (0.71073)
F(000)	1112
θ range / °	2.632−38.412
Total no. of reflections	90133
No. of independent reflections	1232
Observed reflections [$F^2 > 2\sigma(F^2)$]	1180
R_{int}, R_σ	0.0696, 0.0131
Refined parameters / restraints	36 / 1
Flack parameter	–0.006(3)
Goodness of fit (χ^2)	1.168
$R1$ (all data); $R1$ [$F^2 > 2\sigma(F^2)$]	0.0345 / 0.0321
$wR2$ (all data); $wR2$ indices [$F^2 > 2\sigma(F^2)$]	0.0702 / 0.0689
$\Delta\rho_{max}$ / $\Delta\rho_{min}$ [e Å^{-3}]	1.29 / –1.08

In the anionic network, each tetrahedron consists of a Si1 atom in the center. The vertices are formed by two N1 atoms of the imide group and one of each of the nitridic nitrogen atoms N2 and

N3. The nitridic N2 and the imide nitrogen N1 both connect two of the tetrahedra while the nitridic N3 connects three tetrahedra (Figure 4.2c, left). The network is built up from condensed boat-formed *dreier* rings which are further condensed to infinite drilled straps (Figure 4.2c, right). The straps are arranged and interconnected in a way that two of the boat-formed rings face each other. The Rb1 position is located on the connection line between two N3 atoms in the center of these boat-formed units (dashed line, Figure 4.2b). In voids between the drilled straps, pairs of Rb2 atoms are situated. The coordination polyhedra of these neighboring Rb2 atoms share the trigonal plane, formed by three N2 atoms (Figure 4.2b). This coordination leads to very short Rb2–Rb2 distances of approximately 3.28 Å which is only slightly longer than twice the ionic radius of rubidium (r_{Rb} = 1.52 Å).[20] It seems that the network structure enforces this small distance, as for the isotypic potassium compound $K_3Si_6N_5(NH)_6$, very short K2–K2 distances (≈ 3.12 Å) were reported as well.[13] In the homeotypic nitridophosphate $Rb_3P_6N_{11}$, however, the Rb–Rb distances (≈ 4.08 Å) are larger due to the lack of the positively charged protons bound to the N1 atoms of the tetrahedra network (Figure 4.2b).[17]

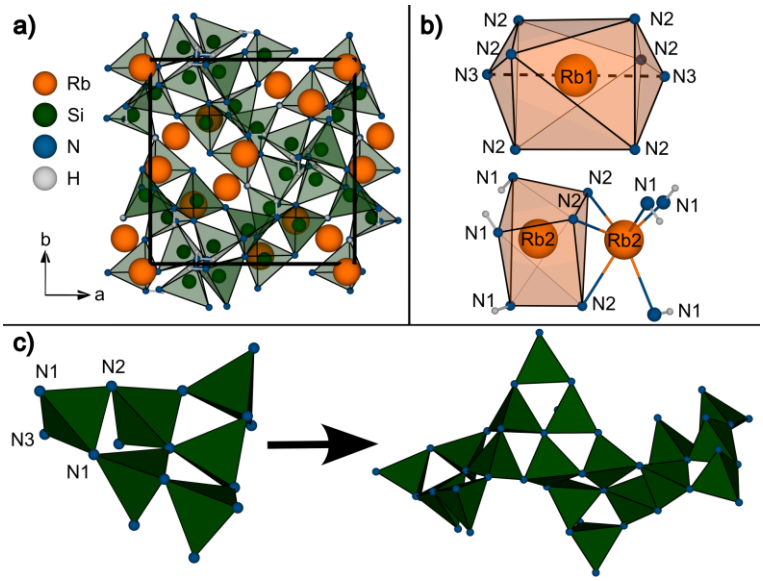

Figure 4.2: Representation of the crystal structure of $Rb_3Si_6N_5(NH)_6$ with Rb in orange, Si in green, N in blue and H in gray (a). The environment of the Rb positions is shown in detail (b). The condensation of the tetrahedra from triplets (c, left), which further condense to drilled straps (c, right), hydrogen atoms were omitted here for clarity.

The hydrogen atoms bound to N1 were refined from the residual electron density map using a DFIX constraint. The refined positions for H1 point away from the Rb atoms towards voids left by the tetrahedra network. For the Si–N bonds, it is observed that the bond to N2 (1.689(2) Å) is shorter than for the other nitrogen atoms (Table 9.21). This is in agreement with reported bond lengths for two-fold connected nitrogen atoms for N2 and for three-fold connected nitrogen atoms for N3 and N1, where the latter is bound to two Si and one H atom.[4] In general, the bond lengths and bonding angles in the tetrahedra network deviate only slightly from the values in $K_3Si_6N_5(NH)_6$ (Table 9.21).[13] Only the lattice parameter and the Rb–N bond lengths are significantly larger than

the values for K–N in the potassium compound due to the larger ionic radius of rubidium compared to potassium.[20] This supports the assumption that the network formation is the main structure-directing force for the formed structure.

CHARDI calculations corroborate the described structure model (see Table 9.24).[21]

The Rietveld refinement results of the powder X-ray diffraction (PXRD) data are given in Figure 4.3, Table 9.22 and Table 9.23. The refinement of the diffractogram shows only little deviation in the difference plot. This confirms the structure model from the single-crystal data and shows no crystalline side phases in the sample.

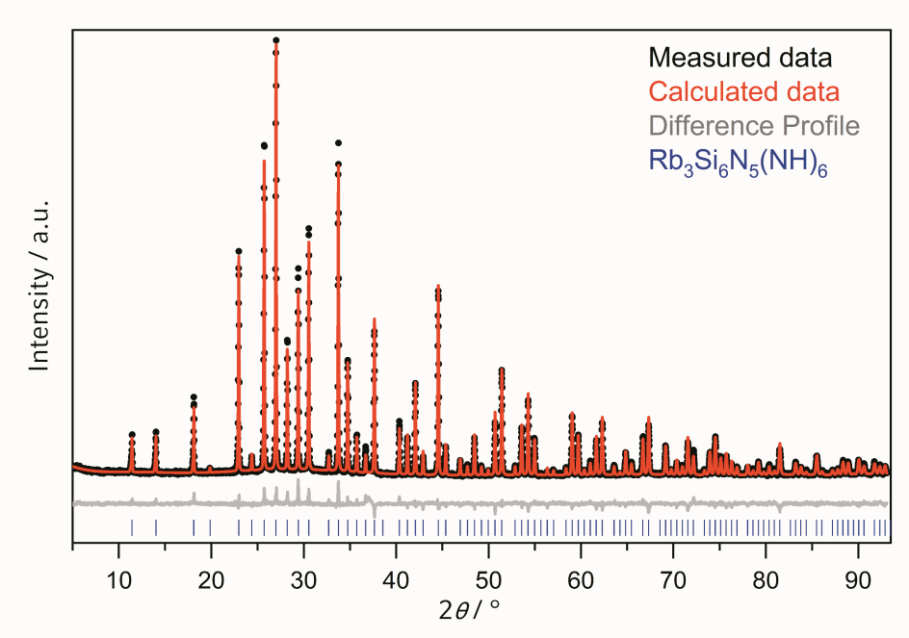

Figure 4.3: Rietveld refinement based on the PXRD data using the structure model obtained from single-crystal XRD data with experimental data (black dots), calculated diffraction pattern (red line), difference profile (gray line) and reflection positions of $Rb_3Si_6N_5(NH)_6$ (blue bars).

4.2.3 Fourier-Transform Infrared Spectroscopy

To detect the presence of the imide group in the compound, a FTIR spectrum of the powder sample was collected (Figure 4.4). The spectrum shows several signals in the range of 400–1500 cm^{-1}, resulting from various lattice vibrations. The weak absorption bands in the area of 1900–2500 cm^{-1} are caused by the ATR unit of the spectrometer. Next to the strong signals from the network, a weak absorption signal indicates the presence of N–H stretching vibrations resulting from the imide group. The position of the maximum at 3346 cm^{-1} is in the range reported for imide groups in rubidium-containing compounds.[22]

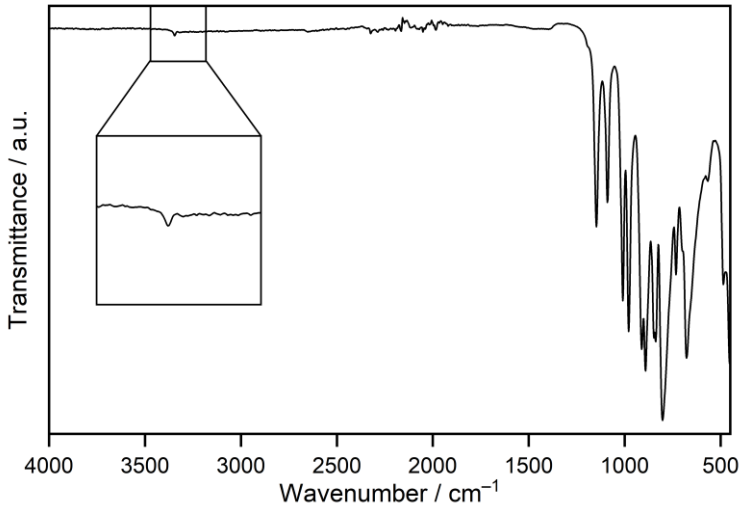

Figure 4.4: FTIR spectrum of $Rb_3Si_6N_5(NH)_6$ with magnification of the area around 3400 cm^{-1} showing the N–H stretching vibration.

4.3 Solid-State MAS NMR Spectroscopy

To further verify the presence of hydrogen in the title compound and the proposed structure model, ^{1}H and cross polarization (CP) $^{15}N\{^{1}H\}$ and $^{29}Si\{^{1}H\}$ solid-state MAS NMR spectra of the $Rb_3Si_6N_5(NH)_6$ sample were recorded. The CP method allows transfer of the polarization from a more abundant nucleus, such as ^{1}H, to less abundant nuclides in close proximity in the structure, in our case ^{15}N and ^{29}Si.[23] Additionally, faster collection of the spectra can be achieved by CP due to the shorter spin-lattice relaxation times of the protons. Therefore, CP allows shorter measurement times without the necessity for the isotopic enrichment of the less abundant nuclides during synthesis.[24]

In the $^{15}N\{^{1}H\}$ NMR spectrum, a single signal with a maximum at –307.3 ppm is observed (Figure 4.5a) which confirms the presence of protons in close proximity to a nitrogen atom and fits to the observation of one crystallographic position (N1) for the imide group. The position of the resonance signal is close to the value range reported for α- and β-Si_3N_4 (–282.2 to –306.7 ppm) which also contain SiN_4 tetrahedra as main building blocks.[25-26] For the two nitridic nitrogen atoms (N2 and N3), no signal in the cross-polarized spectrum is expected due to their larger distance to hydrogen atoms.

The special combination of the crystal structure of $Rb_3Si_6N_5(NH)_6$ containing a single crystallographic position for the nitrogen of the imide group with the possibility of an indirect polarization of this nitrogen resonance via CP allows for this compound to connect the crosslinking pattern of the nitrogen atom with silicon with a chemical shift in the NMR spectroscopy. Based on our results, it is consistent to say that this chemical shift of –307.3 ppm originates from the nitrogen N1 of the imide group, which is bridging two silicon atoms. To the best of our knowledge, this is

the first reported value for a ^{15}N chemical shift in nitridosilicate environment, which may be helpful for the assignment of ^{15}N NMR signals in the future.

The cross-polarized $^{29}Si\{^1H\}$ MAS spectrum shows a single signal at –43.0 ppm (Figure 4.5b) which further verifies the presence of hydrogen in the silicon-containing product. Furthermore, a single signal is in accordance with the single crystallographic position for silicon in the presented structure model. Here, the comparison with values reported for α- and β-Si_3N_4 (–46.8 to –48.7 ppm) shows only little deviation.[25,27] For amorphous samples of SDI, values from –40 to –42 ppm are reported which show an upfield shift upon dehydrogenation at elevated temperatures reaching finally the value range reported for Si_3N_4.[28] This fits our observation of a downfield-shifted signal compared to Si_3N_4 which is caused by the presence of the imide group in $Rb_3Si_6N_5(NH)_6$. Furthermore, the determined maximum value for the rubidium compound is close to the chemical shift of –44.7 reported for the structurally closely related nitride imide Si_2N_2NH.[29]

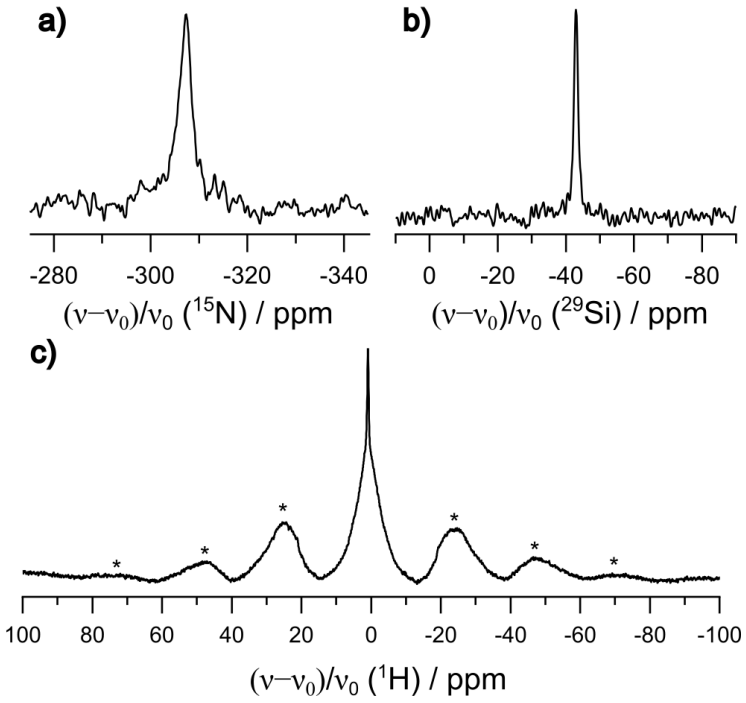

Figure 4.5: Solid-state MAS NMR spectra of the $^{15}N\{^1H\}$ (a), $^{29}Si\{^1H\}$ (b) and ^1H measurements (c), at 10 kHz MAS rate. Rotation side bands are marked with an asterisk.

In the ^1H MAS NMR spectrum, a single signal with a maximum at 0.9 ppm is observed (Figure 4.5c). The broadening of the signal is most likely caused by heteronuclear dipolar coupling of the hydrogen atoms with the nearby nitrogen atoms of the imide group, which is not fully suppressed by a MAS rate of 10 kHz. The observation of a single resonance is consistent with the single crystallographic position for hydrogen from the structure model. In comparison to the ^1H NMR signal of SDI, which is reported at 4 ppm, an upfield shift of the signal is observed.[30] This shift could be caused by the higher electron density of the rubidium atoms in close proximity to the hydrogen atoms in $Rb_3Si_6N_5(NH)_6$.

4.4 Conclusions

We report the successful ammonothermal synthesis of the first rubidium imidonitridosilicate $Rb_3Si_6N_5(NH)_6$. The structural characterization of the compound reveals a three-dimensional network with rubidium atoms in its voids, isotypic to the potassium compound. The presence of hydrogen in the imide groups is verified by FTIR and solid-state MAS NMR methods. The NMR data from CP experiments fit well to reported data from the literature for Si_3N_4, Si_2N_2NH and SDI showing a shift for most signals due to the presence of the electron-rich rubidium in the structure. Additionally, a first value for a ^{15}N resonance of a nitrogen atom bridging two silicon atoms in nitridosilicate environment could be observed which can be helpful as a reference mark in the future. Our work also proves that the ammonothermal method is a suitable tool to stabilize the heavy alkali metal rubidium in nitridic environment for which only few examples exist.[17,31-37] The characterization of such intermediate products of the ammonothermal synthesis is crucial for the optimization and an increased control over the reaction outcome. This knowledge might be useful to extend the variety of nitridosilicates accessible by the ammonothermal synthesis. Furthermore, the ammonothermal route offers an alternative synthesis route to the well-established SDI approach and might lead to new nitridosilicates containing heavy alkali metal ions for the first time.

4.5 Experimental Section

Some starting materials and the product of the reaction are instable towards air and moisture, therefore all manipulations were performed under inert gas conditions using either argon-filled gloveboxes (MBraun, O_2 < 1 ppm, H_2O < 1 ppm) or flame-dried Schlenk-type glassware and a vacuum line ($\rho \leq 0.1$ Pa) with argon and ammonia supply. Both employed gases Ar and NH_3 (Air liquide, 99.999%) passed for purification through gas cartridges Micro Torr FT400-902 for Ar and Micro Torr MC400-702FV for NH_3, respectively (both SAES Pure Gas Inc.), reaching a final purity level of < 1ppbV H_2O, O_2 and CO_2. The ammonia amount condensed in the autoclave was determined using a mass flow meter D-6320-DR (Bronkhorst).

4.5.1 Synthesis of $Rb(NH_2)$

$Rb(NH_2)$ was synthesized from supercritical ammonia starting from Rb (Thermo Scientific, ≥ 99,75%) at 370 K. Powder X-ray diffraction data of the resulting sample and a comparison to the reflection positions and intensity from the literature is given in Figure 9.3 in the Supporting Information.[38]

4.5.2 Ammonothermal Synthesis

$Rb_3Si_6N_5(NH)_6$ was synthesized at ammonothermal conditions using a custom-built Inconel® 718 autoclave (max. 900 K, 300 MPa, volume: 100 mL). The autoclave was equipped with a hand

valve (SITEC) connected to a pressure transmitter (HBM P2VA1/5000 bar) and a bursting disk holder (SITEC) with a bursting disk (Dieckers GmbH & Co. KG, pressure limit: 330 MPa). The starting materials $RbNH_2$ (492.4 mg, 4.852 mmol) and Si (Alfa Aesar, 99.99%, 140.4 mg, 5.000 mmol) were placed in a niobium liner and the liner was closed with a perforated lid to allow intrusion of ammonia into the liner. The liner was transferred into the autoclave which was sealed with a silver-coated Inconel® 718 ring (GFD seals) and cooled with an ethanol/ liquid nitrogen bath to condense ammonia (ca. 54 mL) in the autoclave. The reaction mixture was heated in a tube furnace to 670 K in 4 h, held at that temperature for 10 h and subsequently heated to 870 K in 4 h. This temperature was held for 180 h reaching a maximum pressure of 230 MPa, before the furnace was switched off. After cooling to room temperature, residual ammonia was removed from the autoclave and the white, crystalline product was isolated from the liner in a glovebox.

4.5.3 Single-Crystal X-ray Diffraction

A transparent crystal (0.03 × 0.04 × 0.09 mm^3) was isolated from the sample under inert-gas conditions under a microscope and placed in a capillary. Diffraction data were collected using a Bruker D8 Quest diffractometer with Mo-K_α radiation (λ = 0.71073 Å) using a combined Φ-ω-scan. Indexing and integration of the data was performed using the program APEX3. Semi-empirical absorption correction (SADABS) and space group determination were performed using APEX3 as well.[39-40] The crystal structure was solved using XPREP and SHELXT and refined by full-matrix least-squares methods (SHELXL) employing the program WINGX.[41-45]

4.5.4 Powder X-ray Diffraction

The sample for the collection of the powder X-ray diffraction data was ground in an agate mortar and filled into a glass capillary (d = 0.3 mm, wall thickness 0.01 mm, Hilgenberg GmbH) at argon atmosphere. Subsequently, the capillary was sealed and the measurements were conducted on a STOE STADI P diffractometer using Cu-$K_{\alpha1}$ radiation (λ = 0.71073 Å), a Ge(111) monochromator and a Mythen 1K detector in modified Debye-Scherrer geometry. A Rietveld-refinement of the diffraction data was performed with the TOPAS software package.[46]

4.5.5 Fourier-Transform Infrared (FTIR) Spectroscopy

FTIR spectroscopy data were collected using an Alpha II FTIR spectrometer (Bruker) using a diamond attenuated total reflectance (ATR) unit in an argon-filled glovebox. The spectrum was collected at ambient temperature in the range of 400–4000 cm^{-1} with a resolution of 2 cm^{-1} using the program OPUS 8.7.[47]

4.5.6 Solid-Sate Magic-Angle Spinning (MAS) NMR Spectroscopy

^1H, $^{15}N\{^1H\}$ and $^{29}Si\{^1H\}$ spectra were collected using an Avance III 500 spectrometer (Bruker) operating at a ^1H frequency of 500.25 MHz (magnetic field strength 11.7 T). A ZrO_2 rotor with an outer diameter of 4 mm was filled with the ground sample of $Rb_3Si_6N_5(NH)_6$ in a glovebox, inserted into a MAS probe (Bruker) and rotated with a frequency of 10 kHz. The analysis of the obtained

data was performed with device-specific software. The ^{1}H resonance of 1% $Si(CH_3)_4$ (TMS) in $CDCl_3$ was used as an external secondary reference, using the Ξ values for ^{15}N relative to CH_3NO_2 and for ^{29}Si relative to 1% TMS in $CDCl_3$ as reported by the IUPAC.[48]

4.5.7 Scanning Electron Microscopy

Micrographs of the sample were collected on a scanning electron microscope Dualbeam Helios Nanolab G3 UC (FEI). Prior to the measurements, crystallites of the sample were mounted on adhesive carbon pads and coated with a conductive carbon film using a high-vacuum sputter coater BAL-TEC MED 020 (Bal Tec A) at ambient conditions.

4.6 Acknowledgements

The authors gratefully thank Christian Minke for the MAS NMR measurements and SEM images and Lukas Nusser (both at Department of Chemistry, LMU Munich) for the collection of single-crystal data. Open Access funding enabled and organized by Projekt DEAL.

4.7 References

[1] E. Meissner, R. Niewa, (Eds.), "Ammonothermal Synthesis and Crystal Growth of Nitrides – Chemistry and Technology", Springer, Cham, **2021**.

[2] T. M. M. Richter, R. Niewa, "Chemistry of Ammonothermal Synthesis", *Inorganics* **2014**, *2*, 29–78.

[3] W. Schnick, H. Huppertz, "Nitridosilicates – A Significant Extension of Silicate Chemistry", *Chem. Eur. J.* **1997**, *3*, 679–683.

[4] M. Zeuner, S. Pagano, W. Schnick, "Nitridosilicates and Oxonitridosilicates: From Ceramic Materials to Structural and Functional Diversity", *Angew. Chem.* **2011**, *123*, 7898–7920; *Angew. Chem. Int. Ed.* **2011**, *50*, 7754–7775.

[5] H. Jacobs, H. Mengis, "Preparation and Crystal Structure of a Sodium Silicon Nitride, $NaSi_2N_3$", *Eur. J. Solid State Inorg. Chem.* **1993**, *30*, 45–53.

[6] J. Häusler, R. Niklaus, J. Minár, W. Schnick, "Ammonothermal Synthesis and Optical Properties of Ternary Nitride Semiconductors Mg-*IV*-N_2, Mn-*IV*-N_2 and Li-IV_2-N_3 (*IV*=Si, Ge)", *Chem. Eur. J.* **2018**, *24*, 1686–1693.

[7] J. Häusler, S. Schimmel, P. Wellmann, W. Schnick, "Ammonothermal Synthesis of Earth-Abundant Nitride Semiconductors $ZnSiN_2$ and $ZnGeN_2$ and Dissolution Monitoring by In Situ X-ray Imaging", *Chem. Eur. J.* **2017**, *23*, 12275–12282.

[8] M. Mallmann, R. Niklaus, T. Rackl, M. Benz, T. G. Chau, D. Johrendt, J. Minár, W. Schnick, "Solid Solutions of Grimm-Sommerfeld Analogous Nitride Semiconductors *II*-*IV*-N_2 with *II* = Mg, Mn, Zn; *IV* = Si, Ge – Ammonothermal Synthesis and DFT Calculations", *Chem. Eur. J.* **2019**, *25*, 15887–15895.

[9] J. Häusler, L. Neudert, M. Mallmann, R. Niklaus, A.-C. L. Kimmel, N. S. A. Alt, E. Schlücker, O. Oeckler, W. Schnick, "Ammonothermal Synthesis of Novel Nitrides: Case Study on $CaGaSiN_3$", *Chem. Eur. J.* **2017**, *23*, 2583–2590.

[10] M. Mallmann, C. Maak, W. Schnick, "Ammonothermal Synthesis and Crystal Growth of the Chain-type Oxonitridosilicate $Ca_{1+x}Y_{1-x}SiN_{3-x}O_x$ ($x > 0$)", *Z. Anorg. Allg. Chem.* **2020**, *646*, 1539–1544.

[11] H. Jacobs, H. Mengis, "Synthese und Kristallstruktur von Alkalimetalldiamidodioxosilicaten $M_2SiO_2(NH_2)_2$ mit M ≙ K, Rb und Cs", *Z. Anorg. Allg. Chem.* **1993**, *619*, 303–310.

[12] D. Peters, H. Jacobs, "Ammonothermalsynthese von kristallinem Siliciumnitridimid, Si_2N_2NH", *J. Less-Common Met.* **1989**, *146*, 241–249.

[13] D. Peters, E. F. Paulus, H. Jacobs, "Darstellung und Kristallstruktur eines Kaliumimidonitridosilicats, $K_3Si_6N_5(NH)_6$", *Z. Anorg. Allg. Chem.* **1990**, *584*, 129–137.

[14] J. David, Y. Laurent, J. P. Charlot, J. Lang, "Etude cristallographique d'un nitrure I 42 53. La structure tetraedrique type wurtzite de $LiSi_2N_3$", *Bull. Soc. Fr. Mineral. Cristallogr.* **1973**, *96*, 21–24.

[15] A. Vitola, J. Ronis, T. Millers, "Crystal structure of sodium-phosphorus nitride $Na_3P_6N_{11}$", *Latv. PSR Zinat. Akad. Vestis, Kim. Ser.* **1990**, *90*, 35–36.

[16] H. Jacobs, R. Nymwegen, "Darstellung und Kristallstruktur eines Kaliumnitridophosphats, $K_3P_6N_{11}$", *Z. Anorg. Allg. Chem.* **1997**, *623*, 429–433.

[17] K. Landskron, W. Schnick, "$Rb_3P_6N_{11}$ and $Cs_3P_6N_{11}$ – New Highly Condensed Nitridophosphates by High-Pressure High-Temperature Synthesis", *J. Solid State Chem.* **2001**, *156*, 390–393.

[18] J. Häusler, W. Schnick, "Ammonothermal Synthesis of Nitrides: Recent Developments and Future Perspectives", *Chem. Eur. J.* **2018**, *24*, 11864−11879.

[19] Deposition Number 2341243 contains the supplementary crystallographic data for this paper. These data are provided free of charge by the joint Cambridge Crystallographic Data Centre and Fachinformationszentrum Karlsruhe Access Structures service.

[20] R. Shannon, "Revised effective ionic radii and systematic studies of interatomic distances in halides and chalcogenides", *Acta Crystallogr., Sect. A: Found. Adv.* **1976**, *32*, 751−767.

[21] M. Nespolo, "Charge distribution as a tool to investigate structural details. IV. A new route to heteroligand polyhedra", *Acta Crystallogr., Sect. B: Struct. Sci., Cryst. Eng. Mater.* **2016**, *72*, 51−66.

[22] A. Santoru, C. Pistidda, M. Brighi, M. R. Chierotti, M. Heere, F. Karimi, H. Cao, G. Capurso, A.-L. Chaudhary, G. Gizer, S. Garroni, M. H. Sørby, B. C. Hauback, R. Černý, T. Klassen, M. Dornheim, "Insights into the Rb–Mg–N–H System: an Ordered Mixed Amide/Imide Phase and a Disordered Amide/Hydride Solid Solution", *Inorg. Chem.* **2018**, *57*, 3197–3205.

[23] A. Pines, M. G. Gibby, J. S. Waugh, "Proton-enhanced NMR of dilute spins in solids", *J. Chem. Phys.* **1973**, *59*, 569–590.

[24] W. Kolodziejski, J. Klinowski, "Kinetics of Cross-Polarization in Solid-State NMR: A Guide for Chemists", *Chem. Rev. (Washington, DC, U. S.)* **2002**, *102*, 613−628.

[25] E. Leonova, J. Grins, M. Shariatgorji, L. L. Ilag, M. Edén, "Solid-state NMR investigations of Si-29 and N-15 enriched silicon nitride", *Solid State Nucl. Magn. Reson.* **2009**, *36*, 11−18.

[26] R. K. Harris, M. J. Leach, D. P. Thompson, "Synthesis and magic-angle spinning nuclear magnetic resonance of ^{15}N-enriched silicon nitrides", *Chem. Mater.* **1990**, *2*, 320-323.

[27] K. R. Carduner, C. S. Blackwell, W. B. Hammond, F. Reidinger, G. R. Hatfield, "^{29}Silicon NMR Characterization of α- and β-Silicon Nitride", *J. Am. Chem. Soc.* **1990**, *112*, 4676-4679.

[28] S. Kaskel, K. Schlichte, B. Zibrowius, "Pore size engineering of mesoporous silicon nitride materials", *Phys. Chem. Chem. Phys.* **2002**, *4*, 1675−1681.

[29] S. Kaskel, M. Khanna, B. Zibrowius, H.-W. Schmidt, D. Ullner, "Crystal growth in supercritical ammonia using high surface area silicon nitride feedstock", *J. Cryst. Growth* **2004**, *261*, 99−104.

[30] H. Fujimori, K. Ioku, S. Goto, T. Yamada, "Solid-State NMR Study of Crystallizing Process of Silicon Nitride Powder Synthesized by the Thermal Decomposition Method of Imide", *J. Ceram. Soc. Jpn.* **2001**, *109*, 132−136.

[31] F. Golinski, H. Jacobs, "Synthese und Kristallstruktur von $Rb_8[P_4N_6(NH)_4](NH_2)_2$ mit dem adamantanartigen Anion $[P_4N_6(NH)_4]^{6-}$", *Z. Anorg. Allg. Chem.* **1995**, *621*, 29−33.

[32] R. Niewa, H. Jacobs, "Synthesis and crystal structure of alkali metal oxo nitrido dimetallates(VI), $A_6[M_2N_4O_3]$ (A = K, Rb, Cs; M = Mo, W)", *J. Alloys Compd.* **1995**, *217*, 38–43.

[33] R. Niewa, H. Jacobs, "$NaRb_4((WN_{2.5}O_{0.5})_2)$ and $NaCs_4((WN_{2.5}O_{0.5})_2)$, the First Oxo Nitrido Tungstates(VI) with Infinite Chains", *Eur. J. Solid State Inorg. Chem.* **1996**, *33*, 463–470.

[34] R. Niewa, H. Jacobs, "$Na_5Rb[(WN_3)_2]$ and $Na_5Cs[(WN_3)_2]$, two new sodium nitrido tungstates(VI) with the heavier alkali metals rubidium and cesium", *J. Alloys Compd.* **1996**, *234*, 171–177.

[35] R. Niewa, H. Jacobs, "$Na_2K[WN_3]$ and $Na_{11}Rb[(WN_3)_4]$, two new alkali metal nitrido tungstates(VI) with closely related structures", *J. Alloys Compd.* **1996**, *233*, 61–68.

[36] R. Niewa, H. Jacobs, "Crystal structure of dirubidium oxodinitridotungstate(VI), $Rb_2[WN_2O]$", *Z. Kristallogr. - New Cryst. Struct.* **2000**, *215*, 17–18.

[37] H. Stegen, H. Jacobs, "Alkalimetallnitrido-tecto-metallate(VI) mit Netzwerken von Sechsringen spitzenverknüpfter Tetraeder $[(MNN_{3/2})_6]$ mit M=Mo, W der unerwarteten Zusammensetzung $A_{9+x}[M_6N_{15}]$ mit A=Rb, Cs und $0<x<1$", *Z. Anorg. Allg. Chem.* **2000**, *626*, 639–644.

[38] R. Juza, H. Jacobs, W. Klose, "Die Kristallstrukturen der Tieftemperaturmodifikationen von Kalium- und Rubidiumamid", *Z. Anorg. Allg. Chem.* **1965**, *338*, 171–178.

[39] Bruker-AXS, *APEX3*, Vers.2016.5-0, Karlsruhe, Germany, **2016**.

[40] G. M. Sheldrick, *SADABS*: Multi-Scan Absorption Correction, 2016-2, Bruker-AXS, Madison, WI, USA, **2012**.

[41] Bruker-AXS, *XPREP*: Reciprocal Space Exploration, Vers.6.12, Karlsruhe, Germany, **2001**.

[42] G. M. Sheldrick, *SHELXT 2018/2*: A programm for crystal structure solution, University of Göttingen, Germany, **2018**.

[43] G. M. Sheldrick, "SHELXT - Integrated space-group and crystal-structure determination", *Acta Crystallogr., Sect. A: Found. Adv.* **2015**, *71*, 3−8.

[44] G. M. Sheldrick, *SHELXL-2018/3*: A programm for crystal structure refinement, University of Göttingen, Germany, **2018**.

[45] G. M. Sheldrick, "Crystal structure refinement with SHELXL", *Acta Crystallogr., Sect. C: Cryst. Struct. Commun.* **2015**, *71*, 3–8.

[46] A. Coelho, *TOPAS Academic*, Version 6, Coelho Software, Brisbane, Australia, **2016**.

[47] Bruker Optik GmbH, *OPUS V8.7*, Ettlingen, Germany, **2012**.

[48] R. K. Harris, E. D. Becker, S. M. C. d. Menezes, P. Granger, R. E. Hoffman, K. W. Zilm, "Further conventions for NMR shielding and chemical shifts (IUPAC Recommendations 2008)", *Pure Appl. Chem.* **2008**, *80*, 59–84.

5 Synthesis of Known Nitridosilicate Compounds Using the Ammonothermal Technique

Unpublished results

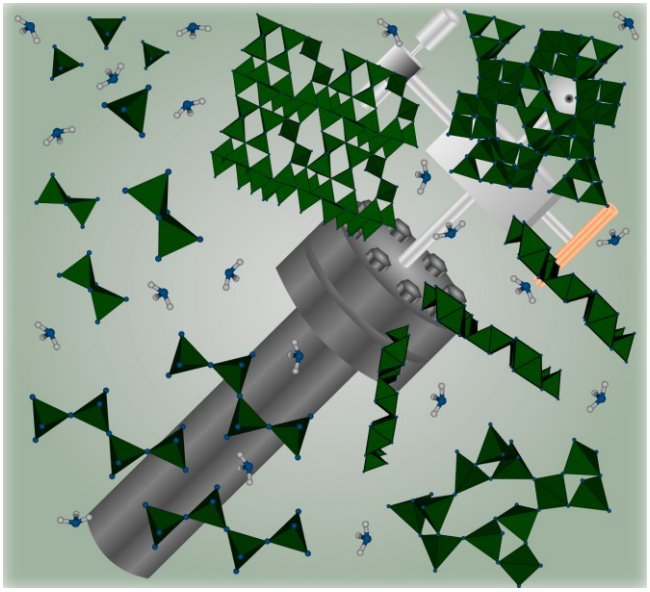

Abstract: Nitridosilicate compounds represent one of the best-investigated compound classes among the nitrides. In analogy to the oxosilicates, they form a variety of different crystal structures comprising SiN_4 tetrahedra as a central building block. Here, the first ammonothermal preparations of the literature-known nitridosilicate compounds $AESiN_2$ (AE = Sr, Ba), $Li_2CaSi_2N_4$ and $Ba_2AlSi_5N_9$ is reported. Their identification among the products was performed using X-ray diffraction. The synthesized nitridosilicates comprise structural motifs, namely tetrahedra layers and complex three-dimensional networks, which were not observed from ammonothermal reactions before. Together with preliminary work, this shows that the ammonothermal method offers a universal approach towards the high structural variability of nitridosilicate compounds. Additionally, the results show that the selection of starting materials allows the preparation of ternary nitrides but at the same time, their formation can be circumvented to yield phase-pure quaternary nitridosilicate compounds. This is an advantage of the ammonothermal method compared to other synthesis methods where often binary or ternary nitrides are preferably formed over quaternary compounds. Furthermore, this ammonothermal access towards nitridosilicates enables a drastic reduction of the synthesis temperature compared to the established high-temperature routes.

5.1 Introduction

As presented in Chapter 4, only few imide nitride compounds containing silicon were reported in the literature, mainly received from ammonothermal preparations. In contrast to that, the compound class of nitridosilicates presents one of the best-investigated systems among the nitrides reported in literature with a multitude of different representatives.[1-3] Nitridosilicates are closely related to the oxosilicates and form in analogy to them SiN_4 tetrahedra as central building blocks. The possibilities for connection of these building blocks hereby even surpass the possibilities in oxosilicates due to the longer Si−N bonds which have a more covalent character compared to Si−O.[4] Therefore, the effective charge of two adjacent Si^{4+} is reduced and simultaneously their spatial distance to each other is increased which comes with a decrease in the electrostatic repulsion between them. This allows, next to the connection of the tetrahedra via common vertices, also tetrahedra connections with shared edges. Additionally, connections of three or even four SiN_4 tetrahedra at a single common nitrogen atom are possible (Figure 5.1).[5-8] Next to isolated tetrahedra, such as in Ca_4SiN_4, these connection possibilities lead to structures comprising isolated units such as bow-tie shaped double tetrahedra in $Ba_5Si_2N_6$. Furthermore, the tetrahedra can be condensed forming one-dimensional chains, e.g. in Eu_2SiN_3, two-dimensional layers, e.g. in $AESiN_2$ (AE = Sr, Ba), up to complex three-dimensional networks such as in Li_2SiN_2.[5-6,9-12]

A main parameter to characterize the formed nitridosilicate networks is the condensation degree κ. It is defined as the ratio of the tetrahedra centers, in nitridosilicate compounds mainly occupied by Si, to the vertices of the tetrahedra, formed by N atoms. Here, again, the higher structural variability of nitridosilicates compared to oxosilicates is visualized by the possible range that κ can attain in the different compound classes. The lower limit is formed by the smallest building blocks of the networks, the SiO_4 and SiN_4 tetrahedra, respectively, to $\kappa = \frac{1}{4}$. The upper limit meanwhile is achieved in the binary compounds and therefore a significantly higher value of $\kappa = \frac{3}{4}$ is attained in silicon nitride Si_3N_4 compared to silicon dioxide SiO_2 with $\kappa = \frac{1}{2}$.

The structural variety which was first assumed from the described relation to the structurally versatile oxosilicates and later proven by the synthesis of many nitridosilicate representatives, allows the application of Eu^{2+}-doped nitridosilicates as inorganic phosphors for phosphor-converted light-emitting diodes (pcLED).[1,3] The most prominent nitridosilicate system for this application is $M_2Si_5N_8$ (M = Ca, Sr, Ba, Eu) which shows beneficial properties for inorganic phosphors such as high chemical and thermal stability, a small Stokes shift as well as a tunable emission.[13-17]

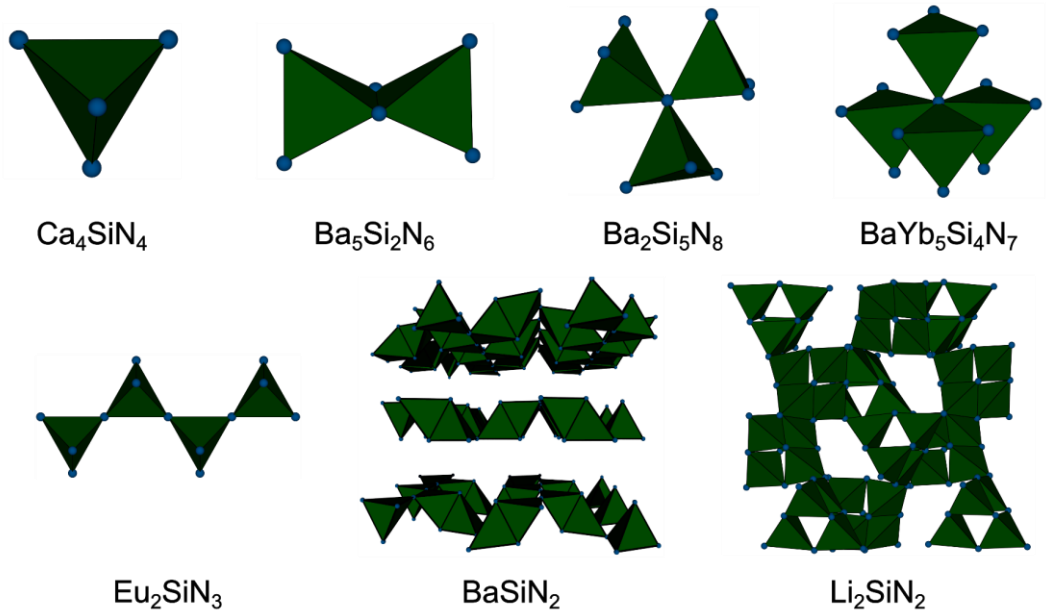

Figure 5.1: Representation of different tetrahedra-based structural motifs observed in nitridosilicate compounds together with the compound examples they were observed in. For clarity, only the nitridosilicate tetrahedra are depicted without counter cations.

Over the years, several synthetic strategies were developed to give access to the structural variety of nitridosilicates. All methods have in common that high reaction temperatures (> 970 K) are required and oxygen has to be excluded from the reaction atmosphere to avoid incorporation of oxide anions into the product. Already for the preparation of the first nitridosilicate Li_5SiN_3, the respective binary nitrides were chosen as starting material.[18] Another already early applied route involves the nitridation of metallic compounds such as metals or intermetallic phases with elemental nitrogen at elevated temperatures as it was used e.g. for the preparation of $Ln_3Si_6N_{11}$ (*Ln* = La, Ce, Pr, Nd, Sm).[19-20] In a third approach, a metallic flux of the alkali metals Li or Na is used which is advantageous as it often yields well-crystallized products. As nitrogen source the respective azides LiN_3 or NaN_3 are employed. The amount of azide added to the reaction mixture also allows synthetic control over the reaction outcome as the nitrogen amount and pressure generated *in situ* in the closed reaction vessels is influenced by this parameter.[6,21] As the most recently developed method, an ion exchange route employing metal chlorides in excess next to pre-synthesized nitridosilicates was presented, but currently this approach is limited to the system $M_2Si_5N_8$ with a variety of different elements *M* = Mg, Ca, Sr, Fe, Sc, U, Pb.[22-25] The most universal access towards nitridosilicates found until now is provided by the employment of the reactive silicon-containing starting material silicon diimide (SDI, $Si(NH)_2$). The combination of SDI with different elemental metals as well as metal amides, nitrides, or halides as starting material yielded numerous nitridosilicate compounds from high-temperature syntheses particularly using high-frequency furnaces.[1-2] Next to SDI, also other reactive silicon sources such as $Si(CN_2)_2$ or amorphous Si_3N_4 were employed to synthesize nitridosilicate compounds.[12,26-28]

Next to this high-temperature route, the solution-based ammonothermal method was also used to obtain nitridosilicate compounds. By now, only few examples for the preparation of nitridosilicate compounds from the ammonothermal synthesis are reported, although $NaSi_2N_3$, the first nitridosilicate prepared from ammonothermal conditions, was already described in 1993.[29] Other example compounds are $MSiN_2$ (M = Mg, Mn, Zn) with their solid solutions as well as $LiSi_2N_3$ which could be prepared ammonothermally.[30-32] All of these ternary double nitrides crystallize in wurtzite-related crystal structures with not only silicon but also the counter cations in tetrahedral coordination. Additionally, two nitridosilicates comprising three-dimensional structures other than the wurtzite structure type were observed as side phases, namely Li_2SiN_2 and $Ca_{16}Si_{17}N_{34}$.[31,33] Next to these nitridosilicate compounds with three-dimensional structure types, with Eu_2SiN_3 and $Ca_{1+x}Y_{1-x}SiN_{3-x}O_x$ ($x > 0$) two examples of chain-type nitridosilicates were observed from ammonothermal conditions as well.[34-35] Additionally, incorporation of other network forming cations next to silicon led to the ammonothermal synthesis of the quaternary nitridoalumosilicate compounds $AEAlSiN_3$ (AE = Ca, Sr) as well as to the first nitridogallosilicate $CaGaSiN_3$ which, again, all three crystallize in wurtzite-related structures.[33,36-37] During the preparation of these compounds, the observation was made that potassium-based mineralizers such as KN_3 seem to be beneficial for the preparation of nitridosilicate compounds as well as for the dissolution of elemental Si as starting material.[38]

These findings are generally promising for an evolving progress in ammonothermal synthesis of nitridosilicates as a variety of elements could already be incorporated into nitridosilicate compounds and even quaternary compounds could be stabilized. Nevertheless, the structural variability of the ammonothermally obtained nitridosilicates falls short of the mentioned opportunities with mostly wurtzite-related structure types. This was the motivation for the explorative synthesis attempts which are presented within this chapter. In the following, the systematic synthetic accessibility towards nitridosilicate compounds using the ammonothermal method was confirmed and expanded. The literature-known ternary nitridosilicate compounds $SrSiN_2$ and $BaSiN_2$ as well as the quaternary compounds $Li_2CaSi_2N_4$ and $Ba_2AlSi_5N_9$ were observed from ammonothermal reactions. These examples together with the presented preliminary work on the ammonothermal synthesis of nitridosilicate compounds show that different structural motifs can be realized in the nitridosilicate compound class employing this approach.

5.2 Ammonothermal Synthesis of Layered Nitridosilicates $SrSiN_2$ and $BaSiN_2$

5.2.1 Experimental Details

All compounds presented in this chapter were synthesized in high-pressure, high-temperature autoclaves and analyzed by X-ray diffraction analogously to the procedure described in detail in Section 6.4.

For the ammonothermal synthesis of $SrSiN_2$, the starting materials Sr (Sigma-Aldrich, 99.9%, 175.2 mg, 2.000 mmol), Si (Alfa Aesar, 99.99%, 56.2 mg, 2.00 mmol) and the mineralizer KN_3 (Sigma-Aldrich, 99.9%, 405.6 mg, 5.000 mmol) were ground together and filled into a tantalum liner. The liner was placed in a Haynes 282 autoclave which was closed and subsequently filled with approximately 3.8 mL NH_3 under cooling. The autoclave was heated to 670 K in 2 h, held at that temperature for 10 h and subsequently heated to 1070 K in 3 h. The synthesis temperature was maintained for 192 h, reaching a maximum pressure of 125 MPa before the autoclave was cooled to room temperature by switching off the furnace. The colorless product was isolated from the liner under argon atmosphere and analyzed by X-ray powder diffraction using Cu-$K_{\alpha1}$ radiation.

To prepare $BaSiN_2$, the starting materials Ba (Sigma-Aldrich, 99.9%, 274.6 mg, 2.000 mmol), Si (Alfa Aesar, 99.99%, 56.2 mg, 2.00 mmol) as well as the mineralizer KN_3 (Sigma-Aldrich, 99.9%, 486.7 mg, 6.000 mmol) were ground together and filled into a tantalum liner. The liner was placed in a Haynes 282 autoclave which was closed and subsequently filled with approximately 3.9 mL NH_3 under cooling. The autoclave was heated to 670 K in 2 h, held at that temperature for 15 h and then heated to 1070 K in 3 h. The synthesis temperature was maintained for 96 h, reaching a maximum pressure of 150 MPa before the autoclave was cooled to room temperature by switching off the furnace. The colorless product was isolated from the liner under argon atmosphere and analyzed using X-ray powder diffraction with Mo-$K_{\alpha1}$ radiation.

5.2.2 Results and Discussion

The PXRD pattern of the product for the Sr-containing sample shows $SrSiN_2$ as the main phase and unreacted Si as a minor side phase (ca. 5 wt%) as depicted in the Rietveld refinement plot (Figure 5.2). Additionally, the sample contains a minor unidentified side phase as it can be observed from the difference plot. Further details on the refinement are summarized in Table 9.25 and Table 9.26 in the Supporting Information.

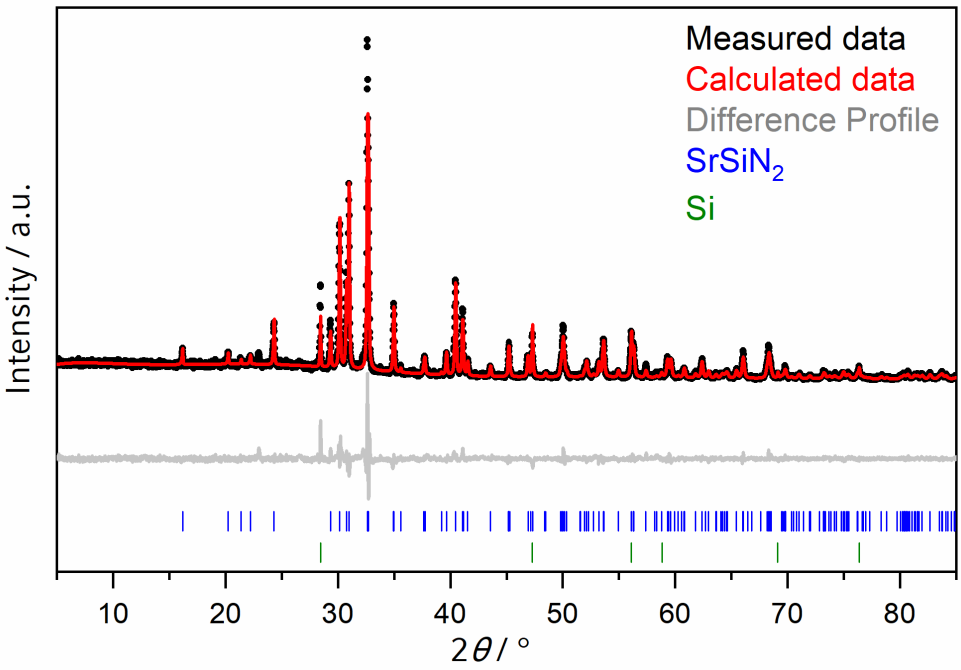

Figure 5.2: Rietveld refinement plot based on PXRD data of $SrSiN_2$ with experimental data (black dots), calculated diffraction pattern (red line), difference profile (gray line) and reflection positions of $SrSiN_2$ (blue bars) and Si (green bars).

For the Ba-containing sample, $BaSiN_2$ was observed as the only known product in the PXRD pattern next to an unknown minor side phase (Figure 5.3). Further details on the refinement are summarized in Table 9.27 and Table 9.28 in the Supporting Information.

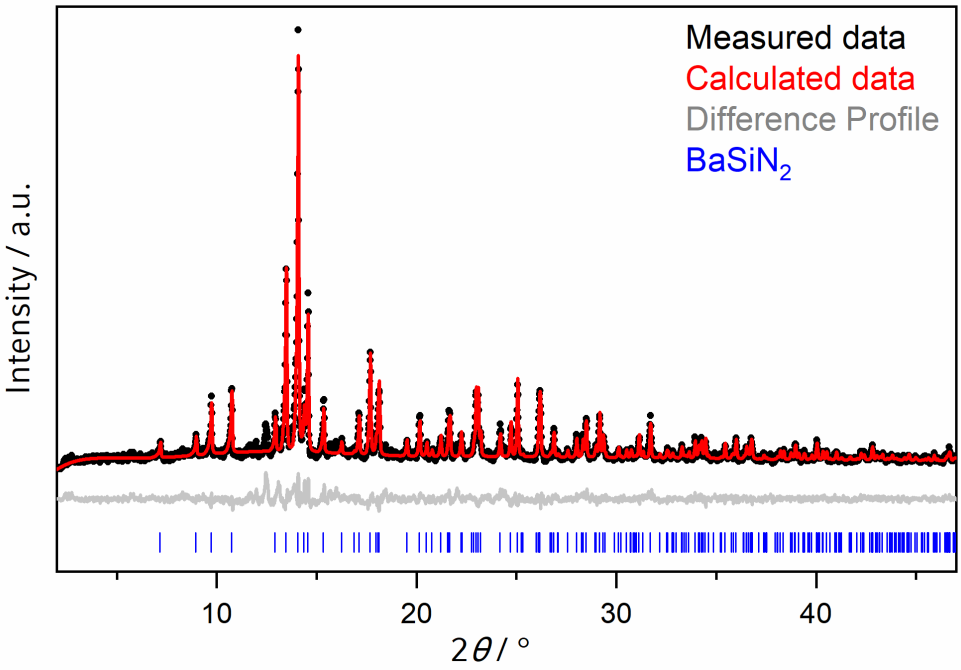

Figure 5.3: Rietveld refinement plot based on PXRD data of $BaSiN_2$ with experimental data (black dots), calculated diffraction pattern (red line), difference profile (gray line) and reflection positions of $BaSiN_2$ (blue bars).

$SrSiN_2$ crystallizes in space group $P2_1/c$ (no. 14) with lattice parameters a = 5.97234(17) Å, b = 7.3170(2) Å, c = 5.49965(17) Å, and β = 113.5077(18)°. $BaSiN_2$ crystallizes in space group *Cmce* (no. 64) with lattice parameters a = 5.6040(2) Å, b = 11.3622(5) Å and c = 7.5881(4) Å.[10-11] Both structures comprise layers of SiN_4 tetrahedra which are separated by the respective alkaline earth metal cations (Figure 5.4).[11] While $BaSiN_2$ shows a symmetric orientation of the SiN_4 tetrahedra within the layers, the layers in $SrSiN_2$ are slightly distorted. The layers are built up from edge-sharing bow-tie-shaped Si_4N_8 double tetrahedra which are interconnected via common vertices.[11]

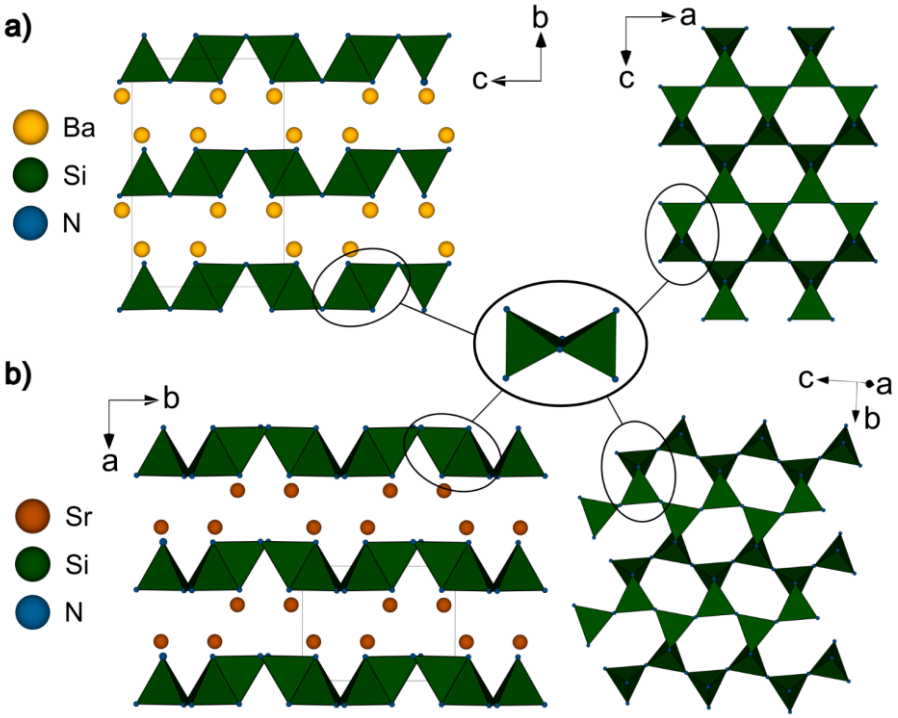

Figure 5.4: Depiction of the crystal structures of $BaSiN_2$ along [100] with a top view on the layers (a) and of the crystal structure of $SrSiN_2$ along [001] together with a top view on the distorted layers (b). In the middle, the central Si_2N_8 double tetrahedra that build up the layers are shown.

The ammonothermal syntheses of $SrSiN_2$ and $BaSiN_2$ present the first examples for the successful formation of the structural motif of nitridosilicate layers using this synthesis method. In comparison to the reported syntheses at 1170–1370 K from molten sodium, the ammonothermal route offers a further reduction of the synthesis temperature to 1070 K.[11] This might be achieved by the employment of the more reactive NH_3 instead of N_2 gas and the applied higher pressures during the synthesis. Additionally, the results proof that also extremely air-sensitive compounds such as $SrSiN_2$, which could be only stabilized in metal flux reactions before are accessible using the ammonothermal synthesis.

5.3 Ammonothermal Synthesis of Quaternary Network Nitridosilicate $Li_2CaSi_2N_4$

5.3.1 Experimental Details

Li_2CaSi was synthesized as a starting material according to the literature from Ca (Sigma-Aldrich, 99.99%, 200.4 mg, 5.000 mmol) and Si (Alfa Aesar, 99.99%, 140.4 mg, 5.000 mmol) in combination with an excess of Li (Alfa Aesar, 99%,173.6 mg, 25.00 mmol) as flux.[39] The employed Li excess during the synthesis of the starting material was subsequently used as a mineralizer and therefore not removed from the products. The starting material was filled in a molybdenum liner and transferred to a Haynes 282 autoclave which was sealed and subsequently filled with ammonia (approx. 3.4 mL) under cooling. The autoclave was heated to 670 K in 2 h, held at that temperature for 16 h and heated to 1070 K in 3 h. The synthesis temperature was maintained for 96 h, reaching a maximum pressure of 128 MPa before the autoclave was cooled to room temperature by switching off the furnace. The colorless product was isolated from the liner under argon atmosphere and analyzed using X-ray powder diffraction with Cu-$K_{\alpha1}$ radiation.

5.3.2 Results and Discussion

$Li_2CaSi_2N_4$ was observed among the products in the PXRD pattern of the sample next to the ternary nitridosilicate $Ca_{16}Si_{17}N_{34}$ and the oxides CaO and Li_2O as one of the main products (Figure 5.5). The formation of the oxide side products may occur due to contaminations arising from the autoclave wall.

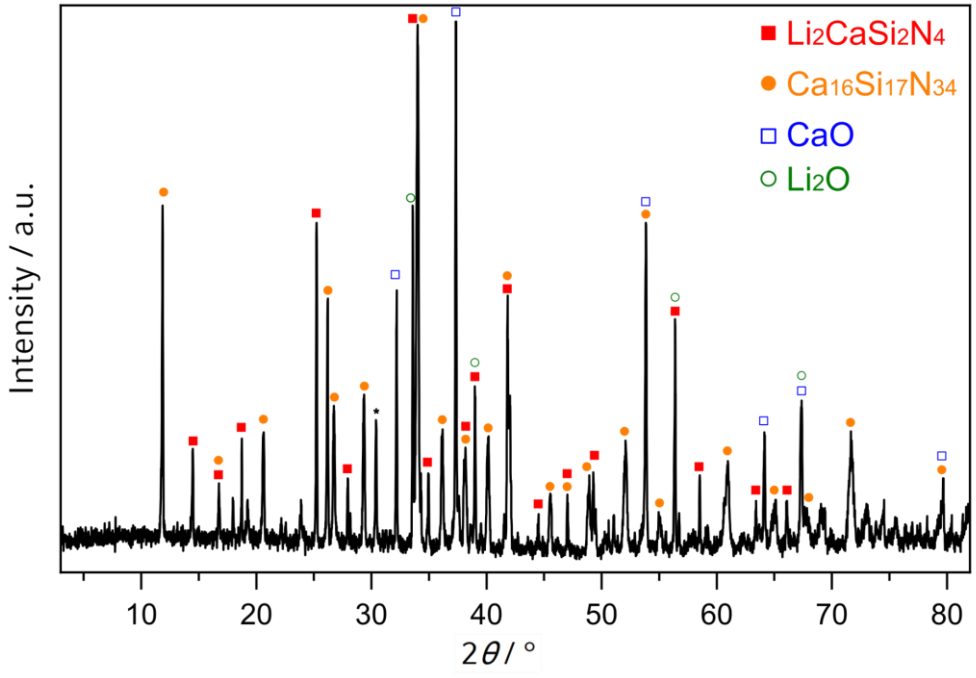

Figure 5.5: PXRD pattern of the sample containing $Li_2CaSi_2N_4$ (black line) with the highlighted reflections of $Li_2CaSi_2N_4$ (red squares), $Ca_{16}Si_{17}N_{34}$ (orange circles), CaO (blue squares) and Li_2O (green circles).

$Li_2CaSi_2N_4$ crystallizes in space group $Pa\bar{3}$ (no. 205) with lattice parameter a = 1056.9(12) Å. The structure comprises a three-dimensional cubic nitridosilicate network with exclusively corner-sharing tetrahedra. The counter cations Li and Ca are filling the voids left by the network (Figure 5.6a).[40] The central nitridosilicate substructure comprises four *dreier* rings which are interconnected via common vertices forming a *siebener* ring (Figure 5.6b).[41-42] This network is forming the first representative of *Net39* according to the network topology classification by O'Keeffe *et al*. observed in nitridosilicates.[40,43]

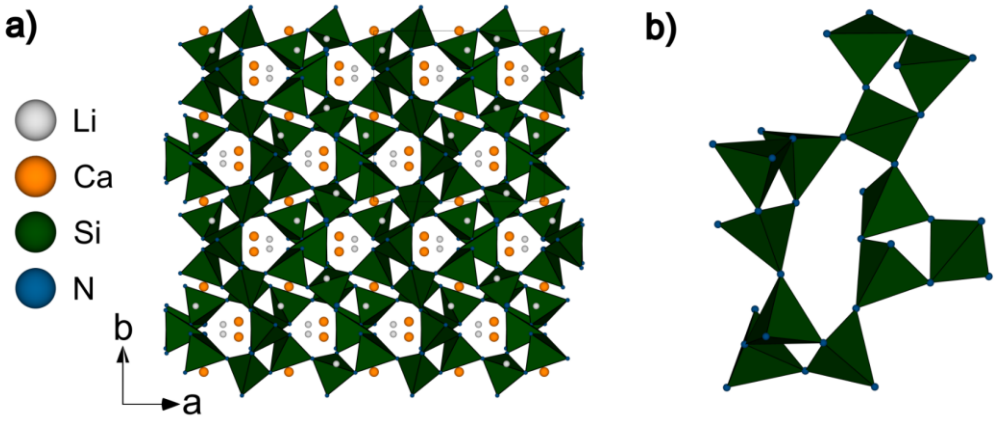

Figure 5.6: Representation of the crystal structure of $Li_2CaSi_2N_4$ along [001] (a) with the central building unit of the nitridosilicate substructure (b).

The ammonothermal synthesis of $Li_2CaSi_2N_4$ presents the first observation of a quaternary nitridosilicate comprising both alkali metal and alkaline earth metal counter cations. Before the synthesis of $Li_2CaSi_2N_4$, intermetallic starting materials were already employed to obtain nitridosilicates ammonothermally, e.g. for the preparation of $CaGaSiN_3$ and $Ca_{1+x}Y_{1-x}SiN_{3-x}O_x$ ($x > 0$).[33,35] Therefore, the suitability of such starting materials for the ammonothermal synthesis of nitridosilicates is emphasized by the presented results. It seems that the reaction product can be controlled by a pre-orientation of the elements in such an intermetallic phase as $Li_2CaSi_2N_4$ was not observed among the products when elemental Li, Ca and Si were used as separate starting materials. Again, the synthesis temperature could be slightly reduced using the ammonothermal method from 1170 K in tantalum ampoules to 1070 K in supercritical ammonia. As the nitrogen pressure was already discussed as a crucial parameter for the synthesis of the condensed structure of $Li_2CaSi_2N_4$, the ammonothermal high-pressure method directly addresses this demand during the preparation.[40] As $Li_2CaSi_2N_4$ is another compound for which the synthesis from metal flux reactions could be replaced by the ammonothermal synthesis, it might be possible to also obtain lower condensed nitridosilicates using the ammonothermal method in the future, as such nitridosilicates are often prepared from reactions in metal fluxes.[5]

5.4 Ammonothermal Synthesis of Network Nitridoalumosilicate $Ba_2AlSi_5N_9$

5.4.1 Experimental Details

$Ba_2AlSi_5N_9$ was synthesized from the metals Ba (Sigma-Aldrich, 99.99%, 274.6 mg, 2.000 mmol), Al (Acros, 99.97%, 27.0 mg, 1.00 mmol), Si (Alfa Aesar, 99.99%, 140.4 mg, 5.000 mmol) and an excess of the mineralizer KN_3 (Sigma-Aldrich, 99.9%, 811.0 mg, 11.00 mmol). The starting materials were ground together and filled into a tantalum liner. The liner was placed into a Haynes 282 autoclave which was closed and subsequently filled with ammonia (ca. 3.9 mL) under cooling. The autoclave was heated to 670 K in 2 h, held at that temperature for 17 h and then heated to 1070 K in 3 h. The synthesis temperature was maintained for 96 h, reaching a maximum pressure of 140 MPa, before the autoclave was cooled to room temperature by switching off the furnace. The colorless product was isolated from the liner under argon atmosphere and analyzed using X-ray diffraction with Mo-$K_{\alpha1}$ radiation.

5.4.2 Results and Discussion

A Rietveld refinement of the PXRD pattern of the sample showed $Ba_2AlSi_5N_9$ as the only crystalline reaction product (Figure 5.7). Further details on the refinement are summarized in Table 9.29 and Table 9.30 in the Supporting Information.

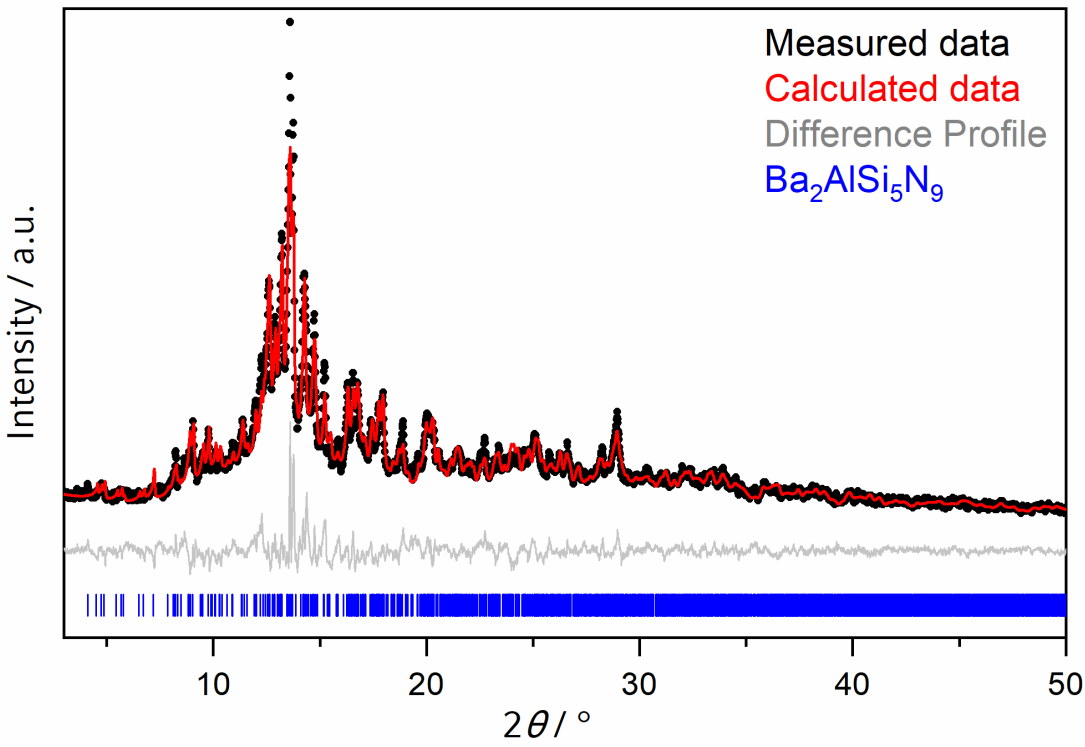

Figure 5.7: Rietveld refinement plot based on PXRD data of $Ba_2AlSi_5N_9$ with experimental data (black dots), calculated diffraction pattern (red line), difference profile (gray line) and reflection positions of $Ba_2AlSi_5N_9$ (blue bars).

$Ba_2AlSi_5N_9$ crystallizes in the triclinic space group *P*1 (no. 1) with lattice parameters a = 9.875(3) Å, b = 10.294(3) Å, c = 10.359(3) Å, α = 90.144(12)°, β = 118.526(13)°, and γ = 103.770(15)°. The structure consists of a highly condensed nitridoalumosilicate tetrahedra network with barium cations in its voids (Figure 5.8a).[44] The centers of the tetrahedra in the anionic network are statistically occupied by Al and Si while the vertices are formed by N. The network comprises layers of *dreier* rings formed by these $(Si/Al)N_4$ tetrahedra with a characteristic up-down sequence of the tetrahedra vertices (Figure 5.8b). The layers are interconnected by two different *vierer* ring-based motifs as further described by Kechele *et al*.[44]

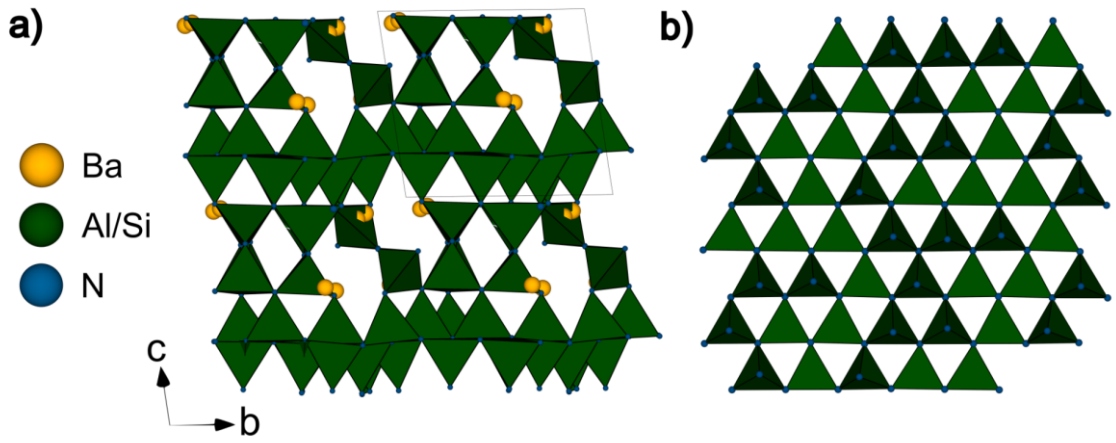

Figure 5.8: Representation of the crystal structure of $Ba_2AlSi_5N_9$ along [001], neglecting less occupied alternative positions for clarity (a) with a depiction of the up-down sequence within the layer-like parts of the structure (b).

$Ba_2AlSi_5N_9$ presents another example of a nitridoalumosilicate which is accessible using the ammonothermal synthesis next to the wurtzite-type compounds $AEAlSiN_3$ (*AE* = Ca, Sr).[36-37] Hereby, the synthesis temperature of $Ba_2AlSi_5N_9$ could be radically reduced compared to the high-temperature synthesis from 2000 K to 1070 K using the ammonothermal process. This might be enabled as elemental Al and Si could be employed as more reactive starting materials compared to the binary nitrides AlN and Si_3N_4. Additionally, the more reactive nitrogen-containing supercritical ammonia was employed as a solvent instead of nitrogen gas. Furthermore, $Ba_2AlSi_5N_9$ was received without crystalline side phases that were observed before in the high-temperature synthesis such as $Ba_2Si_5N_8$ or $BaSi_7N_{10}$.[44]

$Ba_2AlSi_5N_9$ has the same condensation degree $\kappa = \frac{2}{3}$ as $AEAlSiN_3$ (*AE* = Ca, Sr) but does not form a wurtzite-related structure. They differ in their cation ration (*CR*) which is defined as the ratio of counter cations that do not form the network (Ba for $Ba_2AlSi_5N_9$) to the network-forming cations in the tetrahedra centers (Si and Al for nitridoalumosilicates).[45-46] This value allows to visualize the broad variety of possible elemental compositions even at a fixed condensation degree κ.

Furthermore, the formation of two different highly condensed structures can be explained by their different *CR* values of $\frac{1}{3}$ and $\frac{1}{2}$ for $Ba_2AlSi_5N_9$ and *AE*$AlSiN_3$ (*AE* = Ca, Sr), respectively.

The observation of two nitridoalumosilicates with the same condensation degree shows that the ammonothermal synthesis allows access to diverse, highly condensed structural motifs at different *CR* values for nitridosilicate compounds. Therefore, the ammonothermal synthesis provides a suitable tool to access the high structural variability offered by the compound class of nitridosilicates.

5.5 Conclusions

The ammonothermal preparations of *AE*SiN_2 (*AE* = Sr, Ba), $Li_2CaSi_2N_4$ and $Ba_2AlSi_5N_9$ presented in this chapter show that the ammonothermal synthesis presents a suitable tool to access ternary as well as quaternary nitride compounds in the nitridosilicate system. Here, the selection of the starting materials and the mineralizer are powerful ways to influence the reaction outcome. This enables an aimed synthesis procedure either towards the ternary compounds as observed for $BaSiN_2$, while their formation can as well be circumvented to receive phase-pure quaternary compounds such as $Ba_2AlSi_5N_9$. During the preparation of quaternary and higher nitride species often stable binary and ternary nitrides are observed as side phases. It seems that the ammonothermal solution-based reaction mechanism, which involves the formation of dissolved intermediate species, may help to prevent the unintentional formation of such binary or ternary compounds. This is demonstrated by the phase-pure preparation of $Ba_2AlSi_5N_9$ using the ammonothermal method while the high-temperature synthesis yielded multiple side phases.[44]

Furthermore, the ammonothermal approach can be used to synthesize a variety of tetrahedra-based structural motifs in nitridosilicate compounds. Next to the already observed motifs of chains and wurtzite-like three-dimensional networks, in this chapter, layers and highly condensed three-dimensional structures could be presented in the ammonothermal reaction products $SrSiN_2$, $BaSiN_2$, $Li_2CaSi_2N_4$ and $Ba_2AlSi_5N_9$. As starting materials for these compounds, not only intermetallic silicides, but also elemental silicon were used and showed together with previous results that a pre-orientation of the elements in intermetallic compounds can be performed, but is not absolutely required to obtain quaternary nitridosilicates. The reaction route from literature, starting from elemental silicon at, for nitridosilicate synthesis, relatively low temperatures up to 1070 K could be enhanced with further examples and might be considered as a universal ammonothermal synthesis approach towards nitridosilicates, analogously to the procedure presented for multiple structural motifs in nitridophosphates.[47] This approach provides an access to nitridosilicate compounds without the need for reactive starting materials such as SDI. Furthermore, it can be used to prepare extremely air-sensitive compounds such as $SrSiN_2$ which were only observed from metal flux reactions before. This might allow the incorporation of isolated

low-dimensional motifs, such as double tetrahedra or isolated tetrahedra, using the ammonothermal synthesis in the future. The results also show that different mineralizers than KN_3 can be suitable for the preparation of nitridosilicates, as shown for $Li_2CaSi_2N_4$ where the Li excess from the preparation of Li_2CaSi served as mineralizing agent. Next to silicon, also other network forming agents can be incorporated into nitridosilicate compounds using the ammonothermal synthesis such as Al or Ga, as already shown before.[33,36-37] Additionally, the preparation of $Ba_2AlSi_5N_9$ demonstrates that different nitridosilicate structure types are accessible ammonothermally by maintaining the same condensation degree.

The results presented in this chapter in combination with the preliminary work show that the ammonothermal synthesis offers a universal access towards various structural motifs in nitridosilicate compounds starting from elemental silicon or intermetallic compounds. An initial exploration of this synthetic access towards new compounds within this structurally diverse compound class will be presented in the following chapter.

5.6 References

[1] M. Zeuner, S. Pagano, W. Schnick, "Nitridosilicates and Oxonitridosilicates: From Ceramic Materials to Structural and Functional Diversity", *Angew. Chem.* **2011**, *123*, 7898–7920; *Angew. Chem. Int. Ed.* **2011**, *50*, 7754–7775.

[2] W. Schnick, H. Huppertz, "Nitridosilicates – A Significant Extension of Silicate Chemistry", *Chem. Eur. J.* **1997**, *3*, 679–683.

[3] S.-L. Chung, S.-C. Huang, W.-C. Chou, W. W. Tangguh, "Phosphors based on nitridosilicates: synthesis methods and luminescent properties", *Curr. Opin. Chem. Eng.* **2014**, *3*, 62–67.

[4] A. F. Holleman, N. Wiberg, "Lehrbuch der Anorganischen Chemie", *Vol. 102*, DeGruyter, Berlin, Boston, **2008**.

[5] H. Yamane, H. Morito, "Synthesis and Crystal Structures of Ca_4SiN_4 and New Polymorph of $Ca_5Si_2N_6$", *Inorg. Chem.* **2013**, *52*, 5559-5563.

[6] H. Yamane, F. J. DiSalvo, "Preparation and crystal structure of a new barium silicon nitride, $Ba_5Si_2N_6$", *J. Alloys Compd.* **1996**, *240*, 33–36.

[7] H. Huppertz, W. Schnick, "Edge-sharing SiN_4 Tetrahedra in the Highly Condensed Nitridosilicate $BaSi_7N_{10}$", *Chem. Eur. J.* **1997**, *3*, 249–252.

[8] H. Huppertz, W. Schnick, "$BaYbSi_4N_7$ – Unexpected Structural Possibilities in Nitridosilicates", *Angew. Chem.* **1996**, *108*, 2115–2116; *Angew. Chem. Int. Ed.* **1996**, *35*, 1983–1984.

[9] M. Zeuner, S. Pagano, P. Matthes, D. Bichler, D. Johrendt, T. Harmening, R. Pöttgen, W. Schnick, "Mixed Valence Europium Nitridosilicate Eu_2SiN_3", *J. Am. Chem. Soc.* **2009**, *131*, 11242–11248.

[10] P. E. D. Morgan, "X-ray powder diffraction pattern and unit cell of $BaSiN_2$", *J. Mater. Sci. Lett.* **1984**, *3*, 131–132.

[11] Z. A. Gál, P. M. Mallinson, H. J. Orchard, S. J. Clarke, "Synthesis and Structure of Alkaline Earth Silicon Nitrides: $BaSiN_2$, $SrSiN_2$, and $CaSiN_2$", *Inorg. Chem.* **2004**, *43*, 3998–4006.

[12] S. Pagano, M. Zeuner, S. Hug, W. Schnick, "Single-Crystal Structure Determination and Solid-State NMR Investigations of Lithium Nitridosilicate Li_2SiN_2 Synthesized by a Precursor Approach Employing Amorphous "$Si(CN_2)_2$"", *Eur. J. Inorg. Chem.* **2009**, *2009*, 1579–1584.

[13] T. Schlieper, W. Schnick, "Nitrido-silicate. I. Hochtemperatur-Synthese und Kristallstruktur von $Ca_2Si_5N_8$", *Z. Anorg. Allg. Chem.* **1995**, *621*, 1037–1041.

[14] T. Schlieper, W. Milius, W. Schnick, "Nitrido-silicate. II. Hochtemperatur-Synthesen und Kristallstrukturen von $Sr_2Si_5N_8$ und $Ba_2Si_5N_8$", *Z. Anorg. Allg. Chem.* **1995**, *621*, 1380–1384.

[15] H. Huppertz, W. Schnick, "$Eu_2Si_5N_8$ and $EuYbSi_4N_7$. The First Nitridosilicates with a Divalent Rare Earth Metal", *Acta Crystallogr., Sect. C: Cryst. Struct. Commun.* **1997**, *53*, 1751–1753.

[16] R. Mueller-Mach, G. Mueller, M. R. Krames, H. A. Höppe, F. Stadler, W. Schnick, T. Juestel, P. Schmidt, "Highly efficient all-nitride phosphor-converted white light emitting diode", *Phys. Status Solidi A* **2005**, *202*, 1727–1732.

[17] M. Zeuner, P. J. Schmidt, W. Schnick, "One-Pot Synthesis of Single-Source Precursors for Nanocrystalline LED Phosphors $M_2Si_5N_8$:Eu^{2+} (M = Sr, Ba)", *Chem. Mater.* **2009**, *21*, 2467–2473.

[18] R. Juza, H. H. Weber, E. Meyer-Simon, "Über ternäre Nitride und Oxonitride von Elementen der 4. Gruppe", *Z. Anorg. Allg. Chem.* **1953**, *273*, 48–64.

[19] J. David, J. Lang, "Sur un nitrure double de magnesium et de silicium", *C. R. Hebd. Seances Acad. Sci.* **1965**, *261*, 1005–1007.

[20] M. Woike, W. Jeitschko, "Preparation and Crystal Structure of the Nitridosilicates $Ln_3Si_6N_{11}$ (Ln = La, Ce, Pr, Nd, Sm) and $LnSi_3N_5$ (Ln = Ce, Pr, Nd)", *Inorg. Chem.* **1995**, *34*, 5105–5108.

[21] S. Pagano, S. Lupart, M. Zeuner, W. Schnick, "Tuning the Dimensionality of Nitridosilicates in Lithium Melts", *Angew. Chem.* **2009**, *121*, 6453–6456; *Angew. Chem. Int. Ed.* **2009**, *48*, 6335–6338.

[22] P. Bielec, W. Schnick, "Increased Synthetic Control – Gaining Access to Predicted $Mg_2Si_5N_8$ and β-$Ca_2Si_5N_8$", *Angew. Chem.* **2017**, *129*, 4888–4891; *Angew. Chem. Int. Ed.* **2017**, *56*, 4810–4813.

[23] P. Bielec, O. Janka, T. Block, R. Pöttgen, W. Schnick, "$Fe_2Si_5N_8$: Access to Open-Shell Transition-Metal Nitridosilicates", *Angew. Chem.* **2018**, *130*, 2433–2436; *Angew. Chem. Int. Ed.* **2018**, *57*, 2409–2412.

[24] P. Bielec, L. Eisenburger, H. L. Deubner, D. Günther, F. Kraus, O. Oeckler, W. Schnick, "Targeting Vacancies in Nitridosilicates: Aliovalent Substitution of M^{2+} (M=Ca, Sr) by Sc^{3+} and U^{3+}", *Angew. Chem.* **2019**, *131*, 850–853; *Angew. Chem. Int. Ed.* **2019**, *58*, 840–843.

[25] P. Bielec, R. Nelson, R. P. Stoffel, L. Eisenburger, D. Günther, A.-K. Henß, J. P. Wright, O. Oeckler, R. Dronskowski, W. Schnick, "Cationic Pb_2 Dumbbells Stabilized in the Highly Covalent Lead Nitridosilicate $Pb_2Si_5N_8$", *Angew. Chem.* **2019**, *131*, 1446–1450; *Angew. Chem. Int. Ed.* **2019**, *58*, 1432–1436.

[26] S. Pagano, O. Oeckler, T. Schröder, W. Schnick, "$Ba_6Si_6N_{10}O_2(CN_2)$ – A Nitridosilicate with a NPO-Zeolite Structure Type Containing Carbodiimide Ions", *Eur. J. Inorg. Chem.* **2009**, 2678–2683.

[27] C. Maak, P. Strobel, V. Weiler, P. J. Schmidt, W. Schnick, "Unprecedented Deep-Red Ce^{3+} Luminescence of the Nitridolithosilicates $Li_{38.7}RE_{3.3}Ca_{5.7}[Li_2Si_{30}N_{59}]O_2F$ (*RE* = La, Ce, Y)", *Chem. Mater.* **2018**, *30*, 5500−5506.

[28] L. Gamperl, G. Krach, P. J. Schmidt, W. Schnick, "Synthesis of $RE_{6-x}Ca_{1.5x}Si_{11}N_{20}O$ (*RE*=Yb, Lu; $x\approx2.2$) with $Lu_{6-x}Ca_{1.5x}Si_{11}N_{20}O:Ce^{3+}$ Offering Interesting Spectral Properties for Yellow-Emitting Phosphors in 1pcLEDs", *Eur. J. Inorg. Chem.* **2019**, *2019*, 4985−4993.

[29] H. Jacobs, H. Mengis, "Preparation and Crystal Structure of a Sodium Silicon Nitride, $NaSi_2N_3$", *Eur. J. Solid State Inorg. Chem.* **1993**, *30*, 45−53.

[30] J. Häusler, S. Schimmel, P. Wellmann, W. Schnick, "Ammonothermal Synthesis of Earth-Abundant Nitride Semiconductors $ZnSiN_2$ and $ZnGeN_2$ and Dissolution Monitoring by In Situ X-ray Imaging", *Chem. Eur. J.* **2017**, *23*, 12275−12282.

[31] J. Häusler, R. Niklaus, J. Minár, W. Schnick, "Ammonothermal Synthesis and Optical Properties of Ternary Nitride Semiconductors Mg-*IV*-N_2, Mn-*IV*-N_2 and Li-IV_2-N_3 (*IV*=Si, Ge)", *Chem. Eur. J.* **2018**, *24*, 1686−1693.

[32] M. Mallmann, R. Niklaus, T. Rackl, M. Benz, T. G. Chau, D. Johrendt, J. Minár, W. Schnick, "Solid Solutions of Grimm-Sommerfeld Analogous Nitride Semiconductors *II*-*IV*-N_2 with *II* = Mg, Mn, Zn; *IV* = Si, Ge – Ammonothermal Synthesis and DFT Calculations", *Chem. Eur. J.* **2019**, *25*, 15887–15895.

[33] J. Häusler, L. Neudert, M. Mallmann, R. Niklaus, A.-C. L. Kimmel, N. S. A. Alt, E. Schlücker, O. Oeckler, W. Schnick, "Ammonothermal Synthesis of Novel Nitrides: Case Study on $CaGaSiN_3$", *Chem. Eur. J.* **2017**, *23*, 2583−2590.

[34] J. Häusler, "Ammonothermal Synthesis of Functional Ternary and Multinary Nitrides", Doctoral thesis, Ludwig-Maximilians-Universität München (Munich), **2018**.

[35] M. Mallmann, C. Maak, W. Schnick, "Ammonothermal Synthesis and Crystal Growth of the Chain-type Oxonitridosilicate $Ca_{1+x}Y_{1-x}SiN_{3-x}O_x$ ($x > 0$)", *Z. Anorg. Allg. Chem.* **2020**, *646*, 1539–1544.

[36] J. Li, T. Watanabe, H. Wada, T. Setoyama, M. Yoshimura, "Low-Temperature Crystallization of Eu-Doped Red-Emitting $CaAlSiN_3$ from Alloy-Derived Ammonometallates", *Chem. Mater.* **2007**, *19*, 3592−3594.

[37] T. Watanabe, K. Nonaka, J. Li, K. Kishida, M. Yoshimura, "Low temperature ammonothermal synthesis of europium-doped $SrAlSiN_3$ for a nitride red phosphor", *J. Ceram. Soc. Jpn.* **2012**, *120*, 500−502.

[38] J. Häusler, W. Schnick, "Ammonothermal Synthesis of Nitrides: Recent Developments and Future Perspectives", *Chem. Eur. J.* **2018**, *24*, 11864−11879.

[39] D. Stoiber, M. Bobnar, P. Höhn, R. Niewa, "Lithium alkaline earth tetrelides of the type Li_2AeTt (*Ae*=Ca, Ba, *Tt*=Si, Ge, Sn, Pb): synthesis, crystal structures and physical properties", *Z. Naturforsch., B: J. Chem. Sci.* **2017**, *72*, 847−853.

[40] M. Zeuner, S. Pagano, S. Hug, P. Pust, S. Schmiechen, C. Scheu, W. Schnick, "$Li_2CaSi_2N_4$ and $Li_2SrSi_2N_4$ – a Synthetic Approach to Three-Dimensional Lithium Nitridosilicates", *Eur. J. Inorg. Chem.* **2010**, *2010*, 4945–4951.

[41] The terms *dreier*, *vierer*, *sechser*, *siebener* and *achter* rings were coined by Liebau and are derived from the German words„dreier, vierer, sechser, siebener and achter"; a *dreier* ring comprises three tetrahedra centers,a *vierer* ring four tetrahedra centers, and so on.

[42] F. Liebau, "Structural Chemistry of Silicates", Springer, Berlin, **1985**.

[43] M. O'Keeffe, "Uninodal 4-connected 3D nets. II. Nets with 3-rings", *Acta Crystallogr., Sect. A: Found. Adv.* **1992**, *48*, 670–673.

[44] J. A. Kechele, C. Hecht, O. Oeckler, J. Schmedt auf der Günne, P. J. Schmidt, W. Schnick, "$Ba_2AlSi_5N_9$ – A New Host Lattice for Eu^{2+}-Doped Luminescent Materials Comprising a Nitridoalumosilicate Framework with Corner- and Edge-Sharing Tetrahedra", *Chem. Mater.* **2009**, *21*, 1288–1295.

[45] R. M. Pritzl, N. Prinz, P. Strobel, P. J. Schmidt, D. Johrendt, W. Schnick, "From Framework to Layers Driven by Pressure – The Monophyllo-Oxonitridophosphate β-$MgSrP_3N_5O_2$ and Comparison to its α-Polymorph", *Chem. Eur. J.* **2023**, *29*, e202301218.

[46] M. Dialer, M. M. Pointner, S. L. Wandelt, P. Strobel, P. J. Schmidt, L. Bayarjargal, B. Winkler, W. Schnick, "Order and Disorder in Mixed (Si, P)–N Networks $Sr_2SiP_2N_6$:Eu^{2+} and $Sr_5Si_2P_6N_{16}$:Eu^{2+}", *Adv. Opt. Mater.* **2024**, *12*, 2302668.

[47] M. Mallmann, S. Wendl, W. Schnick, "Crystalline Nitridophosphates by Ammonothermal Synthesis", *Chem. Eur. J.* **2020**, *26*, 2067–2072.

6 Nitride Zeolites from Ammonothermal Synthesis

Published in: *Chem. Eur. J.* **2024**, e202404405

Authors: Florian M. Engelsberger and Wolfgang Schnick

DOI: 10.1002/chem.202404405

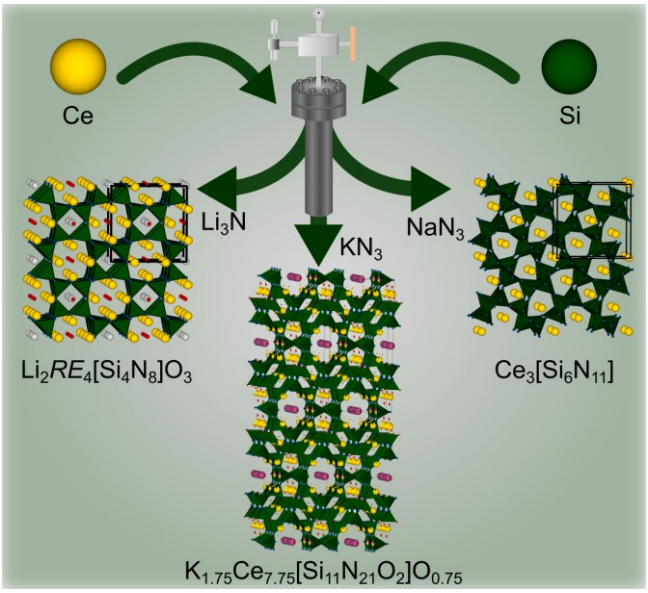

Abstract: Oxide zeolites are synthesized from aqueous solutions in an established way employing hydrothermal synthesis. Transferring this approach to nitride zeolites requires a solvent providing nitrogen for which ammonia has proven to be particularly suitable. We present the successful ammonothermal synthesis of the (oxo)nitridosilicate compounds $Ce_3[Si_6N_{11}]$, $Li_2RE_4[Si_4N_8]O_3$ (*RE* = La, Ce) and $K_{1.25}Ce_{7.75}[Si_{11}N_{21}O_2]O_{0.75}$. Within this procedure, the usage of supercritical ammonia as a solvent as well as the utilization of the mineralizers NaN_3, Li_3N and KN_3, respectively, allowed the targeted synthesis of large single crystals. Formation of these (oxo)nitridosilicates depends mainly on the employed mineralizer despite their similar degree of condensation. The three compounds were structurally characterized using X-ray diffraction and their crystal structures contain a wide range of different ring sizes within their tetrahedra networks. The zeolite(-like) crystal structures are elucidated and compared to known nitridosilicate representatives of the respective structure types. Their elemental composition was investigated using energy-dispersive X-ray (EDX) spectroscopy and incorporation of the O rather than N–H functionality was confirmed by Fourier-Transform infrared (FTIR) spectroscopy as well as by charge distribution (CHARDI) and bond valence sum (BVS) calculations. The presented examples demonstrate that ammonothermal synthesis provides a one-step access from elemental starting materials towards nitride zeolites.

6.1 Introduction

Zeolites are a family of crystalline materials which are in most cases built up from anionic alumosilicate tetrahedra networks in combination with counter cations. Their areas of application range from ion exchange over adsorption-separation processes to catalysis.[1] This material class is commonly synthesized using the hydrothermal approach.[2-4] In close relation to this synthesis method, the ammonothermal synthesis was developed to synthesize amides, imides and nitrides by using supercritical ammonia instead of water as a solvent.[5] Additionally, so-called mineralizers can improve the solubility of inorganic starting materials in supercritical ammonia. The selection of the mineralizer thereby allows to influence the reaction environment and so ammonobasic (NH_2^- predominant), ammononeutral and ammonoacidic (NH_4^+ predominant) reactions can be realized.[6] The ammonothermal method recently opened an additional synthetic access to the structurally versatile compound class of (oxo)nitridosilicates at lower temperatures next to the established high-temperature synthesis.[7-11] This might allow the synthesis of networks containing channels, as the temperature was found to play a crucial role on the dimensionality of tetrahedra networks before.[12] Furthermore, the number of zeolites containing nitride-based instead of the oxygen-based tetrahedra connections, like e.g. the zeolites NPO and NPT, increased in recent years.[13-19] Among these nitride zeolites are also representatives of the nitridosilicate compound class, such as $Li_2Sr_4[Si_4N_8]O$ and $LiAE_4[Si_4N_8]F$ (AE = Ca, Sr), forming distorted BCT zeolite networks.[12,20] In addition, some nitridosilicates forming zeolite-like networks were reported as well.[21-22] Nitridosilicate networks are built up from $[SiN_4]$ tetrahedra in which the nitrogen atoms at the vertices can be bound to a maximum of four silicon atoms. This enables a larger structural variability than for alumosilicates where only up to two tetrahedral centers can be connected through oxygen.[23] Additionally, the formation of anionic networks with high silicon content is easier incorporating only N^{3-} anions as the higher negative charge compared to O^{2-} can be balanced by the higher positive charge of Si^{4+} compared to Al^{3+}. These broad structural possibilities given in nitridosilicate networks enable several possible areas of applications from which phosphor materials for white light emitting diodes (LEDs) is the most prominent one.[23-25]

Regarding the progress in ammonothermal synthesis of nitridosilicates and the increasing number of zeolite structures formed by this compound class, a combination of the ammonothermal synthesis and the compound class of nitridosilicates presents a promising single-step approach to obtain nitride zeolites from elemental silicon as an alternative to post-synthetic nitridation of oxide zeolites in ammonia flow or the necessity for reactive precursors such as silicon diimide in high-temperature synthesis.[26-27]

6.2 Results and Discussion

Due to the high number of reported cerium (oxo)nitridosilicates, elemental cerium and silicon were selected as starting materials for our investigations.[28-46] Surprisingly, the choice of the utilized mineralizer had a major influence on the reaction outcome and so it was possible to isolate the literature-known nitridosilicate $Ce_3[Si_6N_{11}]$ with NaN_3 as well as the novel compounds $Li_2RE_4[Si_4N_8]O_3$ (*RE* = La, Ce) with Li_3N and $K_{1.25}Ce_{7.75}[Si_{11}N_{21}O_2]O_{0.75}$ with KN_3 as respective mineralizers.[29-30] Detailed information on the synthesis is summarized in the Experimental Section. All products were obtained as well-crystallized powders with crystallite sizes of up to 100 µm (Figure 6.1). The presented compounds are insensitive towards hydrolysis and were washed with HCl for purification resulting in phase-pure samples except for $K_{1.25}Ce_{7.75}[Si_{11}N_{21}O_2]O_{0.75}$ which could only be synthesized next to an unidentified minor side phase as depicted in the Supporting Information (SI, Figure 9.4–Figure 9.6 and Figure 9.8). The oxygen content in the products arises from contaminations from the autoclave wall as already observed before in ammonothermal reactions.[11] Subsequent experiments showed that addition of oxygen-containing starting materials such as Li_2O favors the formation of the (oxo)nitridosilicate oxides $Li_2Ce_4[Si_4N_8]O_3$ and $K_{1.25}Ce_{7.75}[Si_{11}N_{21}O_2]O_{0.75}$ as main phases. The incorporation of imide groups in the structures was excluded using infrared spectroscopy where no N–H vibrations were detected (Figure 9.9). Further experiments with the three mineralizers using La instead of Ce only resulted in the corresponding lanthanum phase $Li_2La_4[Si_4N_8]O_3$ for the experiments using the mineralizer Li_3N.

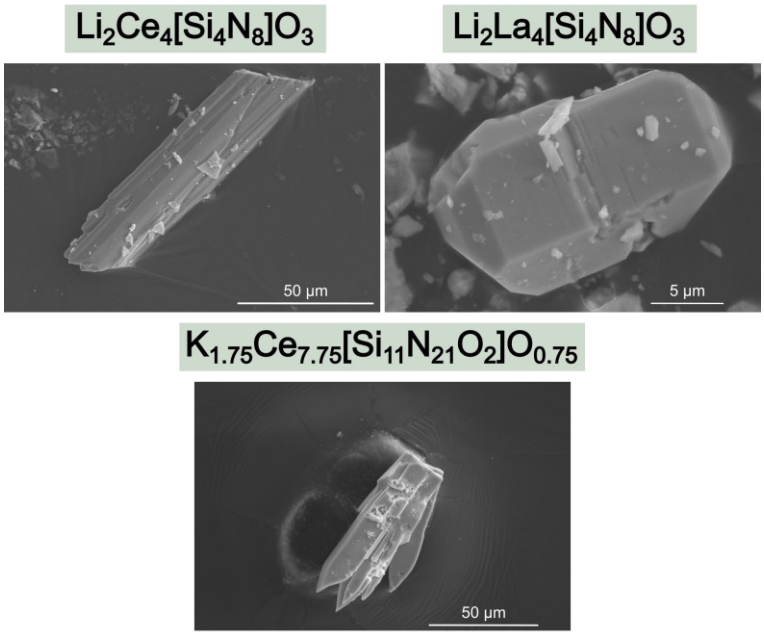

Figure 6.1: SEM images of crystallites of $Li_2RE_4[Si_4N_8]O_3$ (RE = La, Ce) and $K_{1.25}Ce_{7.75}[Si_{11}N_{21}O_2]O_{0.75}$.

The nitridosilicate oxides $Li_2RE_4[Si_4N_8]O_3$ (*RE* = La, Ce) crystallize isotypically in the BCT zeolite structure type with the highest possible symmetry of the network in space group *I*4/*mmm* (no. 139).[47] Information on the structure solution and refinements is given in Table 9.31–Table 9.38 in the SI.[48] The nitridosilicate network, which is built up from all-side vertex sharing (Q^4-type) [SiN_4] tetrahedra, forms *vierer* ring channels along [001] that are interconnected via common vertices to form *achter* ring channels.[49-50] Along [100], the tetrahedra connection results in *sechser* ring channels (Figure 6.2a, b). The *vierer* ring channels are nominally filled with Li_2O chains, as it was already observed in $Li_2Sr_4[Si_4N_8]O$ and $Li_2AE_4[Al_2Ta_2N_8]O$ (*AE* = Sr, Ba). Meanwhile, the *achter* rings are filled with cerium position Ce1 and the oxygen position O2 in the middle, which all form chains along [001].[12,51-52] Compared to $Li_2Sr_4[Si_4N_8]O$, this additional oxygen position in the *achter* rings, which is necessary to balance the higher charge of Ce^{3+} instead of Sr^{2+}, results in a more symmetric form of the *achter* rings.[12] The described anionic network results in a square pyramidal coordination of the lithium atoms and a ninefold coordination of the cerium atoms (Figure 6.2c, d). An assignment of oxygen and nitrogen positions among the anionic positions was conducted due to the shorter Li–O and Ce–O distances compared to Li–N and Ce–N distances to the closest neighboring atoms (Table 9.34) and is in accordance with literature values in nitridosilicates as well as charge distribution (CHARDI) and bond valence sum (BVS) calculations (Table 9.46 and Table 9.47).[40-41] The elemental composition was confirmed using energy-dispersive X-ray (EDX) spectroscopy (Table 9.49 and Table 9.50). Doping experiments with Ce^{3+} for the La compound $Li_2La_4[Si_4N_8]O_3$ did not result in luminescent samples. A possible reason for this might be high defect concentrations within the prepared samples due to contaminations from the autoclave wall.

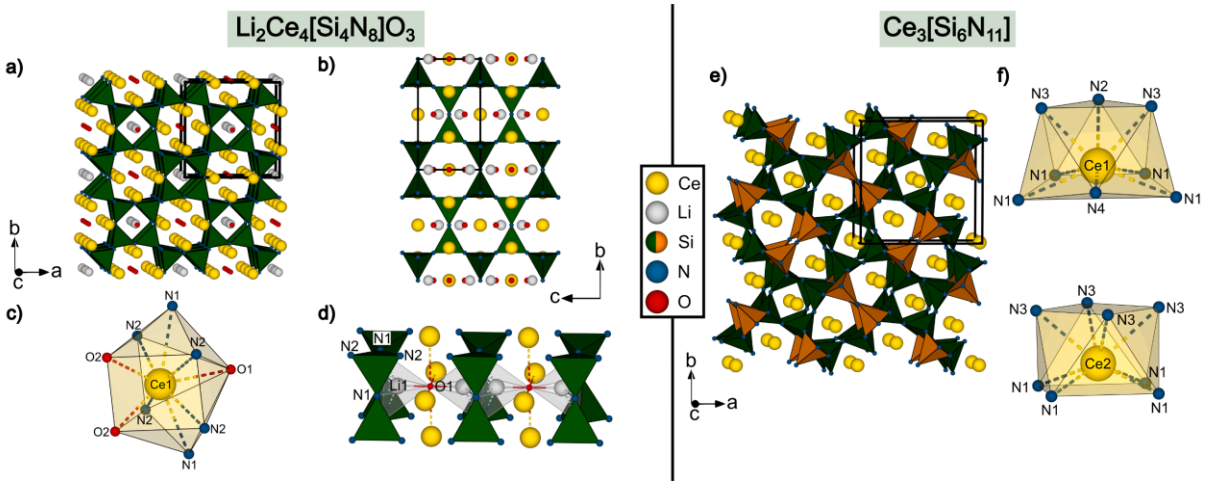

Figure 6.2: Left: Representation of the crystal structure of $Li_2Ce_4[Si_4N_8]O_3$ (a) with view along [100] (b), coordination of Ce1 and depiction of the Li_2O units in the vierer rings (d). Right: Representation of the crystal structure of $Ce_3[Si_6N_{11}]$ (e) with coordination of the cerium atoms (f).

In this study, the influence of different ammonobasic mineralizers was tested and therefore NaN_3 was used as a second mineralizer after Li_3N. Experiments employing NaN_3 yielded $Ce_3[Si_6N_{11}]$ as

main phase. The nitridosilicate known from literature forms layers of *achter* and *vierer* rings (Figure 6.2e, green tetrahedra) which are interconnected by $[Si_2N_7]$ tetrahedra double (Figure 6.2e, orange).[29-30] As the tetrahedra double bridge the achter rings, sechser ring channels are formed next to the vierer ring channels along [001] which are all filled with cerium atoms. This results in eightfold coordination of the cerium atoms as distorted bicapped trigonal prism for position Ce1 and as a tetragonal antiprism for position Ce2 (Figure 6.2f). In this experiment, no incorporation of sodium from the mineralizer was observed. A possible reason for this could be that the condensed network is already thermodynamically stable. As only one nitridosilicate containing sodium is reported in the literature, it seems that the contribution of Na incorporation in nitridosilicate environment to the lattice energy is small and therefore, it might be too small to allow for incorporation of Na in the cerium nitridosilicate network.[53]

The first potassium cerium oxonitridosilicate oxide $K_{1.25}Ce_{7.75}[Si_{11}N_{21}O_2]O_{0.75}$ known so far was isolated from experiments applying the mineralizer KN_3 and crystallizes in a highly disordered variant of the zeolite-like $Ba_2Nd_7Si_{11}N_{23}$ structure type.[21] Details on the structure refinement are summarized in Table 9.39–Table 9.45 in the SI.[48] The structure comprises an oxonitridosilicate network forming *achter* ring channels along [001] which are occupied by potassium and a semi-occupied oxygen position while a cerium split position and a mixed-occupied cerium/potassium position are observed at the edges of the *achter* ring channels (Figure 6.3a, b). Additionally, *dreier*, *vierer*, *sechser* and *siebener* rings are present in the structure. The network is built up from both Q^4-type and Q^2-type silicon-centered tetrahedra in an atomic ratio of 10:1. Therefore, $K_{1.25}Ce_{7.75}[Si_{11}N_{21}O_2]O_{0.75}$ is not a classical zeolite according to the definition of the international zeolite association (IZA) which only includes compounds built up solely from Q^4-type tetrahedra. Nevertheless, large cavities and channels are formed in the structure of $K_{1.25}Ce_{7.75}[Si_{11}N_{21}O_2]O_{0.75}$. The zeolite-like character of the network is as well illustrated by the low framework density. This measure is defined as the number of tetrahedral centers within 1000 $Å^3$. For $K_{1.25}Ce_{7.75}[Si_{11}N_{21}O_2]O_{0.75}$, a value of roughly 17.6 was calculated which is in the typical range for zeolites.[54] The terminal Q^2-type SiO_2N_2 tetrahedra are located at split position Si5A/B and show strong distortion. This may be explained by a tilting of the tetrahedra to both sides along [100] with an atomic ratio of tilted to regular positions that was refined to 34%:66% (Figure 6.3c). Such distortions and the several split positions, especially in proximity to the *achter* ring channels, were already observed before for this structure type in $Ba_{1.63}La_{7.39}Si_{11}N_{23}Cl_{0.42}:Ce^{3+}$.[22] It seems that the formation of the stable (oxo)nitridosilicate network in this structure type tolerates the incorporation of a variety of different ions filling the space left by the tetrahedra network. For $K_{1.25}Ce_{7.75}[Si_{11}N_{21}O_2]O_{0.75}$, an additional anion position O12 within the *sechser* rings along [001] is observed as well, which is neither observed in $Ba_2Nd_7[Si_{11}N_{23}]$ nor in $Ba_{1.63}La_{7.39}[Si_{11}N_{23}]Cl_{0.42}$. This additional position with an occupation fixed to 0.5 due to symmetry considerations, leads to a distortion of the *achter* rings along [010] in comparison to the other two representatives of the

structure type leaving space for the additional oxygen position (Figure 6.3d). The cerium positions in $K_{1.25}Ce_{7.75}[Si_{11}N_{21}O_2]O_{0.75}$ are coordinated by seven to nine nitrogen or oxygen atoms while the potassium position K6 within the *achter* rings is only in local proximity to the O13 position in the *achter* ring channels (Figure 6.3b and Figure 9.7). The ratio of Ce:K at the mixed-occupied position Ce/K5 was fixed to 0.75:0.25 after free refinement resulted in values close to this ratio. According to CHARDI calculations (Table 9.48) and Pauling's second rule, the terminal split positions O7A/B/C were chosen as oxygen positions within the tetrahedra network next to the extra-network oxygen positions.[55-56] These restrictions to the refinement allowed to obtain a charge-neutral sum formula which is in agreement with the results of the EDX measurements for the heavier elements (Table 9.51). The deviations from the calculated values for the lighter elements oxygen and nitrogen might arise from surface oxidation during the washing process with HCl.

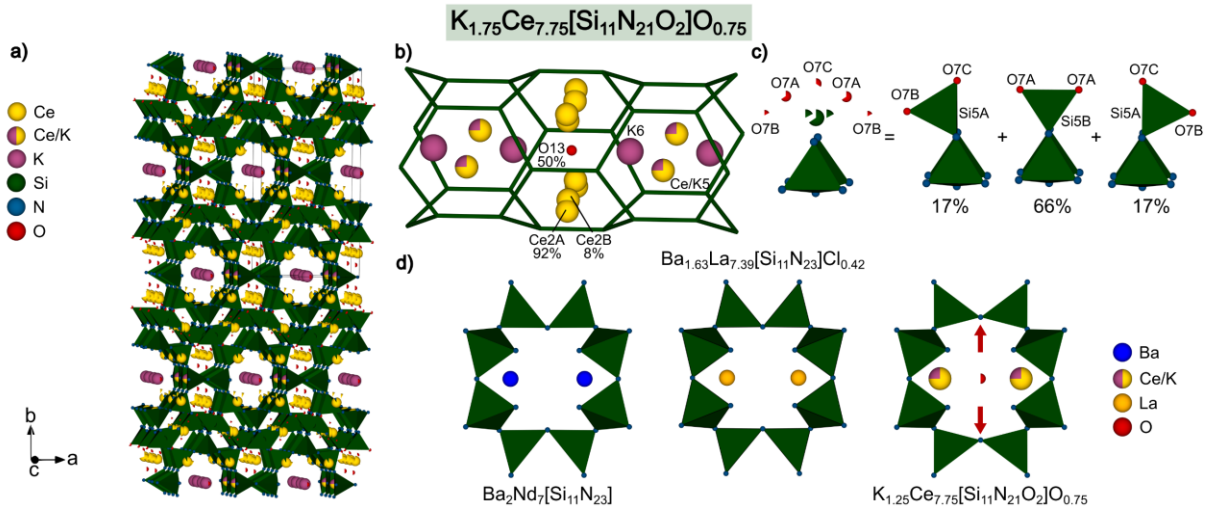

Figure 6.3: Representation of the crystal structure of $K_{1.25}Ce_{7.75}[Si_{11}N_{21}O_2]O_{0.75}$ (a) with detailed depiction of the achter ring channels (b), the distortion at positions Si5A/B (c) and comparison to the sechser rings in $Ba_2Nd_7[Si_{11}N_{23}]$ and $Ba_{1.63}La_{7.39}[Si_{11}N_{23}]Cl_{0.42}$ showing the tetrahedra tilting that allows the insertion of oxygen at the semi-occupied position O12 (d). Partially or mixed occupied positions are shown according to their site occupation factor or occupation is given in percentage.

The condensation degree κ of a network is defined as the ratio of its tetrahedral centers (here Si) to its tetrahedral vertices (here N and also O for $K_{1.25}Ce_{7.75}[Si_{11}N_{21}O_2]O_{0.75}$). For the three observed cerium compounds these condensation degrees are all close to each other and equal or close to $\kappa = 0.5$ (approx. 0.48 for $K_{1.25}Ce_{7.75}[Si_{11}N_{21}O_2]O_{0.75}$, 0.5 for $Li_2Ce_4[Si_4N_8]O_3$ and approx. 0.55 for $Ce_3[Si_6N_{11}]$). Therefore, it would be difficult to control the reaction products only by altering the weight proportions of the starting materials. Especially, since the nitrogen amount is provided in excess by the solvent ammonia during ammonothermal synthesis. Additionally, one would expect to obtain the (oxo)nitridosilicates presented in this work as well as other ternary nitridosilicates with κ-values close to 0.5 such as Li_2SiN_2 as side phases. Particularly, as the latter one has been reported as a side phase from ammonothermal syntheses earlier.[9] From the products in this work, $Ce_3Si_6N_{11}$ could theoretically be formed from the starting materials in all three synthesis attempts,

regardless of the employed mineralizer, but was only observed in experiments involving NaN_3. Here, the ammonothermal synthesis provides a useful tool to control the synthesis outcome by the utilization of mineralizers which allows to obtain not only different products as respective main phases in three different reactions despite their similar condensation degrees but also two novel quinary nitridosilicate phases. Additionally, the ammonothermal approach is the only one that allowed to stabilize potassium cations in a nitridosilicate environment, which was only observed in a single compound before, namely the imidonitridosilicate $K_3[Si_6N_5(NH)_6]$.[57] The transfer of this procedure to the lanthanum compounds led to phase-pure $Li_2La_4[Si_4N_8]O_3$ as only the second yet reported quinary phase after $LiLa_5[Si_4N_{10}O]$ containing the elements Li, La, Si, N and O and the first nitridosilicate oxide incorporating both Li and La atoms.[58]

6.3 Conclusions

Our results substantiate that the ammonothermal synthesis is a suitable tool to obtain nitride zeolites in general and especially representatives from the nitridosilicate compound class. Here, synthetic control is given by the utilization of different mineralizers towards phase-pure samples from elemental starting materials. This approach allowed the synthesis of the nitridosilicate compounds $Li_2RE_4[Si_4N_8]O_3$ (*RE* = La, Ce), $Ce_3[Si_6N_{11}]$, and $K_{1.25}Ce_{7.75}[Si_{11}N_{21}O_2]O_{0.75}$. In the context of these investigations, different unknown side phases were observed as exemplarily shown for the synthesis of $K_{1.25}Ce_{7.75}[Si_{11}N_{21}O_2]O_{0.75}$. These side phases may be accessed at different synthesis conditions or by the employment of even more different mineralizers in future investigations. While the presented study only focused on three ammonobasic mineralizers, the ammonoacidic environment seems to be worth for further investigation as well. Additionally, other elemental combinations which are rarely found in nitride environment yet, might be accessible using the ammonothermal synthesis as several quinary phases and the rare combination of K, Si and N in a single compound could be already implemented. Additionally, further characterization of magnetic and optical properties as well as ion exchange and desorption experiments with the presented compounds might pave the way for nitride zeolites towards possible applications in the future.

6.4 Experimental Section

Due to the sensitivity towards air and moisture of some starting materials, all manipulations were performed under inert gas conditions either in argon-filled glove boxes (MBraun, $O_2 < 1$ ppm, $H_2O < 1$ ppm) or using a vacuum line ($\rho \leq 0.1$ Pa) with argon and ammonia supply. The gases Ar and NH_3 (Air liquide, 99.999%) were purified with gas cartridges Micro Torr FT400-902 for Ar and Micro Torr MC400-702FV for NH_3, respectively (both SAES Pure Gas Inc.). This procedure resulted in a final purity level of < 1ppbV for H_2O, O_2 and CO_2, respectively. The amount of ammonia used for the reactions was determined with a mass flow meter D-6320-DR (Bronkhorst).

6.4.1 Ammonothermal Synthesis

The (oxo)nitridosilicates were synthesized in custom-built high-temperature autoclaves made of Haynes® 282® (max. 1100 K, 170 MPa, volume: 11 mL) equipped with a hand valve (SITEC), a bursting disk (Dieckers GmbH & Co. KG, pressure limit: 330 MPa) in a bursting disk holder (SITEC) and a pressure transmitter (HBM P2VA1/5000 bar). The autoclave design is described in the literature.[8,59] The starting materials were ground together with the respective mineralizer, filled into niobium liners and transferred into the autoclave in a glove box. The autoclave was sealed using a silver-coated Inconel® 718 ring (GFD seals) by tightening the autoclave screws. Afterwards, the autoclave was cooled using a mixture of liquid nitrogen and ethanol. Ammonia (ca. 4 mL, purification described above) was condensed in the autoclave. When the autoclave regained room temperature, it was placed in a tube furnace and heated according to the respective furnace program, reaching the respective maximum pressure. After cooling to room temperature by switching off the furnace, residual ammonia was removed from the autoclave and the reaction product was separated from the liner wall in a glove box. The samples were washed with concentrated hydrochloric acid to remove side phases.

6.4.2 Synthesis of $Li_2Ce_4[Si_4N_8]O_3$

$Li_2Ce_4[Si_4N_8]O_3$ was synthesized from filed Ce metal (abcr, 99.9%, 140.1 mg, 1.000 mmol), Si (Alfa Aesar, 99.99%, 28.1 mg, 1.00 mmol), Li_2O (Schuchardt, 98%, 22.4 mg, 0.750 mmol), and Li_3N (Alfa Aesar, 99.4%, 87.1 mg, 2.50 mmol) as a mineralizer. The autoclave was heated to 670 K in 2 h, held at that temperature for 13 h and subsequently heated to 1070 K in 3 h. The reaction temperature was held for 48 h, reaching a maximum pressure of 150 MPa, then the autoclave was cooled to 670 K in 48 h before the furnace was switched off. $Li_2Ce_4[Si_4N_8]O_3$ was received as red crystals.

6.4.3 Synthesis of $Li_2La_4[Si_4N_8]O_3$

$Li_2La_4[Si_4N_8]O_3$ was synthesized from filed La metal (smartelements, 99.9%, 208.4 mg, 1.500 mmol), Si (Alfa Aesar, 99.99%, 28.1 mg, 1.00 mmol), and Li_3N (Alfa Aesar, 99.4%, 104.5 mg, 3.000 mmol) as a mineralizer. The oxygen content arose from the autoclave wall. The autoclave was heated to 670 K in 2 h, held at that temperature for 14 h and subsequently heated to 1070 K in 3 h. The reaction temperature was held for 48 h, reaching a maximum pressure of 140 MPa, then the autoclave was cooled to 670 K in 48 h before the furnace was switched off. $Li_2La_4[Si_4N_8]O_3$ was received as red crystals.

6.4.4 Synthesis of $Ce_3[Si_6N_{11}]$

$Ce_3[Si_6N_{11}]$ was obtained ammonothermally starting from filed Ce metal (abcr, 99.9%, 140.1 mg, 1.000 mmol), Si (Alfa Aesar, 99.99%, 84.3 mg, 3.00 mmol), and NaN_3 (Sigma-Aldrich, 99.5%, 390.1 mg, 6.000 mmol). The autoclave was heated to 670 K in 2 h, held at that temperature for 12 h and subsequently heated to 1070 K in 3 h. The reaction temperature was held for 96 h,

reaching a maximum pressure of 150 MPa before the furnace was switched off. $Ce_3[Si_6N_{11}]$ was isolated from the liner as yellow powder.

6.4.5 Synthesis of $K_{1.25}Ce_{7.75}[Si_{11}N_{21}O_2]O_{0.75}$

$K_{1.25}Ce_{7.75}[Si_{11}N_{21}O_2]O_{0.75}$ was synthesized from filed Ce metal (abcr, 99.9%, 140.1 mg, 1.000 mmol), Si (Alfa Aesar, 99.99%, 38.6 mg, 1.38 mmol), and KN_3 (Sigma-Aldrich, >99.9%, 243.4 mg, 3.000 mmol) as a mineralizer. The autoclave was heated to 670 K in 2 h, held at that temperature for 13 h and subsequently heated to 1070 K in 3 h. The reaction temperature was held for 48 h, reaching a maximum pressure of 140 MPa and the autoclave was subsequently cooled to 670 K in 48 h before the furnace was switched off. $K_{1.25}Ce_{7.75}[Si_{11}N_{21}O_2]O_{0.75}$ was received as red crystals.

6.4.6 Single-Crystal X-ray Diffraction

Diffraction data of the investigated crystals were collected using a combined Φ-ω-scan on a Bruker D8 Quest diffractometer with Mo-K_α radiation (λ = 0.71073 Å). The program APEX3 was used for indexing and integration of the data, semi-empirical absorption correction (SADABS) and determination of the space group were performed in APEX3 as well.[60-61] For the solution of the structures XPREP and SHELXT were used, while the data was refined using full-matrix least-squares methods (SHELXL) in the program suite WINGX.[62-66]

6.4.7 Powder X-ray Diffraction

Powder X-ray diffraction data were collected of ground samples sealed into glass capillaries (d = 0.2 mm or 0.3 mm, wall thickness 0.01 mm, Hilgenberg GmbH) on a STOE STADI P diffractometer using Ag-$K_{\alpha1}$ radiation (λ = 0.5594217 Å) equipped with a Ge(111) monochromator and a Mythen 1K detector in modified Debye-Scherrer geometry. Rietveld refinements of the diffraction data was conducted with the software TOPAS.[67]

6.4.8 Scanning Electron Microscopy (SEM)

Electron microscope images of the crystallites and energy dispersive X-ray (EDX) spectroscopy data were collected using a Dualbeam Helios Nanolab G3UC (FEI) electron microscope equipped with an X-Max80 SSD detector (Oxford instruments). The samples were fixed on an aluminum holder using carbon foil and carbon-coated using a high-vacuum sputter coater (CCU-010, Safematic GmbH) to prevent electrostatic charging and subsequently transferred to the electron microscope.

6.4.9 Fourier-Transform Infrared (FTIR) Spectroscopy

The FTIR spectroscopy data were collected using the program OPUS 8.7 and an Alpha II FTIR spectrometer (Bruker) equipped with a diamond attenuated total reflectance (ATR) unit.[68] The spectra were recorded in the range of 400–4000 cm^{-1} with a resolution of 2 cm^{-1} at ambient temperature under argon atmosphere.

6.5 Acknowledgements

The authors thank Christian Minke, Dr. Lisa Gamperl and Amalina Buda for the collection of SEM images and EDX data. Additionally, Dr. Peter Mayer's (all at Department of Chemistry, LMU Munich) contribution to this work in form of the conduction of the single-crystal X-ray diffraction measurements is gratefully acknowledged.

6.6 References

[1] J. Čejka, A. Corma, S. Zones (Eds.), "Zeolites and Catalysis: Synthesis, Reactions and Applications", *Vol. 1*, Wiley-VCH Verlag GmbH & Co.KGaA, Weinheim, **2010**.

[2] C. S. Cundy, P. A. Cox, "The Hydrothermal Synthesis of Zeolites: History and Development from the Earliest Days to the Present Time", *Chem. Rev. (Washington, DC, U. S.)* **2003**, *103*, 663−702.

[3] C. S. Cundy, P. A. Cox, "The hydrothermal synthesis of zeolites: Precursors, intermediates and reaction mechanism", *Microporous Mesoporous Mater.* **2005**, *82*, 1−78.

[4] J. Li, A. Corma, J. Yu, "Synthesis of new zeolite structures", *Chem. Soc. Rev.* **2015**, *44*, 7112−7127.

[5] R. Niewa in: "*Ammonothermal Synthesis and Crystal Growth of Nitrides – Chemistry and Technology*" (Eds.: E. Meissner, R. Niewa), Springer, Cham, **2021**, pp. 3−12.

[6] T. M. M. Richter, R. Niewa, "Chemistry of Ammonothermal Synthesis", *Inorganics* **2014**, *2*, 29−78.

[7] J. Häusler, S. Schimmel, P. Wellmann, W. Schnick, "Ammonothermal Synthesis of Earth-Abundant Nitride Semiconductors $ZnSiN_2$ and $ZnGeN_2$ and Dissolution Monitoring by In Situ X-ray Imaging", *Chem. Eur. J.* **2017**, *23*, 12275−12282.

[8] J. Häusler, L. Neudert, M. Mallmann, R. Niklaus, A.-C. L. Kimmel, N. S. A. Alt, E. Schlücker, O. Oeckler, W. Schnick, "Ammonothermal Synthesis of Novel Nitrides: Case Study on $CaGaSiN_3$", *Chem. Eur. J.* **2017**, *23*, 2583−2590.

[9] J. Häusler, R. Niklaus, J. Minár, W. Schnick, "Ammonothermal Synthesis and Optical Properties of Ternary Nitride Semiconductors Mg-*IV*-N_2, Mn-*IV*-N_2 and Li-IV_2-N_3 (*IV*=Si, Ge)", *Chem. Eur. J.* **2018**, *24*, 1686−1693.

[10] M. Mallmann, R. Niklaus, T. Rackl, M. Benz, T. G. Chau, D. Johrendt, J. Minár, W. Schnick, "Solid Solutions of Grimm-Sommerfeld Analogous Nitride Semiconductors *II*-*IV*-N_2 with *II* = Mg, Mn, Zn; *IV* = Si, Ge – Ammonothermal Synthesis and DFT Calculations", *Chem. Eur. J.* **2019**, *25*, 15887–15895.

[11] M. Mallmann, C. Maak, W. Schnick, "Ammonothermal Synthesis and Crystal Growth of the Chain-type Oxonitridosilicate $Ca_{1+x}Y_{1-x}SiN_{3-x}O_x$ ($x > 0$)", *Z. Anorg. Allg. Chem.* **2020**, *646*, 1539–1544.

[12] S. Pagano, S. Lupart, M. Zeuner, W. Schnick, "Tuning the Dimensionality of Nitridosilicates in Lithium Melts", *Angew. Chem.* **2009**, *121*, 6453–6456; *Angew. Chem. Int. Ed.* **2009**, *48*, 6335–6338.

[13] W. Schnick in: "*Zeolites and Related Microporous Materials: State of the Art 1994*", *Vol. 84* (Eds.: J. Weitkamp, H.G. Karge, H. Pfeifer, W. Hölderich), **1994**, pp. 2221−2228.

[14] S. Correll, O. Oeckler, N. Stock, W. Schnick, "$LiH_{12-x-y+z}[P_{12}O_yN_{24-y}]Cl_z$ — An Oxonitridophosphate with a Zeolitelike Framework Structure Composed of 3-Rings", *Angew. Chem.* **2003**, *115*, 3674–3677; *Angew. Chem. Int. Ed.* **2003**, *42*, 3549–3552.

[15] S. J. Sedlmaier, M. Döblinger, O. Oeckler, J. Weber, J. Schmedt auf der Günne, W. Schnick, "Unprecedented Zeolite-Like Framework Topology Constructed from Cages with 3-Rings in a Barium Oxonitridophosphate", *J. Am. Chem. Soc.* **2011**, *133*, 12069–12078.

[16] A. J. D. Barnes, T. J. Prior, M. G. Francesconi, "Zeolite-like nitride–chlorides with a predicted topology", *Chem. Commun.* **2007**, 4638–4640.

[17] S. Pagano, O. Oeckler, T. Schröder, W. Schnick, "$Ba_6Si_6N_{10}O_2(CN_2)$ – A Nitridosilicate with a NPO-Zeolite Structure Type Containing Carbodiimide Ions", *Eur. J. Inorg. Chem.* **2009**, 2678–2683.

[18] A. Marchuk, W. Schnick, "$Ba_3P_5N_{10}Br:Eu^{2+}$: A Natural-White-Light Single Emitter with a Zeolite Structure Type", *Angew. Chem.* **2015**, *127*, 2413–2417; *Angew. Chem. Int. Ed.* **2015**, *54*, 2383–2387.

[19] S. Wendl, M. Zipkat, P. Strobel, P. J. Schmidt, W. Schnick, "Synthesis of Nitride Zeolites in a Hot Isostatic Press", *Angew. Chem.* **2021**, *133*, 4520–4523; *Angew. Chem. Int. Ed.* **2021**, *60*, 4470–4473.

[20] K. Horky, W. Schnick, "$LiCa_4Si_4N_8F$ and $LiSr_4Si_4N_8F$: Nitridosilicate Fluorides with a BCT-Zeolite-Type Network Structure", *Eur. J. Inorg. Chem.* **2017**, *7*, 1107–1112.

[21] H. Huppertz, W. Schnick, "$Ba_2Nd_7Si_{11}N_{23}$ — A Nitridosilicate with a Zeolite-Analogous Si–N Structure", *Angew. Chem.* **1997**, *109*, 2765–2767; *Angew. Chem. Int. Ed.* **1997**, *36*, 2651–2652.

[22] P. Schultz, D. Durach, W. Schnick, O. Oeckler, "$Ba_{1.63}La_{7.39}Si_{11}N_{23}Cl_{0.42}:Ce^{3+}$ – A Nitridosilicate Chloride with a Zeolite-Like Structure", *Z. Anorg. Allg. Chem.* **2016**, *642*, 603–608.

[23] M. Zeuner, S. Pagano, W. Schnick, "Nitridosilicates and Oxonitridosilicates: From Ceramic Materials to Structural and Functional Diversity", *Angew. Chem.* **2011**, *123*, 7898–7920; *Angew. Chem. Int. Ed.* **2011**, *50*, 7754–7775.

[24] S.-L. Chung, S.-C. Huang, W.-C. Chou, W. W. Tangguh, "Phosphors based on nitridosilicates: synthesis methods and luminescent properties", *Curr. Opin. Chem. Eng.* **2014**, *3*, 62–67.

[25] N. Hirosaki, T. Takeda, S. Funahashi, R.-J. Xie, "Discovery of New Nitridosilicate Phosphors for Solid State Lighting by the Single-Particle-Diagnosis Approach", *Chem. Mater.* **2014**, *26*, 4280–4288.

[26] M. Srasra, S. Delsarte, E. M. Gaigneaux, "Nitrided Zeolites: A Spectroscopic Approach for the Identification and Quantification of Incorporated Nitrogen Species", *J. Phys. Chem. C* **2010**, *114*, 4527–4535.

[27] W. Schnick, H. Huppertz, "Nitridosilicates – A Significant Extension of Silicate Chemistry", *Chem. Eur. J.* **1997**, *3*, 679–683.

[28] P. E. D. Morgan, P. J. Carroll, "The crystal structures of $CeSiO_2N$ and $LaSiO_2N$", *J. Mater. Sci.* **1977**, *12*, 2343–2344.

[29] T. Schlieper, W. Schnick, "Nitrido-silicate. III. Hochtemperatur-Synthese, Kristallstruktur und magnetische Eigenschaften von Ce3[Si6N11]", *Z. Anorg. Allg. Chem.* **1995**, *621*, 1535–1538.

[30] M. Woike, W. Jeitschko, "Preparation and Crystal Structure of the Nitridosilicates $Ln_3Si_6N_{11}$ (*Ln* = La, Ce, Pr, Nd, Sm) and $LnSi_3N_5$ (*Ln* = Ce, Pr, Nd)", *Inorg. Chem.* **1995**, *34*, 5105–5108.

[31] M. Woike, W. Jeitschko, "Crystal structure of cerium silicon nitride (1/3/5), $CeSi_3N_5$", *Z. Kristallogr.* **1996**, *211*, 813–813.

[32] K. Köllisch, W. Schnick, "$Ce_{16}Si_{15}O_6N_{32}$ – An Oxonitridosilicate with Silicon Octahedrally Coordinated by Nitrogen", *Angew. Chem.* **1999**, *111*, 368–370; *Angew. Chem. Int. Ed.* **1999**, *38*, 357–359.

[33] E. Irran, K. Köllisch, S. Leoni, R. Nesper, P. F. Henry, M. T. Weller, W. Schnick, "$Ce_4[Si_4O_4N_6]O$-A Hyperbolically Layered Oxonitridosilicate Oxide with an Ordered Distribution of Oxygen and Nitrogen", *Chem. Eur. J.* **2000**, *6*, 2714–2720.

[34] A. Lieb, W. Schnick, "$Ce_{10}[Si_{10}O_9N_{17}]Br$, $Nd_{10}[Si_{10}O_9N_{17}]Br$ and $Nd_{10}[Si_{10}O_9N_{17}]Cl$ oxonitridosilicate halides with a new layered structure type", *J. Solid State Chem.* **2005**, *178*, 3323–3335.

[35] A. Lieb, M. T. Weller, P. F. Henry, R. Niewa, R. Pöttgen, R.-D. Hoffmann, H. E. Höfer, W. Schnick, "Oxonitridosilicate chlorides — synthesis, single-crystal X-ray and neutron powder diffraction, chemical analysis and properties of $Ln_4[Si_4O_{3+x}N_{7-x}]Cl_{1-x}O_x$ with *Ln*=Ce, Pr, Nd and x≈0.2", *J. Solid State Chem.* **2005**, *178*, 976–988.

[36] C. Schmolke, D. Bichler, D. Johrendt, W. Schnick, "Synthesis and crystal structure of the first chain-type nitridosilicates $RE_5Si_3N_9$ (RE=La, Ce)", *Solid State Sci.* **2009**, *11*, 389–394.

[37] C. Schmolke, O. Oeckler, D. Bichler, D. Johrendt, W. Schnick, "Complex Interrupted Tetrahedral Frameworks in the Nitridosilicates $M_7Si_6N_{15}$ (M=La, Ce, Pr)", *Chem. Eur. J.* **2009**, *15*, 9215–9222.

[38] Juliane A. Kechele, C. Schmolke, S. Lupart, W. Schnick, "$Ln_3[SiON_3]O$ (*Ln* = La, Ce, Pr) – Three Oxonitridosilicate Oxides with Crystal Structures Derived from the Anti-Perovskite Structure Type", *Z. Anorg. Allg. Chem.* **2010**, *636*, 176–182.

[39] S. Lupart, M. Zeuner, S. Pagano, W. Schnick, "Chain-Type Lithium Rare-Earth Nitridosilicates – $Li_5Ln_5Si_4N_{12}$ with Ln = La, Ce", *Eur. J. Inorg. Chem.* **2010**, *2010*, 2636–2641.

[40] S. Lupart, D. Durach, W. Schnick, "$Li_{35}Ln_9Si_{30}N_{59}O_2F$ with *Ln* = Ce, Pr – Highly Condensed Nitridosilicates", *Z. Anorg. Allg. Chem.* **2011**, *637*, 1841–1844.

[41] S. Lupart, G. Gregori, J. Maier, W. Schnick, "$Li_{14}Ln_5[Si_{11}N_{19}O_5]O_2F_2$ with Ln = Ce, Nd — Representatives of a Family of Potential Lithium Ion Conductors", *J. Am. Chem. Soc.* **2012**, *134*, 10132–10137.

[42] N. C. George, A. Birkel, J. Brgoch, B.-C. Hong, A. A. Mikhailovsky, K. Page, A. Llobet, R. Seshadri, "Average and Local Structural Origins of the Optical Properties of the Nitride Phosphor $La_{3-x}Ce_xSi_6N_{11}$ ($0 < x \leq 3$)", *Inorg. Chem.* **2013**, *52*, 13730–13741.

[43] W. B. Park, Y. S. Jeong, S. P. Singh, K.-S. Sohn, "A Yellow-Emitting Oxynitride Phosphor: $Ce_{4-x}Ca_xSi_{12}O_{3+x}N_{18-x}:Eu^{2+}$", *ECS J. Solid State Sci. Technol.* **2013**, *2*, R3100.

[44] C. Maak, P. Strobel, V. Weiler, P. J. Schmidt, W. Schnick, "Unprecedented Deep-Red Ce^{3+} Luminescence of the Nitridolithosilicates $Li_{38.7}RE_{3.3}Ca_{5.7}[Li_2Si_{30}N_{59}]O_2F$ (*RE* = La, Ce, Y)", *Chem. Mater.* **2018**, *30*, 5500–5506.

[45] H.-W. Zheng, X.-M. Wang, H.-W. Wei, Y. Zheng, C.-L. Yin, Z.-P. Yang, H. Jiao, "Narrow-band red emitting oxonitridosilicate phosphor $La_{4-x}Sr_{2+x}Si5N_{12-x}O_x:Pr^{3+}$ ($x \approx 1.69$)", *Chem. Commun.* **2021**, *57*, 3761–3764.

[46] L. Gamperl, P. Strobel, P. J. Schmidt, W. Schnick, "Synthesis and Luminescence Properties of Amber Emitting $La_7Sr[Si_{10}N_{19}O_3] : Eu^{2+}$ and Syntheses of the Substitutional Variants $RE_{8-x}AEx[Si_{10}N_{20-x}O_{2+x}] : Eu^{2+}$ with *RE*=La, Ce; *AE*=Ca, Sr, Ba; $0 \leq x \leq 2$", *Chem. Eur. J.* **2022**, *28*, e202200760.

[47] W. A. Dollase, C. R. Ross, "Crystal structures of body-centered tetragonal tectosilicates: $K_{1.14}Mg_{0.57}Si_{1.43}O_4$, $K_{1.10}Zn_{0.55}Si_{1.45}O_4$, and $K_{1.11}Fe_{1.11}Si_{0.89}O_4$", *Am. Mineral.* **1993**, *78*, 627–632.

[48] Deposition Numbers 2390327 for $Li_2La_4[Si_4N_8]O_3$, 2390328 for $Li_2Ce_4[Si_4N_8]O_3$ and 2390329 for $K_{1.25}Ce_{7.75}[Si_{11}N_{21}O_2]O_{0.75}$ contain the supplementary crystallographic data for this paper. These data are provided free of charge by the joint Cambridge Crystallographic Data Centre and Fachinformationszentrum Karlsruhe Access Structures service.

[49] The terms *dreier*, *vierer*, *sechser*, *siebener* and *achter* rings were coined by Liebau and are derived from the German words„dreier, vierer, sechser, siebener and achter“; a *dreier* ring comprises three tetrahedra centers,a *vierer* ring four tetrahedra centers, and so on.

[50] F. Liebau, "Structural Chemistry of Silicates", Springer, Berlin, **1985**.

[51] P. Pust, W. Schnick, "$Li_2Sr_4Al_2Ta_2N_8O$, a Nitridoalumotantalate with BCT-Zeolite Type Structure", *Z. Anorg. Allg. Chem.* **2012**, *638*, 352–356.

[52] D. S. Wimmer, M. Seibald, D. Baumann, K. Wurst, H. Huppertz, "$Li_2Ba_4Al_2Ta_2N_8O$, the First Barium Nitridoalumotantalate with BCT-Zeolite Type Structure", *Chem. Eur. J.* **2023**, *29*, e202202448.

[53] H. Jacobs, H. Mengis, "Preparation and Crystal Structure of a Sodium Silicon Nitride, $NaSi_2N_3$", *Eur. J. Solid State Inorg. Chem.* **1993**, *30*, 45–53.

[54] C. Baerlocher, L. B. McCusker, D. H. Olson, "Atlas of Zeolite Framework Types", 6th ed., Elsevier, Amsterdam, **2007**.

[55] L. Pauling, "The principles determining the structure of complex ionic crystals", *J. Am. Chem. Soc.* **1929**, *51*, 1010–1026.

[56] A. Fuertes, "Prediction of Anion Distributions Using Pauling's Second Rule", *Inorg. Chem.* **2006**, *45*, 9640–9642.

[57] D. Peters, E. F. Paulus, H. Jacobs, "Darstellung und Kristallstruktur eines Kaliumimidonitridosilicats, $K_3Si_6N_5(NH)_6$", *Z. Anorg. Allg. Chem.* **1990**, *584*, 129–137.

[58] S. Lupart, W. Schnick, "$LiLa_5Si_4N_{10}O$ and $LiPr_5Si_4N_{10}O$ – Chain-Type Oxonitridosilicates", *Z. Anorg. Allg. Chem.* **2012**, *638*, 94–97.

[59] E. Meissner, R. Niewa, (Eds.), "Ammonothermal Synthesis and Crystal Growth of Nitrides – Chemistry and Technology", Springer, Cham, **2021**.

[60] Bruker-AXS, *APEX3*, Vers.2016.5-0, Karlsruhe, Germany, **2016**.

[61] G. M. Sheldrick, *SADABS*: Multi-Scan Absorption Correction, 2016-2, Bruker-AXS, Madison, WI, USA, **2012**.

[62] Bruker-AXS, *XPREP*: Reciprocal Space Exploration, Vers.6.12, Karlsruhe, Germany, **2001**.

[63] G. M. Sheldrick, *SHELXT 2018/2*: A programm for crystal structure solution, University of Göttingen, Germany, **2018**.

[64] G. M. Sheldrick, "SHELXT - Integrated space-group and crystal-structure determination", *Acta Crystallogr., Sect. A: Found. Adv.* **2015**, *71*, 3–8.

[65] G. M. Sheldrick, *SHELXL-2018/3*: A programm for crystal structure refinement, University of Göttingen, Germany, **2018**.

[66] G. M. Sheldrick, "Crystal structure refinement with SHELXL", *Acta Crystallogr., Sect. C: Cryst. Struct. Commun.* **2015**, *71*, 3–8.

[67] A. Coelho, *TOPAS Academic*, Version 6, Coelho Software, Brisbane, Australia, **2016**.

[68] Bruker Optik GmbH, *OPUS V8.7*, Ettlingen, Germany, **2012**.

7 Summary

This cumulative dissertation presents explorative research using the ammonothermal synthesis as central method. Employing custom-built high-pressure autoclaves, it was possible to obtain different amide, imide nitride, oxide nitride, and pure nitride compounds using different starting materials and mineralizers. The potential of this approach to access a variety of structural features is demonstrated by the structural characterization of these different compounds. Especially for the compound class of nitridosilicates, a universal ammonothermal synthesis access is presented.

The combination of several analytical methods allowed the determination of the different anionic species amide, imide, oxide, and nitride ions within the synthesized compounds. This comprehensive characterization of the synthesis product results in some benchmark values which might be useful during the analysis of similar nitride-based compounds in the future.

The findings contribute not only to a better understanding of intermediate species formed during the complex and only rarely understood dissolution processes at ammonothermal conditions, but also showcase possible diverse application possibilities of the method for the production of functional nitride materials. Additionally, synthetic control during ammonothermal reactions was improved by choosing suitable starting materials and mineralizers.

In the following, the content of the different chapters is summarized in brief providing an overview of the respective results as well as an indication on their publication in peer-reviewed scientific journals.

7.1 Ammonothermal Synthesis and Crystal Structure of the Ternary Amide $Na_2Ba(NH_2)_4$

Published in: F.M. Engelsberger, K. Witthaut, W. Schnick, *Z. Anorg. Allg. Chem.* **2024**, *650*, e202400053

Access via: 10.1002/zaac.202400053

Reprinted at: Chapter 2, Supporting Information at Chapter 9.2

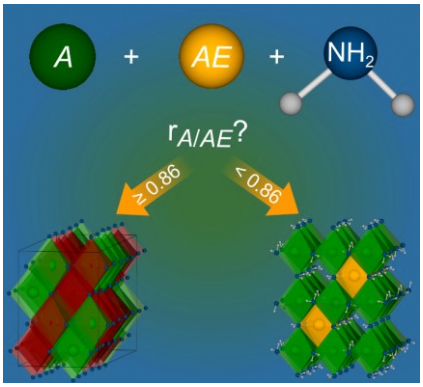

Ternary amides consisting of an alkali metal and an alkaline earth metal are commonly prepared using the ammonothermal technique. The new member $Na_2Ba(NH_2)_4$ was synthesized at ammonothermal conditions (870 K, 135 MPa) employing custom-built high-pressure autoclaves. The structural characterization of the compound using X-ray diffraction showed that it crystallizes in space group *Pccn* (no. 56) with lattice parameters $a = 10.6492(2)$, $b = 7.8064(2)$ and $c = 8.1046(2)$ Å. The structure can be described as a defective variant of the NaCl structure type showing an ordering in the occupation of the octahedral voids. This is, to the best of our knowledge, the first time that this structure type is observed in ternary amides. The amide ions in the structure were detected using Fourier-transform infrared (FTIR) spectroscopy. A comparison of the experimental spectrum to a theoretical spectrum obtained from density functional theory (DFT) calculations together with literature values for the side phase $NaNH_2$ allowed to assign the different vibration modes of $NaBa(NH_2)_4$. This newest member complements the range of reported ternary alkali metal alkaline earth metal amides with the smallest ion radius ratio of $r_{A/AE} = 0.76$. A structural classification of these ternary amides is performed and the $r_{A/AE}$ was identified as structure-directing value which may as well allow the prediction of structure types for the ternary amides in the future. The isolation and characterization of such intermediate species formed during the ammonothermal synthesis is crucial for an improved understanding of dissolution mechanisms at ammonothermal conditions and may be useful for the synthetic control during the formation of nitrides.

7.2 Ammonothermal Synthesis of Luminescent Imidonitridophosphate $Ba_4P_4N_8(NH)_2:Eu^{2+}$

Published in: F.M. Engelsberger, R.M. Pritzl, J. Steinadler, K. Witthaut, T. Bräuniger, P.J. Schmidt, W. Schnick, *Chem. Eur. J.* **2024**, *30*, e202402743

Access via: 10.1002/chem.202402743

Reprinted at: Chapter 3, Supporting Information at Chapter 9.3

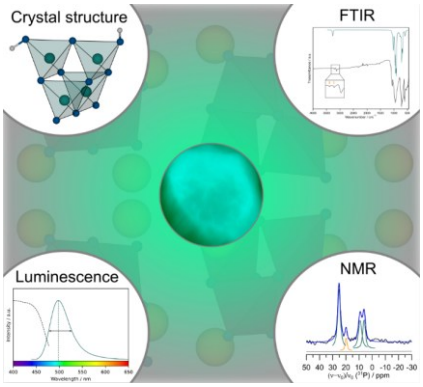

Imidonitridophosphates are a structurally versatile compound class which recently came into focus of research on phosphor-converted light-emitting diodes (pcLEDs). $Ba_4P_4N_8(NH)_2:Eu^{2+}$ presents another representative of this compound class and the first imidonitridophosphate which could be prepared ammonothermally without the incorporation of amide ions. The crystal structure of $Ba_4P_4N_8(NH)_2$ is elucidated by X-ray diffraction and it crystallizes in space group *Cc* (no. 9) with lattice parameters $a = 12.5250(3)$, $b = 12.5566(4)$, $c = 7.3882(2)$ Å, and $\beta = 102.9793(10)°$. The structure comprises adamantane-type (imido)nitridophosphate anions $[P_4N_8(NH)_2]^{8-}$ for the first time next to metal ions other than the alkali metals. A multi-step analytical process combining quantum chemical calculations, FTIR, and solid-state NMR spectroscopy, allowed the verification of imide groups in the structure as well as the identification of preferred imide positions among the different crystallographic nitrogen positions. The optical properties of Eu^{2+} doped samples were investigated using luminescence spectroscopy and show a narrow-band emission in the cyan range of the visible spectrum ($\lambda_{max} = 498$ nm, *fwhm* = 50 nm/1981 cm^{-1}). Additionally, a first impressive benchmark value for the internal quantum efficiency (IQE) of 41 % was determined for imidonitridophosphates in $Ba_4P_4N_8(NH)_2:Eu^{2+}$. Despite showing the highest ratio of imide ions among the luminescent imidonitridophosphates, which was considered to be hindering the observation of luminescence, $Ba_4P_4N_8(NH)_2$ shows a efficient luminescence. The results present another step towards industrial application of imidonitridophosphates due to the accessibility of larger amounts of the compound by the ammonothermal approach compared to the multianvil technique which produced most representatives of this compound class until now.

7.3 Ammonothermal Synthesis and Solid-State NMR Study of the Imidonitridosilicate $Rb_3Si_6N_5(NH)_6$

Published in: F.M. Engelsberger, T.G. Chau, T. Bräuniger, W. Schnick, *Chem. Eur. J.* **2024**, *30*, e202401238

Access via: 10.1002/chem.202401238

Reprinted at: Chapter 4, Supporting Information at Chapter 9.4

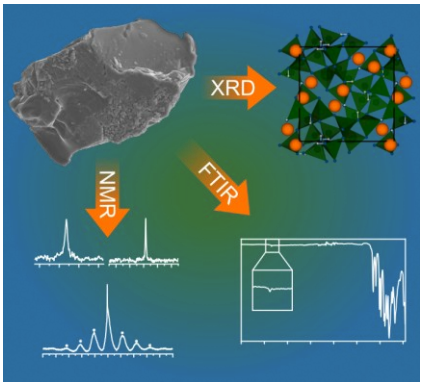

Imidonitridosilicates represent a compound class which is until now only accessible using the ammonothermal synthesis. $Rb_3Si_6N_5(NH)_6$, being only the second representative of this compound class, was synthesized ammonothermally at 870 K and 230 MPa. The elucidation of its crystal structure was performed using X-ray diffraction and revealed a structure model in space group $P4_132$ with the lattice parameter a = 10.9422(4) Å. $Rb_3Si_6N_5(NH)_6$ shows an isotypic structure to the respective potassium compound comprising a three-dimensional tetrahedra-based network. To verify the presence of imide ions within the structure, FTIR and magic-angle spinning (MAS) NMR spectroscopy, using cross polarization $^{15}N\{^1H\}$ and $^{29}Si\{^1H\}$ experiments, were performed. From the latter, a first benchmark value for a ^{15}N chemical shift in nitridosilicate environment could be determined due to the special circumstances in the crystal structure of $Rb_3Si_6N_5(NH)_6$. The compound represents a possible intermediate during the ammonothermal synthesis of nitridosilicates and is one of the rare examples where rubidium ions could be stabilized in nitride environment. This shows the potential of ammonothermal synthesis to enable rare element combinations in nitride materials and provides insights into the reaction pathway from ammonothermal solutions toward nitrides in general and especially for the nitridosilicates.

7.4 Synthesis of Known Nitridosilicate Compounds Using the Ammonothermal Technique

Unpublished results

Printed at: Chapter 5, Supporting Information at Chapter 9.5

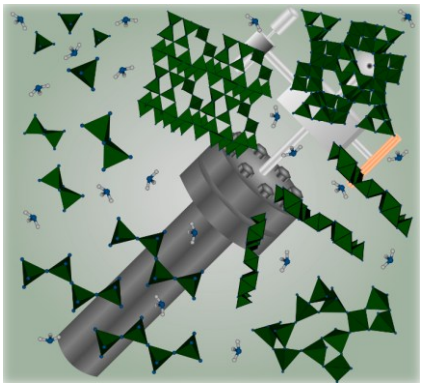

Nitridosilicate compounds represent one of the best-investigated compound classes among the nitrides. In analogy to the oxosilicates, they form a variety of different crystal structures comprising SiN_4 tetrahedra as a central building block. Here, the first ammonothermal preparations of the literature-known nitridosilicate compounds $AESiN_2$ (*AE* = Sr, Ba), $Li_2CaSi_2N_4$ and $Ba_2AlSi_5N_9$ is reported. Their identification among the products was performed using X-ray diffraction. The synthesized nitridosilicates comprise structural motifs, namely tetrahedra layers and complex three-dimensional networks, which were not observed from ammonothermal reactions before. Together with preliminary work, this shows that the ammonothermal method offers a universal approach towards the high structural variability of nitridosilicate compounds. Additionally, the results show that the selection of starting materials allows the preparation of ternary nitrides but at the same time, their formation can be circumvented to yield phase-pure quaternary nitridosilicate compounds. This is an advantage of the ammonothermal method compared to other synthesis methods where often binary or ternary nitrides are preferably formed over quaternary compounds. Furthermore, this ammonothermal access towards nitridosilicates enables a drastic reduction of the synthesis temperature compared to the established high-temperature routes.

7.5 Nitride Zeolites from Ammonothermal Synthesis

Published in: F.M. Engelsberger, W. Schnick, *Chem. Eur. J.* **2024**, e202404405

Access via: 10.1002/chem.202404405

Reprinted at: Chapter 6, Supporting Information at Chapter 9.6

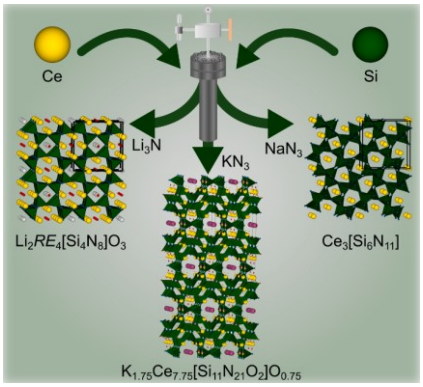

Zeolite structures comprise large cavities which enable a huge variety of different applications. Therefore, a universal access towards this class of materials is desirable. For oxide zeolites, an established preparation employs the hydrothermal synthesis. In this chapter, a transfer of this solvothermal approach towards nitride zeolites is presented which involves the highly reactive solvent supercritical ammonia. The ammonothermal synthesis of the (oxo)nitridosilicate compounds $Ce_3[Si_6N_{11}]$, $Li_2RE_4[Si_4N_8]O_3$ (*RE* = La, Ce), and $K_{1.25}Ce_{7.75}[Si_{11}N_{21}O_2]O_{0.75}$ shows as a proof of principle that different zeolite-like structures can be prepared from this method. The compounds are structurally characterized using X-ray diffraction. Their crystal structures contain a wide range of different ring sizes within their tetrahedral networks which form the channels and cavities that are usually observed in zeolites. The elemental composition of all compounds was investigated using energy-dispersive X-ray (EDX) spectroscopy. The structural model and incorporation of oxide rather than imide functionality was confirmed by FTIR spectroscopy as well as by charge distribution (CHARDI) and bond valence sum (BVS) calculations. Synthetic control over the reaction outcome is given within the ammonothermal method by the selection of the mineralizer. So, for the three different mineralizers NaN_3, Li_3N, and KN_3, the three mentioned nitridosilicate compounds were obtained as main product, respectively. This might be useful for the conceptualization of future syntheses regarding the similar degrees of condensation in the three compounds. The presented examples therefore demonstrate that ammonothermal synthesis provides a one-step access from elemental starting materials towards nitride zeolites.

8 Conclusions and Outlook

This dissertation deals with the explorative ammonothermal synthesis of multinary amide, imide and nitride compounds. The presented results can be subdivided into three main topics that are addressed. The first topic is the synthesis and structural investigation of ternary mixed alkali metal alkaline earth metal amides, for which a new representative $Na_2Ba(NH_2)_4$ could be prepared as described in Chapter 2. The following Chapters 3 and 4 cover the ammonothermal synthesis of novel imide nitrides $Ba_4P_4N_8(NH)_2$ and $Rb_3Si_6N_5(NH)_6$ as well as the characterization of their properties as members of this scarcely investigated compound class. The last part of the dissertation aims to establish an ammonothermal access towards the structurally versatile compound class of nitridosilicates. The imidonitridosilicate $Rb_3Si_6N_5(NH)_6$ serves here as a bridging compound as it might be formed as an intermediate species during the formation of nitridosilicates. Building on the preliminary work on ammonothermal preparations of silicon-containing compounds, Chapter 5 establishes a general synthesis approach to many structural motifs in nitridosilicate compounds. This approach is then used and further extended to the preparation of novel nitridosilicate compounds $Li_2RE_4[Si_4N_8]O_3$ (RE = La, Ce) and $K_{1.25}Ce_{7.75}[Si_{11}N_{21}O_2]O_{0.75}$ in Chapter 6.

8.1 Ternary Amides

The preparation of well-crystallized amides was one of the initial motifs for the development of the ammonothermal method.[1] This is as well reflected in the group of ternary mixed alkali metal alkaline earth metal amides which were mainly prepared using this synthesis method by Jacobs and coworkers.[2-9] The preparation of the ternary amide $Na_2Ba(NH_2)$ therefore complements an already well-investigated compound class. A main outcome of Chapter 2 is represented in the compilation of Table 2.1 which is reprinted here again. Within this representation, the correlation of the ion radius ratio of the alkali metal and the alkaline earth metal $r_{A/AE}$ and the formed crystal structure becomes evident. This time-honored concept establishes $Na_2Ba(NH_2)_4$ as the new endpoint of this series with the lowest value of $r_{A/AE}$ = 0.76. This low value comes with a new structure type exhibiting an ordering in the occupation of octahedral voids which has not been observed before in ternary amides.

The relevance of the comprehensive investigation of ternary amide species arises from the utilization of mineralizing agents during the ammonothermal process. As mainly alkali metal compounds are used during ammonobasic preparations, an improved understanding of possible intermediate species formed during the dissolution of alkaline earth metals might enable an increased synthetic control during ammonothermal preparations. Additionally, the classification according to the $r_{A/AE}$ presents a useful tool for the structural prediction of novel ternary mixed alkali metal alkaline earth metal amides in the future. Furthermore, the preparation of

$Na_2Ba(NH_2)_4$ shows that in well-investigated compound classes novel representatives can be found, even 40 years after the last report on a new representative of these ternary amides.

Table 2.1: Summary of the Shannon radii ratios of the ternary A-AE-amides and their respective crystal structure features.

Formula	Ratio $r_{A/AE}$ of ionic radii A^+/AE^{2+}[10]	Structural group and structure type description
$RbBe(NH_2)_3$[11]	3.38	1 – Isolated trigonal planar units
$KBe(NH_2)_3$[11]	3.07	1 – Isolated trigonal planar units, related to $RbBe(NH_2)_3$
$Cs_2[Mg(NH_2)_4]$[2]	2.93	2 – Isolated tetrahedra
$Rb_2[Mg(NH_2)_4]$[3]	2.67	2 – Isolated tetrahedra, similar to $Cs_2[Mg(NH_2)_4]$
$K_2[Mg(NH_2)_4]$[3]	2.42	2 – Isolated tetrahedra, related to β-K_2SO_4
$CsCa(NH_2)_3$[4]	1.67	4 – Octahedra, hexagonal perovskite
$RbCa(NH_2)_3$[5]	1.52	3 – Octahedra chains, similar to $CsCuCl_3$
$CsSr(NH_2)_3$[4]	1.42	4 – Octahedra, hexagonal perovskite
$KCa(NH_2)_3$[6]	1.38	3 – Octahedra chains, similar to $CsCuCl_3$
$CsBa(NH_2)_3$[7]	1.23	5 – Double octahedra chains, related to NH_4CdCl_3
$KSr(NH_2)_3$[8]	1.17	6 – Octahedra, similar to $KEu(NH_2)_3$
$RbBa(NH_2)_3$[9]	1.13	6 – Octahedra, similar to $KEu(NH_2)_3$
$KBa(NH_2)_3$[9]	1.02	6 – Octahedra, similar to $KEu(NH_2)_3$
$NaCa(NH_2)_3$[9]	1.02	6 – Octahedra, similar to $KEu(NH_2)_3$
$Na_2Sr_3(NH_2)_8$[8]	0.86	6 – Octahedra, similar to $Na_2Sr_3(NH_2)_8$
$Na_2Ba(NH_2)_4$	0.76	Octahedra, related to Mn_2SnS_4

8.2 Imide Nitrides

Ammonothermally prepared imide nitrides were mainly regarded as intermediate species formed during the ammonothermal dissolution process which should be followed by a further reaction to desired nitrides.[12-13] The investigations on these compounds were therefore mainly limited to their structural characterization and some vibrational spectroscopy studies. Possible application fields were not considered due to the air sensitivity of most compounds.

The observation of the two luminescent imidonitridophosphate systems $Ba_4P_6N_{10}NH:Eu^{2+}$ and $AE_2AlP_8N_{15}(NH):Eu^{2+}$ (AE = Ca, Sr, Ba) then revealed a possible application as phosphor materials.[14-15] The observation of luminescence in doped imidonitridophosphate samples was considered to be unrealizable as quenching effects were expected in the presence of the oscillator N−H. With the preparation of $Ba_4P_4N_8(NH)_2:Eu^{2+}$, presented in this work, the first luminescent imidonitridophosphate from ammonothermal conditions is reported. The characterization of the luminescent behavior shows narrow-band emission in the cyan spectral region which is able to

compete with industrially employed phosphor materials. Next to the highest ratio of imide anions among the luminescent imidonitridophosphates, $Ba_4P_4N_8(NH)_2$ consists of isolated adamantane-type anions. Both of these characteristics are not normally associated with the observation of luminescence at all or a narrow-band emission in particular. Additionally, the investigations on the luminescent behavior of doped samples of $Ba_4P_4N_8(NH)_2:Eu^{2+}$ revealed an impressive IQE of 41% which is a first benchmark value for this compound class. All these findings substantiate the suitability of imidonitridophosphates for a possible application as phosphor materials. Here, the ammonothermal approach offers a scalable synthetic access towards larger amounts of the compounds compared to preparations in a multianvil press. This ammonothermal strategy has already proven to be suitable for the related nitridophosphates and therefore allows to discover a wide range of compounds in the future.[16]

For $Rb_3Si_6N_5(NH)_6$, such direct applications were not yet found. Nevertheless, the combination of different analytical techniques allowed for both of the novel imide nitrides the verification of the imide functionality as well as the identification of preferred imide positions among the possible crystallographic nitrogen positions. Furthermore, for $Rb_3Si_6N_5(NH)_6$, a first benchmark value for the chemical shift of a ^{15}N NMR signal in nitridosilicate environment was obtained. Here, the special conditions of the highly symmetric crystal structure and the imide functionality of the compound allowed to obtain this value without the necessity for ^{15}N enrichment, as cross polarization experiments could be conducted. This first value on this model compound might contribute to structural investigations on nitridosilicate compounds in the future.

The examples of these two imide nitrides show that these compounds are worth investigation beyond their structural properties and should not only be regarded as intermediate species on the reaction pathway towards functional nitrides. The presented analytical approach proved to be suitable to detect the imide functionality in the synthesized compounds and can be followed in future investigations. The preparation of the two imide nitrides $Ba_4P_4N_8(NH)_2$ and $Rb_3Si_6N_5(NH)_6$ shows as well a significant extension of the ammonothermally prepared imide nitrides as only few compounds were reported from ammonothermal reactions before this work.

8.3 Ammonothermal Access Towards Nitridosilicate Compounds

While early investigations towards the ammonothermal synthesis of Si_3N_4, the parent compound of nitridosilicates, often yielded imide nitride compounds such as Si_2N_2NH and $K_3Si_6N_5(NH)_6$, the application of higher synthesis temperatures enabled the formation of silicon-containing nitrides in recent years.[12-13,17-18] Nevertheless, the structural variability provided by the nitridosilicates in general remained underrepresented among the ammonothermally prepared examples which mainly crystallize in wurtzite-related structures.[17] The presented successful ammonothermal preparation of the literature-known nitridosilicates $AESiN_2$ (*AE* = Sr, Ba), $Li_2CaSi_2N_4$, $Ce_3Si_6N_{11}$

and $Ba_2AlSi_5N_9$ demonstrates that tetrahedra-based two-dimensional layers and complex three-dimensional networks are accessible by the ammonothermal route. Together with the preliminary work that showed tetrahedra-based chains in nitridosilicate environment, this proofs that the ammonothermal synthesis offers a universal synthesis access towards various structural motifs in nitridosilicates.[18-19] The promising results might allow to access isolated tetrahedra motifs in the future as it was already demonstrated for the ammonothermal synthesis of nitridophosphates.[16,20]

For the literature-known nitridosilicates, various preparation methods from medium-temperature approaches in metal fluxes in the case of $AESiN_2$ (*AE* = Sr, Ba) and $Li_2CaSi_2N_4$ up to high-temperature preparations of $Ce_3Si_6N_{11}$ and $Ba_2AlSi_5N_9$ at temperatures of up to 2000 K could be replaced by a unified ammonothermal approach at a reduced synthesis temperature of 1070 K. The reported temperature reduction is enabled by the employment of the reactive solvent supercritical ammonia in combination with mineralizing agents that enable a dissolution of the starting material. That the crystal growth of nitridosilicate is based on a solution recrystallization process is suggested by the presented electron microscope images which show some well-defined crystal shapes. Next to the solution-based reaction mechanism of the ammonothermal method, this reduced synthesis temperatures can additionally contribute to an improved crystal growth. This can be expected as the number of nucleation sites decreases at lower temperatures and lower thermal stress and defects in the crystallized products are normally observed at reduced temperatures due to lower growth rates. These effects might be exploited in the future for the controlled synthesis of nitridosilicates with larger crystal sizes. These would be beneficial for the construction of pcLED devices, where nitridosilicate phosphors are commonly employed. Larger crystal sizes of the phosphor could here lead to more efficient devices that show reduced thermal quenching as grain boundary effects could be reduced.[21] Therefore, doping experiments on ammonothermally prepared nitridosilicate compounds should be conducted in future studies.

Next to application fields in optoelectronic devices, the presented access towards the nitride zeolite(-like) compounds $Ce_3[Si_6N_{11}]$, $Li_2RE_4[Si_4N_8]O_3$ (*RE* = La, Ce), and $K_{1.25}Ce_{7.75}[Si_{11}N_{21}O_2]O_{0.75}$ emphasizes that the ammonothermal approach offers various advantages. Here, the preparation of three nitridosilicate compounds with similar condensation degrees is observed which is mainly controlled by the choice of the mineralizer. This already shows a powerful way to influence the reaction outcome in ammonothermal preparations. Future investigations might expand the possibilities by the utilization of other mineralizers that could as well generate ammonoacidic environments. The similarities of the ammonothermal to the hydrothermal synthesis, which already produced numerous zeolite compounds, marks the high potential that lies within the presented approach. This is emphasized by the fact that it already produced three novel compounds using only the two different counter ions La and Ce.

The ammonothermal synthesis as an addition to the synthetic toolkit for the preparation of nitridosilicates offers a simplification in the employed starting materials as well. Here, elemental silicon, an industrially commonly available starting material which can be purchased in high purities, proofed to be suitable for ammonothermal reactions. Especially in comparison to the commonly used starting material SDI, which has to be washed several times to remove chloride contaminations, this presents a facilitation of the synthesis process. Therefore, the precedent synthesis of reactive starting materials such as SDI or the activation of elemental or nitride starting materials at high temperatures can be rendered unnecessary by the ammonothermal approach. Possibly, this is enabled by the formation of reactive intermediate species during the dissolution of silicon in supercritical ammonia. Here, the investigations on $Rb_3Si_6N_5(NH)_6$ offer further information on possible intermediate species which might enable even more reaction control.

The observation of $Rb_3Si_6N_5(NH)_6$ and $K_{1.25}Ce_{7.75}[Si_{11}N_{21}O_2]O_{0.75}$ present two of the limited examples where the heavier alkali metals potassium and rubidium could be stabilized in nitride environment. In nitridosilicate environment, only the ammonothermally prepared $K_3Si_6N_5(NH)_6$ was observed before and no rubidium-containing compound at all.[12] Due to the large ion radii and low charges of K^+ and Rb^+, their contribution to the lattice energy in nitrides is usually not sufficient to form stable compounds. The ammonothermal synthesis seems to be a suitable approach to stabilize these rare element combinations. The generation of alkali metal amides from mineralizers might here play a crucial role for the formation of these compounds. Future studies could aim to stabilize cesium ions as well in nitridosilicate compounds, as the ammonothermal method already was used for the preparation of cesium-containing tetrahedra-based compounds such as $Cs_5[P(NH)_4](NH_2)_2$.[22]

In summary, the ammonothermal synthesis provides an access towards the nitridosilicates that is capable to produce ternary and multinary compounds from elemental Si as starting material offering different structural motifs among the products and synthetic control of the reaction outcome via the selection of both starting materials and mineralizers. This work established this access by a significant extension of the ammonothermally synthesized nitridosilicate compounds with the five literature-known compounds $SrSiN_2$, $BaSiN_2$, $Li_2CaSi_2N_4$, $Ba_2AlSi_5N_9$, and $Ce_3[Si_6N_{11}]$ and the four novel compounds $Rb_3Si_6N_5(NH)_6$, $Li_2La_4[Si_4N_8]O_3$, $Li_2Ce_4[Si_4N_8]O_3$, and $K_{1.25}Ce_{7.75}[Si_{11}N_{21}O_2]O_{0.75}$. This universal access might enable not only the preparation of novel nitridosilicate compounds in the future but as well the production of large single crystals of established nitridosilicate phosphors for an improved efficiency in pcLEDs.

8.4 Concluding Remarks

This dissertation presents a broad application of the ammonothermal synthesis on different challenges from preparation of intermediate species and their characterization up to the preparation

of complex multinary nitride species with possible application as functional materials in different fields. The presented increased synthetic control during this process and the number of prepared multinary compounds marks only a starting point to unleash the full synthetic potential of ammonothermal synthesis for the preparation of multinary amide, imide and nitride compounds.

8.5 References

[1] R. Juza, H. Jacobs, "Ammonothermal Synthesis of Magnesium and Beryllium Amides", *Angew. Chem.* **1966**, *78*, 208–208; *Angew. Chem. Int. Ed.* **1966**, *5*, 247–247.

[2] H. Jacobs, J. Birkenbeul, D. Schmitz, "Strukturverwandtschaft des Dicaesiumamidomagnesats, $Cs_2[Mg(NH_2)_4]$, zum β-K_2SO_4-Typ", *J. Less-Common Met.* **1982**, *85*, 79–86.

[3] H. Jacobs, J. Birkenbeul, J. Kockelkorn, "Darstellung und Eigenschaften der Amidomagnesate des Kaliums und Rubidiums $K_2[Mg(NH_2)_4]$- und $Rb_2[Mg(NH_2)_4]$-Verbindungen mit isolierten $[Mg(NH_2)_4]^{2-}$-Tetraedern", *J. Less-Common Met.* **1984**, *97*, 205–214.

[4] H. Jacobs, J. Kockelkorn, "Über Cäsiumamidometallate ($CsM(NH_2)_3$) des Calciums, Strontiums und Europiums; Verbindungen mit der Struktur "hexagonaler Perowskite"", *J. Less-Common Met.* **1981**, *81*, 143–154.

[5] H. Jacobs, J. Kockelkorn, "Darstellung und Kristallstruktur des Rubidiumcalciumamids, $RbCa(NH_2)_3$", *Z. Anorg. Allg. Chem.* **1979**, *456*, 147–154.

[6] H. Jacobs, U. Fink, "Darstellung und Kristallstruktur von $KCa(NH_2)_3$", *Z. Anorg. Allg. Chem.* **1977**, *435*, 137–145.

[7] H. Jacobs, J. Birkenbeul, J. Kockelkorn, "Darstellung und Eigenschaften des Caesiumbarium-Amids, $CsBa(NH_2)_3$: Strukturverwandtschaft zum NH_4CdCl_3-Typ", *J. Less-Common Met.* **1982**, *85*, 71–78.

[8] H. Jacobs, U. Fink, "Über Natrium- und Kaliumamidometallate des Calciums, Strontiums und Europiums", *J. Less-Common Met.* **1979**, *63*, 273–286.

[9] H. Jacobs, J. Kockelkorn, J. Birkenbeul, "Struktur und Eigenschaften der ternären Metallamide $NaCa(NH_2)_3$, $KBa(NH_2)_3$, $RbBa(NH_2)_3$, $RbEu(NH_2)_3$ und $RbSr(NH_2)_3$", *J. Less-Common Met.* **1982**, *87*, 215–224.

[10] R. Shannon, "Revised effective ionic radii and systematic studies of interatomic distances in halides and chalcogenides", *Acta Crystallogr., Sect. A: Found. Adv.* **1976**, *32*, 751–767.

[11] M. G. B. Drew, J. E. Goulter, L. Guémas-Brisseau, P. Palvadeau, J. Rouxel, P. Herpin, "Etude structurale d'amido-béryllates de rubidium et de potassium", *Acta Crystallogr., Sect. B: Struct. Crystallogr. Cryst. Chem.* **1974**, *30*, 2579–2582.

[12] D. Peters, E. F. Paulus, H. Jacobs, "Darstellung und Kristallstruktur eines Kaliumimidonitridosilicats, $K_3Si_6N_5(NH)_6$", *Z. Anorg. Allg. Chem.* **1990**, *584*, 129–137.

[13] D. Peters, H. Jacobs, "Ammonothermalsynthese von kristallinem Siliciumnitridimid, Si_2N_2NH", *J. Less-Common Met.* **1989**, *146*, 241-249.

[14] S. Wendl, L. Eisenburger, M. Zipkat, D. Günther, J. P. Wright, P. J. Schmidt, O. Oeckler, W. Schnick, "$BaP_6N_{10}NH:Eu^{2+}$ as a Case Study – An Imidonitridophosphate Showing Luminescence", *Chem. Eur. J.* **2020**, *26*, 5010–5016.

[15] M. M. Pointner, R. M. Pritzl, J. M. Albrecht, L. Blahusch, J. P. Wright, E. Lawrence Bright, C. Giacobbe, O. Oeckler, W. Schnick, "Multicationic Tetrahedra Networks: Alkaline-Earth-Centered Polyhedra and Non-Condensed AlN_6-Octahedra in the Imido-nitridophosphates $AE_2AlP_8N_{15}(NH)$ (AE = Ca, Sr, Ba)", *Chem. Eur. J.* **2024**, *30*, e202400766.

[16] M. Mallmann, S. Wendl, W. Schnick, "Crystalline Nitridophosphates by Ammonothermal Synthesis", *Chem. Eur. J.* **2020**, *26*, 2067–2072.

[17] J. Häusler, W. Schnick, "Ammonothermal Synthesis of Nitrides: Recent Developments and Future Perspectives", *Chem. Eur. J.* **2018**, *24*, 11864–11879.

[18] M. Mallmann, C. Maak, W. Schnick, "Ammonothermal Synthesis and Crystal Growth of the Chain-type Oxonitridosilicate $Ca_{1+x}Y_{1-x}SiN_{3-x}O_x$ (x > 0)", *Z. Anorg. Allg. Chem.* **2020**, *646*, 1539–1544.

[19] J. Häusler, "Ammonothermal Synthesis of Functional Ternary and Multinary Nitrides", Doctoral thesis, Ludwig-Maximilians-Universität München (Munich), **2018**.

[20] S. Wendl, M. Mallmann, P. Strobel, P. J. Schmidt, W. Schnick, "Ammonothermal Synthesis of Ba_2PO_3N – An Oxonitridophosphate with Non-Condensed PO_3N Tetrahedra", *Eur. J. Inorg. Chem.* **2020**, *2020*, 841–846.

[21] B. Wen, D. Zhang, N. Zhang, J. Feng, B. Jiang, F. Pan, Y. Zhang, L. Yang, "Effect of grain size on the luminescent properties of Ce^{3+} doped $Y_3Al_5O_{12}$ ceramic phosphor plates", *Ceram. Int.* **2020**, *46*, 10452–10456.

[22] H. Jacobs, F. Golinski, "Synthese und Struktur eines Caesium-tetraimidophosphat-diamids, $Cs_5[P(NH)_4](NH_2)_2$ = $Cs_3[P(NH)_4] \cdot 2\ CsNH_2$", *Z. Anorg. Allg. Chem.* **1994**, *620*, 531–534.

9 Appendix

9.1 List of Abbreviations

A	**A**lkali
AE	**A**lkaline **E**arth
ATR	**A**ttenuated **T**otal **R**eflectance
approx.	**approx**imately
BVS	**B**ond **V**alence **S**ums
CC	**C**ounter **C**ation
CHARDI	**Cha**rge **Di**stribution in Solids
CN	**C**oordination **N**umber
CN	**C**ross **P**olarization
CR	**C**ation **R**atio
DFG	**D**eutsche **F**orschungs**g**emeinschaft
DFT	**D**ensity **F**unctional **T**heory
DFPT	**D**ensity **F**unctional **P**ertubation **T**heory
Eds	**Ed**itor**s**
EDX	**E**nergy **D**ispersive **X**-Ray Diffraction
FTIR	**F**ourier-**T**ransform **I**nfra**r**ed
FWHM	**F**ull **W**idth at **H**alf **M**aximum
GGA	**G**eneralized **G**radient **A**pproximation
GOOF	**Go**odness **o**f **F**it
II	bivalent metal
IV	tetravalent metal
IR	**I**nfra**r**ed
IQE	**I**nternal **Q**uantum **E**fficiency

IZA	**I**nternational **Z**eolite **A**ssociation
LED	**L**ight **E**mitting **D**iode
Ln	**L**anthanoide metal
NFC	**N**etwork-**F**orming **C**ation
NMR	**N**uclear **M**agnetic **R**esonance
no.	**n**umber
M	**M**etal
MAS	**M**agic-**A**ngle **S**pinning
pc-LED	**P**hosphor **C**onverted **L**ight **E**mitting **D**iode
PAW	**P**rojector **A**ugmented **W**aves
PBE	**P**erdew, **B**urke and **E**rnzerhof (developer of this DFT functional)
PL	**P**hoto**l**uminescence
PLE	**P**hoto**l**uminescence **E**xcitation
(P)XRD	(**P**owder) **X**-**R**ay **D**iffraction
RE	**R**are-**E**arth
SDI	**S**ilicon **Di**imide
SEM	**S**canning **E**lectron **M**icroscopy
SI	**S**upporting **I**nformation
VASP	**V**ienna **a**b **i**nitio **S**imulation **P**ackage
UV	**U**ltra **V**iolet

9.2 Supporting Information for Chapter 2

9.2.1 Additional Crystallographic Data

Table 9.1: Wyckoff positions, atomic coordinates and isotropic displacement parameters of $Na_2Ba(NH_2)_4$ obtained from single-crystal X-ray diffraction, standard deviations are given in parentheses.

Atom	Wyckoff position	*x*	*y*	*z*	U_{eq} / Å^2	S.O.F.
Ba1	4*d*	1/4	3/4	0.51378(2)	0.02184(3)	1
Na1	8*e*	0.50956(8)	0.5414(3)	0.2926(2)	0.0432(4)	0.952(6)
Na2	8*e*	0.4944(17)	0.972(5)	0.249(3)	0.0432(4)	0.048(6)
N1	8*e*	0.75405(14)	0.49595(15)	0.23955(12)	0.0269(2)	1
H1	8*e*	0.7377(15)	0.571(2)	0.158(2)	0.0320	1
H2	8*e*	0.7700(15)	0.573(2)	0.318(2)	0.0320	1
N2	8*e*	0.50621(11)	0.7475(2)	0.53277(16)	0.0342(2)	1
H3	8*e*	0.584(2)	0.722(2)	0.555(2)	0.0410	1
H4	8*e*	0.524(2)	0.831(2)	0.475(2)	0.0410	1

Table 9.2: Anisotropic displacement parameters [Å^2] of $Na_2Ba(NH_2)_4$, standard deviations are given in parentheses.

Atom	U_{11}	U_{22}	U_{33}	U_{23}	U_{13}	U_{12}
Ba1	0.01826(4)	0.03120(6)	0.01607(4)	0	0	0.00340(5)
Na1	0.0321(3)	0.0592(8)	0.0381(4)	−0.0025(6)	0.0022(4)	0.0114(4)
Na2	0.0321(3)	0.0592(8)	0.0381(4)	−0.0025(6)	0.0022(4)	0.0114(4)
N1	0.0324(5)	0.0234(4)	0.0249(4)	0.0012(4)	−0.0003(5)	0.0006(5)
N2	0.0205(5)	0.0426(7)	0.0396(6)	0.0010(7)	−0.0018(4)	−0.0001(8)

Table 9.3: Selected interatomic distances for $Na_2Ba(NH_2)_4$.

Bond	*d* / Å	Bond	*d* / Å
Ba1 – N2	2.7328(12) 2x	Na1 – N1	2.749(2)
Ba1 – N1	2.7722(10) 2x	Na1 – Na2	0.64(4)
Ba1 – N1	2.8113(10) 2x	Na2 – N2	2.46(2)
Na1 – N2	2.526(3)	Na2 – N1	2.65(2)
Na1 – N1	2.663(2)	Na2 – N1	2.69(2)
Na1 – N2	2.668(2)	Na2 – N2	2.81(2)
Na1 – N2	2.674(2)	Na2 – N2	2.88(4)

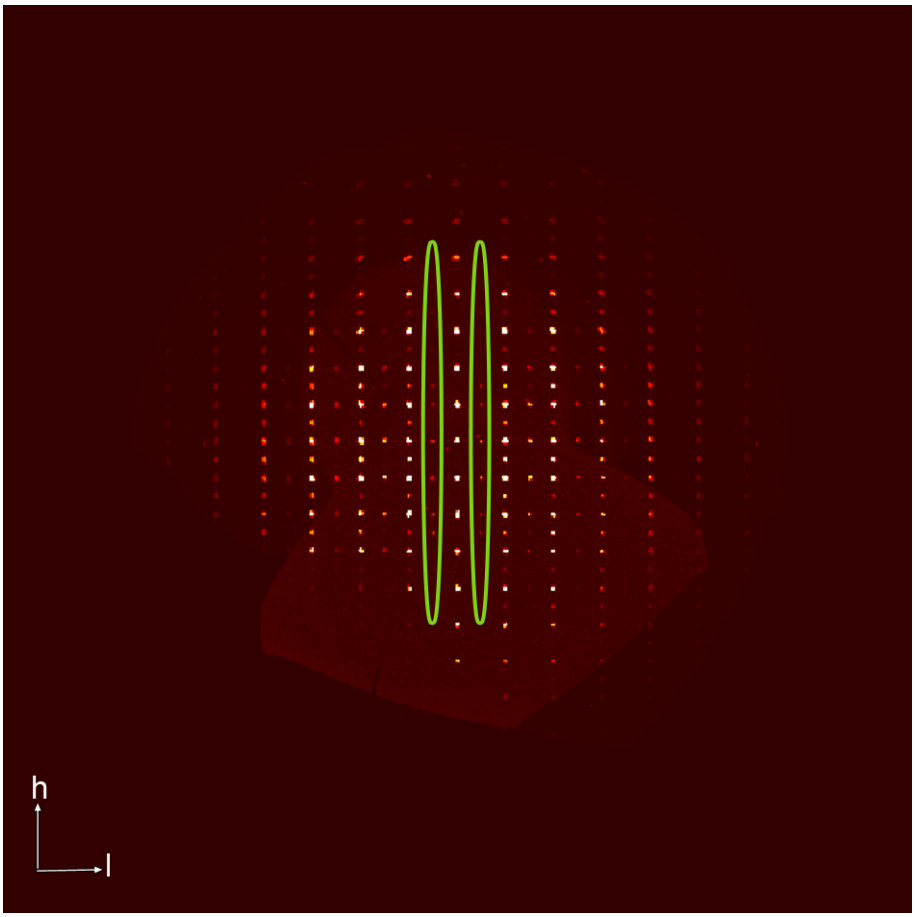

Figure 9.1: Precession image of the h1l plane with the superstructure reflections highlighted in green circles.

Table 9.4: Crystallographic data for $Na_2Ba(NH_2)_4$ and $NaNH_2$ obtained by Rietveld refinement, standard deviations given in parentheses. Starting values for $NaNH_2$ were taken from literature.[1]

Formula	$Na_2Ba(NH_2)_4$	$NaNH_2$
Crystal system	Orthorhombic	
Space group	*Pccn* (no. 56)	*Fddd* (no. 70)
Lattice parameters / Å	a = 10.6289(11) b = 7.8378(12) c = 8.0832(10)	a = 8.939(9) b = 10.563(10) c = 8.011(9)
Cell volume / Å^3	673.39(15)	756.4(13)
Density / g·cm^{-3}	2.46(4)	1.370(2)
Formula units / cell	4	16
T / K	293(2)	
Diffractometer	STOE STADI P	
Detector	Mythen 1K	
Monochromator	Ge(111)	
Radiation / Å	Ag-Kα_1 (λ = 0.5594)	
2θ range / °	$2 \leq 2\theta \leq 56$	
Profile function	fundamental parameters model	
Background function	Shifted Chebyshev	
Data points	3601	
Number of reflections	1707	484
Refined parameters (thereof background)	3 (9)	
R values	R_p = 0.0572 R_{wp} = 0.0673	
	R_{Bragg} = 0.0191	R_{Bragg} = 0.0185
Goodness of fit	0.974	

Table 9.5: Wyckoff positions and atomic coordinates of $Na_2Ba(NH_2)_4$ obtained from Rietveld refinement, standard deviations are given in parentheses.

Atom	Wyckoff position	*x*	*y*	*z*	U_{eq} / Å^2	S.O.F.
Ba1	4*d*	1/4	3/4	0.5154(6)	0.700	1
Na1	8*e*	0.520(5)	0.973(7)	0.785(6)	0.700	0.68(10)
Na2	8*e*	0.498(7)	1.064(11)	0.285(15)	0.700	0.32(10)
N1	8*e*	0.727(3)	0.485(2)	0.260(6)	0.700	1
H1	8*e*	0.7375	0.571	0.1583	0.700	1
H2	8*e*	0.7700	0.573	0.318	0.700	1
N2	8*e*	0.5117(15)	0.734(7)	0.498(6)	0.700	1
H3	8*e*	0.523	0.831	0.4751	0.700	1
H4	8*e*	0.5841	0.722	0.555	0.700	1

9.2.2 Additional IR Spectroscopy Data

Table 9.6: Assignment of the IR signals in the spectrum to their respective vibrational modes for $Na_2Ba(NH_2)_4$.

Vibrational mode	exp. IR shifts / cm^{-1}	Calc. IR shifts / cm^{-1}
$\delta(NH_2^-)$		587
$\delta(NH_2^-)$	599	601
δ(HNH) of $NaNH_2$[2]	1531	
δ(HNH)	1547	1514
δ(HNH)	1572	1543
$\nu_s(NH_2^-)$	3208	3288
$\nu_{as}(NH_2^-)$	3243	3371
$\nu_{as}(NH_2^-)$ of $NaNH_2$[2]	3257	

9.3 Supporting Information for Chapter 3

9.3.1 Additional Crystallographic Data

Table 9.7: Wyckoff positions, atomic coordinates and isotropic displacement parameters of the $Ba_4P_4N_8(NH)_2$ model without hydrogen obtained from single-crystal X-ray diffraction, standard deviations are given in parentheses.

Atom	Wyckoff position	*x*	*y*	*z*	U_{eq} / Å^2	S.O.F.
Ba1	4*a*	0.06468(4)	0.11831(3)	0.65352(6)	0.01010(9)	1
Ba2	4*a*	0.32375(4)	0.56189(4)	0.18616(6)	0.01035(9)	1
Ba3	4*a*	0.37268(4)	0.15616(4)	0.87359(6)	0.01102(9)	1
Ba4	4*a*	0.55661(4)	0.08864(4)	0.39712(6)	0.01054(8)	1
P1	4*a*	0.2838(2)	0.1336(2)	0.4023(3)	0.0073(3)	1
P2	4*a*	0.14267(15)	0.30739(15)	0.4109(3)	0.0068(3)	1
P3	4*a*	0.0979(2)	0.15362(15)	0.1353(3)	0.0071(3)	1
P4	4*a*	0.2734(2)	0.29443(15)	0.1476(3)	0.0069(3)	1
N1	4*a*	0.3663(5)	0.0497(5)	0.5295(9)	0.0088(12)	1
N2	4*a*	0.3381(6)	0.3626(6)	0.0256(10)	0.0095(12)	1
N3	4*a*	0.0000(5)	0.0854(5)	0.0000(9)	0.0091(12)	1
N4	4*a*	0.5936(6)	0.1192(5)	0.0443(9)	0.0090(12)	1
N5	4*a*	0.3529(5)	0.2012(5)	0.2766(9)	0.0077(11)	1
N6	4*a*	0.1811(6)	0.0685(5)	0.2696(9)	0.0087(11)	1
N7	4*a*	0.2333(5)	0.2187(5)	0.5344(8)	0.0064(11)	1
N8	4*a*	0.1696(5)	0.2239(5)	0.0127(8)	0.0077(11)	1
N9	4*a*	0.2153(6)	0.3735(5)	0.2825(9)	0.0079(11)	1
N10	4*a*	0.0464(5)	0.2361(5)	0.2695(9)	0.0094(11)	1

Table 9.8: Anisotropic displacement parameters [Å²] of the $Ba_4P_4N_8(NH)_2$ model without hydrogen, standard deviations are given in parentheses.

Atom	U_{11}	U_{22}	U_{33}	U_{23}	U_{13}	U_{12}
Ba1	0.0083(2)	0.0104(2)	0.0111(2)	0.0022(2)	0.0011(2)	−0.0012(2)
Ba2	0.0108(2)	0.0111(2)	0.0095(2)	−0.0015(2)	0.0028(2)	0.0012(2)
Ba3	0.0102(2)	0.0120(2)	0.0104(2)	−0.0005(2)	0.0014(2)	0.0023(2)
Ba4	0.0090(2)	0.0106(2)	0.0117(2)	0.0027(2)	0.0016(2)	−0.0009(2)
P1	0.0076(8)	0.0067(8)	0.0080(8)	−0.0001(6)	0.0026(7)	0.0010(6)
P2	0.0064(8)	0.0081(8)	0.0070(8)	−0.0004(6)	0.0035(7)	0.0001(6)
P3	0.0073(8)	0.0067(8)	0.0074(8)	−0.0001(6)	0.0018(7)	−0.0012(6)
P4	0.0064(8)	0.0073(8)	0.0074(8)	−0.0006(6)	0.0021(7)	−0.0014(6)
N1	0.007(3)	0.008(3)	0.012(3)	−0.004(2)	0.002(2)	0.004(2)
N2	0.011(3)	0.012(3)	0.006(3)	0.000(2)	0.003(2)	−0.005(2)
N3	0.010(3)	0.008(3)	0.007(3)	−0.003(2)	−0.001(2)	−0.003(2)
N4	0.008(3)	0.011(3)	0.007(3)	0.001(2)	0.000(2)	−0.004(2)
N5	0.006(2)	0.008(3)	0.009(3)	0.000(2)	0.002(2)	0.002(2)
N6	0.009(3)	0.008(3)	0.009(3)	−0.002(2)	0.002(2)	−0.002(2)
N7	0.006(2)	0.007(3)	0.007(3)	−0.001(2)	0.004(2)	0.001(2)
N8	0.008(3)	0.008(3)	0.007(3)	0.001(2)	0.002(2)	−0.003(2)
N9	0.011(3)	0.003(3)	0.009(3)	−0.002(2)	0.002(2)	0.001(2)
N10	0.005(3)	0.012(3)	0.012(3)	0.000(2)	0.004(2)	0.000(2)

Table 9.9: Selected interatomic distances and bonding angles for the $Ba_4P_4N_8(NH)_2$ model without hydrogen, standard deviations are given in parentheses.

Bond	*d* / Å	Bond	*d* / Å
Ba1–N7	2.767(6)	P1–N5	1.640(7)
Ba1–N2	2.793(7)	P1–N6	1.649(7)
Ba1–N6	2.793(6)	P1–N7	1.665(6)
Ba1–N3	2.842(7)	P1–Ba3	3.421(2)
Ba1–N3	2.883(7)	P1–Ba4	3.472(2)
Ba1–N8	2.994(6)	P1–Ba1	3.648(2)
Ba1–N10	3.162(7)	P2–N4	1.572(7)
Ba2–N2	2.649(7)	P2–N10	1.668(7)
Ba2–N2	2.792(7)	P2–N9	1.675(7)
Ba2–N3	2.867(7)	P2–N7	1.702(6)
Ba2–N9	2.895(7)	P2–Ba2	3.147(2)
Ba2–N4	2.927(7)	P2–Ba1	3.254(2)
Ba2–N7	3.093(6)	P2–Ba3	3.362(2)
Ba2–N9	3.095(6)	P2–Ba4	3.687(2)
Ba3–N4	2.810(7)	P3–N3	1.639(7)
Ba3–N10	2.812(6)	P3–N6	1.658(7)
Ba3–N7	2.825(6)	P3–N10	1.661(7)
Ba3–N1	2.838(6)	P3–N8	1.665(6)
Ba3–N1	2.858(6)	P3–Ba1	3.446(2)
Ba3–N2	2.896(7)	P3–Ba1	3.518(2)
Ba3–N8	3.070(7)	P3–Ba4	3.665(2)
Ba3–N5	3.095(6)	P3–Ba2	3.720(2)
Ba4–N4	2.775(7)	P4–N2	1.591(7)

Bond	*d* / Å	Bond	*d* / Å
Ba4–N8	2.780(6)	P4–N9	1.684(6)
Ba4–N1	2.815(7)	P4–N5	1.687(7)
Ba4–N4	2.825(7)	P4–N8	1.698(6)
Ba4–N5	2.878(6)	P4–Ba3	3.129(2)
Ba4–N9	3.121(7)	P4–Ba4	3.27(2)
P1–N1	1.620(7)	P4–Ba2	3.417(2)
Angle	Bonding angle / °	Angle	Bonding angle / °
N1–P1–N5	108.4(4)	N3–P3–N6	108.2(3)
N1–P1–N6	109.5(3)	N3–P3–N10	110.6(3)
N5–P1–N6	111.1(4)	N6–P3–N10	108.8(3)
N1–P1–N7	110.8(3)	N3–P3–N8	111.5(3)
N5–P1–N7	108.6(3)	N6–P3–N8	108.9(3)
N6–P1–N7	108.5(3)	N10–P3–N8	108.9(3)
N4–P2–N10	112.2(4)	N2–P4–N9	111.2(4)
N4–P2–N9	113.7(3)	N2–P4–N5	112.5(4)
N10–P2–N9	108.6(3)	N9–P4–N5	110.7(3)
N4–P2–N7	110.8(3)	N2–P4–N8	111.6(3)
N10–P2–N7	106.6(3)	N9–P4–N8	106.2(3)
N9–P2–N7	104.3(3)	N5–P4–N8	104.3(3)

Table 9.10: Crystallographic data for $Ba_4P_4N_8(NH)_2$ model with hydrogen atoms obtained from single-crystal X-ray diffraction, standard deviations are given in parentheses.

Formula	**$Ba_4P_4N_8(NH)_2$**
Crystal system	monoclinic
Space group	*Cc* (no. 9)
Lattice parameters / Å, °	*a* = 12.5250(3) *b* = 12.5566(4) *c* = 7.3882(2) *β* = 102.9793(10)
Cell volume / Å^3	1132.27(5)
Formula units *Z* / cell	4
Density / g·cm^{-3}	4.783
μ / mm^{-1}	14.285
T / K	298(2)
Diffractometer	Bruker D8 Venture
Radiation (λ / Å)	Mo-K_α (0.71073)
F(000)	1424
θ range / °	3.245−36.965
Total no. of reflections	8923
No. of independent reflections	4321
Observed reflections [$F^2 > 2\sigma(F^2)$]	4077
R_{int}, R_σ	0.0328, 0.0514
Refined parameters / restraints	145 / 4
Flack parameter	0.028(18)
Goodness of fit (χ^2)	1.043
*R*1 (all data) / *R*1 [$F^2 > 2\sigma(F^2)$]	0.0335 / 0.0296
*wR*2 (all data) / *wR*2 indices [$F^2 > 2\sigma(F^2)$]	0.0548 / 0.0533
$\Delta\rho_{max}$ / $\Delta\rho_{min}$ [eÅ^{-3}]	1.63 / –1.94

Table 9.11: Wyckoff positions, atomic coordinates and isotropic displacement parameters of the $Ba_4P_4N_8(NH)_2$ model with hydrogen atoms obtained from single-crystal X-ray diffraction, standard deviations are given in parentheses.

Atom	Wyckoff position	*x*	*y*	*z*	U_{eq} / Å^2	S.O.F.
Ba1	4*a*	0.06458(4)	0.11831(3)	0.65354(6)	0.01011(8)	1
Ba2	4*a*	0.32364(4)	0.56189(4)	0.18617(6)	0.01036(9)	1
Ba3	4*a*	0.37256(4)	0.15616(4)	0.87358(6)	0.01103(9)	1
Ba4	4*a*	0.55650(4)	0.08864(4)	0.39712(6)	0.01054(8)	1
P1	4*a*	0.28374(16)	0.13356(15)	0.4023(3)	0.0073(3)	1
P2	4*a*	0.14259(15)	0.30738(15)	0.4109(3)	0.0069(3)	1
P3	4*a*	0.0978(2)	0.15363(15)	0.1354(3)	0.0071(3)	1
P4	4*a*	0.27328(15)	0.29449(15)	0.1476(3)	0.0070(3)	1
N1	4*a*	0.3662(5)	0.0501(5)	0.5288(10)	0.0089(12)	1
H1	4*a*	0.352(8)	0.004(6)	0.096(14)	0.13(3)	1
N2	4*a*	0.3377(6)	0.3626(6)	0.0254(10)	0.0094(12)	1
N3	4*a*	−0.0001(5)	0.0857(5)	−0.0002(9)	0.0092(12)	1
H2	4*a*	0.45(2)	0.37(2)	0.44(2)	0.12(11)	1
N4	4*a*	0.5934(6)	0.1192(5)	0.0442(9)	0.0090(12)	1
N5	4*a*	0.3528(5)	0.2012(5)	0.2765(9)	0.0078(11)	1
N6	4*a*	0.1809(6)	0.0684(5)	0.2696(9)	0.0087(11)	1
N7	4*a*	0.2331(5)	0.2186(5)	0.5345(8)	0.0064(11)	1
N8	4*a*	0.1696(5)	0.2240(5)	0.0127(8)	0.0077(11)	1
N9	4*a*	0.2152(6)	0.3736(5)	0.2821(9)	0.0080(11)	1
N10	4*a*	0.0462(5)	0.2361(5)	0.2697(9)	0.0092(11)	1

Table 9.12: Anisotropic displacement parameters [Å²] of the $Ba_4P_4N_8(NH)_2$ model with hydrogen atoms, standard deviations are given in parentheses.

Atom	U_{11}	U_{22}	U_{33}	U_{23}	U_{13}	U_{12}
Ba1	0.0083(2)	0.0104(2)	0.0103(2)	0.0111(2)	0.00113(15)	−0.0011(2)
Ba2	0.0108(2)	0.0111(2)	0.0095(2)	−0.0015(2)	0.0029(2)	0.0012(2)
Ba3	0.0102(2)	0.0121(2)	0.0104(2)	−0.0005(2)	0.0014(2)	0.0023(2)
Ba4	0.0090(2)	0.0106(2)	0.0116(2)	0.0027(2)	0.0016(2)	−0.0009(2)
P1	0.0076(8)	0.0068(8)	0.0080(8)	−0.0002(6)	0.0025(7)	0.0009(6)
P2	0.0064(8)	0.0081(8)	0.0071(8)	−0.0004(6)	0.0036(7)	0.0001(6)
P3	0.0073(8)	0.0067(8)	0.0074(8)	0.0000(6)	0.0018(7)	−0.0012(6)
P4	0.0065(8)	0.0073(8)	0.0074(8)	−0.0006(6)	0.0021(7)	−0.0014(6)
N1	0.008(3)	0.007(3)	0.012(3)	−0.004(2)	0.003(2)	0.004(2)
N2	0.011(3)	0.011(3)	0.006(3)	0.001(2)	0.003(2)	−0.005(2)
N3	0.011(3)	0.008(3)	0.008(3)	−0.003(2)	−0.001(2)	−0.002(2)
N4	0.008(3)	0.011(3)	0.007(3)	0.001(2)	0.000(2)	−0.004(2)
N5	0.006(2)	0.009(3)	0.009(3)	−0.004(2)	0.001(2)	0.002(2)
N6	0.009(3)	0.008(3)	0.009(3)	−0.002(2)	0.002(2)	−0.002(2)
N7	0.006(2)	0.007(3)	0.007(3)	−0.011(2)	0.004(2)	0.001(2)
N8	0.008(3)	0.008(3)	0.007(3)	0.001(2)	0.002(2)	−0.003(2)
N9	0.011(3)	0.003(3)	0.009(3)	−0.002(2)	0.002(2)	0.001(2)
N10	0.005(3)	0.012(3)	0.012(3)	−0.001(2)	0.004(2)	0.000(2)

Table 9.13: Crystallographic data for $Ba_4P_4N_8(NH)_2$ obtained by Rietveld refinement, standard deviations are given in parentheses.

Formula	$Ba_4P_4N_8(NH)_2$
Crystal system	monoclinic
Space group	*Cc* (no. 9)
Lattice parameters / Å, °	a = 12.5360(8) b = 12.5614(8) c = 7.3868(5) β = 103.020(4)
Cell volume / Å^3	1133.3(2)
Density / g·cm^{-3}	4.7665(5)
Formula units / cell	4
T / K	293(2)
Diffractometer	STOE STADI P
Detector	Mythen 1K
Monochromator	Ge(111)
Radiation / Å	Ag-Kα_1 (λ = 0.5594)
2θ range / °	$2.3 \leq 2\theta \leq 56.4$
Profile function	fundamental parameters model
Background function	Shifted Chebyshev
Data points	3610
Number of reflections	2937
Refined parameters (thereof background)	40 (13)
R values	R_p = 0.0396 R_{wp} = 0.0548 R_{Bragg} = 0.0253
Goodness of fit	1.693

Table 9.14: Wyckoff positions and atomic coordinates of $Ba_4P_4N_8(NH)_2$ obtained from Rietveld refinement, standard deviations are given in parentheses.

Atom	Wyckoff position	*x*	*y*	*z*	U_{eq} / Å^2	S.O.F.
Ba1	4*a*	0.0621(11)	0.1184(4)	0.656(2)	1.10(13)	1
Ba2	4*a*	0.3184(10)	0.5660(4)	0.181(2)	1.5(2)	1
Ba3	4*a*	0.3693(10)	0.1559(4)	0.873(2)	1.20(13)	1
Ba4	4*a*	0.5526(10)	0.0894(4)	0.398(2)	1.1(2)	1
P1	4*a*	0.2838	0.1336	0.4023	0.7	1
P2	4*a*	0.14267	0.30739	0.4109	0.7	1
P3	4*a*	0.0979	0.15362	0.1353	0.7	1
P4	4*a*	0.2734	0.29443	0.1476	0.7	1
N1	4*a*	0.3663	0.0497	0.5295	0.7	1
N2	4*a*	0.3381	0.3626	0.0256	0.7	1
N3	4*a*	0.0000	0.0854	0.0000	0.7	1
N4	4*a*	0.5936	0.1192	0.0443	0.7	1
N5	4*a*	0.3529	0.2012	0.2766	0.7	1
N6	4*a*	0.1811	0.0685	0.2696	0.7	1
N7	4*a*	0.2333	0.2187	0.5344	0.7	1
N8	4*a*	0.1696	0.2239	0.0127	0.7	1
N9	4*a*	0.2153	0.3735	0.2825	0.7	1
N10	4*a*	0.0464	0.2361	0.2695	0.7	1

9.3.2 Results of BVS Calculations

BVS calculations were performed using the program EXPO2014 v1.22.11.[3] For $R_0(P^{5+}–N^{3–})$, an optimized parameter for nitridophosphates was used.[4]

Table 9.15: Results of BVS calculations for the models of $Ba_4P_4N_8(NH)_2$ without hydrogen atoms and the model with hydrogen atoms H1 connected to N1 and H2 connected to N3.

Atom site	Expected charge	Model without H	Model with H
Ba1	2	2.3742	2.3796
Ba2	2	2.4430	2.4414
Ba3	2	2.5984	2.5960
Ba4	2	2.1521	2.1629
P1	5	4.8167	4.8287
P2	5	4.7224	4.7072
P3	5	4.6603	4.6666
P4	5	4.5761	4.5899
H1	1	–	1.3577
H2	1	–	1.3484
N1	−3	2.3970	3.7838
N2	−3	3.1565	3.1607
N3	−3	2.3425	3.7030
N4	−3	2.9718	2.9684
N5	−3	2.8004	2.7953
N6	−3	2.7618	2.7599
N7	−3	3.1802	3.1790
N8	−3	3.0463	3.0439
N9	−3	2.8605	2.8239
N10	−3	2.8262	2.8605

9.3.3 Results of CHARDI Calculations

CHARDI calculations were performed with the program CHARDI2015.[5-6]

Table 9.16: Results of CHARDI calculations for the models of $Ba_4P_4N_8(NH)_2$ without hydrogen atoms and the model with hydrogen atoms H1 connected to N1 and H2 connected to N3.

Atom site	Expected charge	Model without H	Model with H
Ba1	2	2.22	1.99
Ba2	2	2.14	2.00
Ba3	2	2.20	1.98
Ba4	2	2.14	1.99
P1	5	5.57	5.02
P2	5	5.10	5.11
P3	5	5.54	5.01
P4	5	5.08	5.09
H1	1	–	0.91
H2	1	–	0.92
N1	−3	−2.27	−3.31
N2	−3	−2.97	−2.97
N3	−3	−2.25	−3.27
N4	−3	−2.95	−2.95
N5	−3	−2.87	−2.85
N6	−3	−2.82	−2.81
N7	−3	−2.98	−2.98
N8	−3	−3.05	−3.04
N9	−3	−2.93	−2.93
N10	−3	−2.89	−2.89

9.3.4 Results of the EDX Measurements

Table 9.17: SEM EDX measurements of a sample of $Ba_4P_4N_8(NH)_2$, standard deviations of the mean are given in parentheses.

	Ba	P	O	N
Measurement 1	24	23	3	50
Measurement 2	20	21	4	55
Measurement 3	26	23	3	48
Measurement 4	27	24	3	46
Measurement 5	25	23	8	44
Measurement 6	24	22	3	51
Average	**24(2)**	**23(1)**	**4(2)**	**49(4)**
Calculated	22.2	22.2	0	55.5

9.3.5 Additional IR Spectroscopy Data

Table 9.18: Assignment of the IR signals in the spectrum to their respective vibrational modes for $Ba_4P_4N_8(NH)_2$.

Vibrational mode	exp. IR shifts / cm^{-1}	Calc. IR shifts / cm^{-1}
$\delta(NH^{2-})$	601	590
$\delta(NH_2^-)$ of $NaNH_2$[2]	613	
ν_s*(PNP)*	712	679
ν_s*(PNP)*		705
τ*(HNP)*	777	767
ω(HNP)		779
ν_s(PN)	948	909
ν_s(PN)		930
ω(NPN)		958
ν_s(PN)	1024	1020
δ(HNH)	1061	1039
$\nu_s(NH^{2-})$	3132	3264
$\nu_s(NH_2^-)$ of $NaNH_2$[2]	3208	
$\nu_{as}(NH_2^-)$ of $NaNH_2$[2]	3257	

9.3.6 Additional UV/Vis Spectroscopy Data

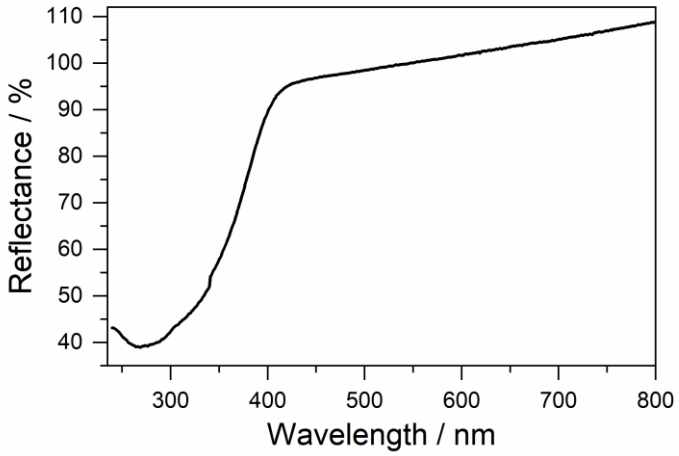

Figure 9.2: Diffuse reflectance spectrum of an undoped sample of $Ba_4P_4N_8(NH)_2$.

9.4 Supporting Information for Chapter 4

9.4.1 Additional Crystallographic Information

Table 9.19: Wyckoff positions, atomic coordinates and isotropic displacement parameters of $Rb_3Si_6N_5(NH)_6$ obtained from single-crystal X-ray diffraction, standard deviations are given in parentheses.

Atom	Wyckoff position	*x*	*y*	*z*	U_{eq} / Å^2	S.O.F.
Rb1	4*a*	1/8	3/8	5/8	0.0308(2)	1
Rb2	8*c*	0.78848(4)	0.78848(4)	0.78848(4)	0.02187(13)	1
Si1	24*e*	0.41384(6)	0.77246(6)	0.80939(7)	0.00678(11)	1
N1	24*e*	0.5256(2)	0.8813(2)	0.7716(2)	0.0103(3)	1
H1	24*e*	0.524(4)	0.885(5)	0.691(2)	0.012	1
N2	12*d*	1/8	0.7926(2)	0.9574(2)	0.0097(4)	1
N3	8*c*	0.2874(2)	0.7874(2)	0.7126(2)	0.0085(5)	1

Table 9.20: Anisotropic displacement parameters [Å^2] of $Rb_3Si_6N_5(NH)_6$, standard deviations are given in parentheses.

Atom	U_{11}	U_{22}	U_{33}	U_{23}	U_{13}	U_{12}
Rb1	0.0308(2)	0.0308(2)	0.0308(2)	0.0089(2)	0.0089(2)	0.0089(2)
Rb2	0.02187(13)	0.02187(13)	0.02187(13)	0.00384(12)	0.00384(12)	0.00384(12)
Si1	0.0075(3)	0.0057(3)	0.0072(3)	−0.0010(2)	−0.0014(2)	0.0006(2)
N1	0.0118(8)	0.0080(8)	0.0111(8)	−0.0025(6)	0.0034(7)	−0.0032(6)
N2	0.0137(12)	0.0077(7)	0.0077(7)	−0.0004(9)	−0.0001(6)	−0.0001(6)
N3	0.0085(5)	0.0085(5)	0.0085(5)	−0.0031(6)	−0.0031(6)	0.0031(6)

Table 9.21: Interatomic distances and bonding angles for $Rb_3Si_6N_5(NH)_6$, standard deviations are given in parentheses.

Bond	*d* / Å	Bond	*d* / Å
Rb1–N3	3.078(4) 2x	Si1–N2	1.689(2)
Rb1–N2	3.4145(6) 6x	Si1–N1	1.738(3)
Rb1–Si1	3.6204(7) 4x	Si1–N3	1.7500(8)
Rb1–Rb2	4.2018(5) 2x	Si1–N1	1.755(3)
Rb2–N1	3.056(3) 3x	Si1–Si1	2.737(2)
Rb2–N2	3.067(3) 3x		
Rb2–Rb2	3.2795(9)		
Rb2–Si1	3.6209(7) 3x		
Angle	Bonding angle / °	Angle	Bonding angle / °
N3–Rb1–N3	180	N1–Si1–N1	105.64(10)
N3–Rb1–N2	51.68(5)	N1–Si1–N2	114.97(12)
	128.32(5)		108.22(10)
N2–Rb1–N2	82.24(10)	N1–Si1–N3	110.1(2)
	85.60(7)		105.99(9)
	110.99 (0.01)	N2–Si1–N3	111.69(10)
	158.47(6)	Si1–N1–Si1	130.9(2)
N1–Rb2–N1	106.01 (5)	Si1–N2–Si1	108.2(2)
N1–Rb2–N2	56.33(5)	Si1–N3–Si1	119.72(2)
	106.01(5)		
	116.18(4)		
	137.14(4)		
N2–Rb2–N2	94.10(4)		

Table 9.22: Crystallographic data for $Rb_3Si_6N_5(NH)_6$ obtained by Rietveld refinement, standard deviations are given in parentheses.

Formula	$Rb_3Si_6N_5(NH)_6$
Crystal system	Cubic
Space group	$P4_132$ (no. 213)
Lattice parameters / Å	a = 10.94389(6)
Cell volume / Å^3	1310.74(2)
Density / g·cm^{-3}	2.96468(5)
Formula units / cell	4
T / K	293(2)
Diffractometer	STOE STADI P
Detector	Mythen 1K
Monochromator	Ge(111)
Radiation / Å	Cu-Kα_1 (λ = 1.5406)
2θ range / °	$5.0 \leq 2\theta \leq 93.00$
Profile function	fundamental parameters model
Background function	Shifted Chebyshev
Data points	5874
Number of reflections	148
Refined parameters (thereof background)	35 (16)
R values	R_p = 6.1815
	R_{wp} = 7.9379
	R_{Bragg} = 4.7150
Goodness of fit	1.273

Table 9.23: Wyckoff positions and atomic coordinates of $Rb_3Si_6N_5(NH)_6$ obtained from Rietveld refinement, standard deviations are given in parentheses.

Atom	Wyckoff position	*x*	*y*	*z*	U_{eq} / Å²	S.O.F.
Rb1	4*a*	1/8	3/8	5/8	0.7	1
Rb2	8*c*	0.78814(6)	0.78814(6)	0.78814(6)	0.7	1
Si1	24*e*	0.4128(2)	0.7712(2)	0.8101(2)	0.7	1
N1	24*e*	0.5231(4)	0.8808(6)	0.7743(4)	0.7	1
H1	24*e*	0.524	0.885	0.691	0.7	1
N2	12*d*	1/8	0.7942(4)	0.9558(4)	0.7	1
N3	8*c*	0.2131(4)	0.2131(4)	0.2131(4)	0.7	1

9.4.2 PXRD Data of the Employed $Rb(NH_2)$

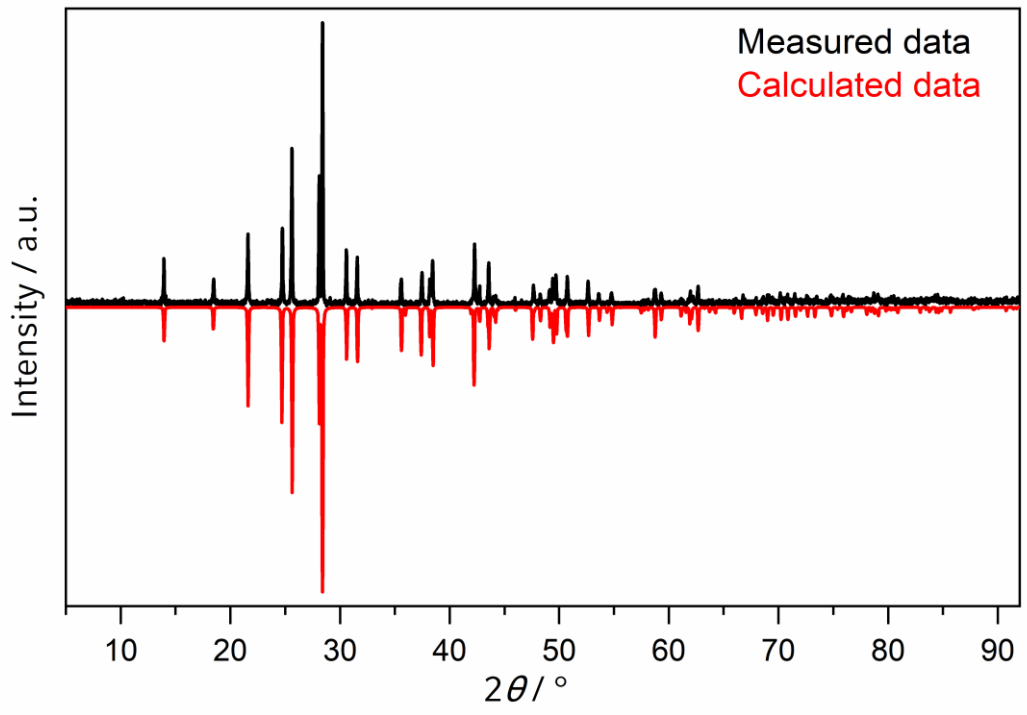

Figure 9.3: Comparison of the experimental PXRD data of the employed $RbNH_2$ (black) and the simulated data from literature (red).[7]

9.4.3 Results of CHARDI calculations

Table 9.24: Results of CHARDI calculations, performed with the program CHARDI2015.[5-6]

Atom site	Expected charge	CHARDI
Rb1	1	1.03
Rb2	1	1.01
Si1	4	4.01
N1	−3	−3.01
H1	1	0.98
N2	−3	−2.98
N3	−3	−3.01

9.5 Supporting Information for Chapter 5

9.5.1 Additional Crystallographic Information

Table 9.25: Crystallographic data for $SrSiN_2$ obtained by Rietveld refinement, standard deviations are given in parentheses.

Formula	**$SrSiN_2$**	**Si**
Crystal system	monoclinic	cubic
Space group	$P2_1/c$ (no. 14)	Fd-3m (no. 277)
Lattice parameters / Å,°	a = 5.97234(17) b = 7.3170(2) c = 5.49965(17) β = 113.5077(18)	a = 5.43111(13)
Cell volume / Å^3	220.386(12)	160.201 (12)
Density / g·cm^{-3}	4.3315(2)	2.32892(17)
Formula units / cell	4	8
T / K	293(2)	
Diffractometer	STOE STADI P	
Detector	Mythen 1K	
Monochromator	Ge(111)	
Radiation / Å	Cu-$K\alpha_1$ (λ = 1.540596)	
2θ range / °	$5 \leq 2\theta \leq 88.4$	
Profile function	fundamental parameters model	
Background function	Shifted Chebyshev	
Data points	5561	
Number of reflections	171	7
Refined parameters (thereof background)	40(12)	
R values	R_p = 0.0870 R_{wp} = 0.1138 R_{Bragg} = 4.1276264 R_{Bragg} = 0.0193	
Goodness of fit	1.249	

Table 9.26: Wyckoff positions, atomic coordinates and isotropic displacement parameters of $SrSiN_2$ obtained from powder X-ray diffraction, standard deviations are given in parentheses.

Atom	Wyckoff position	*x*	*y*	*z*	U_{eq} / Å^2	S.O.F.
Sr1	4*e*	0.3372(4)	0.5736(3)	0.1750(5)	3.67(6)	1
Si1	4*e*	0.1043(12)	0.1398(7)	0.0699(13)	3.27(14)	1
N1	4*e*	0.218(2)	0.585(2)	0.588(2)	2.3(3)	1
N2	4*e*	0.223(2)	0.2273(19)	¼	3.6(4)	1

Table 9.27: Crystallographic data for $BaSiN_2$ obtained by Rietveld refinement, standard deviations are given in parentheses.

Formula	**$BaSiN_2$**
Crystal system	orthorhombic
Space group	*Cmce* (no. 64)
Lattice parameters / Å	a = 5.6040(2) b = 11.3622(5) c = 7.5881(4)
Cell volume / Å^3	483.16(4)
Density / g·cm^{-3}	5.3182(4)
Formula units / cell	8
T / K	293(2)
Diffractometer	STOE STADI P
Detector	Mythen 1K
Monochromator	Ge(111)
Radiation / Å	Mo-$K\alpha_1$ (λ = 0.70930)
2θ range / °	$2 \leq 2\theta \leq 47.2$
Profile function	fundamental parameters model
Background function	Shifted Chebyshev
Data points	3015
Number of reflections	216
Refined parameters (thereof background)	32 (14)
R values	R_p = 0.1124 R_{wp} = 0.1494 R_{Bragg} = 0.0460
Goodness of fit	1.225

Table 9.28: Wyckoff positions, atomic coordinates and isotropic displacement parameters of $BaSiN_2$ obtained from powder X-ray diffraction, standard deviations are given in parentheses.

Atom	Wyckoff position	*x*	*y*	*z*	U_{eq} / Å^2	S.O.F.
Ba1	8*f*	0	0.3350(2)	0.0654(3)	1.48(7)	1
Si1	8*f*	0	0.0474(12)	0.1387(16)	1.3(3)	1
N1	8*f*	0	0.409(2)	0.417(5)	1.9(8)	1
N2	8*e*	¼	0.100(2)	¼	0.2(6)	1

Table 9.29: Crystallographic data for $Ba_2AlSi_5N_9$ obtained by Rietveld refinement, standard deviations are given in parentheses.

Formula	**$Ba_2AlSi_5N_9$**
Crystal system	triclinic
Space group	*P*1 (no. 1)
Lattice parameters / Å,°	a = 9.875(3) b = 10.294(3) c = 10.359(3) α = 90.144(12) β = 118.526(13) γ = 103.770(15)
Cell volume / Å^3	890.3(5)
Density / g·cm^{-3}	4.239(2)
Formula units / cell	4
T / K	293(2)
Diffractometer	STOE STADI P
Detector	Mythen 1K
Monochromator	Ge(111)
Radiation / Å	Mo-$K\alpha_1$ (λ = 0.70930)
2θ range / °	$2 \leq 2\theta \leq 50.5$
Profile function	fundamental parameters model
Background function	Shifted Chebyshev
Data points	3240
Number of reflections	3340
Refined parameters (thereof background)	56 (14)
R values	R_p = 0.0550 R_{wp} = 0.0724 R_{Bragg} = 0.0306
Goodness of fit	1.988

Table 9.30: Wyckoff positions, atomic coordinates and isotropic displacement parameters of $Ba_2AlSi_5N_9$ obtained from powder X-ray diffraction, standard deviations are given in parentheses. U_{eq} values were taken from literature.[8]

Atom	Wyckoff position	*x*	*y*	*z*	U_{eq} / Å^2	S.O.F.
Ba1	1*a*	0.121(5)	0.222(4)	0.552(4)	0.01230	1
Ba2	1*a*	0.108(5)	0.430(4)	0.885(4)	0.01276	1
Ba3	1*a*	0.117(4)	0.592(4)	0.496(4)	0.01022	1
Ba4	1*a*	0.045(4)	0.081(4)	0.903(4)	0.01253	1
Ba5	1*a*	0.467(4)	0.082(4)	0.947(4)	0.01453	1
Ba6	1*a*	−0.326(5)	−0.170(5)	0.932(4)	0.0131	0.676
Ba7	1*a*	−0.126(8)	−0.273(7)	0.929(8)	0.0167	0.324
Ba8	1*a*	0.554(5)	0.853(4)	0.557(4)	0.01640	1
Ba9	1*a*	−0.262(5)	0.554(4)	0.497(4)	0.01559	1
Al1	1*a*	0.2086	−0.0777	0.61408	0.0041	0.167
Si1	1*a*	0.2086	−0.0777	0.61408	0.0041	0.833
Al2	1*a*	−0.0509	−0.0822	0.60729	0.0042	0.167
Si2	1*a*	−0.0509	−0.0822	0.60729	0.0042	0.833
Al3	1*a*	0.0181	0.7348	0.83839	0.0076	0.167
Si3	1*a*	0.0181	0.7348	0.83839	0.0076	0.833
Al4	1*a*	0.2748	0.7340	0.84089	0.0060	0.167
Si4	1*a*	0.2748	0.7340	0.84089	0.0060	0.833
Al5	1*a*	0.4577	0.1643	0.57118	0.0061	0.167
Si5	1*a*	0.4577	0.1643	0.57118	0.0061	0.833
Al6	1*a*	−0.2340	0.1924	0.85764	0.0053	0.167
Si6	1*a*	−0.2340	0.1924	0.85764	0.0053	0.833
Al7	1*a*	0.4331	0.4828	0.88110	0.0049	0.167
Si7	1*a*	0.4331	0.4828	0.88110	0.0049	0.833
Al8	1*a*	−0.2388	0.4941	0.8817	0.0033	0.1127
Si8	1*a*	−0.2388	0.4941	0.8817	0.0033	0.563
Al9	1*a*	−0.3241	0.3964	0.8454	0.0033	0.054
Si9	1*a*	−0.3241	0.3964	0.8454	0.0033	0.270
Al10	1*a*	0.4499	0.4623	0.59659	0.0047	0.167
Si10	1*a*	0.4499	0.4623	0.59659	0.0047	0.833
Al11	1*a*	−0.2164	0.1685	0.57330	0.0044	0.167
Si11	1*a*	−0.2164	0.1685	0.57330	0.0044	0.833

Atom	Wyckoff position	*x*	*y*	*z*	U_{eq} / Å^2	S.O.F.
Al12	1*a*	0.3252	−0.1685	1.15523	0.0040	0.167
Si12	1*a*	0.3252	−0.1685	1.15523	0.0040	0.833
Al13	1*a*	0.5291	0.6766	1.1486	0.0045	0.167
Si13	1*a*	0.5291	0.6766	1.1486	0.0045	0.833
Al14	1*a*	0.4720	0.12518	1.29818	0.0033	0.167
Si14	1*a*	0.4720	0.12518	1.29818	0.0033	0.833
Al15	1*a*	−0.2363	0.2742	0.3053	0.0040	0.167
Si15	1*a*	−0.2363	0.2742	0.3053	0.0040	0.833
Al16	1*a*	0.4555	0.3814	1.1461	0.0041	0.167
Si16	1*a*	0.4555	0.3814	1.1461	0.0041	0.833
Al17	1*a*	−0.2515	0.5307	0.15647	0.0037	0.167
Si17	1*a*	−0.2515	0.5307	0.15647	0.0037	0.833
Al18	1*a*	0.3213	0.5570	1.28633	0.0042	0.167
Si18	1*a*	0.3213	0.5570	1.28633	0.0042	0.833
Al19	1*a*	0.0392	0.6809	1.1447	0.0045	0.167
Si19	1*a*	0.0392	0.6809	1.1447	0.0045	0.833
Al20	1*a*	−0.0340	0.3852	1.1574	0.0036	0.167
Si20	1*a*	−0.0340	0.3852	1.1574	0.0036	0.833
Al21	1*a*	−0.1037	0.1000	0.16381	0.0031	0.167
Si21	1*a*	−0.1037	0.1000	0.16381	0.0031	0.833
Al22	1*a*	0.2565	0.2718	0.2965	0.0042	0.167
Si22	1*a*	0.2565	0.2718	0.2965	0.0042	0.833
Al23	1*a*	0.1834	−0.0221	1.3067	0.0061	0.167
Si23	1*a*	0.1834	−0.0221	1.3067	0.0061	0.833
Al24	1*a*	0.6939	−0.0220	1.3029	0.0052	0.167
Si24	1*a*	0.6939	−0.0220	1.3029	0.0052	0.833
Al25	1*a*	−0.1067	0.82523	0.29344	0.29344	0.167
Si26	1*a*	−0.1067	0.82523	0.29344	0.29344	0.833
N1	1*a*	−0.0060	−0.1725	0.4848	0.4848	1
N2	1*a*	0.2282	−0.1779	0.9604	0.9604	1
N3	1*a*	0.3701	0.2971	0.4936	0.4936	1
N4	1*a*	0.4123	0.5820	0.4758	0.4758	1
N5	1*a*	−0.1924	0.0093	0.5067	0.5067	1

Atom	Wyckoff position	*x*	*y*	*z*	U_{eq} / Å^2	S.O.F.
N6	1*a*	−0.1456	0.2973	0.4976	0.4976	1
N7	1*a*	−0.1087	−0.1729	0.7221	0.7221	1
N8	1*a*	−0.2027	0.0732	0.9754	0.9754	1
N9	1*a*	0.2899	0.0099	0.5059	0.5059	1
N10	1*a*	0.4179	0.6426	0.9471	0.9471	1
N11	1*a*	−0.1508	0.3573	0.9625	0.9625	1
N12	1*a*	0.4873	−0.0255	1.2366	1.2366	1
N13	1*a*	0.3502	0.4672	0.6938	0.6938	1
N14	1*a*	0.5719	1.1341	0.4885	0.4885	1
N15	1*a*	−0.1329	0.1907	0.7600	0.7600	1
N16	1*a*	−0.1020	0.6827	0.2054	0.2054	1
N17	1*a*	0.3331	0.8272	0.7266	0.7266	1
N18	1*a*	−0.4350	0.1678	0.7532	0.7532	0.676
N19	1*a*	−0.4232	0.2161	0.7681	0.7681	0.324
N20	1*a*	0.1967	0.8297	0.2273	0.2273	1
N21	1*a*	0.2735	0.1161	1.2411	1.2411	1
N22	1*a*	−0.3066	−0.1749	1.2217	1.2217	1
N23	1*a*	0.3565	0.3527	0.9544	0.9544	1
N24	1*a*	−0.0216	−0.0321	1.2359	1.2359	1
N25	1*a*	0.1491	0.0189	0.7091	0.7091	1
N26	1*a*	−0.0711	0.6430	0.9421	0.9421	0.676
N27	1*a*	−0.040	0.6821	0.9580	0.9580	0.324
N28	1*a*	−0.2260	0.1211	0.2361	0.2361	1
N29	1*a*	−0.3490	0.4878	0.7026	0.0129	1
N30	1*a*	0.3992	0.6904	0.2160	0.0118	1
N31	1*a*	0.0500	0.2528	0.2294	0.0094	1
N32	1*a*	0.0726	0.6355	0.7433	0.0089	1
N33	1*a*	0.5522	0.2573	1.2290	0.0094	1
N34	1*a*	0.3297	0.4018	1.2170	0.0103	1
N35	1*a*	−0.1556	0.4068	0.2370	0.0102	1
N36	1*a*	0.6095	0.5370	1.2108	0.0080	1
N37	1*a*	−0.3583	0.5024	−0.0372	0.0155	1
N38	1*a*	0.1156	0.5411	1.2097	0.0081	1

9.6 Supporting Information for Chapter 6

9.6.1 Additional Crystallographic Data

Single-crystal data of $Li_2Ce_4[Si_4N_8]O_3$

Table 9.31: Crystallographic data for $Li_2Ce_4[Si_4N_8]O_3$ obtained from single-crystal X-ray diffraction, standard deviations are given in parentheses.

Formula	**$Li_2Ce_4[Si_4N_8]O_3$**
Crystal system	tetragonal
Space group	*I*4/*mmm* (no. 139)
Lattice parameters / Å	a = 9.5920(2)
	c = 5.4176(2)
Cell volume / Å^3	498.45(3)
Formula units Z / cell	2
Density / g·cm^{-3}	5.642
μ / mm^{-1}	18.416
T / K	298(2)
Diffractometer	Bruker D8 Venture
Radiation (λ / Å)	Mo-K_α (0.71073)
F(000)	748
θ range / °	4.320–39.511
Total no. of reflections	6538
No. of independent reflections	452
Observed reflections [$F^2 > 2\sigma(F^2)$]	424
R_{int}, R_σ	0.0295, 0.0129
Refined parameters / restraints	24 / 0
Goodness of fit (χ^2)	1.190
$R1$ (all data) / $R1$ [$F^2 > 2\sigma(F^2)$]	0.0186 / 0.0166
$wR2$ (all data) / $wR2$ indices [$F^2 > 2\sigma(F^2)$]	0.0376 / 0.0373
$\Delta\rho_{max}$ / $\Delta\rho_{min}$ [eÅ^{-3}]	0.80 / –1.69

Table 9.32: Wyckoff positions, atomic coordinates and isotropic displacement parameters of $Li_2Ce_4[Si_4N_8]O_3$ obtained from single-crystal X-ray diffraction, standard deviations are given in parentheses

Atom	Wyckoff position	*x*	*y*	*z*	U_{eq} / Å^2	S.O.F.
Ce1	8*j*	0.20522(3)	½	0	0.00948(6)	1
Si1	8*h*	0.17265(7)	*x*	0	0.00306(15)	1
Li1	4*e*	0	0	0.167(4)	0.040(4)	1
N1	8*i*	0.2094(4)	0	0	0.0090(5)	1
N2	8*f*	¼	¼	¼	0.0079(5)	1
O1	2*b*	0	0	½	0.034(2)	1
O2	4*d*	0	½	¼	0.0198(9)	1

Table 9.33: Anisotropic displacement parameters [Å^2] of $Li_2Ce_4[Si_4N_8]O_3$, standard deviations are given in parentheses.

Atom	U_{11}	U_{22}	U_{33}	U_{23}	U_{13}	U_{12}
Ce1	0.01653(11)	0.00519(8)	0.00671(8)	0.000	0.000	0.000
Si1	0.0031(2)	0.0031(2)	0.0030(3)	0.000	0.000	−0.0004(3)
Li1	0.037(6)	0.037(6)	0.044(11)	0.000	0.000	0.000
N1	0.0086(12)	0.0034(10)	0.0150(13)	0.000	0.000	0.000
N2	0.0086(7)	0.0086(7)	0.0064(11)	−0.0025(7)	−0.0025(7)	−0.0004(9)
O1	0.043(3)	0.043(3)	0.015(3)	0.000	0.000	0.000
O2	0.0183(13)	0.0183(13)	0.023(2)	0.000	0.000	0.000

Table 9.34: Selected Interatomic distances and bonding angles for $Li_2Ce_4[Si_4N_8]O_3$, standard deviations are given in parentheses.

Bond	*d* / Å	Bond	*d* / Å
Ce1–O2	2.3894(6) 2x	Si1−N2	1.7133(6) 2x
Ce1–N2	2.7873(1) 4x	Li1−O1	1.80(3)
Ce1–O1	2.8275(3)	Li1−Li1	1.81(5)
Ce1–N1	2.8300(10) 2x	Li1−N1	2.203(10) 4x
Si1–N1	1.6930(9) 2x		
Angle	Bonding angle / °	Angle	Bonding angle / °
O2–Ce1–O2	69.06(1)	N2–Ce1–N1	59.36(1)
O2–Ce1–N2	113.73(1)	N2–Ce1–N1	114.87(2)
O2–Ce1–N2	81.46(1)	O1–Ce1–N1	73.17(7)
N2–Ce1–N2	162.27(1)	N1–Ce1–N1	146.36(15)
N2–Ce1–N2	58.14(1)	N1–Si1–N1	114.0(3)
N2–Ce1–N2	118.70(1)	N1–Si1–N2	109.48(6)
N2–Ce1–N2	162.27(1)	N2–Si1–N2	104.47(5)
O2–Ce1–O1	145.47(1)	O1–Li1–N1	114.3(6)
N2–Ce1–O1	81.14(1)	N1–Li1–N1	80.3(5)
O2–Ce1–N1	141.36(7)	N1–Li1–N1	131.5(11)
O2–Ce1–N1	72.30(7)	Li1–O1–Li1	180

Rietveld refinement data of $Li_2Ce_4[Si_4N_8]O_3$

Table 9.35: Crystallographic data for $Li_2Ce_4[Si_4N_8]O_3$ obtained by Rietveld refinement, standard deviations are given in parentheses.

Formula	**$Li_2Ce_4[Si_4N_8]O_3$**
Crystal system	tetragonal
Space group	*I*4/*mmm* (no. 139)
Lattice parameters / Å	a = 9.59191(19)
	c = 5.41576(18)
Cell volume / Å^3	498.28(3)
Density / g·cm^{-3}	5.6437(3)
Formula units / cell	2
T / K	293(2)
Diffractometer	STOE STADI P
Detector	Mythen 1K
Monochromator	Ge(111)
Radiation / Å	Ag-$K\alpha_1$ (λ = 0.5594)
2θ range / °	$2 \leq 2\theta \leq 56.2$
Profile function	fundamental parameters model
Background function	Shifted Chebyshev
Data points	3619
Number of reflections	403
Refined parameters (thereof background)	19 (6)
R values	R_p = 0.0785
	R_{wp} = 0.1034
	R_{Bragg} = 0.0342
Goodness of fit	2.323

Table 9.36: Wyckoff positions, atomic coordinates and isotropic displacement parameters of $Li_2Ce_4[Si_4N_8]O_3$ obtained from powder X-ray diffraction, standard deviations are given in parentheses. U_{eq} of positions Li1 and O1 could not be refined freely and were taken from the single-crystal data of $Li_2Ce_4[Si_4N_8]O_3$.

Atom	Wyckoff position	*x*	*y*	*z*	U_{eq} / Å^2	S.O.F.
Ce1	8*j*	0.20454(19)	½	0	0.77(3)	1
Si1	8*h*	0.1725(5)	*x*	0	0.04(12)	1
Li1	4*e*	0	0	0.237(15)	3.158	1
N1	8*i*	0.205(2)	0	0	0.7(4)	1
N2	8*f*	¼	¼	¼	2.8(7)	1
O1	2*b*	0	0	½	2.685	1
O2	4*d*	0	½	¼	2.4(7)	1

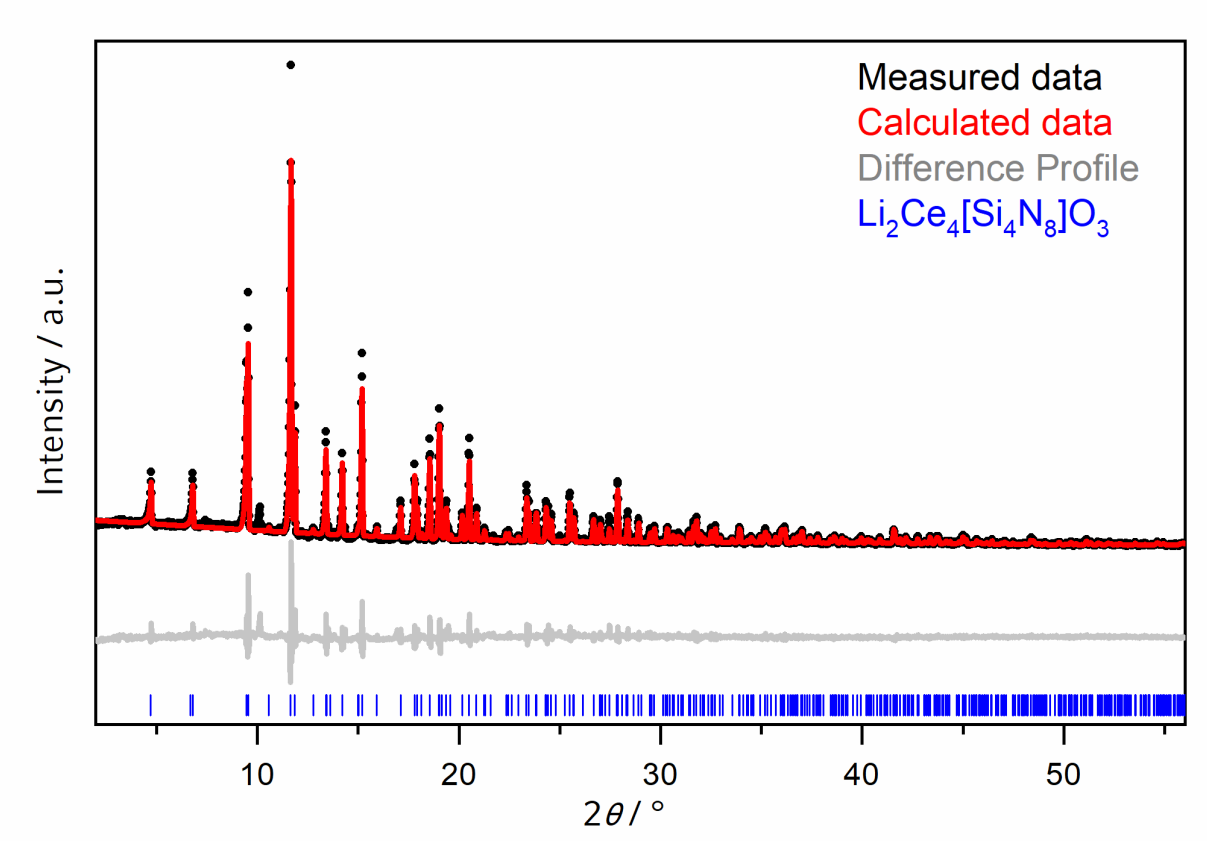

Figure 9.4: Rietveld refinement plot based on PXRD data of $Li_2Ce_4[Si_4N_8]O_3$ with experimental data (black dots), calculated diffraction pattern (red line), difference profile (gray line) and reflection positions of $Li_2Ce_4[Si_4N_8]O_3$ (blue bars).

Rietveld refinement data of $Li_2La_4[Si_4N_8]O_3$

Table 9.37: Crystallographic data for $Li_2La_4[Si_4N_8]O_3$ obtained by Rietveld refinement, standard deviations are given in parentheses.

Formula	**$Li_2La_4[Si_4N_8]O_3$**
Crystal system	tetragonal
Space group	*I*4/*mmm* (no. 139)
Lattice parameters / Å	a = 9.6113(2)
	c = 5.43000(19)
Cell volume / Å^3	501.61(4)
Density / g·cm^{-3}	5.5742(3)
Formula units / cell	2
T / K	293(2)
Diffractometer	STOE STADI P
Detector	Mythen 1K
Monochromator	Ge(111)
Radiation / Å	Ag-$K\alpha_1$ (λ = 0.5594)
2θ range / °	$2 \leq 2\theta \leq 57.7$
Profile function	fundamental parameters model
Background function	Shifted Chebyshev
Data points	3720
Number of reflections	402
Refined parameters (thereof background)	25 (11)
R values	R_p = 0.0587
	R_{wp} = 0.0747
	R_{Bragg} = 0.0193
Goodness of fit	1.101

Table 9.38: Wyckoff positions, atomic coordinates and isotropic displacement parameters of $Li_2La_4[Si_4N_8]O_3$ obtained from powder X-ray diffraction, standard deviations are given in parentheses. U_{eq} of positions Li1 and O2 could not be refined freely and were taken from the single-crystal data of $Li_2Ce_4[Si_4N_8]O_3$.

Atom	Wyckoff position	*x*	*y*	*z*	U_{eq} / Å^2	S.O.F.
La1	8*j*	0.21029(18)	½	0	0.0103(4)	1
Si1	8*h*	0.3285(5)	*x*	0	0.0076(16)	1
Li1	4*e*	0	0	0.180(15)	0.040	1
N1	8*i*	0.2075(19)	0	0	0.006(5)	1
N2	8*f*	¼	¼	¼	0.056(10)	1
O1	2*b*	0	0	½	0.024(13)	1
O2	4*d*	0	½	¼	0.0198	1

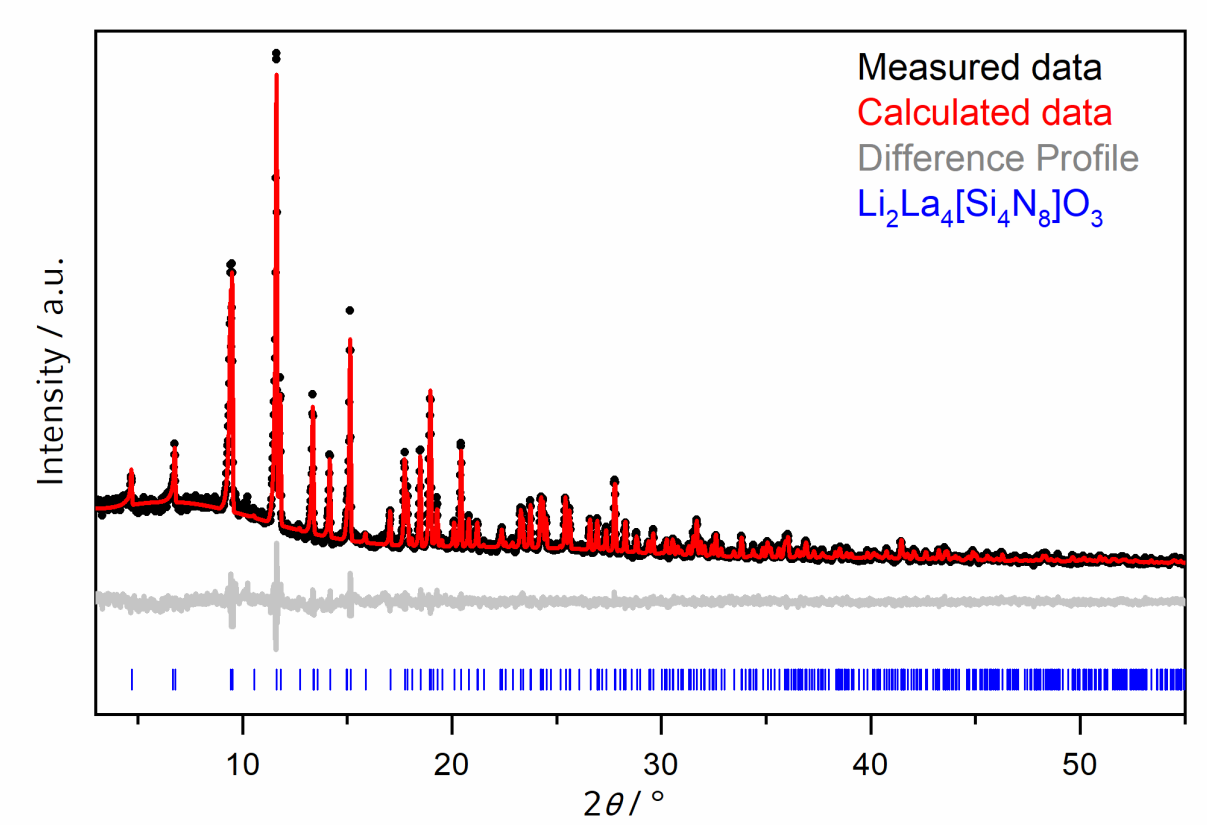

Figure 9.5: Rietveld refinement plot based on PXRD data of $Li_2La_4[Si_4N_8]O_3$ with experimental data (black dots), calculated diffraction pattern (red line), difference profile (gray line) and reflection positions of $Li_2La_4[Si_4N_8]O_3$ (blue bars).

Powder diffraction data of $Ce_3[Si_6N_{11}]$

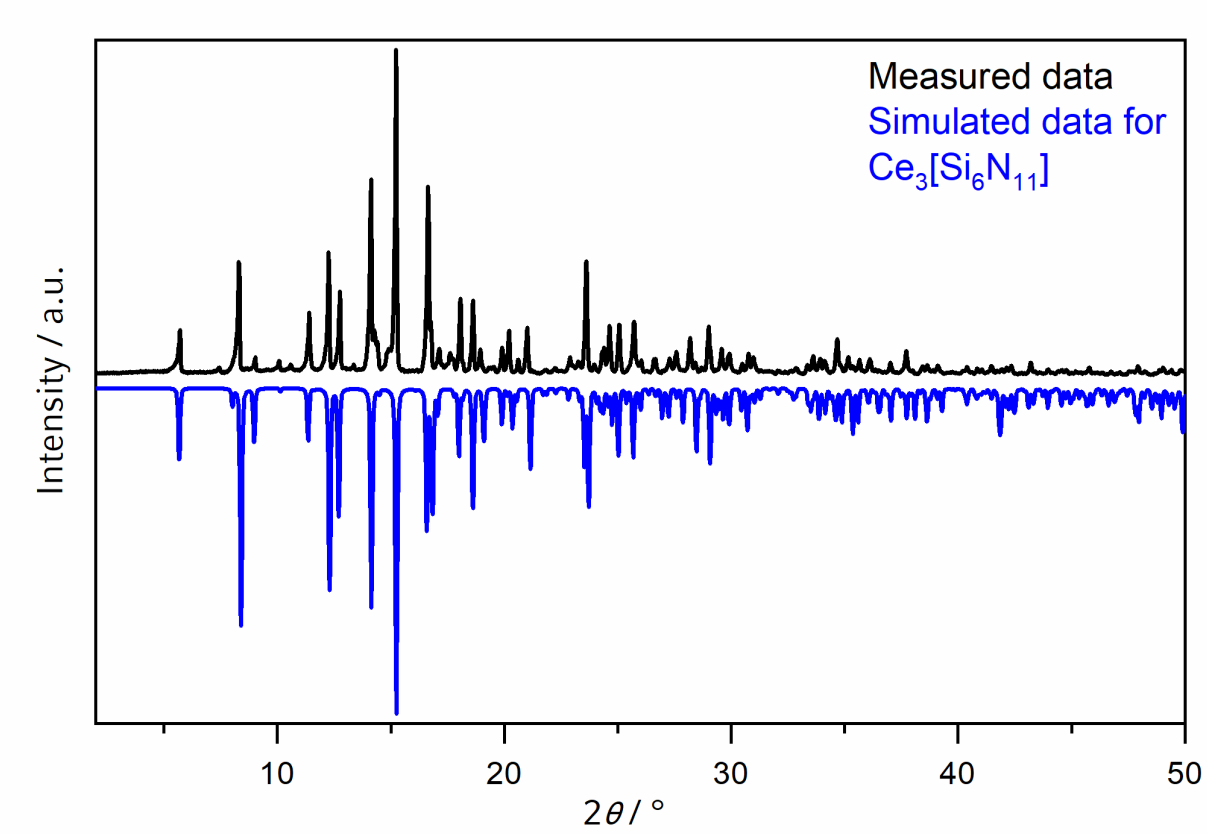

Figure 9.6: Comparison of the experimental (black line) and theoretical X-ray diffraction data (blue line) of $Ce_3[Si_6N_{11}]$.

Single-crystal data of $K_{1.25}Ce_{7.75}[Si_{11}N_{21}O_2]O_{0.75}$

Table 9.39: Crystallographic data for $K_{1.25}Ce_{7.75}[Si_{11}N_{21}O_2]O_{0.75}$ obtained from single-crystal X-ray diffraction, standard deviations are given in parentheses.

Formula	**$K_{1.25}Ce_{7.75}[Si_{11}N_{21}O_2]O_{0.75}$**
Crystal system	orthorhombic
Space group	*Cmmm* (no. 65)
Lattice parameters / Å	a = 11.1733(3) b = 23.2773(5) c = 9.5982(2)
Cell volume / Å^3	2496.34(10)
Formula units Z / cell	4
Density / g·cm^{-3}	4.741
μ / mm^{-1}	14.621
T / K	300(2)
Diffractometer	Bruker D8 Venture
Radiation (λ / Å)	Mo-K_α (0.71073)
F(000)	3185
θ range / °	2.122−34.336
Total no. of reflections	37076
No. of independent reflections	2866
Observed reflections [$F^2 > 2\sigma(F^2)$]	2521
R_{int}, R_σ	0.0565, 0.0314
Refined parameters / restraints	144 / 5
Goodness of fit (χ^2)	1.287
$R1$ (all data) / $R1$ [$F^2 > 2\sigma(F^2)$]	0.0586 / 0.0466
$wR2$ (all data) / $wR2$ indices [$F^2 > 2\sigma(F^2)$]	0.0857 / 0.0821
$\Delta\rho_{max}$ / $\Delta\rho_{min}$ [eÅ^{-3}]	2.91 / –2.36

Table 9.40: Wyckoff positions, atomic coordinates and isotropic displacement parameters of the $K_{1.25}Ce_{7.75}[Si_{11}N_{21}O_2]O_{0.75}$ obtained from single-crystal X-ray diffraction, standard deviations are given in parentheses.

Atom	Wyckoff position	*x*	*y*	*z*	U_{eq} / Å^2	S.O.F.
Ce1	4*j*	0	0.33968(3)	½	0.00771(12)	1
Ce2A	8*p*	0.28513(7)	0.10385(3)	0	0.01156(15)	0.920(2)
Ce2B	8*p*	0.3284(8)	0.0853(4)	0	0.01156(15)	0.080(2)
Ce3	16*r*	0.23363(16)	0.24901(19)	0.22156(6)	0.0131(4)	1
Ce4A	8*n*	0	0.11379(4)	0.21429(12)	0.00955(18)	0.701(2)
Ce4B	8*n*	0	0.10372(10)	0.2639(3)	0.00955(18)	0.299(2)
Ce5	4*h*	0.18083(10)	0	½	0.01614(18)	0.75
K5	4*h*	0.18083(10)	0	½	0.01614(18)	0.25
K6	4*l*	0	½	0.2971(10)	0.136(5)	1
Si1	8*o*	0.1542(2)	0	0.1661(2)	0.0053(4)	1
Si2	8*q*	0.1331(2)	0.20369(10)	½	0.0109(4)	1
Si3	16*r*	0.26433(14)	0.11651(7)	0.33958(15)	0.0065(3)	1
Si4	8*n*	0	0.33047(10)	0.1620(2)	0.0069(4)	1
Si5A	4*i*	0	0.2119(2)	0	0.0020(8)	0.655(11)
Si5B	8*p*	0.0441(13)	0.2120(5)	0	0.0020(8)	0.173(5)
N1	4*g*	0.2082(10)	0	0	0.0101(18)	1
N2	16*r*	0.1471(5)	0.1648(2)	0.3510(5)	0.0109(9)	1
N3	16*r*	0.1266(5)	0.3484(3)	0.2484(6)	0.0155(10)	1
N4	8*n*	0	0.2556(3)	0.1458(7)	0.0109(13)	1
N5	4*i*	0	0.3624(5)	0	0.013(2)	1
N6	8*q*	0.3183(6)	0.0931(3)	½	0.0072(12)	1
O7A	8*p*	0.1265(15)	0.1692(7)	0	0.042(3)	0.655(11)
O7B	8*p*	0.215(6)	0.208(3)	0	0.042(3)	0.173(5)
O7C	4*i*	0	0.1438(19)	0	0.042(3)	0.345(11)
N8	4*k*	0	0	0.1819(15)	0.017(2)	1
N9	16*r*	0.2079(5)	0.0605(2)	0.2443(5)	0.0116(9)	1
N10	4*j*	0	0.2397(4)	½	0.016(2)	1

Atom	Wyckoff position	*x*	*y*	*z*	U_{eq} / Å^2	S.O.F.
N11	8*q*	0.232(2)	0.2580(9)	½	0.012(4)	0.5
O12	4*j*	0	0.0555(14)	½	0.048(8)	0.5
O13	2*b*	½	0	0	0.048(8)	0.5

Table 9.41: Anisotropic displacement parameters [Å^2] of $K_{1.25}Ce_{7.75}[Si_{11}N_{21}O_2]O_{0.75}$, standard deviations are given in parentheses.

Atom	U_{11}	U_{22}	U_{33}	U_{23}	U_{13}	U_{12}
Ce1	0.0080(3)	0.0076(3)	0.0075(3)	0	0	0
Ce2A	0.0145(3)	0.0138(3)	0.00640(19)	0	0	−0.0067(3)
Ce2B	0.0145(3)	0.0138(3)	0.00640(19)	0	0	−0.0067(3)
Ce3	0.0204(11)	0.0088(3)	0.0102(2)	−0.0003(4)	0.0000(3)	0.0012(10)
Ce4A	0.0052(2)	0.0092(3)	0.0143(5)	−0.0037(3)	0	0
Ce4B	0.0052(2)	0.0092(3)	0.0143(5)	−0.0037(3)	0	0
Ce5	0.0310(5)	0.0085(3)	0.0088(3)	0	0	0
K5	0.0310(5)	0.0085(3)	0.0088(3)	0	0	0
K6	0.235(14)	0.107(7)	0.066(5)	0	0	0
Si1	0.0062(9)	0.0043(8)	0.0056(8)	0	−0.0011(7)	0
Si2	0.0187(12)	0.0077(9)	0.0062(9)	0	0	−0.0057(9)
Si3	0.0069(6)	0.0079(6)	0.0046(6)	−0.0003(5)	0.0006(5)	−0.0023(5)
Si4	0.0077(9)	0.0078(9)	0.0053(9)	−0.0005(7)	0	0
N1	0.016(5)	0.005(4)	0.009(4)	0	0	0
N2	0.011(2)	0.012(2)	0.010(2)	0.0003(17)	−0.0028(18)	0.0011(18)
N3	0.015(2)	0.022(3)	0.010(2)	−0.001(2)	−0.0037(19)	−0.008(2)
N4	0.016(3)	0.010(3)	0.007(3)	0.002(2)	0	0
N5	0.014(5)	0.019(5)	0.005(4)	0	0	0
N6	0.005(3)	0.013(3)	0.004(3)	0	0	0.001(2)

Atom	U_{11}	U_{22}	U_{33}	U_{23}	U_{13}	U_{12}
N8	0.003(4)	0.010(4)	0.038(7)	0	0	0
N9	0.012(2)	0.010(2)	0.013(2)	−0.0032(17)	−0.0037(19)	0.0000(18)
N10	0.023(6)	0.004(4)	0.022(5)	0	0	0
N11	0.021(14)	0.014(13)	0.002(4)	0	0	−0.006(8)
O13	0.15(9)	0.05(4)	0.31(16)	0	0	0

Table 9.42: Selected interatomic distances for $K_{1.25}Ce_{7.75}[Si_{11}N_{21}O_2]O_{0.75}$, standard deviations are given in parentheses.

Bond	*d* / Å	Bond	*d* / Å
Ce1–N10	2.328(10)	Ce4A–N9	2.649(5) 2x
Ce1–N6	2.563(7) 2x	Ce4A–N8	2.6669(18)
Ce1–N3	2.806(6) 4x	Ce4A–O7C	2.809(11) 2x
Ce2A–Ce2B	0.647(10)	Ce4B–N2	2.329(5) 2x
Ce2A–O7A	2.337(16)	Ce4B–O12	2.529(15)
Ce2A–N5	2.526(4)	Ce4B–N9	2.538(5) 2x
Ce2A–O7B	2.54(6)	Ce4B–N8	2.539(5)
Ce2A–N1	2.566(4)	Ce4B–O7C	2.699(16)
Ce2A–N9	2.695(5) 2x	Ce/K5–O12	2.398(18) 2x
Ce2A–N3	2.810(6) 2x	Ce/K5–N6	2.656(7) 2x
Ce2B–N5	2.271(9)	Ce/K5–N9	2.845(5) 4x
Ce2B–N1	2.398(9)	K6–O13	2.851(10)
Ce2B–O13	2.761(11)	Si1–N9	1.704(5) 2x
Ce2B–N9	2.765(7) 2x	Si1–N1	1.704(5)
Ce2B–N3	2.884(7) 2x	Si1–N8	1.730(3)
Ce2B–O7A	2.98(2)	Si2–N11	1.68(3)
Ce3–Ce3	0.369(4)	Si2–N2	1.700(5) 2x
Ce3–O7B	2.34(3)	Si2–N10	1.706(6)
Ce3–O7B	2.42(3)	Si2–N11	1.75(3)
Ce3–N2	2.514(6)	Si3–N3	1.708(5)
Ce3–N3	2.617(7)	Si3–N9	1.713(5)
Ce3–N11	2.6809(18)	Si3–N2	1.729(5)
Ce3–N11	2.705(3)	Si3–N6	1.741(4)

Bond	*d* / Å	Bond	*d* / Å
Ce3–N2	2.7104(6)	Si4–N3	1.692(5) 2x
Ce3–N4	2.714(3)	Si4–N5	1.724(6)
Ce3–N3	2.7653 (7)	Si4–N4	1.751(8)
Ce4A–Ce4B	0.530(2)	Si5A–Si5B	0.493(15)
Ce4A–O7C	2.172(15)	Si5A–O7C	1.58(5)
Ce4A–N2	2.415(5) 2x	Si5A–O7A	1.727(17) 2x
Si5A–N4	1.730(8) 2x	Si5B–O7C	1.66(4)
Si5B–O7A	1.36(2)	Si5B–N4	1.797(11) 2x

Table 9.43: Selected bonding angles for $K_{1.25}Ce_{7.75}[Si_{11}N_{21}O_2]O_{0.75}$, standard deviations are given in parentheses.

Angle	Bonding angle / °	Angle	Bonding angle / °
N10–Ce1–N6	127.63 (16)	N5–Ce2B–N1	156.4(6)
N6–Ce1–N6	104.8(3)	N5–Ce2B–O13	78.4(4)
N10–Ce1–N3	94.15(12)	N1–Ce2B–O13	78.0(4)
N6–Ce1–N3	63.68(12)	N5–Ce2B–N9	121.55(16)
N6–Ce1–N3	110.80(14)	N1–Ce2B–N9	63.52(18)
N3–Ce1–N3	171.7(2)	O13–Ce2B–N9	100.8(3)
N3–Ce1–N3	118.8(2)	N9–Ce2B–N9	116.0(3)
O7A–Ce2A–N5	121.2(5)	N5–Ce2B–N3	64.29(19)
O7A–Ce2A–O7B	31.3(14)	N1–Ce2B–N3	122.74(17)
O7B–Ce2A–N5	89.9(14)	O13–Ce2B–N3	105.3(3)
O7A–Ce2A–N1	111.1(5)	N9–Ce2B–N3	59.72(16)
N5–Ce2A–N1	127.7(4)	N9–Ce2B–N3	153.9(5)
O7B–Ce2A–N1	142.4(14)	N3–Ce2B–N3	111.5(3)
O7A–Ce2A–N9	90.1(2)	N5–Ce2B–O7A	106.7(5)
N5–Ce2A–N9	114.89(13)	N1–Ce2B–O7A	96.8(5)
O7B–Ce2A–N9	104.9(6)	O13–Ce2B–O7A	174.9(4)
N1–Ce2A–N9	62.60(12)	N9–Ce2B–O7A	76.6(3)
N9–Ce2A–N9	121.0(2)	N3–Ce2B–O7A	77.4(3)
O7A–Ce2A–N3	90.5(3)	O7B–Ce3–O7B	53(3)
N5–Ce2A–N3	62.83(13)	O7B–Ce3–N2	95.4(14)
O7B–Ce2A–N3	74.5(7)	O7B–Ce3–N2	148.2(13)
N1–Ce2A–N3	119.37(13)	O7B–Ce3–N3	114.3(14)
N9–Ce2A–N3	61.46(15)	O7B–Ce3–N3	80.1(14)
N9–Ce2A–N3	177.53(15)	N2–Ce3–N3	117.70(18)

Angle	Bonding angle / °	Angle	Bonding angle / °
O7B–Ce3–N11	159.4(15)	N2–Ce4A–N9	64.81(16)
O7B–Ce3–N11	147.5(14)	N2–Ce4A–N9	140.16(17)
N2–Ce3–N11	64.3(6)	N9–Ce4A–N9	122.5(2)
N3–Ce3–N11	80.2(4)	O7C–Ce4A–N8	102.1(12)
O7B–Ce3–N11	152.2(15)	N2–Ce4A–N8	123.5(2)
O7B–Ce3–N11	149.1(15)	N9–Ce4A–N8	63.09(12)
N2–Ce3–N11	61.3(6)	O7C–Ce4A–O7A	32.8(5)
N3–Ce3–N11	91.2(4)	N2–Ce4A–O7A	80.2(3)
N11–Ce3–N11	11.7(6)	N2–Ce4A–O7A	121.0(3)
O7B–Ce3–N2	139.9(14)	N9–Ce4A–O7A	81.6(4)
O7B–Ce3–N2	88.7(13)	N9–Ce4A–O7A	137.4(3)
N2–Ce3–N2	122.7(2)	N8–Ce4A–O7A	111.8(4)
N3–Ce3–N2	61.64(18)	O7A–Ce4A–O7A	60.4(7)
N11–Ce3–N2	59.2(6)	N2–Ce4B–N2	89.8(3)
N11–Ce3–N2	61.5(6)	N2–Ce4B–O12	87.1(5)
O7B–Ce3–N4	72.1(15)	N2–Ce4B–N9	156.14(19)
O7B–Ce3–N4	88.3(15)	N2–Ce4B–N9	67.83(17)
N2–Ce3–N4	78.8(2)	O12–Ce4B–N9	83.7(3)
N3–Ce3–N4	62.4(2)	N9–Ce4B–N9	132.4(2)
N11–Ce3–N4	104.8(5)	N2–Ce4B–N8	133.76(15)
N11–Ce3–N4	113.9(5)	O12–Ce4B–N8	81.7(8)
O7B–Ce3–N3	78.4(15)	N9–Ce4B–N8	66.43(12)
O7B–Ce3–N3	106.8(14)	N2–Ce4B–O7C	97.2(6)
N2–Ce3–N3	62.08(19)	O12–Ce4B–O7C	173.9(11)

Angle	Bonding angle / °	Angle	Bonding angle / °
N3–Ce3–N3	166.8(2)	N9–Ce4B–O7C	93.9(4)
N11–Ce3–N3	88.6(4)	N8–Ce4B–O7C	92.2(10)
N11–Ce3–N3	77.2(4)	O12–Ce/K5–O12	65.2(13)
O7C–Ce4A–N2	110.9(8)	O12–Ce/K5–N6	92.7(7)
N2–Ce4A–N2	85.8(3)	O12–Ce/K5–N6	157.9(7)
O7C–Ce4A–N9	104.7(5)	N6–Ce/K5–N6	109.3(3)
O12–Ce/K5–N9	79.8(3)	N3–Si3–N6	110.8(3)
O12–Ce/K5–N9	110.9(3)	N9–Si3–N6	111.1(3)
N6–Ce/K5–N9	62.29(11)	N2–Si3–N6	114.2(3)
N6–Ce/K5–N9	110.02(12)	N3–Si4–N3	113.4(4)
N9–Ce/K5–N9	167.8(2)	N3–Si4–N5	109.6(3)
N9–Ce/K5–N9	59.3(2)	N3–Si4–N4	106.8(3)
N9–Ce/K5–N9	119.2(2)	N5–Si4–N4	110.5(4)
N9–Si1–N9	111.4(4)	O7C–Si5A–O7A	54.9(6)
N9–Si1–N1	106.7(3)	O7A–Si5A–O7A	109.8(11)
N9–Si1–N8	108.2(3)	O7C–Si5A–N4	126.0(3)
N1–Si1–N8	115.8(6)	O7A–Si5A–N4	1097(3)
N11–Si2–N2	109.9(3)	N4–Si5A–N4	108.0(5)
N2–Si2–N2	114.5(4)	O7C–Si5B–O7A	60.0(10)
N11–Si2–N10	101.7(6)	O7A–Si5B–O7A	105.1(13)
N2–Si2–N10	110.0(2)	O7C–Si5B–N4	117.2(6)
N11–Si2–N11	18.3(10)	O7A–Si5B–N4	126.9(5)
N2–Si2–N11	101.0(3)	N4–Si5B–N4	102.3(8)
N10–Si2–N11	120.0(6)	O7A–Si5B–O7B	44.2(19)
N3–Si3–N9	110.7(3)	O7A–Si5B–O7B	149(2)

Angle	Bonding angle / °	Angle	Bonding angle / °
N3–Si3–N2	105.2(3)	O7C–Si5B–O7B	104(2)
N9–Si3–N2	104.5(3)	N4–Si5B–O7B	107.7(12)

9.6.2 Cerium coordination polyhedra in $K_{1.25}Ce_{7.75}[Si_{11}N_{21}O_2]O_{0.75}$

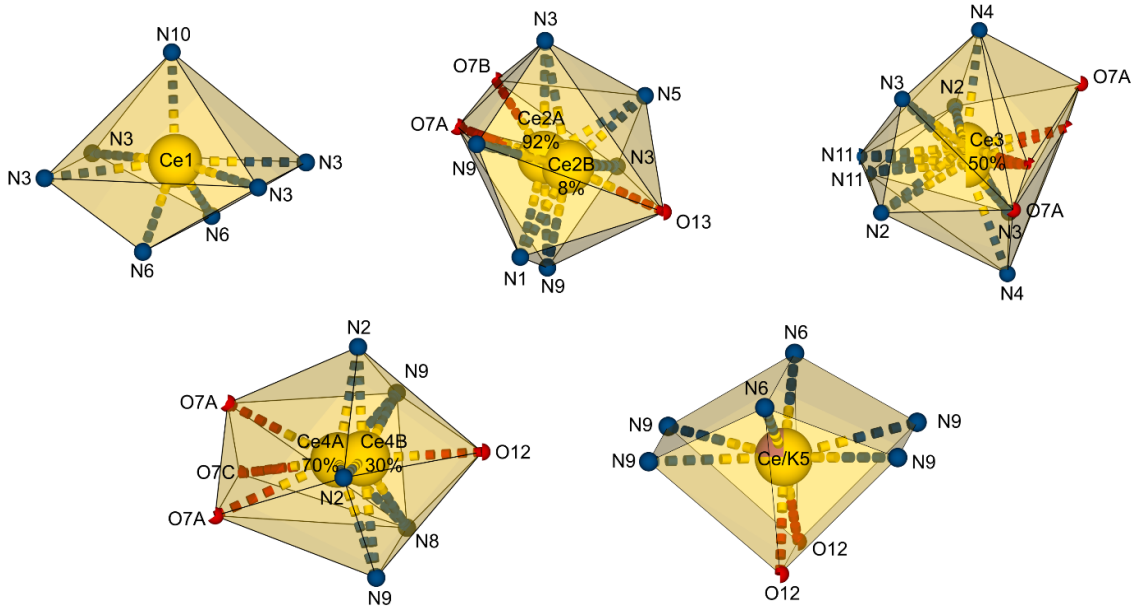

Figure 9.7: Coordination polyhedra of the cerium and mixed occupied cerium/potassium positions in $K_{1.25}Ce_{7.75}[Si_{11}N_{21}O_2]O_{0.75}$. Partially or mixed occupied positions are shown according to their site occupation factor or occupation is given in percentage.

9.6.3 Rietveld refinement data of $K_{1.25}Ce_{7.75}[Si_{11}N_{21}O_2]O_{0.75}$

Table 9.44: Crystallographic data for $K_{1.25}Ce_{7.75}[Si_{11}N_{21}O_2]O_{0.75}$ obtained by Rietveld refinement, standard deviations are given in parentheses.

Formula	**$K_{1.25}Ce_{7.75}[Si_{11}N_{21}O_2]O_{0.75}$**
Crystal system	orthorhombic
Space group	*Cmmm* (no. 65)
Lattice parameters / Å	a = 11.1693(11) b = 23.260(2) c = 9.5915(8)
Cell volume / Å^3	2491.9(4)
Density / g·cm^{-3}	4.750(15)
Formula units / cell	4
T / K	293(2)
Diffractometer	STOE STADI P
Detector	Mythen 1K
Monochromator	Ge(111)
Radiation / Å	Ag-$K\alpha_1$ (λ = 0.5594)
2θ range / °	$2 \leq 2\theta \leq 56.2$
Profile function	fundamental parameters model
Background function	Shifted Chebyshev
Data points	3619
Number of reflections	3525
Refined parameters (thereof background)	43 (10)
R values	R_p = 0.0659
	R_{wp} = 0.0920
	R_{Bragg} = 0.0491
Goodness of fit	2.215

Table 9.45: Wyckoff positions and atomic coordinates of $K_{1.25}Ce_{7.75}[Si_{11}N_{21}O_2]O_{0.75}$ obtained from Rietveld refinement, standard deviations are given in parentheses.

Atom	Wyckoff position	*x*	*y*	*z*	U_{eq} / Å^2	S.O.F.
Ce1	4*j*	0	0.3389(6)	½	0.7	1
Ce2A	8*p*	0.2829(9)	0.1040(4)	0	0.7	0.873(11)
Ce2B	8*p*	0.338(6)	0.053(3)	0	0.7	0.127(11)
Ce3	16*r*	0.2274(12)	0.2518(9)	0.2230(10)	0.7	1
Ce4A	8*n*	0	0.151(2)	0.246(4)	0.7	0.195(17)
Ce4B	8*n*	0	0.1109(6)	0.2304(11)	0.7	0.805(17)
Ce5	4*h*	0.1838(13)	0	½	0.7	0.75
K5	4*h*	0.1838(13)	0	½	0.7	0.25
K6	4*l*	0	½	0.315(4)	0.7	1
Si1	8*o*	0.137(3)	0	0.168(4)	0.7	1
Si2	8*q*	0.142(3)	0.2000(18)	½	0.7	1
Si3	16*r*	0.263(2)	0.1183(11)	0.357(3)	0.7	1
Si4	8*n*	0	0.3321(18)	0.164(4)	0.7	1
Si5A	4*i*	0	0.2119	0	0.7	0.655
Si5B	8*p*	0.0441	0.2120	0	0.7	0.173
N1	4*g*	0.2082	0	0	0.7	1
N2	16*r*	0.1471	0.1648	0.3510	0.7	1
N3	16*r*	0.1266	0.3484	0.2484	0.7	1
N4	8*n*	0	0.2556	0.1458	0.7	1
N5	4*i*	0	0.3624	0	0.7	1
N6	8*q*	0.3183	0.0931	½	0.7	1
O7A	8*p*	0.1265	0.1692	0	0.7	0.655
O7B	8*p*	0.215	0.208	0	0.7	0.173
O7C	4*i*	0	0.1438	0	0.7	0.345
N8	4*k*	0	0	0.1819	0.7	1

Atom	Wyckoff position	*x*	*y*	*z*	U_{eq} / Å^2	S.O.F.
N9	16*r*	0.2079	0.0605	0.2443	0.7	1
N10	4*j*	0	0.2397	½	0.7	1
N11	8*q*	0.232	0.2580	½	0.7	0.5
O12	4*j*	0	0.0555	½	0.7	0.5
O13	2*b*	½	0	0	0.7	0.5

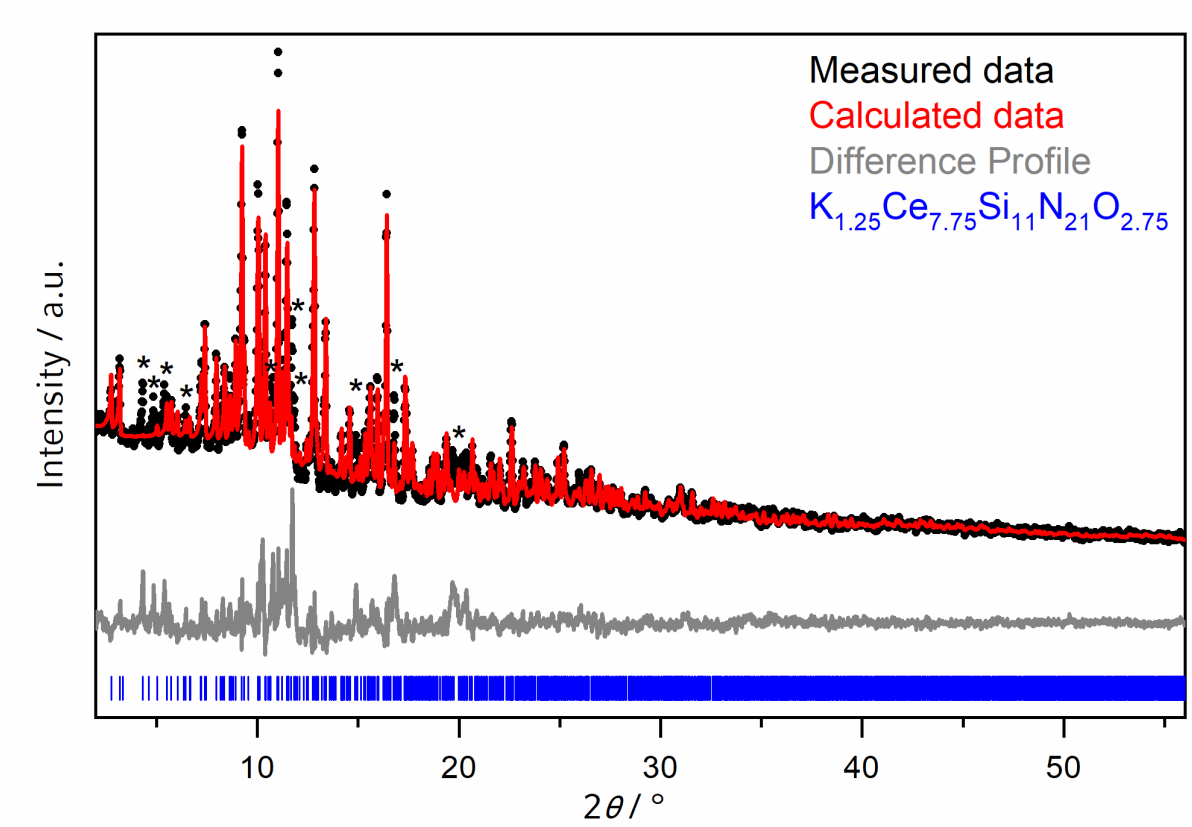

Figure 9.8: Rietveld refinement plot based on PXRD data of $K_{1.25}Ce_{7.75}[Si_{11}N_{21}O_2]O_{0.75}$ with experimental data (black dots), calculated diffraction pattern (red line), difference profile (gray line) and reflection positions of $K_{1.25}Ce_{7.75}[Si_{11}N_{21}O_2]O_{0.75}$ (blue bars). Reflections of an unknown side phase are marked with asterisks.

9.6.4 BVS Calculations

BVS calculations were performed using the program EXPO2014 v1.22.11.[3] For $R_0(Si^{4+}–N^{3–})$, an optimized parameter for nitridosilicates was used.[4] For $K_{1.25}Ce_{7.75}[Si_{11}N_{21}O_2]O_{0.75}$, no reasonable values were obtained which is probably caused by the fact that not reliable value for $R_0(K^{+}–N^{3–})$ is reported in the literature since only few examples of potassium in nitridic environment are reported in the literature. Additionally, the isolated atoms along the *achter* rings can also only be insufficiently described by the BVS theory.

Table 9.46: Results of BVS calculations for $Li_2Ce_4[Si_4N_8]O_3$ and $Li_2La_4[Si_4N_8]O_3$.

Atom site	Expected charge	$Li_2Ce_4[Si_4N_8]O_3$	$Li_2La_4[Si_4N_8]O_3$
Ce1/La1	3	2.3277	2.5335
Si1	4	4.3134	4.2930
Li1	1	1.2066	1.2472
N1	–3	2.9625	3.0853
N2	–3	2.8708	2.9915
O1	–2	1.4447	1.8070
O2	–2	2.1000	1.8429

9.6.5 CHARDI Calculations

CHARDI calculations were performed with the program CHARDI2015.[5-6]

Table 9.47: Results of CHARDI calculations for $Li_2Ce_4[Si_4N_8]O_3$ and $Li_2La_4[Si_4N_8]O_3$.

Atom site	Expected charge	$Li_2Ce_4[Si_4N_8]O_3$	$Li_2La_4[Si_4N_8]O_3$
Ce1/La1	3	2.95	2.98
Si1	4	4.01	4.01
Li1	1	1.07	1.03
N1	–3	–2.84	–2.99
N2	–3	–3.17	–3.01
O1	–2	–1.85	–1.96
O2	–2	–2.06	–2.02

Table 9.48: Results of CHARDI calculations for $K_{1.25}Ce_{7.75}[Si_{11}N_{21}O_2]O_{0.75}$.

Atom site	Expected charge	$K_{1.25}Ce_{7.75}[Si_{11}N_{21}O_2]O_{0.75}$
Ce1	3	2.93
Ce2A	2.76	1.85
Ce2B	0.24	1.39
Ce3	1.5	1.57
Ce4A	2.10	1.77
Ce4B	0.90	1.02
Ce5/K5	2.5	2.12
K6	1	1.01
Si1	4	5.49
Si2	4	3.76
Si3	4	3.91
Si4	4	3.84
Si5A	2.62	0.82
Si5B	0.69	1.34
N1	−3	−2.16
N2	−3	−3.09
N3	−3	−3.01
N4	−3	−4.17
N5	−3	−2.72
N6	−3	−3.18
O7A	−1.31	−1.77
O7B	−0.346	−0.35
O7C	−0.69	−0.79
N8	−3	−2.37
N9	−3	−2.82
N10	−3	−3.13
N11	−1.5	−1.56
O12	−1	−1.17
O13	−1	−0.99

9.6.6 EDX Measurements

Table 9.49: SEM EDX measurements of a sample of $Li_2Ce_4[Si_4N_8]O_3$, standard deviations of the mean are given in parentheses.

	Ce	Si	O	N
Measurement 1	18	23	9	50
Measurement 2	18	23	8	51
Measurement 3	18	23	9	50
Measurement 4	23	26	8	43
Measurement 5	15	22	11	52
Measurement 6	15	22	12	51
Measurement 7	14	21	11	54
Average	**17(3)**	**23(2)**	**10(2)**	**50(4)**
Calculated	21	21	16	42

Table 9.50: SEM EDX measurements of a sample of $Li_2La_4[Si_4N_8]O_3$, standard deviations of the mean are given in parentheses.

	La	Si	O	N
Measurement 1	14	24	13	49
Measurement 2	14	23	13	50
Measurement 3	15	24	12	49
Measurement 4	20	22	24	34
Measurement 5	20	20	18	42
Measurement 6	15	23	10	52
Measurement 7	14	23	9	54
Average	**16(3)**	**23(2)**	**14(5)**	**47(7)**
Calculated	21	21	16	42

Table 9.51: SEM EDX measurements of a sample of $K_{1.25}Ce_{7.75}[Si_{11}N_{21}O_2]O_{0.75}$, standard deviations of the mean are given in parentheses.

	K	Ce	Si	O	N
Measurement 1	4	18	26	13	40
Measurement 2	4	18	26	13	40
Measurement 3	3	14	24	15	44
Measurement 4	3	18	25	15	40
Measurement 5	3	19	26	13	40
Measurement 6	3	15	24	11	46
Measurement 7	3	19	26	13	40
Measurement 8	3	15	24	11	46
Measurement 9	3	15	24	12	45
Measurement 10	3	18	25	13	41
Measurement 11	3	19	25	13	40
Measurement 12	3	16	23	10	48
Measurement 13	3	15	23	15	43
Measurement 14	4	18	26	13	40
Average	**3(1)**	**17(2)**	**24(1)**	**13(2)**	**43(3)**
Calculated	3	18	25	6	48

9.6.7 FTIR Analysis

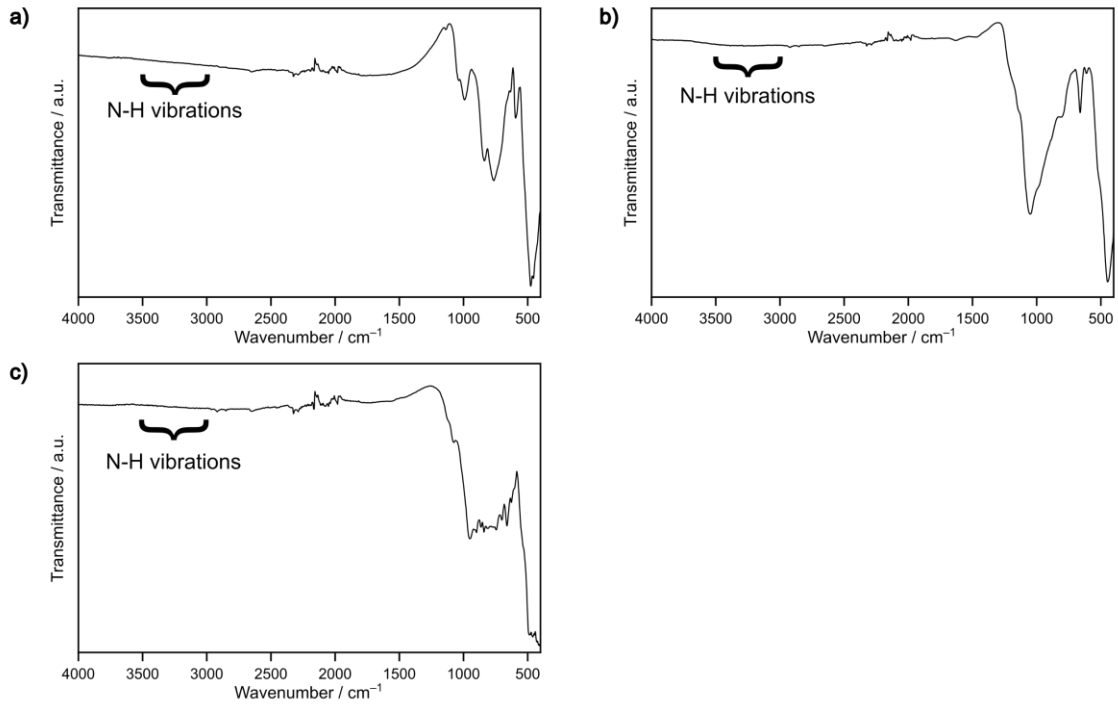

Figure 9.9: FTIR spectra of $Li_2La_4[Si_4N_8]O_3$ (a), $Li_2Ce_4[Si_4N_8]O_3$ (b) and $K_{1.25}Ce_{7.75}[Si_{11}N_{21}O_2]O_{0.75}$ (c) with the region highlighted, where typical N−H stretching vibrations would be expected (3000−3500 cm^{-1}).

9.7 References

[1] M. Nagib, H. Kistrup, H. Jacobs, "Neutron diffraction by sodiumdeuteroamide, $NaND_2$", *Atomkernenerg./Kerntech.* **1975**, *26*, 87–90.

[2] L. Bonometti, F. Kraus, T. Graubner, A. J. Karttunen, B. Civalleri, L. Donà, L. Maschio, "A Fresh Look at a Well-Known Solid: Structure, Vibrational Spectra, and Formation Energy of $NaNH_2$", *J. Phys. Chem. C* **2023**, *127*, 12287−12294.

[3] A. Altomare, C. Cuocci, C. Giacovazzo, A. Moliterni, R. Rizzi, N. Corriero, A. Falcicchio, "EXPO2013: a kit of tools for phasing crystal structures from powder data", *J. Appl. Crystallogr.* **2013**, *46*, 1231−1235.

[4] M. Dialer, M. M. Pointner, S. L. Wandelt, P. Strobel, P. J. Schmidt, L. Bayarjargal, B. Winkler, W. Schnick, "Order and Disorder in Mixed (Si, P)–N Networks $Sr_2SiP_2N_6$:Eu^{2+} and $Sr_5Si_2P_6N_{16}$:Eu^{2+}", *Adv. Opt. Mater.* **2024**, *12*, 2302668.

[5] M. Nespolo, "Charge distribution as a tool to investigate structural details. IV. A new route to heteroligand polyhedra", *Acta Crystallogr., Sect. B: Struct. Sci., Cryst. Eng. Mater.* **2016**, *72*, 51−66.

[6] M. Nespolo, B. Guillot, "CHARDI2015: charge distribution analysis of non-molecular structures", *J. Appl. Crystallogr.* **2016**, *49*, 317−321.

[7] R. Juza, H. Jacobs, W. Klose, "Die Kristallstrukturen der Tieftemperaturmodifikationen von Kalium- und Rubidiumamid", *Z. Anorg. Allg. Chem.* **1965**, *338*, 171–178.

[8] J. A. Kechele, C. Hecht, O. Oeckler, J. Schmedt auf der Günne, P. J. Schmidt, W. Schnick, "$Ba_2AlSi_5N_9$ – A New Host Lattice for Eu^{2+}-Doped Luminescent Materials Comprising a Nitridoalumosilicate Framework with Corner- and Edge-Sharing Tetrahedra", *Chem. Mater.* **2009**, *21*, 1288−1295.

10 Miscellaneous

10.1 List of Publications Within This Dissertation

In the following the publications contained in this dissertation are listed in the order of their appearance in the text together with the respective author contributions:

1 **Ammonothermal Synthesis and Crystal Structure of the Ternary Amide $Na_2Ba(NH_2)_4$**
Florian M. Engelsberger, Kristian Witthaut, and Wolfgang Schnick
Z. Anorg. Allg. Chem. **2024**, *650*, e202400053

F. M. Engelsberger: Formal analysis: Lead; Investigation: Lead; Validation: Lead; Visualization: Lead; Writing – original draft: Lead; Writing – review & editing: Equal
K. Witthaut: Formal analysis: Supporting; Investigation: Supporting; Validation: Supporting; Writing – original draft: Supporting; Writing – review & editing: Supporting
W. Schnick: Conceptualization: Lead; Funding acquisition: Lead; Project administration: Lead; Resources: Lead; Supervision: Lead; Validation: Supporting; Writing – original draft: Supporting; Writing – review & editing: Supporting

2 Ammonothermal Synthesis of Luminescent Imidonitridophosphate $Ba_4P_4N_8(NH)_2:Eu^{2+}$

Florian M. Engelsberger, Reinhard M. Pritzl, Jennifer Steinadler, Kristian Witthaut, Thomas Bräuniger, Peter J. Schmidt, and Wolfgang Schnick

Chem. Eur. J. **2024**, *30*, e202402743

F. M. Engelsberger: Formal analysis: Lead; Investigation: Lead; Validation: Equal; Visualization: Lead; Writing – original draft: Lead; Writing – review & editing: Lead

R. M. Pritzl: Formal analysis: Supporting; Investigation: Supporting; Validation: Supporting; Writing – original draft: Supporting; Writing – review & editing: Supporting

J. Steinadler: Formal analysis: Supporting; Investigation: Supporting; Validation: Supporting; Visualization: Supporting; Writing – original draft: Supporting; Writing – review & editing: Supporting

K. Witthaut: Formal analysis: Supporting; Investigation: Supporting; Validation: Supporting; Writing – original draft: Supporting; Writing – review & editing: Supporting

T. Bräuniger: Formal analysis: Supporting; Investigation: Supporting; Methodology: Supporting; Supervision: Supporting; Validation: Supporting; Writing – original draft: Supporting; Writing – review & editing: Supporting

P. J. Schmidt: Conceptualization: Equal; Formal analysis: Supporting; Funding acquisition: Supporting; Investigation: Supporting; Resources: Supporting; Supervision: Supporting; Validation: Supporting; Writing – original draft: Supporting; Writing – review & editing: Supporting

W. Schnick: Conceptualization: Equal; Funding acquisition: Lead; Project administration: Lead; Resources: Lead; Supervision: Lead; Validation: Equal; Writing – original draft: Supporting; Writing – review & editing: Supporting

3 **Ammonothermal Synthesis and Solid-State NMR Study of the Imidonitridosilicate $Rb_3Si_6N_5(NH)_6$**

Florian M. Engelsberger, Thanh G. Chau, Thomas Bräuniger, and Wolfgang Schnick

Chem. Eur. J. **2024**, *30*, e202401238

F. M. Engelsberger: Formal analysis: Lead; Investigation: Lead; Validation: Lead; Visualization: Lead; Writing – original draft: Lead; Writing – review & editing: Equal

T. G. Chau: Investigation: Supporting; Writing – original draft: Supporting; Writing – review & editing: Supporting

T. Bräuniger: Formal analysis: Supporting; Investigation: Supporting; Methodology: Supporting; Supervision: Supporting; Validation: Supporting; Writing – original draft: Supporting; Writing – review & editing (Supporting)

W. Schnick: Conceptualization: Lead; Funding acquisition: Lead; Project administration: Lead; Resources: Lead; Supervision: Lead; Validation: Supporting; Writing – original draft: Supporting; Writing – review & editing: Supporting

4 **Nitride Zeolites from Ammonothermal Synthesis**

Florian M. Engelsberger and Wolfgang Schnick

Chem. Eur. J. **2024**, e202404405

F. M. Engelsberger: Formal analysis: Lead; Investigation: Lead; Validation: Equal; Visualization: Lead; Writing – original draft: Lead; Writing – review & editing: Equal

W. Schnick: Funding acquisition: Lead; Project administration: Lead; Resources: Lead; Supervision: Lead; Validation: Equal; Writing – review & editing: Equal

10.2 Conference Contributions and Oral Presentations

1 **Ion Exchange in Oxonitridosilicates $M Si_2O_2N_2$: Eu^{2+}**
Florian M. Engelsberger, Phillipp Bielec, and Wolfgang Schnick
Poster, URCUP 2018
Irsee (Germany), 20.10.2018

2 **Ammonothermal Synthesis of Ternary Grimm-Sommerfeld Analogous Nitride Semiconductors *II-IV*-N_2 (*II* = Mg, Mn, Zn; *IV* = Si, Ge)**
Florian M. Engelsberger, Mathias Mallmann, Jonas Häusler, and Wolfgang Schnick
Poster, e-conversion Conference
Venice (Italy), 10.09.2019

3 **Ammonothermal Synthesis of Oxide Nitrides I-IV-O-N (I = Li, Na, K; IV = Ge, Si)**
Florian M. Engelsberger
Talk, 5. Obergurgl-Seminar Festkörperchemie
Obergurgl (Austria), 29.01.2020

4 **Ammonothermal Synthesis of Oxide Nitrides I-IV-O-N (I = Li, Na, K; IV = Ge, Si)**
Florian M. Engelsberger
Talk, Schnick Group Seminar
Munich (Germany), 06.05.2020

5 **Ammonothermalsynthese von Nitridosilicaten**
Florian M. Engelsberger
Talk, Schnick Group Seminar
Munich (Germany), 30.06.2021

6 **Allerlei Ammonothermales**
Florian M. Engelsberger
Talk, Schnick Group Seminar
Munich (Germany), 01.06.2022

7 **Ammonothermal Synthesis of the Ternary Amide $Na_2Ba(NH_2)_4$**
Florian M. Engelsberger and Wolfgang Schnick
Poster, 21. Vortragstagung für Anorganische Chemie der Fachgruppen Wöhler-Vereinigung und Festkörperchemie und Materialforschung
Munich (Germany), 27.09.2022

8 **Ammonothermal Synthesis of Ternary and Quaternary Lithium Nitridosilicates**
Amelie Heilmaier, Florian M. Engelsberger, and Wolfgang Schnick
Poster, URCUP 2022
Irsee (Germany), 22.10.2022

9 **El Camino – Auf Jacobs Wegen**

Florian M. Engelsberger

Talk, 6. Obergurgl-Seminar Festkörperchemie

Obergurgl (Austria), 27.01.2023

10 **Ammonothermal Synthesis of Rare-Earth (Oxo)Nitridosilicates**

Florian M. Engelsberger and Wolfgang Schnick

Poster, 11th International Symposium on Nitrides

Saint-Malo (France), 03.05.2023

11 **Ammonothermalsynthese von Nitridosilicaten – Von Intermediaten zu Netzwerken**

Florian M. Engelsberger

Talk, Schnick Group Seminar

Munich (Germany), 24.05.2023

12 **Ammonothermal Synthesis of $Ba_4P_4N_8(NH)_2$**

Florian M. Engelsberger

Talk, Lumileds Meeting

Aachen (Germany), 20.09.2023

13 **Ammonothermal Synthesis of Functional Ternary and Multinary Lanthanoid (Oxo)nitridosilicates**

Kilian Möchel, Florian M. Engelsberger, and Wolfgang Schnick

Poster, URCUP 2023

Irsee (Germany), 21.10.2023

14 **VerCerrte Welt**

Florian M. Engelsberger

Talk, 7. Obergurgl-Seminar Festkörperchemie

Obergurgl (Austria), 31.01.2024

10.3 Deposited Crystal Structures

The Crystallographic Information Files (CIF) of the investigated compounds are provided free of charge by the joint Cambridge Crystallographic Data Centre and Fachinformationszentrum Karlsruhe Access Structures service (http:www.ccdc.cam.ac.uk/structures) by quoting the corresponding deposition number.

Compound	**Deposition Number**
$Na_2Ba(NH_2)_4$	2348264
$Ba_4P_4N_8(NH)_2$ (refinement without H positions)	2372017
$Ba_4P_4N_8(NH)_2$ (refinement with H positions)	2372022
$Rb_3Si_6N_5(NH)_6$	2341243
$Li_2La_4[Si_4N_8]O_3$	2390327
$Li_2Ce_4[Si_4N_8]O_3$	2390328
$K_{1.25}Ce_{7.75}[Si_{11}N_{21}O_2]O_{0.75}$	2390329